SISSA
INTERNATIONAL SCHOOL OF ADVANCED STUDIES

TRIESTE, ACADEMIC YEAR 2019-2020

Non-equilibrium fluctuations and dynamics in isolated quantum many-body systems

Author:
Gabriele PERFETTO

Supervisor:
Prof. Andrea GAMBASSI

A thesis submitted in fulfillment of the requirements for the degree of Doctor of Philosophy (Ph.D.)

in

STATISTICAL PHYSICS

Abstract

This thesis concerns a very active area of current research in theoretical physics, which is non-equilibrium statistical mechanics. More specifically, the focus will be on isolated many body systems driven out of equilibrium. We shall consider primarily quantum systems, albeit many of the theoretical techniques that will be used can be applied to both classical and quantum statistical systems.

Equilibrium phenomena have been understood since two centuries within statistical mechanics, as the latter provides a general framework to classify the macroscopic behavior of equilibrium phases and phase transitions in systems that are composed by many particles in interaction. Non-equilibrium systems show, instead, a much richer behavior than equilibrium ones, which is therefore harder to encompass within a general set of broadly applicable principles. Research in this direction proceeds mainly on a case-by-case basis. The development of analytical techniques which are, to some extent, universally applicable for the description of the non-equilibrium physics of many-body systems is therefore of paramount importance.

To make progresses in this direction a particular relevant framework has emerged in theoretical physics: *large deviation theory*. This framework builds on the computation of the large deviation function, which provides the statistics of rare but significant fluctuations. It generalizes to non-equilibrium conditions the concepts of entropy, thermodynamic phases and phase transitions, that are canonical quantities for describing the equilibrium statistical mechanics of many-body systems.

An ideal field to apply the large deviation formalism is the one of isolated many body quantum systems. As a matter of fact, advances in the experimental techniques in ultra-cold atomic gases have enabled the realization of highly isolated quantum many-body systems that can be brought out of equilibrium with high-precision control of the Hamiltonian's parameters. No coupling with an external bath is present, and therefore no ad hoc assumption to describe the interaction between the bath and the system is needed. As a consequence, the latter evolves in time purely according to the laws of quantum mechanics.

The aim of the thesis is to study the non-equilibrium dynamics and fluctuations of isolated many-body quantum systems. The novel contribution of this work is two-fold. First, we have developed new analytical techniques to study exactly the large deviation statistics of physical quantities relevant for the description of systems driven out of equilibrium, like the work or the time-integrated current, discussed in Part I of the thesis. Second, we have singled out a class of experimentally relevant non-disordered quantum systems showing a dramatically slow approach to thermal equilibrium and we have provided quantitative predictions for this behavior, which is discussed in Part II.

The structure of the thesis is as follows. Part I is composed by Chapters 1, 2, 3 and 4. Chapter 1 provides an introduction to the theoretical background necessary for understanding the non-equilibrium dynamics of isolated many-body quantum systems. In this context, the large deviation theory is moreover introduced as the natural mathematical language which overarches equilibrium thermodynamics, while, at the same time, it provides the right organizing principles to generalize this description to the dynamical non-equilibrium world. In Chapter 2 we put this program into practice by considering a quantity characteristic of equilibrium thermodynamics: the work. With the aim of studying its non-equilibrium fluctuations we study the work in a far from equilibrium dynamical situation, which is named *quantum quench*. The latter is an abrupt change of one of the Hamiltonian parameters. This operation can be considered as a thermodynamic transformation that drives the system out of equilibrium. In this context, the work is considered as a stochastic variable characterized by a probability distribution. Aiming at the statistics of the quantum fluctuations of the work we exactly compute the associated large deviation function for the interacting one-dimensional Bose gas. In Chapter 3 we consider another ubiquitous non-equilibrium phenomenon, whose statistical properties cannot be encompassed within equilibrium statistical mechanics: transport of energy, matter, charge etc... The heat flow between two leads kept at different temperatures, in particular, has ubiquitous technological applications and can be accessed with current cold atoms experiments. We then model the non-equilibrium dynamics generated by connecting two identical subsystems initially prepared at different temperatures. As a consequence of the initial inhomogeneous temperature profile, an energy current flow develops, the dynamics in space and time of which we quantitatively describe for the quantum Ising and harmonic chains. Going beyond mean values, we then calculate exactly the large deviation function of the energy current providing a complete characterization of its statistical fluctuations. In Chapter 4 we consider again the dynamics ensuing from inhomogeneous initial conditions, but we extend the analysis of Chapter 3 to interacting systems via the *generalized hydrodynamics* formalism. First a thorough description of the dynamical two-point correlation functions is given. Then, we exploit the latter result in order to exactly determine the non-equilibrium fluctuations of the total transferred energy, charge, matter from one subsystem to the other.

Part II is composed by Chapter 5. Therein we explore the non-equilibrium dynamics which emerges in inhomogeneous systems, such as those considered in Chapters 3 and 4, but in the presence of confinement of excitations, which alter qualitatively the ensuing dynamics. Confinement is a well-known phenomenon not only in high-energy physics, but also in condensed matter. In Chapter 5 we first discuss the physics of confinement in quantum statistical systems and we connect it with lattice gauge theories. Then, the dynamical effects of confinement on the real-time evolution are presented. Particular emphasis will be given in contrasting the dynamics ensuing in models experiencing confinement against the fundamental mechanism of thermalization, i.e., the approach to thermal equilibrium. Our results, indeed, shows that models exhibiting confinement, despite being non-disordered and despite not-possessing any particular symmetry, avoid thermalization within the accessible time-scales.

List of Publications

Part I of the thesis is adapted from the following publications and preprints:

[1] **G. Perfetto** and A. Gambassi,
Ballistic front dynamics after joining two semi-infinite quantum Ising chains,
Phys. Rev. E **96**, 012138 (2017).

[2] **G. Perfetto**, L. Piroli and A. Gambassi,
Quench action and large deviations: Work statistics in the one-dimensional Bose gas,
Phys. Rev. E **100**, 032114 (2019).

[3] F. S. Møller, **G. Perfetto**, B. Doyon and J. Schmiedmayer
Euler-scale dynamical correlations in integrable systems with fluid motion,
SciPost Phys. Core **3**, 16 (2020).

[4] **G. Perfetto** and A. Gambassi,
Dynamics of large deviations in the hydrodynamic limit: non-interacting systems,
Phys. Rev. E **102**, 042128 (2020).

[5] **G. Perfetto** and B. Doyon,
Euler-scale dynamical fluctuations in non-equilibrium interacting integrable systems,
arXiv:2012.06496 (2020).

Part II of the thesis is based on the content of the following publications

[6] P. P. Mazza, **G. Perfetto**, A. Lerose, M. Collura and A. Gambassi
Suppression of transport in non-disordered quantum spin chains due to confined excitations,
Phys. Rev. B **99**, 180302(R) (2019).

[7] A. Lerose, F. M. Surace, P. P. Mazza, **G. Perfetto**, M. Collura and A. Gambassi
Quasilocalized dynamics from confinement of quantum excitations,
Phys. Rev. B **102**, 041118(R) (2020). **Editors' suggestion**

Contents

Chapter 1

An introduction to non-equilibrium dynamics

This Chapter is meant to introduce the field of non-equilibrium dynamics in many-body isolated quantum systems. We first review basic concepts about equilibrium statistical mechanics in Sec. 1.1. The large deviation theory is then introduced in Sec. 1.2 starting from the statistical mechanics description of equilibrium systems. In Sec. 1.3 we recall the fundamental aspects about the non-equilibrium dynamics in isolated systems which are relevant for the present discussion. In Sec. 1.4 we specialize the discussion to integrable models, as this class of systems has been the subject of our original contribution presented in Part I of the thesis. In Sec. 1.5 we discuss, instead, non-integrable models, particularly those displaying quantum confinement of excitations, which will be discussed at length in Part II of the thesis. The original results of the thesis are also briefly anticipated while presenting the research topics. Section 1.6 concludes this Chapter by drawing, for the reader's convenience, a brief and schematic presentation of the structure of the thesis and of the results contained within it.

1.1 Equilibrium statistical mechanics

The paradigmatic situation analyzed in statistical physics [8] is the one of systems, e.g., a magnet, composed by many particles, of the order of the Avogadro number $N_A = 6.02 \cdot 10^{23}$, interacting among themselves via short-range forces. It is immediate to realize that with such a huge number it is utterly intractable to attempt to study the *macroscopic* behavior of the system by considering the equation of motion, classical or quantum, for each of the *microscopic* constituents. A statistical description is then needed. This is precisely the point where statistical mechanics comes to our rescue.

To briefly illustrate this approach we will use perhaps the most famous lattice model of statistical mechanics: the two-dimensional Ising model on a square lattice

$$H = -J \sum_{(i,j)} \sigma_i \sigma_j - K \sum_{(i,k)} \sigma_i \sigma_k, \tag{1.1}$$

where J and K denote the ferromagnetic couplings between the nearest neighbors lattice sites (i,j) and (i,k) along the two spatial directions. $\sigma_i = \pm 1$ is a binary variable representing the spin at lattice site i. Remarkably, exploiting the transfer matrix approach [9], the two dimensional Ising model can be mapped onto the

one-dimensional transverse field quantum Ising chain (TFIC) in the scaling limit $J \to 0$, $K \to \infty$ with fixed ratio $J/\mathrm{e}^{-2K} = h$,

$$H = -\sum_i \sigma_i^x \sigma_{i+1}^x - h \sum_i \sigma_i^z, \tag{1.2}$$

where now σ_i^α, with $\alpha = \{x, y, z\}$, are Pauli spin 1/2 operators.

Statistical mechanics provides the complete description of the thermodynamic properties of the system, e.g., the pressure, the entropy and the magnetization, in terms of derivatives of the free energy density f. The importance of the Ising model in Eq. (1.1), or equivalently its quantum version in Eq. (1.2), lies in the fact that it can be exactly solved and therefore the free energy density and the whole equilibrium properties of the system can be computed exactly. In particular, the free energy density associated to the canonical distribution at temperature T of the classical Ising model in Eq. (1.1) is given by the celebrated Onsager solution [10–12]

$$f = -\frac{1}{\beta} \int_{-\pi}^{\pi} \frac{\mathrm{d}k}{2\pi} \mathcal{F}(k), \tag{1.3}$$

with

$$\mathcal{F}(k) = \ln \left\{ 2 \left[\cosh(2J\beta) \cosh(2K\beta) + h^{-1} (h^2 - 2h \cos k + 1)^{1/2} \right] \right\}. \tag{1.4}$$

k_B is the Boltzmann constant and $\beta = 1/(k_B T)$ the inverse temperature. The free energy f is also important as its analytical structure as a function of T locate *thermal phase transitions*, i.e., transitions driven by thermal fluctuations. For the two-dimensional classical Ising model the free energy f in Eqs. (1.3) and (1.4) turns out to have a singularity at $T = T_c$ in proximity of which it behaves as [10–12]

$$f(t) \sim t^2 \ln \quad \text{as} \quad |t| \quad t \to 0, \tag{1.5}$$

where $t = (T - T_c)/T_c$ is the reduced temperature for brevity. The second derivative of $f(t)$ is therefore discontinuous implying a second-order phase transition from a paramagnetic to a ferromagnetic phase as the temperature T decreases from above to below the critical value T_c. This transition is associated with the spontaneous breaking of the $\mathbb{Z}_2$ symmetry. In terms of the quantum Ising chain in Eq. (1.2) this behavior translates into an equilibrium *quantum phase transition*, i.e., a zero-temperature transition controlled by quantum fluctuations as the transverse field h crosses the critical value $h_c = 1$ [13]. Namely, $h < h_c$ corresponds to the ferromagnetic-ordered phase, where the longitudinal magnetization $\langle \sigma_i^x \rangle$ has non-vanishing expectation value in the ground state of the model. $h > h_c$, instead, corresponds to the paramagnetic-disordered phase $\langle \sigma_i^x \rangle = 0$. At the critical point $h = h_c$ the large distance behavior of the model is captured by a conformal field theory of non-interacting Majorana fermions with central charge $c = 1/2$ [14]. Note that the transition at $h = h_c$ has an intrinsic quantum nature as it is necessarily driven by quantum fluctuations since it takes place only at zero-temperature, i.e., in the ground state of the model. At finite temperature the quantum Ising chain in Eq. (1.2) belongs, as a matter of fact, to the same universality class as the one-dimensional classical Ising model [13], which is known to undergo no phase

transition at finite temperature.

1.2 Large deviation theory in a nutshell

One can say that there are two main possible approaches to the large deviation theory:

1. Within a mathematically oriented perspective one looks at the large deviation theory as an extension of the law of large numbers and the central limit theorem.

2. In the perspective of physics one considers the large deviation theory as a systematic method to compute entropies and free energies.

Historically, the mathematical framework has been developed in the 1960's and 1970's by Donsker and Varadhan in Refs. [15–18], while the connections with statistical physics are mainly due to Ellis in Refs. [19–21], see Ref. [22] for a comprehensive review. For concreteness we now introduce the large deviation theory via a very simple example drawn from Ref. [23] which explains the deep relation between the mathematical viewpoint, in Subsec. 1.2.1, and the physical one, in Subsec. 1.2.2.

1.2.1 The approach of mathematics

Consider the experiment where we toss a coin N times. The possible outcome N_i of the i-th trial is 1 (head, H) or 0 (tail, T) with equal probabilty $p = 1/2$. The number N_H of times the outcome H is obtained is a discrete random variable ranging in the set $\{0, 1, 2 \dots N\}$

$$N_H = \sum_{i=1}^{N} N_i. \tag{1.6}$$

The probability $P_N(N_H = M)$ of having $N_H = M$ is simply obtained in terms of the binomial coefficient

$$P_N(N_H = M) = \frac{1}{2^N} \binom{N}{M}. \tag{1.7}$$

The mean value μ and the variance σ^2 of P_N are readily calculated:

$$\begin{aligned} \mu &= \langle N_H \rangle = N/2, \\ \sigma^2 &= \langle N_H^2 \rangle - \langle N_H \rangle^2 = N/4. \end{aligned} \tag{1.8}$$

From Eq. (1.8) we notice that the mean value is extensive $\mu \sim N$, while fluctuations are of the order of $\sigma \sim \sqrt{N}$. This kind of fluctuations are usually referred to as *typical* fluctuations and they are described by the central limit theorem, which asserts that the sum of a large number N of independent random variables has a

Gaussian distribution

$$P_N(N_H = M) \simeq \sqrt{\frac{1}{2\pi\sigma^2}}\, \mathrm{e}^{-(M-\mu)^2/(2\sigma^2)}, \tag{1.9}$$

with μ and σ in our case given in Eq. (1.8). However, large *atypical* fluctuations, e.g., deviations from μ of order N, are not described by the Gaussian approximation provided by the central limit theorem. Quantifying the statistics of these rare-atypical fluctuations is the main objective of large deviation theory. Since we are interested in the limit of N very large and we know that μ grows extensively upon increasing N, we can set $M = uN$, with $0 < u < 1$, in Eq. (1.7) and expand the binomial coefficient by exploiting the Stirling approximation $N! \sim \sqrt{2\pi N}\, \mathrm{e}^{N\ln N - N}$ to get

$$P_N(N_H = uN) \asymp \mathrm{e}^{-NI(u)}, \tag{1.10}$$

with

$$I(u) = u \ln u + (1-u) \ln (1-u) + \ln 2. \tag{1.11}$$

The expression in Eq. (1.10) is named large deviation principle, while the function $I(u)$ is dubbed large-deviation or rate function and it is the cornerstone of the large deviation theory. The notation "$\asymp$" denotes equality of the right and left hand side on a logarithmic scale

$$I(u) = -\lim_{N\to\infty} \frac{1}{N} \ln P_N(u), \tag{1.12}$$

which implies that the leading order dependence of $P_N(u)$ on N is exponentially decaying with rate $I(u)$, while any additional sub-leading N-dependent term is canceled by the limiting procedure of Eq. (1.12). The function $I(u)$ is non-negative and convex with a unique zero at $u = \mu = 1/2$. By expanding $I(u)$ in series close to this value the leading term is found to be

$$I(u) = \frac{(u-\mu)^2}{2\sigma^2} \quad \text{as} \quad u \to \mu. \tag{1.13}$$

By plugging Eq. (1.13) into (1.10) the Gaussian approximation is recovered. The large deviation function therefore captures simulataneously both the small-typical Gaussian fluctuations, and the large-atypical ones. The comparison between $I(u)$ in Eq. (1.11) and its quadratic approximation (1.13) is shown in Fig. 1.1.

It is fundamental to emphasize that in the simple example described in this Section the large deviation principle Eq. (1.10) and the rate function $I(u)$ have been calculated directly by taking the limit $N \to \infty$ of P_N and using the Stirling formula. For continuous random variables and, in general, for more complex cases this approach is not viable. For these situations a more general scheme to compute the large deviation function is provided by a central result of large deviation theory known as Gärtner-Ellis theorem, see, e.g., Ref. [22]. For this purpose a central object to define is the so-called scaled cumulant generating function

(SCGF) $f(\lambda)$ for the random variable N_H

$$f(\lambda) = -\lim_{N\to\infty} \frac{1}{N} \ln\langle e^{-\lambda N_H}\rangle, \tag{1.14}$$

where the average $\langle \dots \rangle$ is performed over the probability distribution of N_H (in the case discussed here, this is provided by Eq. (1.7)). $f(\lambda)$ can be proved to be in general convex. As a consequence, see e.g., Ref. [24], it is continuous in the interior of its domain and it might diverge only at the boundaries of the latter. The domain can be then either a bounded (closed or open) interval or a semi-infinite interval or the whole real line, depending on the specific case analyzed. Because of its convexity, $f(\lambda)$ can further present a numerable set of points of non-differentiability, both in the interior and/or at the boundaries of its domain. The Gärtner-Ellis theorem states that if $f(\lambda)$ exists and it is everywhere differentiable in $\lambda \in \mathbb{R}$, then the large deviation principle in Eq. (1.10) holds and the rate function can be computed as

$$I(u) = -\inf_\lambda\{\lambda u - f(\lambda)\}. \tag{1.15}$$

The mapping between $f(\lambda)$ and $I(u)$ by the infimum is named Legendre-Fenchel transform. The Gärtner-Ellis theorem can be more generally applied even when $f(\lambda)$ is not differentiable for all $\lambda \in \mathbb{R}$. In these cases, this theorem holds pointwise in the whole range where $f(\lambda)$ is differentiable [22]. In particular, when $f(\lambda)$ is strictly convex, i.e., convex with no linear parts, this transform reduces to the Legendre transform with $I(u)$ related to $f(\lambda)$ by the Legendre duality relations

$$u = \frac{\mathrm{d}f(\lambda)}{\mathrm{d}\lambda} \quad \text{and} \quad \lambda = -\frac{\mathrm{d}I(u)}{\mathrm{d}u}. \tag{1.16}$$

From this duality it follows that the slope of $f(\lambda)$ as a function of λ equals u and, vice-versa, the slope of $I(u)$ as a function of u equals λ.

1.2.2 The approach of physics

To make contact with statistical physics one can perform the change of variable $\sigma_i = 2N_i - 1$ into Eq. (1.6) obtaining, up to an irrelevant additive constant,

$$E = -h\sum_{i=1}^{N} \sigma_i, \tag{1.17}$$

with $h = -1/2$ and the change of notation $N_H \to E$, that has the clear physical interpretation as the energy of a set of N non-interacting classical spins. The binomial coefficient in Eq. (1.7), with $E = M$, can then be identified with the microcanonical partition function $\mathcal{N}(E)$ as it counts the number of possible configurations for a fixed value of the total energy E.

$$\mathcal{N}(E) = \binom{N}{E}. \tag{1.18}$$

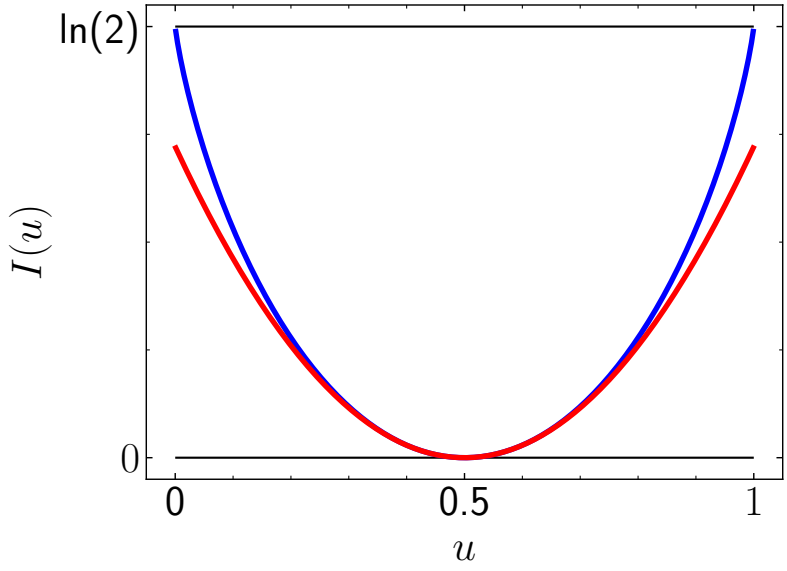

FIGURE 1.1: Comparison between the rate function $I(u)$ in Eq. (1.11) (blue line) and its quadratic expansion (red line) in Eq. (1.13). Close to the mean value $\mu = 1/2$ the two curves coincides, while for large deviations the Gaussian approximation is not correct as it significantly overestimates the probability of rare events since the parabolic approximation is smaller than the actual rate function.

In the limit of large N from Eqs. (1.7) and (1.11) one has

$$\mathcal{N}(E) \asymp \mathrm{e}^{NS(u)}, \tag{1.19}$$

with $S(u)$ being the Boltzmann entropy density as a function of the energy density u:

$$S(u) = \ln 2 - I(u). \tag{1.20}$$

One therefore concludes that the rate function $I(u)$ can be identified, apart from an additive constant, with the negative of the entropy of the microcanonical ensemble. Going further with the analogy, we can consider the canonical partition functon $Z(\beta)$

$$Z(\beta) = \sum_C \mathrm{e}^{-\beta E(C)} = \int \mathrm{d}E \mathcal{N}(E) \mathrm{e}^{-\beta E}, \tag{1.21}$$

where we replaced the summation over all microscopic configurations with an integral over the energy. Plugging in this equation the expression for $\mathcal{N}(E)$ in Eq. (1.19) with a saddle-point approximation for $N \to \infty$ one eventually obtains

$$Z \asymp \mathrm{e}^{-\beta N \, inf_u\{u - S(u)/\beta\}}. \tag{1.22}$$

As usual in statistical mechanics the free energy density $f(\beta)$ can be derived from the partition function in the thermodynamic limit as

$$f(\beta) = -\frac{1}{\beta} \ln Z(\beta), \tag{1.23}$$

and therefore from Eq. (1.22) one finds

$$\beta f(\beta) = \inf_u \{\beta u - S(u)\}. \tag{1.24}$$

Comparing this relationship with Eq. (1.15) we conclude that the free energy density $\beta f(\beta)$ of the canonical ensemble can be identified with the scaled cumulant generating function, which can be obtained via the Legendre-Fenchel transform of the microcanonical entropy density $S(u)$. The Legendre duality relations in Eq. (1.16) in this case reads as

$$\beta = \frac{dS(u)}{du}; \qquad u = \frac{d(\beta f(\beta))}{d\beta}, \tag{1.25}$$

from which all the equilibrium thermodynamics is recovered [8].

An important comment is now in order. In Sec. 1.1 we have seen that phase transitions are signaled by singularities in the free energy density and/or its derivatives. For the two-dimensional classical Ising model, in particular, $f(\beta)$ displays a logarithmic singularity at $\beta = \beta_c$ as explicitly shown in Eq. (1.5). As a consequence of the Lengendre-Fenchel transform also the rate function $S(u)$ is singular at some u_c. Inserting Eq. (1.5) into (1.24) one indeed finds that as $u \to u_c$ the entropy behaves as $S(u) \sim (u - u_c)^2/\ln|u - u_c|$, thereby displaying a discontinuity in the second derivative. The large deviation function therefore not only quantifies large-atypical fluctuations but it also signals phase transitions through its singularities. This fact has been exploited both in classical systems characterized by short-[19, 20, 25, 26] and long range-[27–29] interactions and in random matrix theory [30–34].

In this Section we have introduced the large deviation theory from the perspective of equilibrium statistical mechanics: however, nothing prevents us from applying the definitions in Eqs. (1.14) and (1.15) to non-equilibrium systems. The rate function $I(u)$ and the SCGF $f(\lambda)$ in this case generalize the concepts of entropy and free energy, respectively, to the non-equilibrium realm. Singularities in the large deviation function have been exploited to define non-equilibrium phase transitions both for isolated [35–44] and for open quantum systems [45–48]. The focus of Part I of the thesis will be on the application of large deviation theory to the non-equilibrium dynamics of isolated quantum systems, see Subsecs. 1.4.1, 1.4.2 and 1.4.3.

1.3 Non-equilibrium dynamics of isolated quantum systems

In this Section we outline the basic facts concerning the non-equilibrium dynamics of isolated systems. In Subsec. 1.3.1 we give the main motivations for studying isolated systems and the experimental perspective on ultracold-atomic systems. In Subsec. 1.3.2 we define a paradigmatic out of equilibrium protocol for isolated systems that will be largely studied: the *quantum quench*. In Subsec. 1.3.3 the problem of thermalization in isolated quantum systems will be introduced.

In Subsec. 1.3.4 we explain how the work performed in a quantum quench is defined, while in Subsec. 1.3.5 we will discuss a prominent feature of the quench dynamics which is the light-cone spreading of correlation functions and entanglement entropy. This will allow us to introduce the semi-classical quasi-particle picture of quantum quenches. This picture will be essential for the understanding of many of the results presented in Chapters 3, 4 and 5.

1.3.1 Motivations and experimental perspective

The dynamics of isolated quantum systems has always been a fascinating theoretical framework. The standard approached followed in textbooks of statistical mechanics, indeed, relies on ad hoc assumptions regarding the coupling between the system and the surrounding environment. In this perspective, in isolated systems, one should be able to address fundamental physical questions starting solely from the microscopic quantum mechanical laws ruling the dynamics of the particles, without the need of introducing an external bath and thereby any postulate on the latter. As a matter of fact, understanding the emergence of *macroscopic-collective* equations describing the out of equilibrium dynamics, from *microscopic*, purely quantum-mechanical, laws is a central question of quantum statistical mechanics. Similarly, deriving a statistical distribution, dependent only on the symmetries and the conserved quantities of the system, which describes the long-time behavior of physical observables is of paramount importance. Indeed, this corresponds to what a statistical ensemble is, and it is precisely what, in general, is missing in the non-equilibrium realm. Remarkably, these questions can be addressed in the field of one-dimensional isolated many body-quantum systems.

Despite these motivations, a systematic investigation of the dynamical properties of isolated quantum systems started approximately only in the last fifteen years as a consequence of ground-breaking advances in cold-atomic experiments [49–53]. Cold atoms are experimentally interesting from many reasons. Here we mention a few of them, referring the reader to the various excellent reviews on this subject (see, e.g., Refs. [49, 54]) for further details. First, they allow an unprecedented control of the Hamiltonian's parameters. The inter-particle interaction, for instance, can be controlled by means of Feshbach resonances, in stark contrast with more traditional condensed-matter systems where interactions are a datum of the problem and cannot be significantly and easily modified. Moreover, very long time windows, of the order of hundreds of milliseconds, of unitary and coherent dynamics can be explored, before non-unitary effects such as heating and particle loss become relevant. In addition, by means of periodic optical potentials one can realize and engineer lattice models, in both one and higher spatial dimensions.

A concrete example of cold atoms experiments we cannot avoid to mention is the celebrated "quantum Newton's cradle" presented in Ref. [53], whose schematic representation is reported in the left panel of Fig. 1.2. In this experiment, a two-dimensional Bose-Einstein condensate of ultracold ^{87}Rb atoms is confined in one spatial dimension by means of a tight transverse confining potential and a weaker longitudinal potential $U(z)$. A sequence of two laser

pulses (Bragg pulses) gives to the atomic cloud, initially located in the center of the trap, a superposition of equal but opposite momenta. The cloud then splits into two parts which propagate in opposite directions in the potential $U(z)$. The two clouds are observed to oscillate within the trap with a period τ. For every period they collide twice, as shown in the right panel of Fig. 1.2. The central result of the experiment is that even after thousands collisions the two clouds do not thermalize to a single cloud having zero momentum, but they keep oscillating. This behavior has been ascribed to the fact that the one-dimensional quasi condensate of Rubidium atoms is modelled by the Lieb-Liniger Hamiltonian, which is known to be integrable (see Sec. 1.4). This, in turn, sparked a great attention to the problem of thermalization in one-dimensional isolated systems and to the role integrability might play in escaping this process.

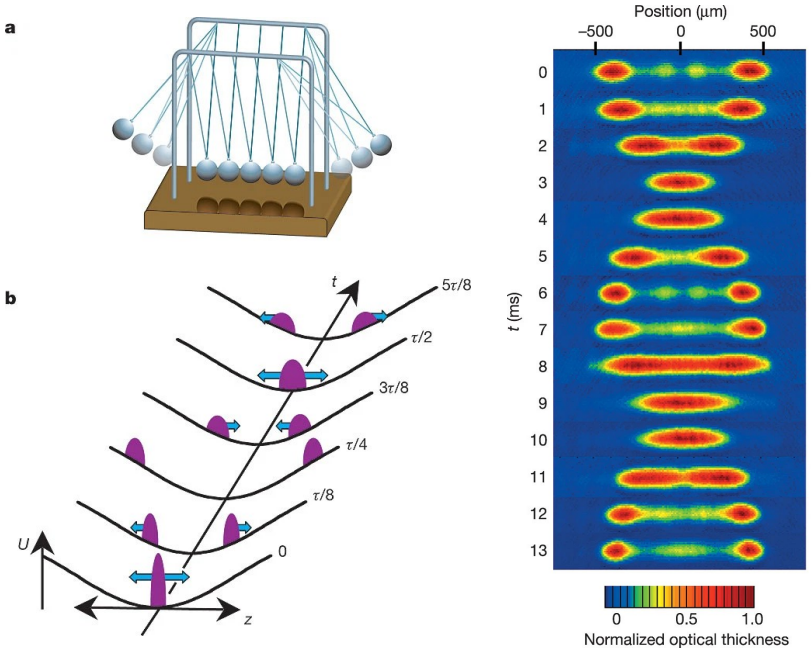

FIGURE 1.2: Quantum Newton cradle experiment. (a) Pictorial representation of the classical Newton cradle and (b) its quantum counterpart, as realized in the experiment. In the experiment, two laser pulses provide a superposition of opposite momenta to the cloud of ^{87}Rb atoms, which therefore splits in two counter-propagating clouds moving in an anharmonic trapping potential $U(z)$. In the left panel a sequence of absorption images of the colliding clouds is shown for the first period of oscillation $\tau = 13ms$. Even after thousands oscillations the two clouds keep oscillating without damping. Image taken from Ref. [53].

From this discussion it is then clear that the study of isolated quantum many-body systems is timely and relevant as it allows to address, starting from the microscopic unitary dynamics of the atoms, fundamental physical questions such as the thermalization, for generic, non-integrable, systems. Integrable models, instead, allows to obtain exotic, non-thermal, collective behaviors. In the next Section we introduce a simple protocol to probe the non-equilibrium dynamics of isolated quantum systems: the *quantum quench*.

1.3.2 Quantum quenches

Consider a one-dimensional system of size L in an initial state $|\Psi_0\rangle_L$, which for the moment we assume to be homogeneous, i.e., translationally invariant. A typical case is when $|\Psi_0\rangle_L$ is the ground-state of an Hamiltonian $H(c_0)$ which depends on some parameter c_0, for instance the inter-particle interaction. We assume that the Hamiltonian $H(c_0)$ is short-ranged and, in this Section, homogeneous. A good example is the transverse field Ising Hamiltonian in Eq. (1.2), with the transverse field h being the parameter modified in the quench. At time $t = 0$ the coupling is suddenly switched, i.e., "quenched", to a different value $c_0 \to c$, and the system then evolves unitarily according to the Hamiltonian $H(c)$:

$$|\Psi(t)\rangle_L = \mathrm{e}^{-iH(c)t}|\Psi_0\rangle_L. \tag{1.26}$$

Since $|\Psi_0\rangle_L$ is generically not an eigenstate of $H(c)$ it evolves in time in a non-trivial way. It is in particular fundamental that $|\Psi_0\rangle_L$ has non-zero overlaps with a number of states exponentially large in the system size L, otherwise the dynamics in Eq. (1.26) is trivial. This protocol to trigger the non-equilibrium unitary time evolution is dubbed *quantum quench* and has been first proposed in Refs. [55, 56], see Ref. [57] for a review. In some cases, to distinguish it from other setups involving inhomogeneous initial states, see Subsec. 1.4.2, one refers to this protocol as *global-homogeneous* quantum quench. The dynamics of any operator $\mathcal{O}$ can then be formally written by expanding the initial state $|\Psi_0\rangle_L$ in the basis of the post-quench eigenstates $\{|n\rangle_L\}$ of the Hamiltonian $H(c)$, i.e.,

$$|\Psi_0\rangle_L = \sum_n c_n |n\rangle_L, \tag{1.27}$$

with $c_n = {}_L\langle n|\Psi_0\rangle_L$, as

$${}_L\langle\Psi(t)|\mathcal{O}|\Psi(t)\rangle_L = \sum_{m,n} c_n^* c_m \, \mathrm{e}^{i(E_n - E_m)t} \, {}_L\langle n|\mathcal{O}|m\rangle_L. \tag{1.28}$$

All the interesting effects characterizing the dynamics come from the double summation in Eq. (1.28), with each sum running over a number of states which is exponentially large in the system size. A crucial property of quantum quenches is that, being the dynamics unitary, the total energy E_L is conserved in time and it is fixed by the initial state $|\Psi_0\rangle_L$:

$$E_L(c) = {}_L\langle\Psi_0|H(c)|\Psi_0\rangle_L. \tag{1.29}$$

In the thermodynamic limit $L \to \infty$, since the Hamiltonian is local, one expects $E_L \sim L$ to scale extensively with respect to L and to be larger than the ground state energy E_0 of the post-quench Hamiltonian $H(c)$. This means that the initial state is "thermodynamical" since it has a finite energy $E_L(c)/L$ above the ground state.

1.3.3 Thermalization in isolated systems

Our intuition on thermalization usually relies on the coupling between the system and the environment. In the case of *isolated* quantum systems is therefore not immediate whether relaxation occurs, and, if this is the case, in which sense it has to be understood. A crucial concept to define the notion of thermalization in isolated quantum systems is the one of *locality*. An operator $\mathcal{O}$ is said to be local if, in the thermodynamic limit $L \to \infty$, it acts non-trivially and therefore has support only on a finite portion of the system. For a quantum spin chain like Eq. (1.2) a local operator acts in thermodynamic limit only on a finite number of lattice sites. An example can be the local magnetization σ_i^x whose support is only the lattice site i. If this condition is met, then one can expect that the remaining part of the system will act as an effective thermal bath for the local observable $\mathcal{O}$ and relaxation to a thermal value might be possible in the long-time limit, as depicted in Fig. 1.3. In formulas, this is expressed by requiring the existence of a

FIGURE 1.3: Schematic illustration of local thermalization in isolated quantum systems. The interval A in blue has a finite extent and it represents the region where the operator $\mathcal{O}$ acts non-trivially. The remaining part of the system, B in red, is infinite as the thermodynamic limit $L \to \infty$ is taken. B will then behave as an effective bath for any local operator $\mathcal{O}$ acting on A, causing relaxation towards a stationary value as in Eqs. (1.30), (1.32) and (1.31).

stationary-state limit $\langle \mathcal{O} \rangle_{SS}$

$$\lim_{t\to\infty} \lim_{L\to\infty} {}_L\langle \Psi(t)|\mathcal{O}|\Psi(t)\rangle_L = \langle \mathcal{O} \rangle_{SS}. \tag{1.30}$$

The order of the limits appearing in Eq. (1.30) is crucial. The thermodynamic limit has to be taken first since for finite systems recurrences will take place [57, 58], such that the time evolved state $|\Psi(t)\rangle_L$ will get back arbitrarily close to the initial one $|\Psi_0\rangle_L$. Thermalization in isolated systems therefore concerns *local* observables $\mathcal{O}$ in the thermodynamic limit. A statistical description emerges if and only if the expectation value in Eq. (1.30) can be equivalently calculated from a statistical-ensemble density matrix ρ_{GE}

$$\langle \mathcal{O} \rangle_{SS} = Tr[\mathcal{O}\rho_{GE}], \tag{1.31}$$

which is nothing but the Gibbs ensemble

$$\rho_{GE} = \frac{e^{-\beta H}}{Z}, \tag{1.32}$$

with Z the partition function. The inverse temperature β is fixed by the initial energy of the system in Eq. (1.29) and it is the only parameter of the stationary-state density matrix which depends on the initial state of the system. For small quenches, i.e., $c - c_0 \sim 0$, the temperature T will be close to zero, while it increases continuously as the depth of the quench $c - c_0$ increases.

We mention that a different perspective on thermalization [52, 59] might be considered, where the long-time limit is considered first. In this case one considers the time-averaged expectation value of the observable $\mathcal{O}$ at finite size L

$$\begin{aligned} {}_L\overline{\langle\Psi(t)|\mathcal{O}|\Psi(t)\rangle}_L &= \lim_{T\to\infty}\frac{1}{T}\int_0^T \mathrm{d}t\ {}_L\langle\Psi(t)|\mathcal{O}|\Psi(t)\rangle_L \\ &= \sum_n |c_n|^2\, {}_L\langle n|\mathcal{O}|n\rangle_L = \mathrm{Tr}\left(\mathcal{O}\,\rho_{DE}^{(L)}\right), \end{aligned} \tag{1.33}$$

where the last equality holds provided the spectrum of the post-quench Hamiltonian is non-degenerate. The density matrix $\rho_{DE}^{(L)}$ introduced in Eq. (1.33) is named *diagonal ensemble* as only diagonal matrix elements appear in Eq. (1.33)

$$\rho_{DE}^{(L)} = \sum_n |c_n|^2 |n\rangle_L\ {}_L\langle n|. \tag{1.34}$$

In the thermodynamic limit $L \to \infty$ it is reasonable to assume that Eqs. (1.33) and (1.34) will coincide with Eq. (1.30). Yet, there is a crucial difference between the Gibbs and the diagonal ensemble. The latter, indeed, retains knowledge of the initial state by means of the very large set of coefficients $\{c_n\}$ and therefore it seems difficult that it can describe the thermal expectation value in Eqs. (1.31) and (1.32), where the only dependence on the initial state is via the value of β. The solution of this conundrum is provided by a very famous result which is known as *Eigenstate Thermalization Hypothesis* (ETH), first proposed in Refs. [60, 61]. Many numerical evidences supporting this assumption are available in the literature [62–66], but no general proof is currently available. The ETH is formulated in terms of the microcanonical density matrix ρ_{MC} in the thermodynamic limit $L \to \infty$

$$\rho_{MC} = \frac{1}{\mathcal{N}(E)}\sum_{n\in I(E)} |n\rangle\langle n|, \tag{1.35}$$

where $\mathcal{N}(E)$ is the microcanonical partition function, that we introduced after Eq. (1.17), and $I(E) = \{n : E_n \in (E - \delta E, E + \delta E)\}$ and δE is the sufficiently small width of the microcanonical shell. In Eq. (1.35) we are considering the thermodynamic limit $L \to \infty$ and therefore we have omitted the dependence on L. The ETH in short asserts that in the thermodynamic limit expectation values $\langle n|\mathcal{O}|n\rangle$ over the energy eigenstates are smooth functions of the energy of the eigenstates $|n\rangle$ solely and they are effectively constant over the energy interval $I(E)$. As a consequence

$$\sum_n |c_n|^2\langle n|\mathcal{O}|n\rangle \approx \frac{1}{\mathcal{N}(E)}\sum_{n\in I(E)}\langle n|\mathcal{O}|n\rangle \approx \langle n|\mathcal{O}|n\rangle. \tag{1.36}$$

In other words, the expectation value of $\mathcal{O}$ over a single energy eigenstate is equal to the average over the microcanonical ensemble constructed at the same energy, see Ref. [59] for a comprehensive review.

1.3.4 Statistics of the work done in a quantum quench

A quantity giving fundamental insights on the quench dynamics is the work W performed upon changing $c_0 \to c$ [67–70], as this quantity measures how much the system is driven out of equilibrium with the quench. W is defined with a protocol involving two measurements of the energy, as first proposed in Ref. [71] and sketched in Fig. 1.4. The first, right before the quench, gives by construction the pre-quench ground state energy $E_0(c_0)$. The second, right after the quench, gives one of the possible energy eigenvalues $E_n(c)$ of the post-quench Hamiltonian $H(c)$. Each of the possible outcomes for $E_n(c)$ is obtained with a probability determined by the square of the overlap between $|\Psi_0\rangle_L$ and the corresponding eigenstate $|n\rangle$, because of the quantum fluctuations in the measurement. As a consequence W is a random variable which can take the values

$$W = E_n(c) - E_0(c_0), \tag{1.37}$$

with mean $\langle W\rangle_L = E_L(c) - E_0(c_0)$ and $E_L(c)$ in Eq. (1.29). As W is an extensive variable, one generically expects that both its mean value $\langle W\rangle_L$ and its fluctuations $\langle(\Delta W)^2\rangle_L = \langle W^2\rangle_L - \langle W\rangle_L^2$ grow proportionally to L as L increases, the latter statement being true whenever W can be seen as resulting from the sum of a number proportional to L of almost independent contributions. This implies that the typical fluctuations in the value of W are of order $\sqrt{L}$, i.e., those of the intensive work $w = W/L$, of order $1/\sqrt{L}$, vanish as $L \to \infty$. Correspondingly, the distribution function $p(w)$ of w approaches a delta function $\delta(w - \bar{w})$ which selects the average value $\bar{w} = \langle W\rangle_L/L$. On the other hand, fluctuations of order 1 of the value of w away from $\bar{w}$ corresponds to fluctuations of order L in W, i.e., to large and atypical fluctuations, which are increasingly rare as L grows. The large deviation formalism of Sec. 1.2 then gives access to the probability density function $p(w)$ of the intensive work $w = W/L$, i.e.,

$$p(w) \asymp \exp[-LI(w)]. \tag{1.38}$$

A detailed analysis of the features of the work probability distribution is presented in Chapter 2 of the thesis, where the large deviation function $I(w)$ of the work w will be exactly calculated for a quench of the one-dimensional interacting Bose gas.

1.3.5 Light cone spreading of correlations and entanglement

Two-point equal-time connected correlation functions of local operators

$$\langle\mathcal{O}(x+l,t)\mathcal{O}(x,t)\rangle_c = \langle\mathcal{O}(x+l,t)\mathcal{O}(x,t)\rangle - \langle\mathcal{O}(x+l,t)\rangle\langle\mathcal{O}(x,t)\rangle \tag{1.39}$$

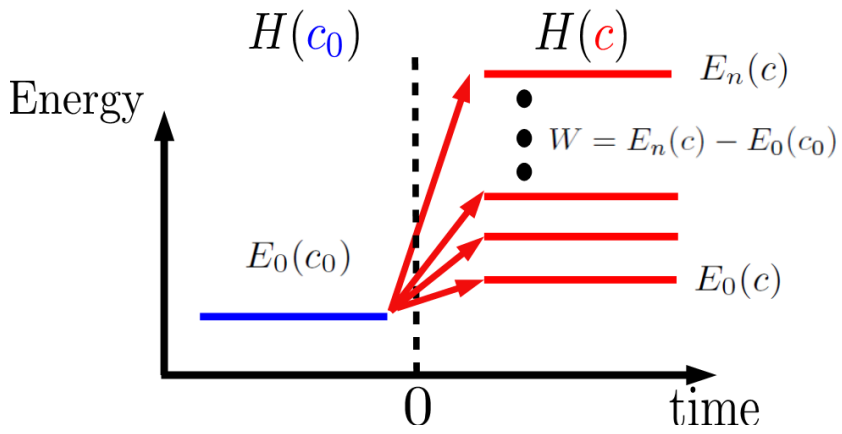

FIGURE 1.4: Sketch of the definition of the work done in a quantum quench $c_0 \to c$. The quench is done at time $t = 0$ (dashed line). The energy levels of the post-quench Hamiltonian are shown in red, while in blue the pre-quench ground state is displayed. The work is given by the difference between the two energy measurements $W = E_n(c) - E_0(c_0)$.

are a key observable to study the spreading of correlations among degrees of freedom across the system. For short-ranged Hamiltonians, a prominent result is the "light-cone effect". This phenomenon can be considered a consequence of a famous result of mathematical physics known as Lieb-Robinson bound [72, 73], which provides an upper bound to the maximal velocity of propagation of quantum information. This theorem applies to short-range quantum spin systems, e.g., the transverse field Ising chain in Eq. (1.2), and it asserts that there exists a maximal velocity v_{LR} such that equal-time connected correlation function in Eq. (1.39) are exponentially suppressed upon increasing the separation l at times $t < l/(2v_{LR})$. This velocity is non-universal as it depends on the specific model considered. Moreover, the theorem does not provide a practical strategy for computing v_{LR}. As a consequence, correlation functions display abrupt changes at time $t = l/(2v_{LR})$ when the information generated by the quench propagating at the finite velocity v_{LR} is received. An example of this structure is shown in Fig. 1.5 for a system which can be mapped to non-interacting fermions. The light-cone effect can be observed in the dynamics of another quantity that crucially characterizes the non-equilibrium quench dynamics: the bipartite entanglement entropy S_A. The latter is defined by considering a bipartition of the system $A \cup B$, see Fig. 1.3, and then the von Neumann entropy of the reduced density matrix ρ_A of the subsystem A of pure state $|\Psi\rangle$ is obtained by tracing out the degrees of freedom of B, i.e.,

$$S_A = -\mathrm{Tr}_B \, \rho_A \ln \rho_A. \tag{1.40}$$

Clearly the entanglement entropy S_B defined with respect to the subsystem B turns out to be equal to S_A as the entanglement depends on the bipartition only. For the entanglement entropy S_A the light-cone effect in global quantum quenches determines an increase in time for $t < l/(2v_{LR})$, with l the length of the interval A, followed by a saturation to a value which is extensive in l, as shown in Refs. [55, 74]. This is exemplified in Fig. 1.6 where the entanglement dynamics for a quantum quench of the transverse field in the Ising quantum chain is shown.

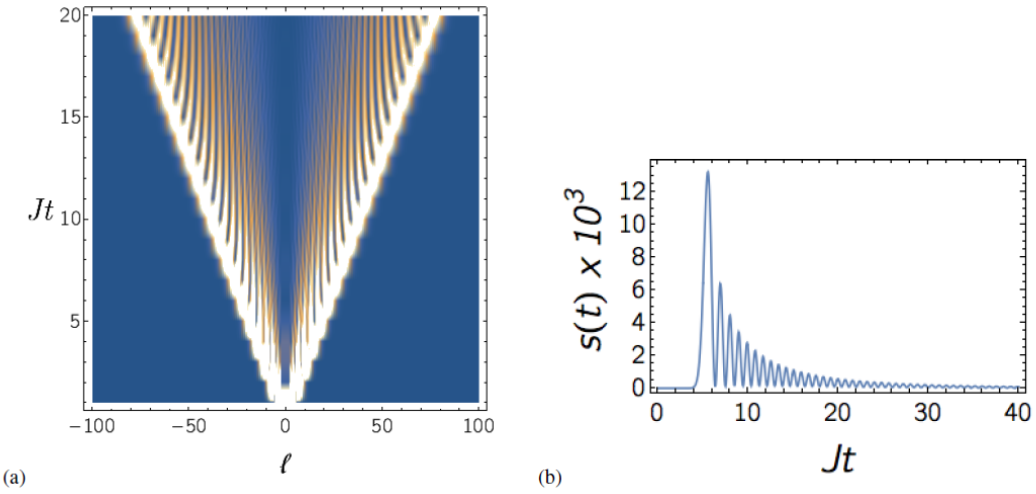

FIGURE 1.5: (a) Light-cone dynamics of correlation functions after a global quantum quench in a free fermionic chain. The local density-density connected correlation function in Eq. (1.39) is shown as a function of the dimensionless time tJ and of l for a system admitting non-interacting fermionic excitations. (b) Plot of the same correlation function as a function of t for fixed $l = 20$. In both graphs the thermodynamic limit has been taken and the stationary, time-independent, contribution has been subtracted. At time $t = l/(2v_{LR})$ the correlation function increases to a maximum and then it relaxes to the stationary value predicted by the GGE (see Sec. 1.4.1). Image taken from Ref. [57].

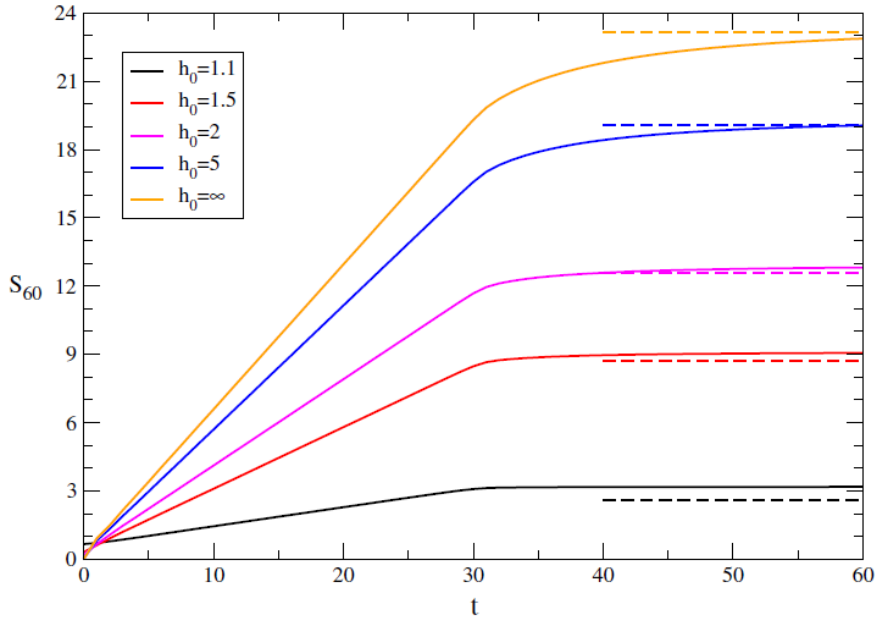

FIGURE 1.6: Light-cone dynamics of the bipartite entanglement entropy S_l of an interval of length $l = 60$ after a global quantum quench. The evolution in time of the bipartite entanglement entropy is shown for a quench of the transverse field from various initial values of $h_0 > 1$ to $h = 1$. The entanglement increases linearly in time for $t < l/(2v_{LR})$, then it saturates to a constant value extensive in l (dashed lines). Image taken from Ref. [74].

So far the light cone spreading of correlations and entanglement entropy has been justified on the basis of the Lieb-Robinson bound. However, this

phenomenon applies more generally as it can be ascribed a to a very clear semiclassical explanation introduced in Refs. [55, 74]. This approach is dubbed "quasi-particle picture" and it holds in the *space-time scaling limit* $t, l \to \infty$ with t/l fixed. Since the initial state $|\Psi_0\rangle$ has finite energy density above the post-quench ground state, as discussed after Eq. (1.29), it will contain quasi-particles excitations. In the case of non-interacting systems, like those considered in Figs. 1.5 and 1.6, these excitations can be identified with the normal modes of the Hamiltonian. For the Ising chain in Eq. (1.2), for example [75],

$$H = E_{GS} + \sum_k \varepsilon(k)\, \Psi^\dagger(k)\Psi(k), \tag{1.41}$$

with E_{GS} the ground-state energy, $\Psi(k)$ obeys fermionic anti-commutation relations $[\Psi(k), \Psi^\dagger(k')]_+ = \delta_{k,k'}$, and $\varepsilon(k) = 2\sqrt{h^2 - 2h\cos k + 1}$ is the single quasi-particle energy spectrum. In the ferromagnetic phase with $h < 1$ these fermionic excitations correspond to freely propagating domain walls interpolating between the two degenerate ground states, while in the paramagnetic phase with $h > 1$ they correspond to local spin flips. In this case, the Lieb-Robinson velocity v_{LR} is simply equal to the maximal group velocity v_{max} of these excitations,

$$v_{max} = \max_k |v_g(k)| \quad \text{where} \quad v_g(k) = \frac{\mathrm{d}\varepsilon(k)}{\mathrm{d}k} \tag{1.42}$$

is the quasi-particles group velocity. For non-interacting models, like the transverse field Ising chain, quasi-particles are stable and they propagate freely along classical trajectories. In each space point a pair of entangled right (right mover) and left (left mover) propagating quasi-particles is emitted. Quasi-particles originated from points further apart are uncorrelated (provided the initial state is not critical thereby displaying long-range correlations). In terms of this picture both the dynamics of the entanglement entropy, in Fig. 1.6, and the one of correlation functions, in Fig. 1.5, is simply understood, as shown in Fig. 1.7. On the basis of

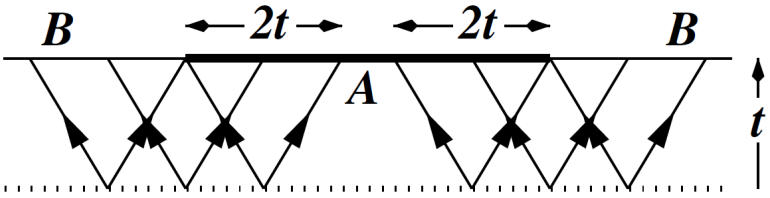

FIGURE 1.7: Quasi-particles picture of the entanglement growth after a global quantum quench. Quasi-particles emitted at the initial time $t = 0$ from points within a distance of the order of the correlation length of the initial state are correlated. At time t there will be pairs such that the right mover is in A and left mover in B (or vice-versa) thereby inducing correlations and entanglement between the two regions. Image taken from Ref. [74].

the semiclassical picture, light-cone effects are expected to be present whenever it is possible to define quasi-particles excitations and when the latter have a finite maximal velocity v_{max}. This is surely true in quantum spin chains and it is implied by the Lieb-Robinson bound, but it applies also to other class of models like relativistic field theories like the sine [76–78] and sinh [79, 80] Gordon model. In these

systems, the existence of v_{max} is ensured by relativistic causality. The presence of the light cone is therefore an intrinsic property of these systems and it does not depend neither on the quench protocol nor on the initial state. Light-cone spreading of correlation functions and entanglement has been indeed studied in a variety of models including non-interacting [81] and interacting [82, 83] spin chains, the Bose-Hubbard model [84, 85], interacting fermions [86] and it has been experimentally observed in cold atoms [87, 88] and trapped ions [89, 90] experiments. In non-relativistic continuum models, e.g., the Lieb-Liniger model which will be analyzed in Chapters 2 and 4, the quasi-particles have an unbounded energy spectrum, v_{max} is infinite and therefore the pure light-cone picture breaks. In this cases it turns out that approximate light-cone effects are present in the sense that the edges of latter becomes smoother as corrections are much larger with respect to the exponential suppression in l predicted by the Lieb-Robinson bound, see Refs. [91, 92]. For the entanglement entropy dynamics the unbounded energy spectrum has been further shown in Ref. [93] to determine an initial non-linear temporal growth of the entanglement.

Some comments about the effect of the interactions on the light-cone are now in order. The analysis carried out here concerns short-range interacting Hamiltonians, which are the main subject of this thesis. For long-range interacting systems, the light-cone picture is significantly different as sufficiently long-range interactions can completely destroy the light-cone structure [94–96]. Another important class of systems where the light-cone does not emerge is the one of systems with quenched disorder [97–99], where excitations in the many-body localized phase are localized and the entanglement entropy shows a slower logarithmic increase as a function of time. Regarding short-range interacting Hamiltonians both integrable and non-integrable models will be considered in Part I and II of the thesis, respectively. For the class of interacting integrable systems, see Sec. 1.4, quasi-particles excitations are stable (i.e., they do not decay) due to the presence of infinitely many conserved charges. However, because of the interaction, determining the velocity of these excitations is significantly more difficult than in free systems (see Eqs. (1.41) and (1.42)). The velocity is indeed renormalized by the interactions and it therefore becomes dependent on the initial state [83]. This aspect will be the main focus of Chapter 4 of the thesis, where the dynamical two-point functions for integrable models will be computed by exploiting the *generalized hydrodynamics* formalism (see Sec. 1.4.2). The case of generic, integrability-breaking, interactions is even more difficult, see Sec. 1.5. In this case quasi-particles have a finite lifetime that depends on the initial state and it is not clear what corresponds to the propagation velocity v_{LR}. The effect of generic, non-integrable, interactions on the light-cone dynamics of the entanglement entropy and other observables will be the main subject of Part II, where models displaying *confined excitations* will be studied. In particular, it will be shown that the dynamics in the presence of confinement may produce localization effects similar to those observed in the aforementioned framework of systems with quenched disorder.

1.4 Non equilibrium dynamics: integrable models

In this Section we introduce the main analytical techniques that will be used in Part I of the thesis for quantum integrable models. In Subsec. 1.4.1 we introduce the generalized Gibbs ensemble, which describes the long-time relaxation behavior of integrable systems, and the *quench action* approach. These techniques applies to global-homogeneous quenches, which have been described in Sec. 1.3. The Quench action method together with the large deviation theory will be at the basis of the results presented in Chapter 2, which are briefly outlined in Subsec. 1.4.1. In Subsec. 1.4.2 we discuss, in the case of non-interacting systems, a generalization of the global quench protocol, i.e., the so-called inhomogeneous quenches. This setup is particularly useful to study transport phenomena in isolated systems. In Subsec. 1.4.3 we introduce the recently developed generalized hydrodynamics framework, which allows us to extend the analysis of Subsec. 1.4.2 to interacting integrable systems. Inhomogeneous quenches will be the main subject of investigation of Chapters 3 and 4 in Part II, whose results are anticipated below in Subsecs. 1.4.2 and 1.4.3.

1.4.1 Homogeneous systems: GGE and quench action

It is worth saying that no commonly accepted definition of quantum integrable systems exists yet [100]. The subtlety lies in the fact that if one attempts to define quantum integrability as the presence of an infinite number of conserved quantities, as in the classical realm [101], an immediate ambiguity arises. Indeed, any Hamiltonian posses an infinite number of conserved quantities, which are the projectors onto the energy eigenstates.

In this thesis we will henceforth rely on a more practical definition of integrability which is the existence, in the thermodynamic limit $L \to \infty$, of an infinite set of *local* conserved quantities $\{Q_i\}$ with $i = 1, 2 \dots \infty$. These observables are also named conserved charges and they commute with the Hamiltonian $[Q_i, H] = 0$ and among themselves $[Q_i, Q_j] = 0$, for any i and j. Interacting integrable models are necessary one-dimensional [102], while integrability in higher dimensions is restricted to free theories. The following discussion therefore applies to systems defined in one spatial dimension. Local conserved charges can be written as integrals (or sums for discrete lattice models) of local densities $\{q_i(x)\}$ having support on a finite interval around x [1]. They satisfy conservation laws with the corresponding current operators $\{j_i(x)\}$:

$$Q_i = \int \mathrm{d}x\, q_i(x) \quad \text{with} \quad \partial_t q_i(x) = -\partial_x j_i(x) \quad \text{and} \quad \frac{\mathrm{d}Q_i}{\mathrm{d}t} = 0. \tag{1.43}$$

The first question that can be asked is whether integrable systems locally relax, in the sense of Subsec. 1.3.3, after a quench starting from some initial homogeneous state $|\Psi_0\rangle$. Based on the discussion of Subsec. 1.3.3 relaxation to the diagonal ensemble in Eq. (1.34) is expected. Hoewever, because of the infinite

[1] In continuum models, more precisely, the local conserved densities are point-wise function of x. In the following, we will mostly refer to the case of lattice models for simplicity. For a discussion of the GGE in continuum models see Refs. [79, 103–105]

number of conserved charges, the ETH is expected not to apply. The aim is then to find an ensemble description preserving the minimum amount of information on the initial state and locally equivalent to the diagonal ensemble. According to the Jaynes maximum entropy principle [106] the stationary state density matrix can be obtained by maximising the entropy $S = -\mathrm{Tr}[\rho \ln \rho]$ under the constraint that the expectation values of the conserved charges $\{Q_i\}$ remain constant. Given that for integrable models an infinite number of conserved charges is present, the stationary state is expected to differ from the thermal one in Eq. (1.32) where just one conserved quantity, the Hamiltonian, is present. The resulting stationary density matrix is referred to as the *generalized Gibbs ensemble* (GGE) and has been first proposed in Ref. [107] as the equivalent of the diagonal ensemble in Eq. (1.34) for integrable models:

$$\rho_{GGE} = \frac{\mathrm{e}^{-\sum_i \beta_i Q_i}}{Z_{GGE}}, \tag{1.44}$$

where Z_{GGE} is the normalization constant. The parameters $\{\beta_i\}$ are the Lagrange multipliers which enforce the initial values of the conserved charges $\{Q_i\}$, i.e., they are determined such that, for each value of i,

$$\langle \Psi_0 | Q_i | \Psi_0 \rangle = \mathrm{Tr}[\rho_{GGE}\, Q_i]. \tag{1.45}$$

Notice that, compared to the diagonal ensemble, the GGE provides a dramatic reduction of the number of degrees of freedom of the initial state necessary for the description of the stationary state. In the diagonal ensemble, from Eq. (1.34), one needs to know a number of coefficients $\{c_n\}$ which grows exponentially fast upon increasing the system size L and therefore the full knowledge of the initial many-body wave function $|\Psi_0\rangle$ is retained. On the contrary, for an integrable system of finite size L there will be L conserved charges and, as a consequence, only L multipliers β_i are needed to fix the GGE density matrix. This is the reason why relaxation to the GGE in integrable models is also named "generalized thermalization" [108]. In the thermodynamic limit $L \to \infty$ infinitely many conserved charges are present in Eq. (1.44), yet one can exploits the fact that the local conserved charges $\{Q_i\}$ have an increasingly extended spatial support as a function of i. Based on this property, it has been shown in Ref. [109] for the transverse field Ising chain, that the relaxation behavior of any operator $\mathcal{O}$ having support across l contiguous sites can be described with a truncated GGE including only a finite number of charges with support of the order of l itself. This approach has been then extended to construct the GGE and compute the stationary value of local observables in interacting integrable models [110–112]. The validity of the GGE is by now completely established, see, e.g., the review in Ref. [113], and it has also been experimentally confirmed [114]. It is also important to emphasize that, according to the way the GGE has been presented here, the conserved charges $\{Q_i\}$ appearing in Eq. (1.44) are the local ones. This is certainly true in free lattice models [115–117], but it needs to be reconsidered in interacting spin chains. In the latter case, also quasi-local charges have to be included in the GGE as shown in Ref. [118, 119], and the review [120], to correctly match the stationary-state behavior obtained numerically from density matrix renormalization group (DMRG) simulations and analytically from the quench actionmethod, see Refs. [119, 121–

123]. Heuristically, quasi-local charges can be considered as an infinite sum of local charges with an increasing support up to infinity, where the weight of each local charge present in the summation is exponentially suppressed as a function of its support. See the review in Ref. [120] for a rigorous definition. The GGE including quasi-local charges is usually named *complete* GGE in contrast to that containing only local charges, which is dubbed *ultra-local* GGE.

The quench action[124, 125] is an analytical method based on the thermodynamic Bethe ansatz (TBA) that allows one to calculate the long-time limit of local observables. This approach is based on the definition of a functional measure in the Hilbert space, the exponential of the quench action, which quantifies the weight of each post-quench eigenstate in the non-equilibrium quench dynamics. The applicability of this method relies on the possibility of computing the overlaps between the initial state $|\Psi_0\rangle$ and the post-quench eigenstates. Once this information is available, the steady state distribution can be obtained in a variational way by finding the stationary point of the quench action. It is important to note that the quench actioncan be considered a functional representation in the thermodynamic limit $L \to \infty$ of the diagonal ensemble. The GGE predictions for the stationary state are therefore expected to converge to the quench action ones in the thermodynamic limit. A detailed explanation of the quench action technique will be given in Chapter 2: for the moment it is sufficient to say that with this method several exact results concerning quenches to truly interacting integrable Hamiltonians have been obtained for quantum spin chains [126–128], the one-dimensional Bose gas [129–132], and in relativistic field theories [133, 134].

In Chapter 2, we will merge the quench action method with the large deviation theory to devise a general approach for the calculation of the rate function $I(w)$ of the intensive work w done in a quantum quench to any interacting integrable model. For the purpose of illustration and due to its experimental relevance, we will consider the specific and prototypical case of the Lieb-Liniger model, which in cold atomic experiments such as the quantum Newton cradle in Fig. 1.2 describes the behavior of the one-dimensional Bose gas, will be considered. In addition, we will show the existence and provide the first complete analytic characterization of a particular "condensation regime" arising when the initial state is critical, which has been discussed so far only in the significantly simpler case without interactions.

1.4.2 Inhomogeneous systems: non-interacting case

After the homogeneous quantum quenches had been understood in terms of the GGE construction and the quench action method, the attention of the community of experimentalitst and theoreticians turned to the study of *inhomogeneous* quenches. In this protocol, the initial state $|\Psi_0\rangle$ of the system, which can be either a pure or a mixed state, is inhomogeneous, in the sense that it breaks translational invariance. In order to make the discussion more concrete, we mention a widely studied inhomogeneous set up which is known as partitioning protocol, where two semi-infinite systems in different macroscopic states are glued together at time $t = 0$ by means of a local interaction between their closest endpoints. At

time $t > 0$ the system evolves according to a translationally invariant Hamiltonian. This protocol is particularly useful to study transport phenomena occurring in isolated systems, for example the transport of energy and magnetization due to an initial inhomogeneity in the temperature, or the magnetization profile. It has to be noticed that transport can be also studied in open quantum systems, see, e.g., Refs. [135–140]. A typical setup in this case is the one of boundary driven one-dimensional spin chains described within the Markovian approximation by a Lindblad equation. The emphasis of this Section is given to isolated systems as they will be the focus of the research presented in this thesis.

Despite the fact that the partitioning protocol is known since very long time [141], it received a systematic attention only in the last decade after a series of works [142, 143] (see also Ref. [144] for a review) where for one-dimensional quantum critical systems the universal properties of the transport have been classified. In particular, using *conformal field theory* (CFT) [14], it has been show that a non-equilibrium steady state (NESS) supporting the flow of a current develops at long times. The results obtained in this way are universal, since they apply to any one-dimensional system at a quantum critical point which is described by a CFT with a particular value of the central charge c. Considering the case of an inhomogeneity in the temperature profile, as depicted in Fig. 1.8, the expressions of the NESS energy current $\mathcal{J}^E_{NESS}$ and density $\mathcal{U}^E_{NESS}$ acquire a universal form in the low-temperature regime of conformal field theory

$$\mathcal{J}^E_{NESS} = \frac{c\pi}{12\hbar} k_B^2 (T_l^2 - T_r^2), \tag{1.46}$$

$$\mathcal{U}^E_{NESS} = \frac{c\pi}{12\hbar} k_B^2 (T_l^2 + T_r^2), \tag{1.47}$$

k_B the Boltzmann constant, while $T_{l,r}$ are the two temperatures characterizing the initial state. The non vanishing value $\mathcal{J}^E_{NESS}$ of the energy current in the NESS, despite the fact that the energy density profile $\mathcal{U}^E_{NESS}$ is homogeneous, shows that Fourier law is broken. Indeed, in CFT transport is ballistic due to the fact that the emergent excitations are given by right- and left- moving quasi-particles that independently propagate at velocity $\pm v_{max}$ (the equivalent of the speed of light in the underlying relativistic massless field theory description).

The picture described by conformal field theory carries over to non-interacting models, where quasi-particles excitations with momentum k propagate independently with group velocity $v_g(k)$ without scattering, analogously as in the case of homogeneous quenches in Sec. 1.3.5. The crucial difference with respect to the analysis of Sec. 1.3.5 is that the quasi-particles are generated in the initial state according to an inhomogeneous distribution, as shown in Fig. 1.8. This leads to a number of exact predictions concerning the NESS [145–148] that allow to verify the emergence of the conformal field theory description in the low-temperature regime from microscopic lattice calculations. Moreover, the quasi-particles description allows, more generally, the calculation of the complete space-time dependence of the energy current and density beyond the stationary limit. The quasi-particle approach becomes, as a matter of fact, exact in the so-called *hydrodynamic, space-time or semi-classical limit* within which the space coordinate x along the chain and the time t are both assumed to be large with fixed ratio $v = x/t$ [1,

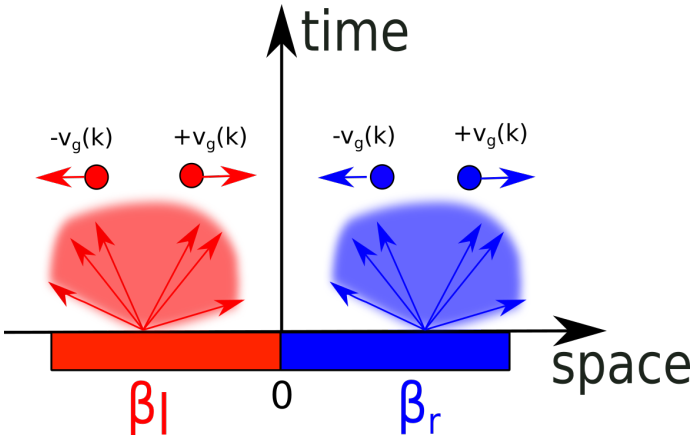

FIGURE 1.8: Quasi-particle picture after an inhomogeneous quantum quench. Two semi-infinite systems initially at equilibrium at the inverse temperatures β_l (in red) and β_r (in blue) are initially joined at $x = 0$. Quasi-particles are present in the initial state according to a thermal distribution at inverse temperature β_l for the left chain, and β_r for the right one. Excitations with momentum k propagate with velocity $\pm v_g(k)$. In the picture we assume $v_g(k) > 0$ for simplicity.

4, 149–158]. In this limit, the space-time profiles of the energy-current and density are expressed by hydrodynamic formulas, which show a high degree of universality. Given the absence of any characteristic length scale in the partitioning protocol initial state these profiles are scaling functions of v, which show a light-cone behavior determined by the maximal velocity v_{max} of the quasi-particles excitations, as sketched in Fig. 1.9.

An important quantity we will consider in detail is the time-integrated energy current

$$\Delta e(x,t) = \int_0^t \mathrm{d}s\, j_E(x,s), \tag{1.48}$$

where the energy current operator j_E is defined from the continuity equation (1.43). For ballistic transport $\Delta e(x,t) \sim t$ depends extensively on t for large times and therefore the large deviation principle in Eq. (1.10) for the intensive variable $J_E = \Delta e(x,t)/t$ applies

$$p(J_E) \asymp \exp[-tI(J_E)]. \tag{1.49}$$

In Chapter 3, by considering the hydrodynamic limit of large space-time scales with fixed $v = x/t$, we present and discuss a general approach for the determination of the large-deviation function $I(J_E)$ in non-interacting quantum models. We shall focus on the transverse field Ising chain in Eq. (1.2) and on the harmonic chain which correspond, respectively, to free fermionic and bosonic theories. A thorough analysis of the similarities and differences between the large deviation functions in these two cases will be also presented here.

1.4.3 Inhomogeneous systems: interacting integrable case

The dynamics from inhomogeneous initial states, e.g., the partitioning protocol, is clearly more complex than the one of the global quantum quenches of Sec. 1.3. It is therefore not surprising that the first studies focused on free models

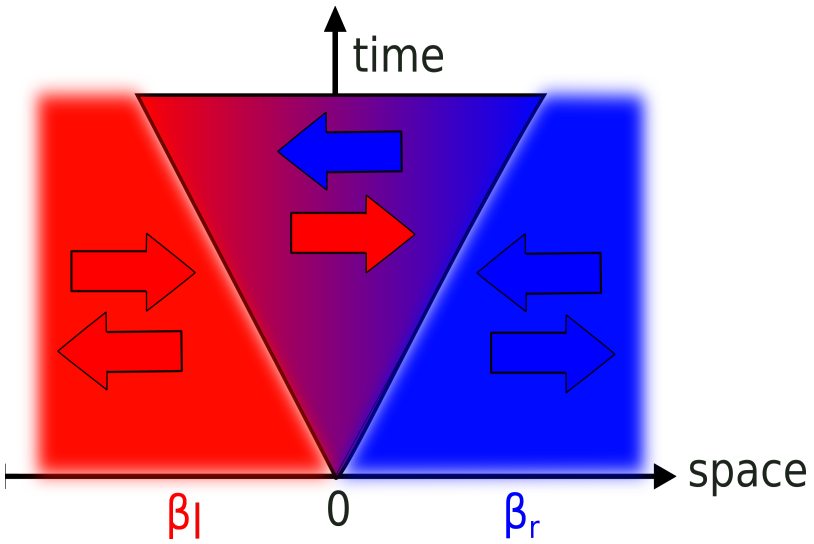

FIGURE 1.9: Light-cone propagation of energy transport in the partitioning protocol. Two identical systems at different temperatures, β_l in red and β_r in blue, are joined at the intial time at $x = 0$. At time $t > 0$ the system evolves in time according to a translationally invariant Hamiltonian. Information spreads from $x = 0$ in a light-cone fashion. Within the latter, an imbalance between the flow of right-moving quasi-particles coming from the left chain (right arrow) and the flow of left-moving quasi-particles from the right chain (blue arrow) determines the development of a non-trivial energy current and density space-time profiles. Outside of the light cone the energy current and density retain their initial equilibrium value, since only quasi-particles from the right chain (blue arrows) or from the left one (red arrows) are present and the net flow is consequently zero.

and on conformal field theory as outlined in the previous Section. The fundamental breakthrough to address inhomogeneous and non-stationary situations in interacting integrable models has been the development of the *generalized hydrodynamics* (GHD) theory in the two indedependent works of Ref. [159] and Ref. [160]. This theory applies to case of inhomogeneities smoothly varying in space. Under this assumption, at any space-time point (x, t) the many-body system can be considered to locally relax to a GGE which depends on the space-time (x, t) point considered. Accordingly, locally at the space-time point (x, t), the state of the system is entirely characterized by the conserved densities $\{q_i(x, t)\}$ in Eq. (1.43) in the spirit of a local-equilibrium approximation [161]. Different space-time points can be connected by exploiting the continuity equation that each of the conserved densities satisfies together with the associated current $\{j_i(x, t)\}$. The result is expressed in terms of hydrodynamic equations that connect GGE at different space-time points. The input of the method is the thermodynamic Bethe ansatz, but it is not restricted to quantum models as it applies also to classical models as well, such as the hard-rod gas [162], the classical sinh-Gordon [163] and the Toda chain [164, 165]. The initial application of the GHD formalism was to the partitioning protocol [159, 160, 162, 163, 165–172], but the versatility of the hydrodynamic equations allows one to study other inhomogeneous setups. For example, the effect of confining potentials $V(x)$, which are always present in cold-atoms experiments, can be included in the hydrodynamic equations [173], which indeed have been used

to model the quantum Newton's cradle experiment [174]. Other successful applications include bump-release protocols [175, 176], correlation functions [177–179] and entanglement spreading [180–183]. We also note that GHD has been experimentally verified in Ref. [184].

In Chapter 4 of the thesis we will focus on two tightly related applications of this theory. First we will consider two-point functions in inhomogeneous and non-stationary situations, whose expressions have been originally derived in Ref. [177]. In this case we will study the spreading of correlations from inhomogeneous initial states in several integrable models, including the Lieb-Liniger model, the sinh-Gordon model and the classical hard-rod gas. In the latter case, we will also compare the GHD results for the two-point functions with the results of microscopic simulations of the hard-rod gas, finding an excellent agreement. This represents the first demonstration of validity of the hydrodynamical predictions for two-point functions in inhomogeneous and non-stationary states. Exploiting the latter results, we will consider the calculation of the scaled cumulant generating function of the time-integrated current at the hydrodynamic scale for interacting integrable models in inhomogeneous and non-stationary initial states. We will show that the scaled cumulant generating function can be computed by biasing the measure of the initial state by the exponential of the time-integrated current. We emphasize that the expression that we get (see, Eqs. (4.59) and (4.60)) is valid for any interacting integrable model, classical or quantum and for generic initial inhomogeneous and non-stationary states. We will also show that in the limit of vanishing interactions Eqs. (4.59) and (4.60), specialized to the partitioning protocol state, coincide with the result of Chapter 3 (see Eqs. (3.94) and (3.95)).

1.5 Non equilibrium dynamics: non-integrable models

The discussion of Sec. 1.4 focused on the non-equilibrium dynamics of integrable Hamiltonians. These models are by construction special, in the sense that interactions are fine-tuned so that the underlying quasi-particle excitations are stabilized by the presence of an infinite amount, in the thermodynamic limit, of conserved charges. However, because of their special nature integrable models cannot be used to test generic features like thermalization and the ETH, see Subsec. 1.3.3, which happen only in generic, non-integrable, systems. Broadly speaking we can say that integrability can be broken in two main ways.

First in a *perturbative* way, by adding to an integrable Hamiltonian H_0 a non-integrable term ϵH_1, with ϵ small, but not zero, resulting into an Hamiltonian $H = H_0 + \epsilon H_1$. In this case, the dynamics of the system is still strongly sensitive to the integrable structure of H_0 and within a certain time span it is described by the general framework known as *prethermalization*, see for instance Refs. [185, 186] and Ref. [54] for a review. Roughly speaking the effect of the integrability breaking term H_1 will be felt after a time scale $\tau \sim 1/\epsilon$, before which relaxation to non-thermal stationary values of local observables predicted by a GGE is expected. After this transient behavior, in the long-time limit, thermalization eventually takes

place. This analysis is clearly very qualitative and heuristic and providing quantitative estimates of the involved time-scales is extremely difficult, albeit very precise theoretical studies on the subject are present [187–195]. It is important to note that the prethermalization picture represents the ultimate reason why it is possible to experimentally realize integrable models and to observe dynamical effects due to integrability. A good example is again the Newton's cradle experiment in Fig. 1.2, where the anharmonic trapping $U(z)$ and imperfect point-like interactions make the underlying description of the Bose gas non-integrable [53]. Since, however, these perturbations in the experiment are small, the prethermalization picture applies and it renders the integrable dynamics observable within the experimental time-scale.

A second, more dramatic, way of breaking integrability is the *non-perturbative* one, thereby obtaining a generic non-integrable Hamiltonian. The dynamics in this case does not display, even at short times, any signature of integrability. Accordingly, these systems can be potentially used to directly probe the ETH assumption as thermalization is generically expected to occur at long times. Note, however, that there are remarkable exceptions that hinder thermalization in non-integrable systems. There are many body localized models, where translational invariance is broken upon introducing disorder into the Hamiltonian, see the reviews in Refs. [196–198]. Another class of systems is provided by models exhibiting the "quantum scars' [199–201], which are eigenstates that do not show the thermal behavior predicted by the ETH in Eq. (1.36). In a semiclassical perspective, these eigenstates corresponds to wavefunctions localized along periodic orbits. In particular, the quantum scars have been shown in Refs. [199, 200] to determine persistent oscillations and a non-thermal dynamics in Rydberg atoms arrays. A common feature, however, of all these cases where integrability is broken in a non-perturbative way is that there is no general prescription to construct the quasi-particles excitations, contrary to the case of non-interacting models discussed in Subsecs. 1.3.5 and 1.4.2 or of the interacting integrable ones discussed in Subsec. 1.4, which have a finite lifetime depending on the initial state. One can therefore wonder about the robustness of generic features of the quench dynamics, like the light-cone spreading of correlations, entanglement and transport, in this case.

In the next Subsection we address the latter point together with the possibility of avoiding the thermalization by considering a particular class of translationally invariant (nondisordered) systems where integrability is broken in a non-perturbative way: one dimensional models exhibiting *confinement* of excitations. This class of systems will be the main subject of Chapter 5 in Part II of the thesis, whose results are anticipated in the next Subsection.

1.5.1 Confinement of excitations

Confinement is a concept originated in high-energy physics where elementary particles, such as quarks, experience spatial confinement into composite particles, due to the strong forces acting at arbitrary distances mediated by gauge fields [202]. An analogous effect is also present in condensed-matter systems. In one spatial dimension, confinement typically arises in the ordered phases of

systems with a spontaneously broken discrete symmetry: their elementary particle/antiparticle excitations consist of kink/antikink configurations which locally connect different degenerate ground states (vacua). Upon breaking the symmetry via external fields, the various vacua acquire different energy densities. As a result, separating a kink-antikink pair requires a configurational energy cost proportional to their distance, which results in their spatial confinement [203–222]. To make a concrete example, one can consider again the quantum Ising chain

$$H = -\sum_i \sigma_i^x \sigma_{i+1}^x - h_z \sum_i \sigma_i^z - h_x \sum_i \sigma_i^x, \tag{1.50}$$

where, as compared to Eq. (1.2), the additional term related to the longitudinal field h_x has been included. While the transverse field is now indicated by h_z to distinguish it from h_x. The latter explicitly breaks the $\mathbb{Z}_2$ symmetry and it is therefore responsible for the confinement of pairs of domain-wall excitations of the transverse field Ising chain into a linearly growing potential. A pioneering work studying the *dynamical* effects of confinement on the non-equilibrium evolution is Ref. [223]. This work will be briefly reviewed in Part II of the thesis. For the time being, it is sufficient to recall that Ref. [223] found that for homogeneous quenches of the Ising Hamiltonian in Eq. (1.50) the light-cone spreading of correlations and entanglement is non-perturbatively suppressed as long as an even very small longitudinal magnetic field h_x is present in the post-quench evolution. This behavior is generic as it relies only on the confinement of the domain-wall excitations in the ferromagnetic phase. Beyond Ref. [223], as a matter of fact, a significant interest on dynamical signatures of confinement has lead to several recent studies of one-dimensional spin chains, which have confirmed that confinement can lead to anomalous real-time dynamics [6, 7, 224–232] and spectral properties [233–235], at finite energy density above the ground state, in contrast with the generically expected thermalization. It is also crucial to observe that the confinement of excitations has been experimentally observed in several quasi one-dimensional compounds, see Ref. [221, 222].

As mentioned above, confinement is a concept characteristic of high-energy physics and it is therefore present also in gauge theories, which provide an essential part of our understanding of nature. Lattice gauge theories (LGTs), first proposed in Refs. [236, 237] (see Ref. [9] for an excellent review on the subject) provide a non-perturbative regularization of such theories. In this thesis we will focus on Abelian $U(1)$ lattice gauge theories in $(1+1)$ space-time dimensions. An example is the so-called lattice Schwinger model [238], which is of fundamental importance as it describes quantum electrodynamics. A variety of numerical techniques is furthermore available to study the Schwinger model due to its reduced dimensionality, see for example Refs. [239–242]. Despite being much simpler than the quantum chromodynamics, which is a non-Abelian $SU(3)$ lattice gauge theory in $(3+1)$ dimensions, it shares important features with the latter, such as confinement. Also for lattice gauge theories, as a matter of fact, it has been shown that confinement may lead to an anomalously slow relaxation behavior [239–251].

Our contribution, presented in Chapter 5 of Part II of the thesis, will be first to understand the effects of confinement on the dynamics ensuing from inhomogeneous initial states, in the spirit of Subsec. 1.4.2. In particular, we will consider

the transport of energy arising from a domain-wall initial state along the longitudinal direction of the Ising chain in Eq. (1.50). Despite the macroscopic energy imbalance in the initial state, the energy transport is found to be *suppressed* within the whole range of numerically accessible time-scales. The initial energy inhomogeneity is therefore not smoothed out by the dynamics and the light-cone picture of Fig. 1.9 is significantly altered. Second, we aim at clarifying the connection between the confinement of quasi-particles excitations and the suppression of thermalization. In order to achieve this target we will derive an exact correspondence between quantum spin chains, like the Ising model in Eq. (1.50) and the XXZ spin chain in a staggered field [219, 221, 222], and $U(1)$ Abelian lattice gauge theories. In terms of this mapping a unified picture explaining the anomalous dynamical behavior in these two classes of systems will be presented. In particular, we will single out the most important phenomena, determined solely by the presence of confinement, which stabilize the nonthermal behavior for a large class of inhomogeneous initial states. It will be further shown that confinement causes a quasilocalized dynamics which resembles the one of disordered systems [196–198], despite the fact that all the models considered in Chapter 5 will be translationally invariant (nondisordered).

1.6 Structure of the thesis

The organization and the results of the thesis have been introduced in this Chapter while presenting the research topics. For the reader's convenience, however, it is useful to schematically summarize here the structure of the thesis. The thesis is divided in two Parts. Part I is divided into the following Chapters:

- Chapter 2, based on Ref. [2]. The main result regards a fully analytical study via the quench action method of the large-deviation statistics of the work done in a non-trivial and experimentally relevant interaction quench of the one-dimensional Bose gas;
- Chapter 3, based on Refs. [1, 4] . We derive, for non-interacting quantum models, exact and universal formulas for the energy current and its large-deviation statistics in the hydrodynamic limit of large space-time scales;
- Chapter 4, based on Refs. [3, 5]. We numerically validate predictions of the generalized hydrodynamics for dynamical correlation functions and we derive an exact formula for the current large-deviation statistics applicable to any interacting integrable model, both classical and quantum.

Part II contains the following Chapter:

- Chapter 5, based on Refs. [6, 7]. We identify confinement of the quasi-particles excitations as a robust mechanism to suppress transport of energy and thermalization over experimentally accessible time scales and we provide an analytical understanding for this behavior.

Each Chapter is to a large extent self-contained so that it can be read independently of the other Chapters. For each Chapter there is an Appendix containing the technical aspects underlying the various results.

Part I

Large deviations in non-equilibrium systems

Chapter 2

Homogeneous systems: work statistics

In this Chapter we investigate the work statistics in homogeneous quantum quenches of integrable models. In particular, we consider an interaction quench of the Lieb-Liniger model describing a one-dimensional gas of N bosons with pointwise repulsive interaction. The definition of the work done in quantum quench, see Subsec. 1.3.4, has been first proposed in Refs. [67, 71, 252, 253] and it has now proven to encode important information on the internal dynamics of the system [67, 68, 254–261] and to display interesting features such as, most prominently, an emergent universal behavior [262] in quenches near a critical point [69, 70, 263]. Moreover, the statistics of the work turned out to be a valuable tool for studying dynamical phase transitions [35–39] and for detecting them.

The probability distribution of the work W can be studied via the large deviation approach of Sec. 1.2 by considering the intensive work $w = W/L$, where L is the system size, as outlined in Subsec. 1.3.4. For free bosonic and fermionic systems the large deviation approach has been successfully applied in Ref. [69] where the rate function $I(w)$ appearing in Eq. (1.38) has been computed. Importantly, it was shown in Ref. [69] that $I(w)$ provides insight into the universal properties of the system for $w \ll \overline{w}$, where $\overline{w} = \langle W \rangle / L$ is the average and typical value of w. Furthermore, it was argued that its qualitative behavior can be inferred based on the knowledge of a few parameters of the quench. The analysis of Ref. [69] also revealed that, for free bosonic models starting from a critical initial state, a further universal behavior appears in the regime $w > \overline{w}$, where $p(w)$ displays a transition from the exponential decay $p(w) \asymp \exp[-LI(w)]$ to an algebraic decay as a function of w. This transition is analogous to well-known phenomenon of Bose-Einstein condensation in quantum statistical physics [8].

The aim of this Chapter is threefold. First, by means of a case study, we show that the quench action method predicts a statistics $p(w)$ of the large deviations of the intensive variable w which takes the exponential form $p(w) \asymp \exp[-LI(w)]$ for $L \to \infty$ at fixed spatial density $D = N/L$ of the gas, i.e., $p(w)$ naturally satisfies the *large deviation principle* [22]. In addition, the quench action method allows the calculation of $I(w)$. Second, from this result we carry out a quantitative analysis of the interaction quench described above, pointing out its most interesting features (strongly depending on the presence of the interactions) which were out of reach of the analysis presented in Ref. [69]. Third, going beyond large deviation theory, we analyze the statistics of w in the region $w > \overline{w}$ where $I(w)$ vanishes identically and $p(w)$ has an algebraic decay upon increasing w. Although, in this case, the

quench action method is no longer sufficient to predict $p(w)$, we are able to determine the exponent of this algebraic tail by performing a finite-size calculation in the limit of vanishing densities D of the bosons. To the best of our knowledge, this provides the first quantitative description of the "condensed regime" characterizing the work statistics of bosonic systems in the presence of interactions for quenches starting from a critical initial state.

The content of this Chapter is organized as follows. Sections 2.1, 2.2 and 2.3 provide an introduction to the topic. In particular, Sec. 2.1 recalls known results on the statistics of the work done in a quantum quench. Section 2.2 briefly reviews the Bethe ansatz formalism which has been successfully used to analyze interacting integrable systems. Section 2.3 introduces the quench action method, which allows one to extend the Bethe ansatz method to quantum quenches. Sections 2.4, 2.5, and 2.6 present the original results of Ref. [2]. In Sec. 2.4 we show how to use the quench action method to calculate exactly the work statistics in interacting integrable models. In Sec. 2.5 we discuss our results for the Lieb-Liniger model. In Sec. 2.6 we provide a quantitative analysis of the condensation transition taking place for $w > \overline{w}$. Section 2.7 presents some final remarks regarding the results obtained and discusses future perspectives. In Appendix 2 the most technical aspects of the calculations required for the derivation of the original results are presented.

2.1 Generic features of the work statistics

We review in this Section some generic features of the work statistics obtained in free models [67, 69–71, 254, 263]. The following discussion will be useful for a comparison with the interacting case analyzed in Secs. 2.4, 2.5, and 2.6. In Subsec. 1.3.4 we defined the work W done in a global quantum quench $c_0 \to c$ in terms of a two-measurements protocol. The probability distribution $P(W)$ of the extensive work W is consequently defined as

$$P(W) = \sum_{n\geq 0} |\langle n|\Psi_0\rangle|^2 \delta(W - (E_n(c) - E_0(c_0))), \tag{2.1}$$

where $|n\rangle$ are the eigenstates of the post-quench Hamiltonian $H(c)$ with corresponding energies $E_n(c)$. $E_0(c_0)$ denotes the energy of the ground-state $|\Psi_0\rangle$ of the pre-quench Hamiltonian. We emphasize here that the initial state $|\Psi_0\rangle$ is homogeneous, i.e., translationally invariant. The case of inhomogeneous initial states will be the subject of Chapters 3 and 4. One immediately notices from Eq. (2.1) that the work has a minimum threshold value $W_{\text{rev}} = E_0(c) - E_0(c_0)$. This has the meaning of reversible work, i.e., the work performed at zero temperature when the transformation $c_0 \to c$ is done adiabatically, i.e., in a reversible way. As a consequence, we will refer the work W to this threshold, focusing on the irreversible contribution $W_{\text{irr}} = W - W_{\text{rev}} \geq 0$, which is related to the irreversible entropy production [52, 253]. For convenience, we will henceforth indicate W_{irr} by W, dropping the subscript:

$$P(W) = \sum_{n\geq 0} |\langle n|\Psi_0\rangle|^2 \delta(W - (E_n(c) - E_0(c))). \tag{2.2}$$

The probability distribution of $P(w)$ will consist, as a consequence of the definition in Eq. (2.2), of a sequence of peaks in correspondence of the allowed transitions between the pre-quench ground state and the post-quench eigenstates, each peak being weighted by the modulus squared of the corresponding overlap. In the thermodynamic limit of infinite system size $L \to \infty$ and number of particles $N \to \infty$ with fixed density $D = N/L$, the fine structure of the peaks will turn into a continuous probability density function. To study the latter it is convenient to introduce the moment generating function $G(s)$ of the extensive irreversible work $W > 0$ as

$$G(s) = \langle \mathrm{e}^{-sW} \rangle = \int_0^\infty \mathrm{d}W \, \mathrm{e}^{-sW} P(w) = \langle \Psi_0 | \mathrm{e}^{-s(H(c)-E_0(c))} | \Psi_0 \rangle, \tag{2.3}$$

where the second equality follows by plugging the expression in Eq. (2.2) for $P(W)$ into the integral over W. For the purpose of the large deviation analysis it is also important to define the corresponding scaled cumulant generating function (SCGF) $f(s)$ in the thermodynamic limit such that

$$G(s) = \mathrm{e}^{-Lf(s)}, \quad \text{i.e.,} \quad f(s) = -\lim_{L\to\infty} \frac{\ln G(s)}{L}. \tag{2.4}$$

We note that the function $f(s)$ in Eq. (2.4) has been defined with a rescaling by the system size L and not by the number of particles N. The two definitions are clearly equivalent since $N = DL$ and the density D is assumed to be fixed. In the case $s = it$ the function $G(s)$ coincides with the return amplitude $L(t) \equiv |G(it)|^2$ or Loschmidt echo. The analytic continuation of $f(s)$ from real to complex values of s is, in general, highly non-trivial, as shown in Ref. [35] for the transverse field Ising chain (1.2), as $f(s)$ in the complex plane of s might display singularities. These points of non-analiticity in the real-time evolution of the Loschmidt echo are present for quenches of the transverse field h across the critical point $h = 1$ and they have been interpreted in Ref. [35] as *dynamical transitions*. In the following analysis we will consider the case of *real values* of $s \in \mathbb{R}$, albeit we will comment on the analytic structure of $G(s)$ in the complex plane in Sec. 2.4 when discussing the novel results regarding interacting integrable models. In the case of real s the moment generating function $G(s)$ can be interpreted for a quantum system in d spatial dimensions via the transfer matrix approach [9], mentioned in Sec. 1.1, as the partition function of a classical system in $d+1$ spatial dimensions on a semi-infinite slab geometry with thickness s and equal boundary states $|\Psi_0\rangle$. For this reason $G(s)$ is also named *dynamical partition function* as it generalizes to the non-equilibrium quench dynamics the concept of the partition function. In the present thesis we will consider the case of quantum quenches in 1 spatial dimension as outlined in Sec. 1.3. In the latter framework, as we have seen in Subsec. 1.3.4, $\langle W \rangle = \langle \Psi_0 | H(c) | \Psi_0 \rangle - E_0^c \sim L$ as $L \to \infty$, which motivates the introduction of the intensive work $w = W/L$ variable. The latter is characterized by a probability density function $p(w)$ which obeys the large deviation principle in Eq. (1.38). The rate function $I(w)$ can be computed by means of the Gärtner-Ellis theorem, introduced in Sec. 1.2, which in the present context reads as

$$I(w) = -\inf_s \{sw - f(s)\}, \tag{2.5}$$

where the infimum has to be taken within the domain in which $f(s)$ is defined. In this case the Legendre duality relations in Eq. (1.16) become

$$w = \frac{\mathrm{d}f(s)}{\mathrm{d}s}; \quad \text{and} \quad s = -\frac{\mathrm{d}I(w)}{\mathrm{d}w}. \tag{2.6}$$

Note that, once the large deviation principle $p(w) \sim \exp[-LI(w)]$ is satisfied, the Gärtner-Ellis theorem can be heuristically derived by a saddle-point approximation of the inverse Laplace transform of $G(s)$ [22, 69]. However, it might be difficult to prove this principle a priori in specific cases, and thus this is usually done a posteriori.

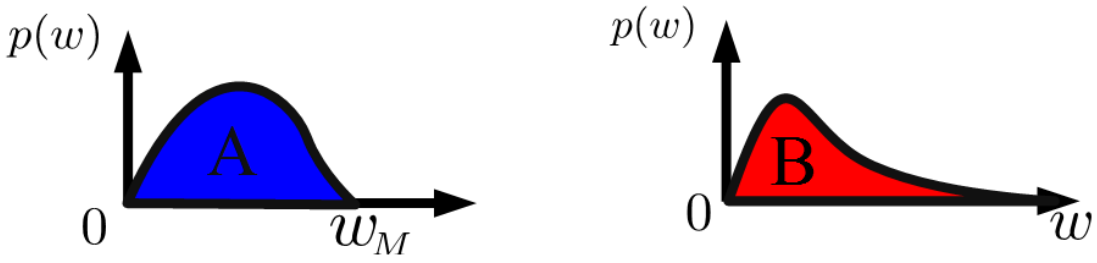

FIGURE 2.1: Probability density function $p(w)$ for systems belonging to class A (left panel) and B (right panel). In case A a finite maximum value w_M of the intensive work exists and $p(w)$ has support only on a finite interval $(0, w_M)$. In case B there is no finite maximum value w_M and $p(w)$ has support over the semi-infinite interval $(0, \infty)$. Notice that in both cases $w > 0$ as we are considering the irreversible work, as discussed before Eq. (2.2).

At this point it is worth introducing a distinction between two main classes of systems, A and B, following the classification scheme of Ref. [69], see Figs. 2.1 and 2.2. In class A the intensive work w has a maximum value w_M and therefore $G(s)$ and the SCGF are defined for all real values of s with a linear asymptotic $f(s) \sim sw_M$ as $s \to -\infty$. In class B, instead, the intensive work w has no finite maximum value and therefore $G(s)$ and the SCGF are defined for $s > -\bar{s}$ ($\bar{s} > 0$) with a singularity in its derivative at $\bar{s}$. Note, however, that this classification is certainly not exhaustive, in the sense that different qualitative features might emerge in particular models. For example, in Ref. [258], it has been shown, for a quench from the superradiant to the normal phase of the Dicke model [264, 265], that $f(s)$ approaches $-\bar{s}$ with a finite derivative. In all the cases, anyhow, the SCGF $f(s)$ saturates to a constant value $2f_0$ as $s \to \infty$. From the Legendre-Fenchel transform in Eqs. (2.5) and (2.6) the rate function function is finite only for $w > 0$ with the value in $w = 0$ related to the behavior of $f(s)$ at $s \to \infty$ as $I(w = 0) = 2f_0$. The average intensive work $\overline{w} = f'(s = 0)$ is the unique zero of $I(\overline{w} = 0)$. Prominently, as shown in Refs. [69, 70], the behavior of $I(w)$ for $w \ll \overline{w}$ becomes universal if the post-quench Hamiltonian is critical

$$I(w) - 2f_0 \propto w^{d/(d+1)}, \tag{2.7}$$

with d the space dimensionality of the system, a fact which can be rationalized via a quantum-to-classical correspondence [13]. The asymptotic of $I(w)$ for $w \gg \overline{w}$ is, instead, in general not universal and it is determined by that of $f(s)$ for $s \to -\infty$. In particular, for class A systems $I(w)$ is finite for $w < w_M$ and infinite otherwise, reflecting the compact support of $p(w)$ as in Fig. 2.1, while for class B systems $I(w)$ is defined for arbitrary large values of w with an asymptotic linear behavior with slope $\bar{s}$. In the aforementioned case analyzed in Ref. [258], the finite slope of $f(s)$ at $s = -\bar{s}$ implies that $I(w)$ has an additional singularity w^*, larger than the mean intensive work $w^* > \overline{w}$, such that it becomes exactly linear for $w > w^*$.

A sketch of $f(s)$ in class A and B systems and the associated rate function $I(w)$ is presented in Fig. 2.1. fermionic lattice models and spin chains belongs to class A since, because of the finite local Hilbert space, the energy spectrum is bounded from above. An example is provided by the transverse field Ising chain in Eq. (1.2), where $G(s)$ has been computed explicitly in Refs. [67, 69, 263]. Continuum models and field theories belong to class B as, in these cases, the energy is unbounded from above and therefore w_M is infinite. An example is provided by the free Gaussian ϕ^2 field theory [69, 70], that will be discussed in the next Section, and the Lieb-Liniger model, which will be the main subject of the original work presented in this Section.

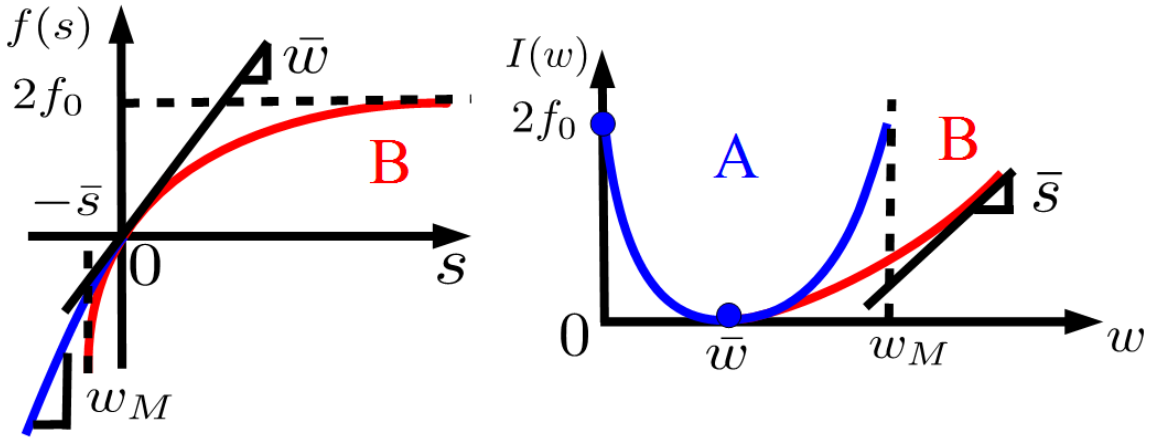

FIGURE 2.2: Left panel: Sketch of $f(s)$ for systems belonging to class A (blue) or B (red). Right panel: the associated rate function $I(w)$, computed from $f(s)$, according to Eqs. (2.5) and (2.6). In both classes, $I(w)$ is defined only for $w > 0$ as we are considering the irreversible work, see the discussion after Eq. (2.2). For class A the domain of the rate function has an upper extreme w_M beyond which $I(w)$ is infinite.

2.1.1 Condensation transition

As we have seen in the previous Section, the asymptotic behavior of $I(w)$ for $w \ll \overline{w}$ displays universal features, while for $w \gg \overline{w}$ the qualitative behavior of the rate function strongly depends on the class of the systems considered. However, restricting now the analysis to class B systems, it has been shown in Ref. [69] that $p(w)$ for free bosonic excitations may feature a different kind of universal behavior also for $w > \overline{w}$. In particular, as the pre-quench initial state is varied from

being non-critical, i.e., having a gapped spectrum of excitations, to critical, i.e., with a gapless spectrum, a transition in the functional form of $p(w)$ takes place such that $I(w)$ vanishes identically for $w \geq \overline{w}$, when the pre-quench initial state becomes critical. This has been identified as a "condensation" transition, in analogy to the Bose-Einstein condensation in equilibrium statistical physics [8]. The vanishing of the rate function, according to Eq. (1.12), implies that $p(w)$ displays a subleading algebraic decay upon increasing w with respect to exponential form predicted the large deviation principle, in Eq. (1.38). The algebraic decay of $p(w)$ goes therefore beyond the predictions of the large deviation theory and it requires an additional analysis.

To make the discussion more concrete, we review the condensation transition in the work statistics of the non-interacting Gaussian ϕ^2 field theory in d spatial dimensions, first analyzed in Refs. [69, 70]. This discussion will be useful for the comparison with the interacting Lieb-Liniger Bose gas in Sec. 2.6. The Hamiltonian of the model is

$$H = \frac{1}{2}\int \frac{\mathrm{d}k^d}{(2\pi)^d}\,\Big[\pi(k)\pi(-k) + \omega^2(m,k)\phi(k)\phi(-k)\Big]\,, \tag{2.8}$$

with $\phi(k)$ and the conjugate momentum operator $\pi(k')$ satisfying equal-time canonical commutation relations $[\phi(k), \pi(k')] = (2\pi)^d\,\delta(k-k')$. The Hamiltonian in Eq. (2.8) can be exactly diagonalized in terms of free bosonic mode operators having the relativistic single-particle dispersion relation $\omega(m,k) = \sqrt{k^2+m^2}$, with m the mass-gap of the excitations. In particular we consider a quench $m_0 \to m$ of the mass m from an initial value m_0. Since the spectrum $\omega(m,k)$ of the model is unbounded from above the scaled cumulant generating function $f(s)$ in Eq. (2.4) belongs to class B according to the classification scheme introduced in Sec. 2.1. The calculation of $f(s)$ can be performed from the exact solution of the Hamiltonian into free bosonic modes [69, 70], and the final result reads

$$f(s) = \frac{1}{2}\int \frac{\mathrm{d}k^d}{(2\pi)^d}\,\ln\left[\frac{1-\lambda^2(k)\,\mathrm{e}^{-2\omega(m,k)s}}{1-\lambda^2(k)}\right]\,, \tag{2.9}$$

with the integral over $\mathbb{R}^d$ and

$$\lambda(k) = \frac{\omega(m_0,k)-\omega(m,k)}{\omega(m_0,k)+\omega(m,k)}, \tag{2.10}$$

carrying information about the mass quench. The SCGF is then defined for

$$s > -\bar{s} = \sup_k\left(\frac{\ln|\omega(m,k)|}{\omega(m,k)}\right)\,, \tag{2.11}$$

in agreement with the general properties of the SCGF for class B systems. A plot of the associated rate function $I(w)$, computed according to Eq. (2.5) is shown in Fig. 2.3. The condensation behavior takes place when the pre-quench mass m_0 is set to zero $m_0 = 0$. In this case, $\overline{w} = f'(s=0) < \infty$ for $d > d_c$, with $d_c = 1$, and $\bar{s} = 0$ from Eq. (2.11). This, in turn, implies that $I(w) \equiv 0$ for $w > \overline{w}$ and the

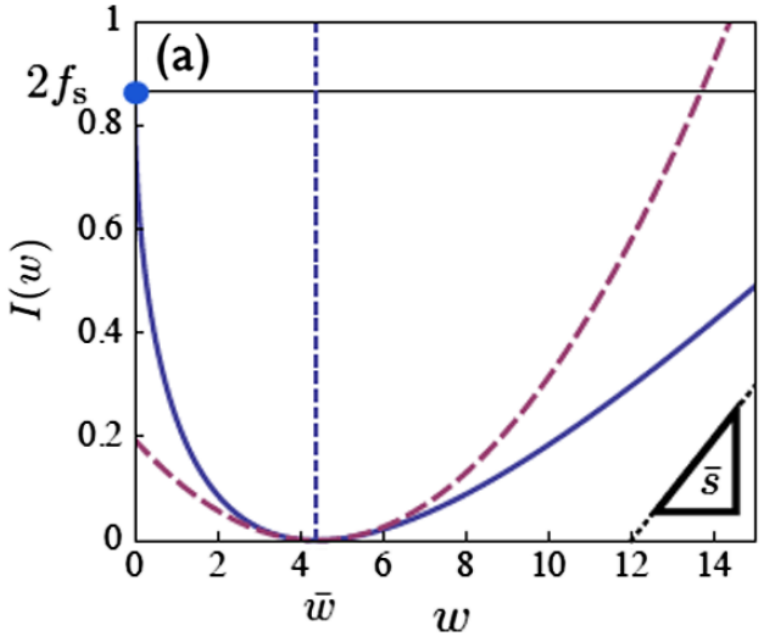

FIGURE 2.3: Plot of the rate function $I(w)$ for a quench of the mass m from the value $m_0 = 20$ to the critical value $m = 0$ in the free bosonic theory in Eq. (2.8). The dashed line corresponds to the Gaussian-quadratic approximation of the rate function valid for $w \to \overline{w}$. Image taken from Ref. [69].

large deviation principle in Eq. (1.10) is violated, in agreement with discussion presented after Eq. (1.12). In turn this is caused by the fact that the probability density $p(w)$ for $m_0 = 0$ exhibits an algebraic decay for $w > \overline{w}$, which cannot be captured by the large deviation theory. Note that the exponent of this algebraic decay as a function of w is left unknown by the analysis of Ref. [69].

In order to understand this feature it is now worth recalling the description of the non-interacting Bose-Einstein condensation in the grand canonical ensemble [8]. Considering the moment generating function $G(s)$ of the particle number N and the associated SCGF $\psi(s)$

$$G(s) = \langle \mathrm{e}^{-sN} \rangle_{\beta,\mu}, \qquad \psi(s) = -\lim_{L\to\infty} \frac{\ln G(s)}{L^d}, \tag{2.12}$$

where the average is done over the grand-canonical distribution, identified by the inverse temperature β and the chemical potential $\mu \leq 0$. With a simple calculation one obtains

$$\psi(s) = \int \frac{\mathrm{d}k^d}{(2\pi)^d} \ln\left[\frac{1-\Lambda(k)\mathrm{e}^{-s}}{1-\Lambda(k)}\right], \tag{2.13}$$

with

$$\Lambda(k) = \mathrm{e}^{-\beta\varepsilon(k)+\mu\beta} \qquad \text{and} \qquad \varepsilon(k) = \frac{\hbar^2 k^2}{2m}. \tag{2.14}$$

From $\psi(s)$ the rate function $I(\rho)$ of the spatial density $\rho = N/L^d$ of bosons can be obtained via the Legendre-Fenchel transform. The expression in Eq. (2.13) has the very same structure as Eq. (2.9), and it can be also assigned to class B, with

domain given by

$$s > -\bar{s}, \qquad \text{with} \qquad \bar{s} = -\beta\mu. \tag{2.15}$$

For $\mu = 0$, analogously as in Eq. (2.11), $\bar{s}$ vanishes and therefore the rate function $I(\rho) \equiv 0$ for $\rho > \rho_c$. The vanishing of the chemical potential μ has a clear meaning in the equilibrium description of the Bose gas as it signals the onset of the Bose-Einstein condensate phase [8]. The value of ρ_c is therefore nothing but the critical density for the Bose-Einstein condensation, i.e.,

$$\rho_c = \frac{1}{l^d}\,\zeta(d/2) \qquad \text{with} \qquad l = \sqrt{\frac{2\pi\beta\hbar^2}{m}}, \tag{2.16}$$

with l the thermal De-Broglie wavelength and ζ the Riemann zeta function. We therefore see that the Bose-Einstein phase transition can be identified with the vanishing of the rate function for $\rho > \rho_c$ when the chemical potential is tuned to its critical value $\mu = 0$. This is shown in Fig. 2.4 where the rate function $I(\rho)$ is plotted for different values of the chemical potential. The behavior of $I(\rho)$ for the equilibrium, non-interacting Bose-gas is completely analogous to the one of $I(w)$ for the mass quench of the free bosonic field theory (2.8). In the latter case, the parameter driving the transition is m_0, with critical value $m_0 = 0$, while in the former the control parameter is μ, with critical value $\mu = 0$. This eventually justifies the name "condensation" transition that is used for the vanishing of $I(w)$ above $\overline{w}$ in quantum quenches. An important difference to mention is that for

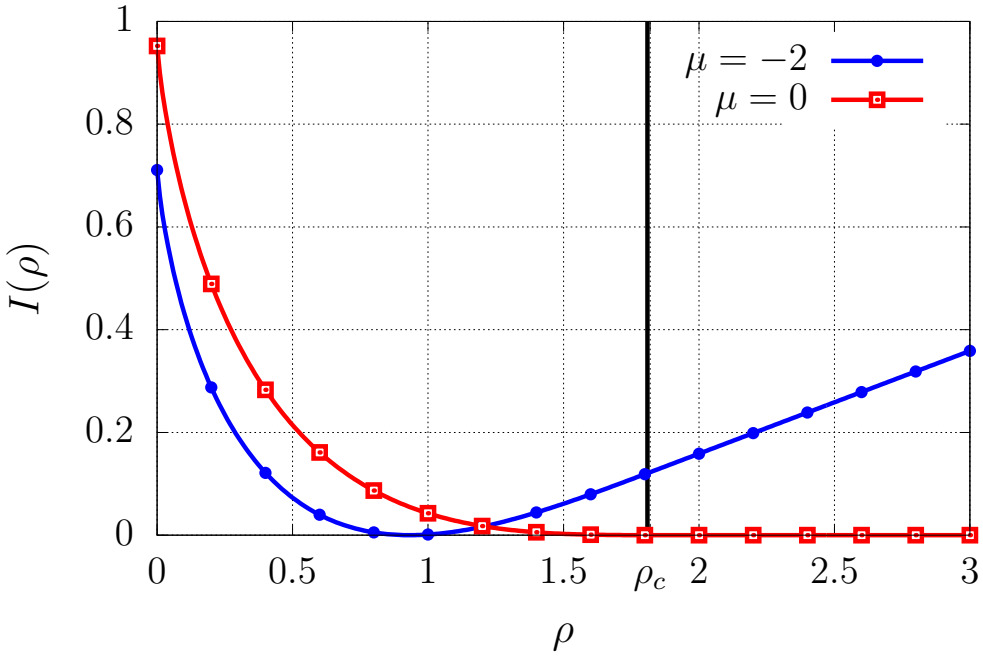

FIGURE 2.4: Plot of the rate function $I(\rho)$ for the equilibrium non-interacting Bose gas in dimension $d = 3$. The blue curve corresponds to a chemical potential with a non-critical value $\mu = -2$, while the chemical potential is poised to its critical value $\mu = 0$ for the red curve. In this case $I(\rho)$ identically vanishes for $\rho > \rho_c$ with ρ_c given in Eq. (2.16) and marked by the vertical black line in the plot.

the equilibrium case the condensation takes place for $d > d_c'$ with $d_c' = 2$, in contrast with the non-equilibrium quench dynamics where $d_c = 1$ as discussed after Eq. (2.11). This property has to be ascribed in Ref [69] to the fact that for $m = 0$ the dependence of $\omega(m, k)$ crosses from quadratic to linear in k.

Although no general expression has been reported so far for such a power-law tail of $p(w)$ in this condensation regime, the latter has been shown to appear also in different non-equilibrium protocols [254]. In this Chapter we will provide the first quantitative prediction for the corresponding exponent in the interacting Lieb-Liniger Bose gas. To do this the Bethe ansatz method, which we now briefly review, will be employed.

2.2 Interacting integrable systems: the Bethe ansatz

In this Section we introduce the Bethe ansatz technique, first proposed by Hans Bethe to solve the XXZ spin chain [266]. The method has been then extended, allowing the exact solution of a large class of one-dimensional quantum systems including spin-chain models, relativistic and non-relativistic field theories and the Hubbard model. These models are usually dubbed Bethe-ansatz integrable. Henceforth in the thesis we will refer to them as integrable models, even though the definition of quantum integrability is more subtle [100] as mentioned in Sec. 1.4 of Chapter 1. It is worth mentioning that the Bethe-ansatz, despite being originally applied to quantum models, can also be used to solve classical statistical systems as well, like the hard-rods gas [162] and the Toda chain [164, 165]. The classical hard-rod gas will be extensively discussed in Chapter 4. In this Section, the focus will be on the quantum Lieb-Liniger model [267, 268], which describes a gas of bosons with point-wise interactions. This choice is motivated not only by the focus of the original results of this Chapter, but also by the fact the Lieb-Liniger Hamiltonian has been by now realized in a variety of (quasi) one-dimensional cold-atoms experiments [269–274], like the quantum Newton's cradle [53] described in Sec. 1.3.1. This Section is organized as follows. In Subsec. 2.2.1 we introduced the so-called *coordinate Bethe ansatz*, which provides the exact expression of the many-body wavefunction of the Lieb-Liniger gas. In Subsec. 2.2.2 the *thermodynamic Bethe ansatz*, which efficiently describes the thermodynamics of the model, is recalled. In Subsec. 2.2.3 we recall a fundamental aspect of interacting one-dimensional systems which is the *dressing* of the single-particle excitations. Only the main aspects of the Bethe ansatz will be reviewed here, while excellent books on this subject where the method is explained with the necessary mathematical rigor and details are Refs. [102, 275].

2.2.1 Coordinate Bethe ansatz

The Lieb-Liniger model [267, 268] describes a gas of N bosons at positions $\{x_1, ..., x_N\}$ with mass m and point-wise repulsive interactions, with Hamiltonian

$$H(c) = -\frac{\hbar^2}{2m}\sum_{j=1}^{N}\frac{\partial^2}{\partial x_j^2} + 2c\sum_{j<k}\delta(x_j - x_k). \tag{2.17}$$

The repulsive interaction strength $c > 0$ is related to the scattering length a_{1D} in one dimension through $c = -\hbar^2/ma_{1D}$ [276] and it can be varied via Feshbach resonances [277]. In the following we set $\hbar = 2m = 1$ and assume that the N bosons are confined within a one-dimensional ring of length L, realizing periodic boundary conditions. The Hamiltonian in Eq. (2.17) can be equivalently rewritten in the second quantization formalism

$$H(c) = \int_0^L \mathrm{d}x \left[\partial_x \Psi^\dagger(x)\partial_x \Psi(x) + c\Psi^\dagger(x)\Psi^\dagger(x)\Psi(x)\Psi(x)\right], \tag{2.18}$$

where $\Psi(x)$ and $\Psi^\dagger(x)$ are bosonic field operators satisfying equal-time canonical commutation relations $[\Psi(x), \Psi^\dagger(x')] = \delta(x - x')$. A generic eigenfunction $|\psi_N\rangle$ of the system can be written as

$$|\psi_N\rangle = \frac{1}{\sqrt{N!}} \int_0^L \mathrm{d}x_1 \cdots \int_0^L \mathrm{d}x_N \, \psi_N(x_1, \ldots x_N)\Psi^\dagger(x_1)\ldots\Psi^\dagger(x_N)|0\rangle, \tag{2.19}$$

where $|0\rangle$ is the Fock space vacuum and periodic boundary conditions are assumed on the field operators $\Psi(x)$ and $\Psi^\dagger(x)$. The Bethe ansatz amounts to a guess on the many-body wavefunction $\psi_N(x_1, \ldots x_N)$ as a superposition of plane waves

$$\psi_N(x_1, \ldots x_N) = \sum_{\mathcal{P}} A(\mathcal{P}) \prod_{j=1}^{N} \mathrm{e}^{i\lambda_{\mathcal{P}_j} x_j}, \qquad x_1 < x_2 \cdots < x_N, \tag{2.20}$$

where the sum runs over the $N!$ permutations $\mathcal{P}$ of the λ_j among the coordinates $x_1, x_2 \ldots x_N$. The parameters $\{\lambda_j\}_{j=1}^N$ are the so-called rapidities or quasi-momenta and, in analogy with the momenta which are relevant in the case of free quantum gases, they parametrize the different eigenstates of the Hamiltonian. In order to fix the coefficients $A(\mathcal{P})$ one writes the eigenvalue equation $H\psi_N = E\psi_N$ with ψ_N in Eq. (2.20) and the Hamiltonian in Eq. (2.17). This results into the condition

$$A(\mathcal{P}') = \frac{\lambda_{\mathcal{P}_j} - \lambda_{\mathcal{P}_{j+1}} + ic}{\lambda_{\mathcal{P}_j} - \lambda_{\mathcal{P}_{j+1}} - ic} A(\mathcal{P}), \tag{2.21}$$

where the permutation $\mathcal{P}'$ is obtained by $\mathcal{P}$ by exchanging $\mathcal{P}_j$ and $\mathcal{P}_{j+1}$, i.e, $\mathcal{P}' = \{\mathcal{P}_1, \ldots \mathcal{P}_{j-1}, \mathcal{P}_{j+1}, \mathcal{P}_j, \mathcal{P}_{j+2}, \ldots \mathcal{P}_N\}$. The fraction $\mathcal{S}(\lambda_{\mathcal{P}_j} - \lambda_{\mathcal{P}_{j+1}})$ on the right hand side of Eq. (2.21) is usually named scattering matrix; since it has unitary modulus it can be written as a phase $\theta(\lambda)$

$$\frac{A(\mathcal{P}')}{A(\mathcal{P})} = \frac{\lambda_{\mathcal{P}_j} - \lambda_{\mathcal{P}_{j+1}} + ic}{\lambda_{\mathcal{P}_j} - \lambda_{\mathcal{P}_{j+1}} - ic} = \mathcal{S}(\lambda_{\mathcal{P}_j} - \lambda_{\mathcal{P}_{j+1}}) = \mathrm{e}^{-i\theta(\lambda_{\mathcal{P}_j} - \lambda_{\mathcal{P}_{j+1}})}, \tag{2.22}$$

with

$$\theta(k) = 2\,\mathrm{arctang}\,(\lambda/c)\,. \tag{2.23}$$

The physical meaning of Eqs. (2.22) and (2.23) resides in the fact that in one-dimension every permutation of a pair of particles having rapidities λ_1 and λ_2 necessarily involves a contact interaction between them. The latter is expressed by the scattering amplitude $\mathcal{S}(\lambda_1 - \lambda_2)$ and it causes a phase shift $\theta(\lambda_1 - \lambda_2)$ of

the many-body wave function. From Eq. (2.22) the functional form of $A(\mathcal{P})$ is further fixed as

$$A(\mathcal{P}) = \Omega_N(-1)^{|\mathcal{P}|}\prod_{j<l}(\lambda_{\mathcal{P}_j} - \lambda_{\mathcal{P}_l} + ic), \tag{2.24}$$

where $|\mathcal{P}|$ denotes the sign of the permutation and Ω_N is a normalization constant we do not need to specify it for our purposes (it is given by the determinant of the Gaudin matrix [102]). In order to completely fix the ansatz in Eq. (2.20) for the wavefunction we further need to specify the rapidities. This can be achieved by enforcing periodic boundary conditions

$$\psi_N(x_1, \dots, x_j, \dots x_N) = \psi_N(x_1, \dots, x_j + L, \dots x_N) \tag{2.25}$$

into ψ_N in Eq. (2.20). Exploiting Eq. (2.22) this implies a set of quantization conditions which are known as Bethe equations [267, 268]

$$\mathrm{e}^{-i\lambda_j L} = \prod_{k\neq j}^{N}\frac{\lambda_k - \lambda_j + ic}{\lambda_k - \lambda_j - ic} = \prod_{k\neq j}^{N} S(\lambda_k - \lambda_j)\,, \quad \text{with} \quad j = 1, \dots, N\,. \tag{2.26}$$

The physical meaning of the Bethe equations is clear in term of the scattering picture. Applying the periodic boundary conditions in Eq. (2.25) amounts to move the particle j through the circle of length L, which implies that particle j scatters with all the other particles in the system. Each scattering event corresponds to a phase shift $\theta(\lambda_k - \lambda_j)$, according to Eqs. (2.22) and (2.23), and the total phase shift accumulated through all the collisions is just the sum of the phase shifts corresponding to each scattering event. This phase has then to equal the opposite of the dynamical phase, i.e., the rapidity λ_j times L, accumulated during the motion of particle j along the ring L. For repulsive interactions $c > 0$, it can be shown that all λ_j's are real [102, 275]; accordingly, it is convenient to consider the logarithm of Eq. (2.26), i.e.,

$$\lambda_j = \frac{2\pi I_j}{L} - \frac{1}{L}\sum_{k=1}^{N}\theta\left(\frac{\lambda_j - \lambda_k}{c}\right), \qquad j = 1, 2 \dots N, \tag{2.27}$$

where we introduced the Bethe numbers I_j. These numbers parametrize the sets of rapidities $\{\lambda_j\}$ and are integers (half-integers) for odd (even) N; note that they have to be chosen in such a way that $I_j \neq I_k$ for $j \neq k$ [102] since in the case of two identical Bethe numbers the wavefunction ψ_N in Eq. (2.20) identically vanishes. In the case of attractive interactions $c < 0$ complex "string" solutions formed by rapidities equispaced along the imaginary axes are present [102, 275]. These solutions correspond to multi-particle bound states, which render the treatment of the model more complex. Henceforth we will always assume the repulsive case $c > 0$. The knowledge of the rapidities $\{\lambda_j\}_{j=1}^{N}$ completely specifies the eigenstate ψ_N in Eq. (2.20) of $H(c)$ and its properties. For example, the eigenvalues of the conserved charges corresponding to the momentum P and the energy E can be

respectively written as

$$P\left[\{\lambda_j\}_{j=1}^N\right] = \sum_{j=1}^N \lambda_j\,, \tag{2.28}$$

and

$$E\left[\{\lambda_j\}_{j=1}^N\right] = \sum_{j=1}^N \lambda_j^2\,. \tag{2.29}$$

λ and λ^2 in the equations above represent the single-particle eigenvalue of the momentum and energy. More generally, following the notation of Sec. 1.4, for a generic conserved charge Q_n with $n = 0, 1, 2 \ldots \infty$, the eigenvalue on a Bethe eigenstate ψ_N is

$$Q_n\left[\{\lambda_j\}_{j=1}^N\right] = \sum_{j=1}^N q_n(\lambda_j) = \sum_{j=1}^N \lambda_j^n\,, \tag{2.30}$$

where $Q_0 = N$ is the number of bosons, $Q_1 = P$ the total momentum and $Q_2 = E$ the total energy. In the following, we will denote the normalized eigenstate of $H(c)$ corresponding to a set of rapidities $\{\lambda_j\}$ as $|\{\lambda_j\}\rangle$.

2.2.2 Thermodynamic Bethe ansatz

When the number N of particles is very large, the explicit form of the wave function in Eq. (2.20) becomes difficult to deal with, and the Bethe equations (2.27) harder to solve numerically. For these reasons, in order to study the thermodynamic limit of the model, it is necessary to employ an appropriate "thermodynamic Bethe ansatz" (TBA) formalism, which for the Lieb-Liniger model has been first proposed in Ref. [278]. We briefly review it in this Section. Here we only report the aspects that are directly relevant to the novel results of this Chapter, while a thorough treatment can be found in Refs. [102, 275, 278].

In order to take the thermodynamic limit $L, N \to \infty$ with fixed density $D = N/L$, it is convenient to rescale the Bethe numbers I_j by the system size L defining $x_j = I_j/L$. One can then rewrite Eq. (2.27) as

$$L\lambda(x) = 2\pi x L - \sum_{k=1}^N \theta\left(\frac{\lambda(x) - \lambda_k}{c}\right), \tag{2.31}$$

where we introduced the counting function $\lambda(x)$ with $x \in \mathbb{R}$. This function is defined such that

$$\lambda(x_j) = \lambda(I_j/L) = \lambda_j, \tag{2.32}$$

for any Bethe number I_j corresponding to a rapidity λ_j present in the set $\{\lambda_j\}_{j=1}^N$ characterizing the eigenstate $|\{\lambda_j\}\rangle$ under consideration. These rapidity values are usually dubbed "particles" of the state $|\{\lambda_j\}\rangle$. Conversely, $\lambda(x = I_m/L) = \lambda_m$ is named "hole", if I_m corresponds to a rapidity λ_m not present in the set $\{\lambda_j\}_{j=1}^N$. In the thermodynamic limit the particles rapidities λ_j of a given eigenstate, whose number also grows to infinity, arrange themselves along the real line according to a smooth distribution function $\rho(\lambda)$, with $\lambda \in (-\infty, +\infty)$, such that $L\rho(\lambda)d\lambda$ is

equal to the number of occupied states (the particles) in $(\lambda, \lambda + d\lambda)$. Complementary to the latter, the holes distribute according to a smooth distribution $\rho^h(\lambda)$, with $L\rho^h(\lambda)d\lambda$ the number of unoccupied states (the holes) in $(\lambda, \lambda + d\lambda)$. The total number of rapidities in the interval $(\lambda, \lambda + d\lambda)$ is eventually given by $L\rho^t(\lambda)d\lambda$ with

$$\rho^t(\lambda) = \rho(\lambda) + \rho^h(\lambda) = \frac{dx}{d\lambda}. \tag{2.33}$$

The functions $\rho(\lambda)$, which is also named root density, and $\rho^h(\lambda)$ are analogous to the distributions of momenta and vacancies for free Fermi gases. However, contrary to the non-interacting case, ρ and ρ^h are related in a non-trivial way. In particular, taking the derivative with respect to λ of Eq. (2.20), and exploiting Eq. (2.33), they satisfy the following integral equation

$$\rho^t(\lambda) = \frac{1}{2\pi} + \frac{1}{2\pi}\int_{-\infty}^{\infty} \mathrm{d}\mu\, K(\lambda - \mu)\rho(\mu)\,, \tag{2.34}$$

where we defined the differential scattering phase shift from Eq. (2.23)

$$K(\lambda) = \frac{d\theta(\lambda)}{d\lambda} = \frac{2c}{\lambda^2 + c^2}\,. \tag{2.35}$$

For future use, we also introduce the following standard definition

$$\eta(\lambda) = \frac{\rho^h(\lambda)}{\rho(\lambda)}\,, \qquad \vartheta(\lambda) = \frac{\rho(\lambda)}{\rho^t(\lambda)}, \tag{2.36}$$

where $\vartheta(\lambda)$ is dubbed filling or mode occupation function. It is widely believed that the knowledge of the rapidity distribution function $\rho(\lambda)$ is sufficient to compute all the thermodynamic properties of the corresponding eigenstate. For example, in the thermodynamic limit, the densities $D[\rho]$ and $e[\rho]$ of particles and energy per unit length can be obtained, respectively, as

$$D[\rho] = \lim_{N,L\to\infty} \frac{N}{L} = \int_{-\infty}^{+\infty} \mathrm{d}\lambda\, \rho(\lambda)\,, \tag{2.37}$$

$$e[\rho] = \lim_{N,L\to\infty} \frac{E}{L} = \int_{-\infty}^{+\infty} \mathrm{d}\lambda\, \rho(\lambda)\lambda^2\,. \tag{2.38}$$

One of the advantages of the thermodynamic description introduced above is the possibility to replace discrete sums over eigenstates with functional integrals over rapidity distribution functions. Notice, however, that Eq. (2.34) does not uniquely fix the root density $\rho(\lambda)$, as its relation with $\rho^h(\lambda)$ is not specified. To unambiguously fix $\rho(\lambda)$ another equation is therefore needed. This is best illustrated in the case of the computation of the thermal partition function, i.e.,

$$\mathcal{Z}(\beta) = \mathrm{tr}\left[\mathrm{e}^{-\beta H}\right] = \sum_{\{\lambda_j\}} \mathrm{e}^{-\beta E\left[\{\lambda_j\}\right]}\,. \tag{2.39}$$

Note that, while each term on the right-hand side is known, the sum runs over all the possible sets of rapidities $\{\lambda_j\}$ and hence it is very difficult to evaluate

in practice for large N. In the thermodynamic limit, however, one can rewrite Eq. (2.39) as a functional integral [275]

$$\mathcal{Z}(\beta) = \int \mathcal{D}\rho \, \mathrm{e}^{-L\, S_{\mathrm{th}}[\beta,\rho]} \,, \tag{2.40}$$

where the functional

$$S_{\mathrm{th}}[\beta,\rho] = \beta e[\rho] - S_{\mathrm{YY}}[\rho] = \int_{-\infty}^{+\infty} \mathrm{d}\lambda \, \left\{ \beta\rho(\lambda)\lambda^2 - s_{YY}[\rho](\lambda) \right\} \,, \tag{2.41}$$

plays the role of a thermal free energy. Here the first term on the right-hand side is derived using Eq. (2.38) for the thermodynamic limit of the energy in Eq. (2.29) and corresponds to the exponential in Eq. (2.39). The second term, instead, is the so-called Yang-Yang entropy [278] $S_{\mathrm{YY}} = \int \mathrm{d}\lambda \, s_{YY}(\lambda)$ with density

$$s_{YY}[\rho](\lambda) = \rho^t(\lambda) \ln \rho^t(\lambda) - \rho(\lambda) \ln \rho(\lambda) - \rho^h(\lambda) \ln \rho^h(\lambda) \,, \tag{2.42}$$

which accounts for the fact that each rapidity distribution function $\rho(\lambda)$ emerges from several "microscopic realizations", i.e., that there are many sets of rapidities $\{\lambda_j\}$ associated with the same function $\rho(\lambda)$ [275]. This way of introducing the entropy is completely analogous to the definition of the entropy in the microcanonical ensemble as explained in Eqs. (1.19) and (1.21) in Subsec. 1.2.2. For $L \to \infty$ the functional integral in Eq. (2.40) can be computed by a saddle-point evaluation of the action $S_{\mathrm{th}}[\beta,\rho]$

$$\frac{\delta S_{\mathrm{th}}[\beta,\rho]}{\delta\rho} = 0, \tag{2.43}$$

which after some algebra yields the following expression for the free energy density $f(\beta)$ associated with the thermal partition function in Eq. (2.39) [102, 275]

$$f(\beta) = -\frac{\ln \mathcal{Z}}{\beta L} = Dh - \frac{1}{2\pi\beta} \int_{-\infty}^{\infty} \mathrm{d}\lambda \ln\left(1 + \mathrm{e}^{-\beta\varepsilon(\lambda)}\right) \,. \tag{2.44}$$

Here $\varepsilon(\lambda)$ is the solution of the *Yang-Yang* [278] non-linear integral equation

$$\varepsilon(\lambda) = \frac{1}{\beta} \ln \eta(\lambda) = \lambda^2 - h - \frac{1}{2\pi\beta} \int_{-\infty}^{+\infty} \mathrm{d}\mu \, K(\lambda-\mu) \ln\left(1 + \mathrm{e}^{-\beta\varepsilon(\mu)}\right) \,, \tag{2.45}$$

and h is a Lagrange multiplier, which can interpreted as the chemical potential, introduced in order to enforce the assigned density of particles, according to Eq. (2.37). The function $\lambda^2 - h$ on the right hand side of Eq. (2.45) is usually named "driving term" of the integral equation. As we will see in Sec. 2.3, the TBA formalism discussed above for the calculation of the equilibrium free energy $f(\beta)$ can be extended to the non-equilibrium dynamics of global-homogeneous quantum quenches via the quench action approach. Note that in models that admit multiple quasi-particle species, as in the attractive case $c < 0$ of the Lieb-Liniger as commented in Subsec. 2.2.1, multiple root densities are present. In this case all integrals over the rapidity transform into integrals over the rapidity of every root

density, where the contribution from each root density is added together.

2.2.3 Dressing of the single-particle excitations

We observe that Eq. (2.44) has the same form as the free energy of a system of non-interacting fermions. The whole complexity of the initial strongly-interacting problem in Eq. (2.41) is hidden into the "effective spectrum" $\varepsilon(\lambda)$, which is non-trivial as it feels the contribution of all the other rapidities μ according to the integral equation in Eq. (2.45). One usually says that the *bare* energy $q_2(\lambda) = \lambda^2 - h$ gets *dressed* by the interaction into the form $\varepsilon(\lambda)$. In this Section we give some additional details about the dressing of single particle excitations in integrable models, as this will be relevant both in the quench action in Sec. 2.3 and in the generalized hydrodynamics in Chapter 4.

Let us consider a system of finite size L in a state characterized by the set of Bethe numbers $\{I_j\}_{j=1}^N$ corresponding to the rapidities $\{\lambda_j\}_{j=1}^N$. In the thermodynamic limit the system is described by a rapidity distribution function $\rho(\lambda)$. The simplest excitation one can construct on top of this eigenstate in the canonical ensemble, the number of particles being fixed, is a "particle-hole" excitation where a Bethe number I_h is removed from the set $\{I_j\}_{j=1}^N$ and simulataneously a new Bethe number I_p is added. All the rapidities, from Eq. (2.27), will rearrange $\lambda_i \to \tilde{\lambda}_i + \delta\lambda_i$, with $\delta\lambda_i$ of order $\mathcal{O}(L^{-1})$. From Eq. (2.31) taking into account that also the counting function gets modified $\lambda(x) \to \tilde{\lambda}(x)$ one has

$$L\tilde{\lambda}(x) = 2\pi x L - \sum_{k=1}^{N} \theta\left(\frac{\tilde{\lambda}(x) - \tilde{\lambda}_k}{c}\right) - \theta\left(\frac{\tilde{\lambda}(x) - \lambda_p}{c}\right) + \theta\left(\frac{\tilde{\lambda}(x) - \lambda_h}{c}\right), \quad (2.46)$$

where λ_h and λ_p are the bare momenta of the added hole and particle excitation. By taking the difference between Eq. (2.46) and (2.31) and expanding in the difference $\tilde{\lambda}_i - \lambda_i$ to order $\mathcal{O}(L^0)$ one obtains the follwing linear integral equation [102, 275]

$$F(\lambda|\lambda_p,\lambda_h) = \frac{1}{2\pi}\int_{-\infty}^{\infty} \mathrm{d}\mu\, K(\lambda-\mu)\vartheta(\mu)F(\mu|\lambda_p,\lambda_h) + \theta(\lambda-\lambda_p) - \theta(\lambda-\lambda_h), \quad (2.47)$$

with the filling function $n(\lambda)$ defined in Eq. (2.36). $F(\lambda|\lambda_p,\lambda_h)$ is named *backflow* function and it is defined as

$$F\left(\lambda\left(\frac{j}{L}\right)|\lambda_p,\lambda_h\right) = \frac{\lambda\left(\frac{j}{L}\right) - \tilde{\lambda}\left(\frac{j}{L}\right)}{\lambda\left(\frac{j+1}{L}\right) - \lambda\left(\frac{j}{L}\right)}. \quad (2.48)$$

It describes the shift of the rapidities $\{\lambda_i\}_{i=1}^N$ as a consequence of the insertion of particle-holes excitations. With the help of the backflow function it is simple to study how the expectation value of a conserved charge Q_n changes as a consequence of the insertion of particle-hole excitations $\Delta\langle Q_n\rangle = Q[\{\tilde{\lambda}_i\} \cup \lambda_p, \lambda_h] -$

$Q[\{\lambda_i\}]$:

$$\begin{aligned}\Delta\langle Q_n\rangle &= q_n(\lambda_p) - q_n(\lambda_h) + \sum_i (q_n(\tilde{\lambda}_i) - q_n(\lambda_i)) \\ &= q_n(\lambda_p) - q_n(\lambda_h) - \frac{1}{2\pi}\int_{-\infty}^{\infty} \mathrm{d}\mu\, q_n'(\mu) F(\mu|\lambda_p,\lambda_h)\vartheta(\mu). \end{aligned} \tag{2.49}$$

The function $q_n(\lambda) = \lambda^n$ is the single-particle eigenvalue of the conserved charge Q_n introduced in Eqs. (2.49). One therefore observes that albeit the *bare* charge carried by the particle (hole) excitation introduced in the system is $q_n(\lambda)$ $(-q_n(\lambda))$, the charge variation of the whole system $\Delta\langle Q_n\rangle$ is different since it gets *dressed* by the rearrangement of all the rapidities as a consequence of the interacting nature of the model. Notice that because of the linearity of Eqs. (2.31) and (2.47) the total variation $\Delta\langle Q_n\rangle$ due multiple excitations is just the sum of the individual contributions in Eq. (2.49) corresponding to each particle-hole pair. In integrable models these excitations behave as stable quasi-particles that are "effectively" free, once the effect of the interaction is taken into account by the dressing procedure in Eq. (2.49). In this respect, it is natural to define the dressed charge $q_n^{\mathrm{dr}*}(\lambda)$ as the solution of the following linear integral equation

$$q_n^{\mathrm{dr}*}(\lambda) = q_n(\lambda) - \frac{1}{2\pi}\int_{-\infty}^{\infty} \mathrm{d}\mu\, q_n'(\mu) F(\mu|\lambda_p,\lambda_h)\vartheta(\mu), \tag{2.50}$$

such that

$$\Delta\langle Q_n\rangle = q_n^{\mathrm{dr}*}(\lambda_p) - q_n^{\mathrm{dr}*}(\lambda_h). \tag{2.51}$$

From this equation, exploiting Eq. (2.47) for the backflow function $F(\lambda|\lambda_p,\lambda_h)$, it readily follows that

$$\partial_\lambda q_n^{\mathrm{dr}*}(\lambda) = \partial_\lambda q_n(\lambda) + \frac{1}{2\pi}\int_{-\infty}^{\infty} \mathrm{d}\mu\, K(\lambda-\mu)\vartheta(\mu)\partial_\mu q_n^{\mathrm{dr}*}(\mu). \tag{2.52}$$

From Eq. (2.52) it is immediate to realize that the energy dressed charge $q_2^{\mathrm{dr}*} = \varepsilon(\lambda)$ is the solution of the Yang-Yang equation (2.45), as anticipated at the beginning of this Section. Inspired from Eq. (2.52) one usually introduces another definition for the dressing operation valid for an arbitrary function $h(\lambda) \to h^{\mathrm{dr}}(\lambda)$ of the rapidity λ:

$$h^{\mathrm{dr}}(\lambda) = h(\lambda) + \frac{1}{2\pi}\int_{-\infty}^{\infty} \mathrm{d}\mu\, K(\lambda-\mu)\vartheta(\mu)h^{\mathrm{dr}}(\mu). \tag{2.53}$$

The definition in Eq. (2.53) is strongly related to the one in Eq. (2.50). Indeed from Eq. (2.52) one realizes that

$$(\partial_\lambda h(\lambda))^{\mathrm{dr}} = \partial_\lambda h^{\mathrm{dr}*}(\lambda). \tag{2.54}$$

The definition of the dressing in Eq. (2.53) will be largely exploited in Chapter 4 within the generalized hydrodynamics theory.

2.3 Homogeneous quantum quenches: the quench action

In Subsec. 2.3.1 we discuss the quench action approach, which is the last piece of technical background needed in order to carry out our analysis of the statistics of the work. In Subsec. 2.3.2 we introduce the interaction quench of the Lieb-Liniger Bose gas, which will be the quench considered for the calculation of the work statistics. In the following, we only review the most relevant aspects for the analysis of Sec. 2.4, a detailed introduction to the quench action method can be found in Ref. [125].

2.3.1 The quench action method

This method is based on the TBA formalism of Subsec. 2.2.2 and it has been introduced in Ref. [124] to tackle the difficult problem of computing the thermodynamic limit $L \to \infty$ of the time averages in Eq. (1.28), i.e.,

$$\langle \Psi(t)|\mathcal{O}|\Psi(t)\rangle = \sum_{n,m} c_n^* c_m \langle n|\mathcal{O}|m\rangle e^{i(E_n - E_m)t}, \tag{2.55}$$

after a global quench. The quench action method provides an efficient functional representation of the double summation over the Hilbert space in Eq. (2.55), which would be otherwise too difficult to be calculated due to the extremely large number of terms it contains. Considering, in particular, the infinite-time limit of Eq. (2.55) and remembering Eq. (1.33), one obtains

$$\begin{aligned}\overline{\langle \Psi(t)|\mathcal{O}|\Psi(t)\rangle} &= \sum_n |\langle n|\Psi_0\rangle|^2 \langle n|\mathcal{O}|n\rangle \\ &= \sum_{\{\lambda_j\}} |\langle \{\lambda_j\}|\Psi_0\rangle|^2 \langle \{\lambda_j\}|\mathcal{O}|\{\lambda_j\}\rangle ,\end{aligned} \tag{2.56}$$

where we used the fact that for the Lieb-Liniger model the eigenstates are parametrized by sets of rapidities $\{\lambda_j\}$. The overbar in Eq. (2.56) denotes the time average as in Eq. (1.33). Indeed, the quench action approach provides a simple prescription to evaluate Eq. (2.56) in the thermodynamic limit, which is based on replacing the spectral sum over the rapidities $\{\lambda_j\}$ with a functional integration, in analogy with what we did in Eq. (2.40):

$$\sum_{\{\lambda_j\}} \to \int \mathcal{D}\rho \, e^{L S_{\rm YY}}, \tag{2.57}$$

with the Yang-Yang entropy $S_{\rm YY}$ given in Eq. (2.42). By doing so into Eq. (2.56), under rather mild assumptions on the operator $\mathcal{O}$ [124, 125], one arrives at the formal expression

$$\overline{\langle \Psi_0|\mathcal{O}(t)|\Psi_0\rangle} = \int \mathcal{D}\rho \, \langle \rho|\mathcal{O}|\rho\rangle e^{-L\, S_{\rm QA}[\rho]}, \tag{2.58}$$

where we denoted by $|\rho\rangle$ a representative eigenstate whose rapidities $\{\lambda_j\}$ approach the distribution $\rho(\lambda)$ in the thermodynamic limit. Here, the functional $S_{\rm QA}[\rho]$, usually called the *quench action* (QA), plays a role analogous to the thermal free energy $S_{\rm th}[\beta,\rho]$ in Eq. (2.41). Explicitly, it reads [124]

$$\begin{aligned} S_{\rm QA}[\rho] &= 2S_O[\rho] - \frac{1}{2}S_{\rm YY}[\rho] + S_N[\rho] \\ &= 2S_O[\rho] - \frac{1}{2}\int_{-\infty}^{+\infty} {\rm d}\lambda\, s_{YY}[\rho](\lambda) + \frac{h}{2}\left[\int_{-\infty}^{+\infty} {\rm d}\lambda\, \rho(\lambda) - D\right], \end{aligned} \tag{2.59}$$

where $S_O[\rho]$ is the functional associated with the extensive part of the logarithm of the overlap term appearing in the spectral sum in Eq. (2.56), i.e.,

$$S_O[\rho] = -\lim_{L\to\infty}\frac{1}{L}\ln|\langle\{\lambda_j\}|\Psi_0\rangle|. \tag{2.60}$$

Note that, since the Hamiltonian in Eq. (2.17) conserves the particle number, which is well-defined in the initial state that will be considered in Subsec. 2.3.2, a Lagrange multiplier h has been introduced in Eq. (2.59) (where the prefactor $1/2$ is for later convenience): this allows us to extend the functional integration over the whole space of rapidity distribution functions. Note also that the Yang-Yang entropy appearing in Eq. (2.59) bears an additional prefactor $1/2$, which is due to the fact that in the quench that will be considered in Subsec. 2.3.2 only parity-invariant eigenstates have non-vanishing overlap with the initial state $|\Psi_0\rangle$ [129]. Parity-invariant eigenstates are defined by the condition

$$\{\lambda_j\}_{j=1}^N = \{\lambda_j^+\}_{j=1}^{N/2}\cup\{-\lambda_j^+\}_{j=1}^{N/2}, \tag{2.61}$$

if N is even and

$$\{\lambda_j\}_{j=1}^N = \{\lambda_j^+\}_{j=1}^{(N-1)/2}\cup\{-\lambda_j^+\}_{j=1}^{(N-1)/2}\cup\{0\}, \tag{2.62}$$

if N is odd, where $\lambda_j^+ > 0$ The factor $1/2$ in front of $S_{\rm YY}$ is then caused by the fact that the number of microscopic realizations corresponding to a macroscopic density $\rho(\lambda)$ under the constraint in Eqs. (2.61) and (2.62) is the square root of the number of realizations in the uncostrained case. A crucial point in the procedure outlined above is the availability of an analytic expression for the functional $S_O[\rho]$ in Eq. (2.60). The major input necessary for the application of the quench action method resides, indeed, in the possibility of calculating analytically the overlaps between the initial state and the post-quench eigenstates $\langle\{\lambda_j\}|\Psi_0\rangle$. If an analytic expression is known for the overlaps, then the extensive part $S_O[\rho]$ can be easily derived. Unfortunately, the calculation of the overlaps $\langle\{\lambda_j\}|\Psi_0\rangle$ turns out to be in general extremely difficult and for arbitrary initial states there is no general scheme to compute them and the problem has to be tackled case by case [279–284]. Note, however, that it was recently shown that for any integrable model it is always possible to find a class of "integrable initial states" for which this can be done [285, 286].

Once the overlap functional $S_O[\rho]$ is known, the integral in Eq. (2.58) can be

computed via the saddle-point method, as done in the thermal case in Eqs. (2.43), by looking for the minimum of the quench action $S_{\rm QA}$

$$\frac{\delta S_{\rm QA}[s,\rho]}{\delta\rho}\Big|_{\rho=\rho_{sp}} \equiv 0\,. \tag{2.63}$$

The kind of integral equations that follow from the condition in Eq. (2.63) will indeed have (cf., Sec. 2.4) the same structure as Eq. (2.45), and they are for this reason dubbed generalized TBA equations. The main difference with the thermal case is that $S_{\rm QA}$ in Eq. (2.59) contains the overlap term $S_O[\rho]$, which is not present in $S_{\rm th}[\beta,\rho]$, implying that the driving terms in Eq. (2.63) are different from those of Eq. (2.43). Once the root density ρ_{sp} is determined from Eq. (2.63) the stationary limit of any local observable $\mathcal{O}$, from Eqs. (2.56) and (2.58) with $S_{QA}[\rho_{sp}]=0$ [124], is given by

$$\overline{\langle\Psi(t)|\mathcal{O}|\Psi(t)\rangle} = \langle\rho_{sp}|\mathcal{O}|\rho_{sp}\rangle. \tag{2.64}$$

This equation implies that the post-quench stationary state can be identified with the root density ρ_{sp} of an excited representative eigenstate. This corresponds to the microcanical representation of the GGE of Ref. [108] and it can be considered as a generalization of the ETH assumption to integrable models, cf. Eq. (1.36) in Subsec. 1.3.3. As a final comment we mention that the quench action method can be extended to account for the whole time evolution beyond the stationary limit [77, 130, 287, 288]. For our results regarding the work statistics, however, the knowledge of the steady state ρ_{sp} is sufficient as it will be shown in Sec. 2.4.

2.3.2 The interaction quench in the Lieb-Liniger model

For the calculation of the work statistics we consider an interaction quench in which the system is initially prepared in the ground state of the non-interacting Lieb-Liniger Hamiltonian $H(c_0=0)$, usually denoted by $|\text{BEC}\rangle$ [1]. The corresponding wave-function $\Psi_N^{(0)}(x_1,x_2\ldots,x_N)=\langle x_1,x_2,\ldots,x_N|\text{BEC}\rangle$ reads

$$\Psi_N^{(0)}(x_1,x_2...x_N) = \frac{1}{L^{N/2}}\,. \tag{2.65}$$

At time $t=0$, a finite inter-particle repulsive interaction $c>0$ is turned on and the gas is subsequently left to evolve unitarily. Our motivation to investigate the above quench is twofold: first, the simplicity of the initial state allows one to derive analytic predictions which would be difficult to obtain in general; second, we will see that this kind of quench leads to interesting features in the work statistics. As a matter of fact, the $|\text{BEC}\rangle$ initial state has a gapless spectrum, since in a non-relativistic free bosonic system the energy spectrum is simply $E(\lambda)=\lambda^2$. One can accordingly expect that the work probability density $p(w)$ for the quench of the interaction c from the $|\text{BEC}\rangle$ initial state will feature the condensation transition discussed in Subsec. 2.1.1. Indeed, as we shall see in Secs. 2.4 and 2.6, this

[1] Notice that the name "condensate" is abused in this context as in one-dimension Bose-Einstein condensation cannot take place. We keep, however, this notation as it is followed by the whole literature on this subject.

is the case and the interaction quench from the initial state in Eq. (2.65) allows for a complete analytical characterization of the condensation transition of $p(w)$ in a fully interacting dynamics, as the post-quench Hamiltonian $H(c)$ is interacting.

The non-equilibrium dynamics arising from the interaction quench $c_0 \to c$ described above has been extensively investigated in the literature [91, 131, 132, 287, 289–293]. From the analytical point of view, an important result has been the discovery in Ref. [129] of an exact formula (later proven in Ref. [294]) for the overlaps between the initial state in Eq. (2.65) and the eigenstates of the Hamiltonian in Eq. (2.17). This formula, which is an essential ingredient for the application of the quench action approach described in Sec. 2.3.1, will be used several times in this Chapter, and is hence reviewed below.

It was first shown in Refs. [129, 294] that the initial state in Eq. (2.65) has a non-vanishing overlap only with eigenstates corresponding to sets $\{\lambda_j\}$ of rapidities which are parity invariant, according to Eqs. (2.61) and (2.62). For these states, the overlap formula is extremely simple. Explicitly, for even N, it reads

$$\langle\{\lambda_j\}|\mathrm{BEC}\rangle = \sqrt{\frac{(cL)^{-N}N!}{\det_{j,k=1}^{N} G_{jk}}}\frac{\det_{j,k=1}^{N/2} G^{Q}_{jk}}{\prod_{j=1}^{N/2}\frac{\lambda_j}{c}\sqrt{\frac{\lambda_j^2}{c^2}+\frac{1}{4}}}\,. \tag{2.66}$$

Here we introduced the matrices G_{jk} and G^{Q}_{jk}, with elements

$$G_{jk} = \delta_{jk}\Big[L+\sum_{l=1}^{N/2}K(\lambda_j-\lambda_l)\Big]-K(\lambda_j-\lambda_k)\,, \tag{2.67}$$

$$G^{Q}_{jk} = \delta_{jk}\Big[L+\sum_{l=1}^{N/2}K^{Q}(\lambda_j,\lambda_l)\Big]-K^{Q}(\lambda_j,\lambda_k)\,, \tag{2.68}$$

where $K^{Q}(\lambda,\mu) = K(\lambda-\mu)+K(\lambda+\mu)$, and $K(\lambda)$ is defined in Eq. (2.35). An analogous result holds for the case of odd N [295]. As we will see further below, our analytic study ultimately hinges on the existence of the exact formula (2.66).

In particular, for the case of the initial state in Eq. (2.65) the function $S_O[\rho]$ in Eq. (2.60) can be obtained by taking the thermodynamic limit of Eq. (2.66)

$$\begin{aligned} S_O[\rho] &= \frac{D}{2}\left[1+\ln\gamma\right] \\ &+ \frac{1}{4}\int_{-\infty}^{+\infty}\mathrm{d}\lambda\,\rho(\lambda)\ln\left[\frac{\lambda^2}{c^2}\left(\frac{\lambda^2}{c^2}+\frac{1}{4}\right)\right], \end{aligned} \tag{2.69}$$

where we introduced the normalized interaction strength

$$\gamma = \frac{c}{D}\,. \tag{2.70}$$

With the result for $S_O[\rho]$ in Eq. (2.69) the quench action approach has been exploited to exactly compute the stationary-state root density ρ_{sp} in Ref. [129]. In

the following Section, instead, we show how to use this method to exactly compute the large deviation function $I(w)$ of the work done in the quench from BEC to Lieb-Liniger.

2.4 Quench action and large deviations

We now present our novel approach and its predictions for the statistics of the work done by the interaction quench introduced in Sec. 2.3.2. We begin by showing that the quench action approach allows us to demonstrate, directly and rather generally, that the large deviation principle $p(w) \asymp \mathrm{e}^{-LI(w)}$ holds and then compute the rate function $I(w)$. To do this the starting point is the expression of the moment generating function $G(s)$ in Eq. (2.3) in which we insert the resolution of the identity operator $\mathbb{I}$ in terms of the post-quench Bethe eigenstates $|\{\lambda_j\}\rangle$

$$\mathbb{I} = \sum_{\{\lambda_j\}} |\{\lambda_j\}\rangle\langle\{\lambda_j\}|, \tag{2.71}$$

obtaining

$$G(s) = \sum_{\{\lambda_j\}} |\langle\{\lambda_j\}|\mathrm{BEC}\rangle|^2 \mathrm{e}^{-s(E[\{\lambda_j\}]-E_0^c)}. \tag{2.72}$$

One then notices that Eq. (2.72) has a structure analogous to that of Eq. (2.56). Accordingly, it can be expressed as the r.h.s of Eq. (2.58) which involves the quench action $S_{\mathrm{QA}}[\rho]$, namely

$$\begin{aligned} G(s) &= \int \mathcal{D}\rho \, \exp[-LS_{\mathrm{QA}}[\rho] - s(E[\{\lambda_j\}] - E_0^c)] \\ &= \int \mathcal{D}\rho \, \exp[-L(S_{\mathrm{QA}}[s,\rho] - se_0(c))] \,, \end{aligned} \tag{2.73}$$

where we introduced the ground-state energy density $e_0(c) = E_0^c/L$, and the modified quench action

$$S_{\mathrm{QA}}[s,\rho] = S_{\mathrm{QA}}[\rho] + s\, e[\rho], \tag{2.74}$$

with $S_{\mathrm{QA}}[\rho]$ given in Eq. (2.59), and $e[\rho]$ in Eq. (2.38). In the thermodynamic limit, the functional integral in Eq. (2.73) can be evaluated via the saddle-point method, leading to

$$G(s) \sim \exp[-L(S_{\mathrm{QA}}[s,\rho_s^*] - se_0(c))] \,. \tag{2.75}$$

Here the function ρ_s^* is determined by the saddle-point condition

$$\frac{\delta S_{\mathrm{QA}}[s,\rho]}{\delta\rho}\Big|_{\rho=\rho_s^*} \equiv 0 \,. \tag{2.76}$$

Note that by straightforward manipulations, Eq. (2.76) can be cast into the explicit form [see also Eqs. (2.59), (2.69), and (2.42)]

$$\varepsilon_s^*(\lambda) = 2\lambda^2 + \frac{1}{s}\ln\left[\frac{\lambda^2}{c^2}\left(\frac{\lambda^2}{c^2}+\frac{1}{4}\right)\right] - \frac{h}{s} - \frac{1}{s}\int_{-\infty}^{\infty}\frac{\mathrm{d}\mu}{2\pi}K(\lambda-\mu)\ln\left(1+\mathrm{e}^{-s\varepsilon_s^*(\mu)}\right), \tag{2.77}$$

involving, instead of ρ_s^*,

$$\varepsilon_s^*(\lambda) = \frac{1}{s}\ln\eta_s^*(\lambda), \tag{2.78}$$

where $\eta(\lambda)$ is defined in Eq. (2.36). Equation (2.77) has to be interpreted as follows. For each value of s, one finds a unique solution for the function $\varepsilon_s^*(\lambda)$, and hence for $\eta_s^*(\lambda)$. Then, by recalling that $\rho^t(\lambda) = \rho(\lambda)(1+\eta(\lambda))$, one plugs the latter function into Eq. (2.34), in order to obtain a final prediction for $\rho_s^*(\lambda)$. Note that the Lagrange multiplier $h(s)$ in Eq. (2.77) has to be chosen such that the prescribed density D is obtained after using Eq. (2.37).

Within the saddle-point approximation in Eq. (2.75) one finds that, from Eq. (2.4),

$$f(s) = -\frac{1}{L}\ln G(s) = S_{\mathrm{QA}}[s,\rho_s^*] - se_0(c) \tag{2.79}$$

and therefore, in order to calculate $I(w)$ according to Eq. (2.5) one has to find the infimum, as a function of s, of $sw - f(s)$. When this is attained in a differentiable point s_w, it is determined by the condition

$$\frac{\mathrm{d}}{\mathrm{d}s}\left(f(s)-sw\right)\Big|_{s=s_w} = 0\,. \tag{2.80}$$

Due to the concavity of $f(s)$ [22], the stationary point $s = s_w$ can only correspond to a minimum. Using now $(\mathrm{d}/\mathrm{d}s) = (\mathrm{d}\rho/\mathrm{d}s)(\delta/\delta\rho)$, and exploiting Eq. (2.76), one can easily show that this condition is in fact equivalent to requiring

$$\int_{-\infty}^{+\infty}\mathrm{d}\lambda\,\rho_{s_w}^*(\lambda)\lambda^2 - e_0(c) = w\,. \tag{2.81}$$

As a consequence, if $f(s)$ is in addition strictly concave, the expression in Eq. (2.5) simplifies as

$$I(w) = -s_w w + f(s_w)\,. \tag{2.82}$$

Importantly, in this derivation, we never had to evaluate the quench action $S_{\mathrm{QA}}[s,\rho]$ at complex values of s, where it has been shown that it might display singular points [296, 297]. As a matter of fact, in all the derivation just presented $s \in \mathbb{R}$, as anticipated in Sec. 2.1. From Eqs. (2.74) and (2.75) one can also see that the calculation of the moment generating function $G(s)$ amounts to a shift of the saddle point from that of $S_{QA}[\rho]$ to the one of $S_{QA}[s,\rho]$. This is a consequence of the fact that the matrix elements of $\exp(-sH(c))$ are exponentially large in the system size L. This is different from the case analyzed in Eqs. (2.58) and (2.64), where the operator $\mathcal{O}$ is assumed to be "thermodynamically finite" [125], i.e, not to have matrix elements exponentially large in L and therefore not to shift the saddle point of $S_{QA}[\rho]$. Note also that the specific form of the overlap term

$S_O[\rho]$, entering only in Eq. (2.77), does not play any role in this derivation. As a consequence, the latter can be generalized straightforwardly to any integrable model where the quench action approach can be applied.

We can now proceed towards the explicit evaluation of the rate function $I(w)$, using Eq. (2.5). First, note that exploiting Eqs. (2.34) and (2.77), the action in Eq. (2.74) can be rewritten in the compact form

$$\begin{aligned} S_{QA}[s,\rho_s^*] &= D\,(\ln\gamma+1) \\ &+ \frac{hD}{2} - \frac{1}{2}\int_{-\infty}^{\infty}\frac{\mathrm{d}\lambda}{2\pi}\ln\left(1+\mathrm{e}^{-s\varepsilon_s^*(\lambda)}\right). \end{aligned} \tag{2.83}$$

Next, one needs to solve Eqs. (2.77) and (2.34) with the constraint in Eq. (2.37). This can be easily done numerically by standard iterative procedures. The resulting solution for $\varepsilon_s^*(\lambda)$ can then be plugged into Eq. (2.83) and integrated numerically. Finally, in order to obtain $f(s)$ in Eq. (2.79), one also needs to compute the ground-state energy $e_0(c)$. In fact, this can be written in terms of the solution of an integral equation (see, e.g., Ref. [275]). In particular, we have

$$e_0(c) = \int_{-Q}^{Q}\mathrm{d}\lambda\,\rho_{\mathrm{GS}}(\lambda)\lambda^2\,, \tag{2.84}$$

where $\rho_{\mathrm{GS}}(\lambda)$ satisfies the Lieb equation

$$\rho_{\mathrm{GS}}(\lambda) = \frac{1}{2\pi} + \frac{1}{2\pi}\int_{-Q}^{Q}\mathrm{d}\mu\,K(\lambda-\mu)\rho_{\mathrm{GS}}(\mu)\,,\quad |\lambda|<Q\,, \tag{2.85}$$

and where the real number Q is determined self-consistently by requiring

$$\int_{-Q}^{Q}\mathrm{d}\lambda\,\rho_{\mathrm{GS}}(\lambda) = D\,. \tag{2.86}$$

We have now all the necessary ingredients to evaluate the rate function $I(w)$, which is obtained by numerically performing the Legendre-Fenchel transform in Eq. (2.5). The latter expression is indeed better suited for a numerical evaluation of $I(w)$ than Eq. (2.82) since $f(s)$ is in general known only numerically from Eq. (2.79). The Legendre transform in Eq. (2.82) will be instead used in order to determine analytically the asymptotic behavior of $I(w)$ both close to $\overline{w}$ and for low values of w. We have implemented the numerical procedure outlined above, which presents no difficulty, and we have worked out analytically the asymptotic of $I(w)$; our results are summarized and discussed in the next Section.

2.5 Exact rate function: analytical results

In this Section we present our results for the scaled cumulant generating function in Eq. (2.79) and for the rate function $I(w)$. We begin by reporting in Sec. 2.5.1 their numerical evaluation based on the exact formulas presented in the previous

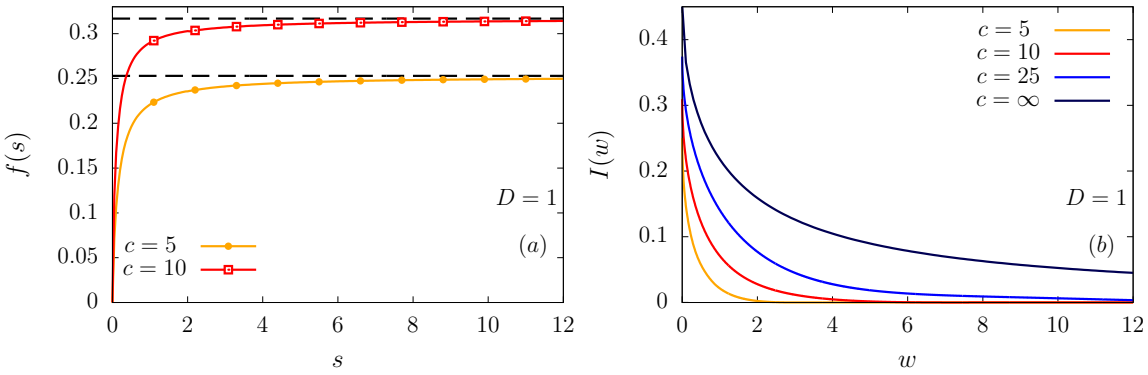

FIGURE 2.5: (a) Numerical determination of the function $f(s)$ for two values of the interaction $c = 5$ and 10 (from bottom to top) and fixed density $D = 1$. Solid lines correspond to the exact numerical values obtained by solving Eq. (2.77), while dashed lines indicate the asymptotic value $2f_0$ determined from, c.f., Eq. (2.111) in Sec. 2.5.2. (b) Large deviation function $I(w)$ for various values of the post-quench interaction c. In black we show, for comparison, $I(w)$ in the Tonks-Girardeau limit $c \to \infty$, evaluated in Sec. 2.5.3. The latter is never identically zero, in contrast to the curves corresponding to $c = 5, 10, 25$ (from bottom to top) which vanish identically for $w \geq \overline{w} = cD^2 - e_0(c)$. Image taken from Ref. [2].

Section, and then work out analytically their asymptotic behavior in Sec. 2.5.2. Finally, we devote Sec. 2.5.3 to a detailed analysis of the so-called Tonks-Girardeau (TG) limit $c \to \infty$, which lends itself to a fully analytical treatment.

2.5.1 The exact rate function: numerical results

We start by presenting our numerical predictions for the scaled cumulant generating function $f(s)$, which are reported in Fig. 2.5(a). The data are obtained using Eq. (2.79), after numerical solution of Eqs. (2.77), (2.34), and (2.85), which is done by standard iterative procedures [298].

We see from Fig. 2.5(a), that $f(s)$ displays many of the generic features discussed in Sec. 2.1 and predicted in Ref. [69]. In particular, it is a concave function defined in a semi-infinite interval $[\bar{s}, \infty)$ of the real line. In this case $\bar{s} = 0$, since the function $f(s)$ diverges for $s < 0$, and $f(s)$ belongs to class B according to the classification scheme recalled in Sec. 2.1. This is in agreement with the fact that the specturm of the Lieb-Liniger model in Eq. (2.29) is unbounded from above. The SCGF $f(s)$ has a singular point in its second derivative at $s = 0$. To see this, one can compute the second derivative of $f(s)$ w.r.t. s, yielding

$$f''(0) = \frac{1}{L}\left(\langle \mathrm{BEC}\,|[H(c) - E_0(c)]|\,\mathrm{BEC}\rangle^2 - \langle \mathrm{BEC}|\,[H(c) - E_0(c)]^2\,|\mathrm{BEC}\rangle\right) \to \infty\,, \tag{2.87}$$

as it can be verified by using the Wick theorem and by noticing that divergent terms arise in the second term on the first line of the r.h.s. of Eq. (2.87). On the contrary, the first derivative of $f(s)$ is finite in $s = 0$ and it gives the average

intensive work $\overline{w}$ performed in the quench. In particular, from Eq. (2.79), we have

$$\overline{w} = -\frac{G'(0)}{L} = f'(0) = \frac{1}{L}\langle \mathrm{BEC}|\left[H(c) - E_0(c)\right]|\mathrm{BEC}\rangle = cD^2 - e_0(c)\,. \tag{2.88}$$

As s approaches zero, $f(s)$ displays a non-analytic behavior, which will be characterized in Sec. 2.5.2 and which is responsible for the divergence of the higher-order cumulants. We also note that the qualitative features of $f(s)$ do not change upon varying c. However, the average work $\overline{w}$, and hence the first derivative in $s = 0$, increases upon increasing the interaction c. This is expected because as the repulsion among the bosons increases, a larger energy is present in the initial BEC state where all the bosons have zero momentum according to Eq. (2.65). In particular, in the Tonks-Girardeau limit $c \to \infty$ the mean intensive work $\overline{w}$ diverges. From Fig. 2.5(*a*) one also sees that $f(s)$ slowly approaches its asymptotic value for $s \to \infty$, which increases upon increasing c. This asymptotic behavior, however, is difficult to analyze numerically and we postpone its discussion to Sec. 2.5.2, where it will be determined analytically.

In Fig. 2.5(*b*) we report our predictions for the rate function $I(w)$ corresponding to $f(s)$ in panel (*a*), which can be obtained after a numerical Legendre-Fenchel transform of $f(s)$, as explained in the previous Section. As we discussed above, the rate function $I(w)$ vanishes at $w = \overline{w}$, while it is identically zero for $w > \overline{w}$. Due to the divergence of the second (and higher-order) cumulants in Eq. (2.87) the central limit theorem does not apply and $I(w)$ is expected to show a non-trivial behavior as $w \to \overline{w}^-$

$$I(w) = \begin{cases} \mathcal{A}(c,D)(w-\overline{w})^{\alpha} & w \to \overline{w}^-, \\ 0 & w > \overline{w}, \end{cases} \tag{2.89}$$

where $\mathcal{A}(c,D)$ is some prefactor dependent on the interaction coupling c and on the density D. The exponent α is surely different from 2 as the central limit does not apply. Due to the limitations in the accuracy of the numerical solutions, it is difficult to characterize the decay of $I(w)$ in Eq. (2.89) numerically, as $I(w)$ becomes very small when $w \simeq \overline{w}$. However, as we show in the next Section, this regime can be successfully studied analytically, so that both $\mathcal{A}(c,d)$ and the exponent α in Eq. (2.89) can be determined exactly. The vanishing of the rate function for $w > \overline{w}$ can be interpreted, based on the discussion in Sec. 2.1.1, as a "condensation" transition of the fluctuations from an exponential to a sub-exponential dependence $C(L,c)$ on the system size L. In fact, assuming a power-law decay for $w \gg \overline{w}$

$$p(w) \sim \begin{cases} \exp[-LI(w)] & w < \overline{w}, \\ C(L,c)\, w^{-\beta} & w \gg \overline{w}\,, \end{cases} \tag{2.90}$$

one can constrain the value of β by taking into account the divergence of cumulants beyond the first one, see Eqs. (2.87) and (2.88). In particular, it must be $2 < \beta < 3$. While the pre-factor $C(L,c)$ and the exponent β can not be determined from large deviation theory, we will show that they can be calculated from the Bethe ansatz in Sec. 2.6, at least in the limit of vanishing density of bosons. This transition in the qualitative form of $p(w)$ for $w \gg \overline{w}$ takes place, as we have seen

in Sec. 2.1.1 and anticipated in Subsec. 2.3.2, when the initial state is tuned such that its single-particle spectrum changes from gapped to gapless. In the quench considered here, the initial BEC state satisfies this condition as its single-particle spectrum $E(\lambda) = \lambda^2$ is gapless and therefore the condensation transition to an algebraic decay for $w \gg \overline{w}$ is observed.

2.5.2 Asymptotic behavior of the rate function: analytical results

As we mentioned in Sec. 1.2, whenever the central limit theorem applies [22] the rate function $I(w)$ has a quadratic expansion around $w = \overline{w}$. This is, for instance, the case for free fermionic models [67, 69, 70, 254, 263], where a Gaussian distribution describes $p(w)$ for small deviations from its mean value $\overline{w}$. In the case under study, however, we have already commented in Eq. (2.89) that the behavior of $I(w)$ near $\overline{w}$ is not Gaussian, meaning that the central limit theorem does not apply. In the following we exactly compute both $\mathcal{A}(c, D)$ and α introduced in Eq. (2.89).

In order to study the behavior of $I(w)$ for $w \to \overline{w}^-$, we exploit Eq. (2.82) which applies to our case since $f(s)$ is strictly concave and therefore $f'(s)$ is invertible. Due to the concavity of $f(s)$, it is easy to show that the behavior of $I(w)$ near $\overline{w}$ is determined by the expansion of $f(s)$ in a neighborhood of $s = 0$. In other words, we are left with the problem of determining the form of $f(s)$ for small s. To this end, we start from Eq. (2.79) and define

$$a_s(\lambda) = \frac{1}{\eta_s^*(\lambda)}\,. \tag{2.91}$$

Differentiating Eq. (2.79) with respect to s, we obtain

$$\frac{\mathrm{d}}{\mathrm{d}s} f(s) = \frac{h'(s)D}{2} - \frac{1}{2}\int_{-\infty}^{+\infty} \frac{\mathrm{d}\lambda}{2\pi} \frac{a_s'(\lambda)}{1 + a_s(\lambda)} - e_0(c)\,. \tag{2.92}$$

Next, differentiating Eq. (2.77) with respect to s, multiplying each side of the resulting equation by $\rho_s^*(\lambda)$ and finally integrating in λ we obtain

$$\frac{h'(s)D}{2} - \frac{1}{2}\int_{-\infty}^{+\infty} \frac{\mathrm{d}\lambda}{2\pi} \frac{a_s'(\lambda)}{1 + a_s(\lambda)} = \int_{-\infty}^{+\infty} \mathrm{d}\lambda\, \rho_s^*(\lambda)\lambda^2\,, \tag{2.93}$$

where the Bethe equations (2.34) have been used. Combining Eqs. (2.92) and (2.93), we obtain the important relation

$$\frac{\mathrm{d}}{\mathrm{d}s} f(s) = \int_{-\infty}^{+\infty} \mathrm{d}\lambda\, \rho_s^*(\lambda)\lambda^2 - e_0(c)\,. \tag{2.94}$$

Accordingly, the small-s behavior of $f(s)$ is determined by that of the integral of $\rho_s^*(\lambda)\lambda^2$ on the r.h.s. Note that for $s = 0$ we obtain that the derivative of $f(s)$ is the energy of the initial state, as it should. In Appendix 2.A we show that

$$\int_{-\infty}^{+\infty} \mathrm{d}\lambda\, \rho_s^*(\lambda)\lambda^2 = cD^2 - c^2D^2\sqrt{\frac{2s}{\pi}} + O(s)\,, \tag{2.95}$$

so that we finally obtain by integrating Eq. (2.94)

$$f(s) = [cD^2 - e_0(c)]s - \frac{2}{3}c^2D^2\sqrt{\frac{2}{\pi}}s^{3/2} + O(s^2)\,. \tag{2.96}$$

We can now plug this expression into Eq. (2.82) and compute the first term in the expansion of $I(w)$ for $w \simeq \overline{w}^-$. By doing so, we obtain that

$$I(w \to \overline{w}^-) = \frac{\pi}{6c^4D^4}(\overline{w} - w)^3 + O((\overline{w} - w)^4) \quad \text{for } w \leq \overline{w}\,, \tag{2.97}$$

which has the form anticipated in Eq. (2.89) with $\mathcal{A}(c, D) = \pi/(6c^4D^4)$ and $\alpha = 3$. The first term of the expansion around $\overline{w}$ is cubic instead of quadratic. We therefore find that small fluctuations have *not* a Gaussian distribution, in stark contrast with the free case.

Next, we study the limit of $I(w)$ for small values of w. From Eq. (2.82), we see that the latter is determined by the behavior of $f(s)$ at $s \to \infty$, which we now work out analytically. This can be done by following the derivation of Refs. [172, 299], where analogous calculations were done in the context of thermal equilibrium. We start by rewriting Eq. (2.83) as

$$S_{QA}[s, \rho_s^*] = D(\ln\gamma + 1) + \frac{hD}{2} - P(s)\,, \tag{2.98}$$

where

$$P(s) = \frac{1}{2}\int_{-\infty}^{+\infty}\frac{\mathrm{d}\lambda}{2\pi}\ln(1 + \mathrm{e}^{-s\varepsilon_s^*(\lambda)}). \tag{2.99}$$

For large s, the function $\varepsilon_s^*(\lambda)$ has two symmetric zeros which we call Q' $(-Q')$, while we name Q $(-Q)$ the zeros of $\varepsilon_\infty(\lambda)$, defined as the solution of the limit $s \to \infty$ of Eq. (2.77), namely by

$$\varepsilon_\infty(\lambda) = 2\lambda^2 - h' + \int_{-Q}^{Q}\frac{\mathrm{d}\mu}{2\pi}K(\lambda - \mu)\varepsilon_\infty(\mu)\,, \tag{2.100}$$

where we made the assumption on the chemical potential h, introduced in Eq. (2.59), that

$$0 < h' = \lim_{s\to\infty}\frac{1}{s}h(s) < \infty\,. \tag{2.101}$$

Assuming the validity of the latter equation we write the following expansion for $h(s)$ at large s

$$h(s) = h's + h_0 + \frac{h_{-1}}{s} + O(s^{-2})\,. \tag{2.102}$$

We computed h', h_0 and h_{-1} by performing a fit against the numerical data for $h(s)$. The expansion in Eq. (2.102) has been numerically checked. Next, we write

Eq. (2.99) as

$$P(s) = \frac{1}{2}\int_{-\infty}^{+\infty}\frac{\mathrm{d}\lambda}{2\pi}\ln\left(1+\mathrm{e}^{-s|\varepsilon_s^*(\lambda)|}\right) - \frac{s}{2}\int_{-Q'}^{-Q}\frac{\mathrm{d}\lambda}{2\pi}\varepsilon_s^*(\lambda) - \frac{s}{2}\int_{Q}^{Q'}\frac{\mathrm{d}\lambda}{2\pi}\varepsilon_s^*(\lambda) - \frac{s}{2}\int_{-Q}^{Q}\frac{\mathrm{d}\lambda}{2\pi}\varepsilon_s^*(\lambda). \tag{2.103}$$

The first term in Eq. (2.103) can be studied by expanding the integrand around the points $Q'(-Q')$

$$\frac{1}{2}\int_{-\infty}^{+\infty}\frac{\mathrm{d}\lambda}{2\pi}\ln\left(1+\mathrm{e}^{-s|\varepsilon_s^*(\lambda)|}\right) = \frac{\pi}{12|\varepsilon_s^{*\prime}(Q')|s} + O(s^{-2}). \tag{2.104}$$

Note that the second and third term in Eq. (2.103) vanish as $O\left((Q-Q')^2\right)$, i.e.,

$$\begin{aligned}\int_{Q}^{Q'}\frac{\mathrm{d}\lambda}{2\pi}\varepsilon_s^*(\lambda) &= -\int_{Q'}^{Q'+(Q-Q')}\frac{\mathrm{d}\lambda}{2\pi}\varepsilon_s^*(\lambda)\\ &= -\frac{1}{4\pi}(Q-Q')^2\varepsilon_s^{*\prime}(Q') + O\left((Q-Q')^3\right).\end{aligned} \tag{2.105}$$

We now make use of the following identities, which are proven in Appendix 2.B:

$$\delta\varepsilon_s^*(\lambda) = \varepsilon_s^*(\lambda) - \varepsilon_\infty(\lambda) = \frac{U_1(\lambda)}{s} + \frac{U_2(\lambda)}{s^2} + O(s^{-3}), \tag{2.106}$$

$$Q' - Q = -\frac{U_1(Q)}{s\varepsilon_\infty'(Q)} + O(s^{-2}), \tag{2.107}$$

where $U_1(\lambda)$ and $U_2(\lambda)$ are obtained as the solution to the following integral equations:

$$U_1(\lambda) = -h_0 + \ln\left[\frac{\lambda^2}{c^2}\left(\frac{\lambda^2}{c^2}+\frac{1}{4}\right)\right] + \int_{-Q}^{Q}\frac{\mathrm{d}\mu}{2\pi}K(\lambda-\mu)U_1(\mu), \tag{2.108}$$

$$\begin{aligned}U_2(\lambda) = \frac{[K(\lambda-Q)+K(\lambda+Q)]}{\varepsilon_\infty'(Q)}\left(-\frac{U_1^2(Q)}{4\pi}-\frac{\pi}{12}\right)\\ - h_{-1} + \int_{-Q}^{Q}\frac{\mathrm{d}\mu}{2\pi}K(\lambda-\mu)U_2(\mu).\end{aligned} \tag{2.109}$$

Plugging the identities (2.106)–(2.109) into Eqs. (2.104) and (2.105) and then into Eq. (2.103), straightforward manipulations finally yield, for $s\to\infty$,

$$f(s) = 2f_0 + \frac{f_1}{s} + O(s^{-2}), \tag{2.110}$$

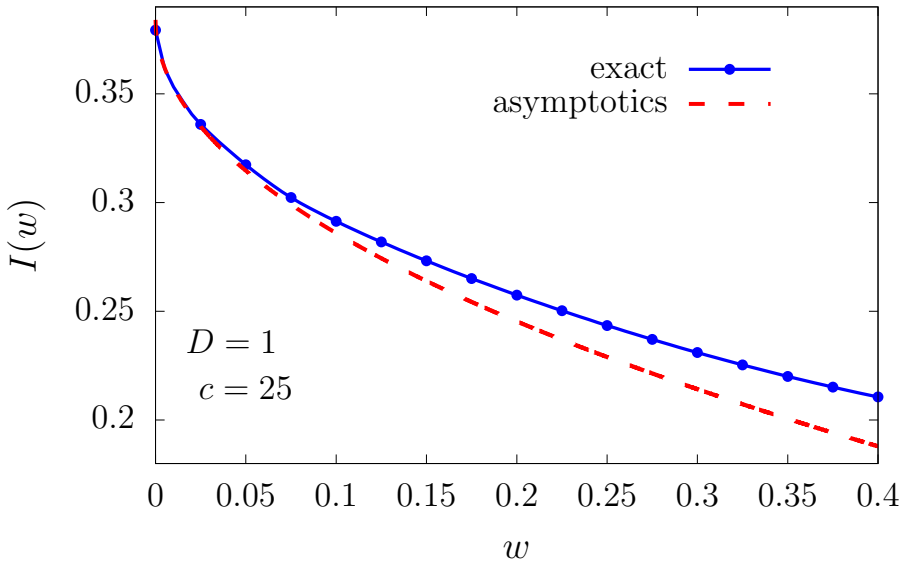

FIGURE 2.6: Rate function $I(w)$ after quenching the interaction parameter to $c = 25$ starting from the $|\text{BEC}\rangle$ initial state. The density of the particles is fixed to $D = 1$. The blue solid and red dashed lines correspond, respectively, to the exact numerical value of $I(w)$ [obtained using Eq. (2.5)], and to the analytic expansion in Eq. (2.114). The qualitative features of the plot do not depend on the specific choice of the value of c as long as it is finite. Image taken from Ref. [2].

with

$$\begin{aligned} f_0 &= \frac{D}{2}\left(\ln\gamma + 1\right) + \frac{1}{4}\int_{-Q}^{Q} \mathrm{d}\lambda\, \rho_{GS}(\lambda) \ln\left[\frac{\lambda^2}{c^2}\left(\frac{\lambda^2}{c^2} + \frac{1}{4}\right)\right], \\ f_1 &= -\frac{1}{v_s}\left(\frac{U_1^2(Q)}{4\pi} + \frac{\pi}{12}\right). \end{aligned} \tag{2.111}$$

Here v_s is the sound velocity of the system defined by

$$v_s = \frac{\varepsilon'_\infty(Q)}{2\pi\rho_{GS}(Q)}. \tag{2.112}$$

The expression of f_0 in Eq. (2.111) coincides with the prediction of Ref. [69], since f_0 can be actually rewritten as

$$f_0 = -\frac{\ln|\langle \text{BEC}|\Psi_0^c\rangle|}{L}, \tag{2.113}$$

where $|\Psi_0^c\rangle$ is the ground state of the post-quench Hamiltonian $H(c)$ in Eq. (2.17).

The expression in Eq. (2.110) finally provides access to the behavior of $I(w)$ for small values of w. Indeed, by plugging Eq. (2.110) into Eq. (2.82) we obtain

$$I(w) = 2f_0 - 2\sqrt{-f_1}w^{1/2} + O(w)\,. \tag{2.114}$$

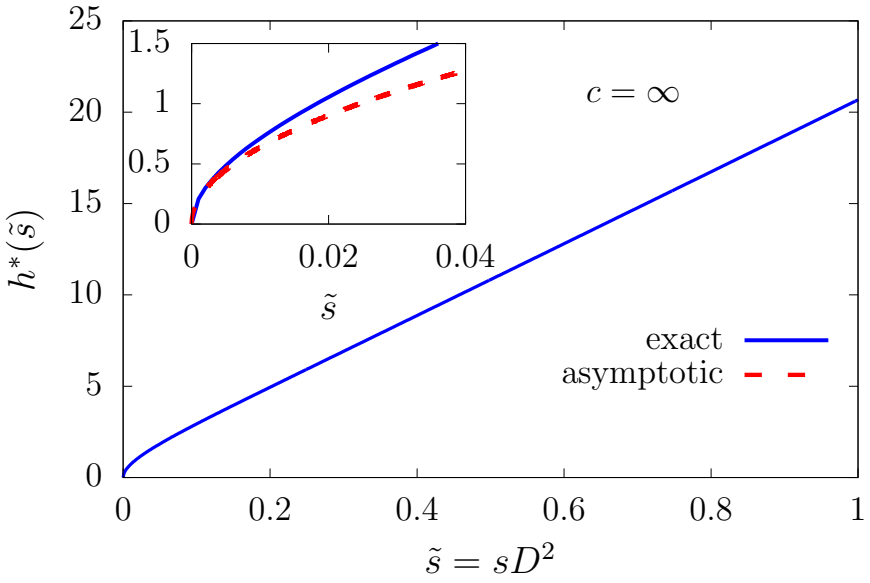

FIGURE 2.7: Lagrange multiplier $h^*(\tilde{s})$ as a function of $\tilde{s} = sD^2$. We note that $h^*(\tilde{s})$ is nearly linear, except for small values of $\tilde{s}$. Inset: behavior of $h^*(\tilde{s})$ close to $\tilde{s} = 0$. Together with the exact curve $h^*(\tilde{s})$ (blue solid line) we report the analytic expansion in Eq. (2.122) (red dashed line). Image taken from Ref. [2].

We compare this expansion with the exact rate function $I(w)$ obtained by the numerical evaluation of the formulas derived in the previous Section for several values of the interaction c. The comparison is displayed in Fig. 2.6 for a representative choice of the relevant parameters, where a good agreement between the two curves is manifest. Note that the leading behavior in the expansion in Eq. (2.114) is in agreement with the predictions of Ref. [69] recalled in Eq. (2.7). In our case, the criticality condition is verified since the Lieb-Liniger spectrum is gapless. It is fundamental to stress that the exact result in Eq. (2.114) represents the first analytic derivation for a strongly interacting model of the universal expression for the low w asymptotics of $I(w)$ predicted in Ref. [69]. Accordingly, large deviations for small values of the work encode signatures of universality as predicted by the quantum-to-classical correspondence [69]. A precise determination of the classical counterpart of the quantum quench analyzed here, however, goes beyond the scope of the analysis presented in this Chapter, and will not be discussed further.

2.5.3 The Tonks-Girardeau limit

In this Section we focus on the Tonks-Girardeau limit [300], corresponding to the quench where the final interactions are taken to be infinitely large. In fact, on the one hand, in this regime the formulas derived in the previous sections simplify, so that one can push the analytical control even further. On the other hand, in this limit, qualitative differences emerge in the statistics of the work, which are worth exploring per se, especially given the great relevance of this regime for cold-atomic experiments [270, 272].

From the computational point of view, in the limit $c \to \infty$, the kernel $K(\lambda)$ in Eq. (2.35), entering the integral equations which characterize the quench action

formalism, vanishes identically, largely simplifying the analysis. In particular, from Eq. (2.77), the solution for $\eta_s^*(\lambda)$ can be explicitly written as

$$\eta_s^*(\lambda) = \frac{\lambda^2}{4c^2} \mathrm{e}^{2s\lambda^2 - h(s)} = \frac{\lambda^2}{4D^2} \mathrm{e}^{2s\lambda^2 - h^*(s,D)} . \tag{2.115}$$

Here we have introduced the following parametrization of the Lagrange multiplier $h(s)$

$$h(s) = h^*(s, D) + \ln\left(\frac{D^2}{c^2}\right) \tag{2.116}$$

which is particularly convenient because, as shown in Ref. [129], for the quench action equations corresponding to $s = 0$ in the present discussion,

$$h(0) = \ln\left(\frac{D^2}{c^2}\right) , \tag{2.117}$$

and therefore $h^*(0, D) = 0$.

Next, from Eq. (2.34) one finds, in the Tonks-Girardeau limit, $\rho^t(\lambda) = 1/(2\pi)$ and thus from $\rho^t(\lambda) = \rho(\lambda)(1 + \eta(\lambda))$

$$\rho_s^*(\lambda) = \frac{1}{2\pi} \frac{1}{1 + \frac{\lambda^2}{4D^2} \mathrm{e}^{2s\lambda^2 - h^*(s,D)}} . \tag{2.118}$$

Accordingly, the density constraint in Eq. (2.37), which determines the parameter $h^*(s, D)$, can be written as

$$\int_{-\infty}^{+\infty} \frac{\mathrm{d}y}{2\pi} \frac{1}{1 + \frac{y^2}{4} \mathrm{e}^{2y^2 D^2 s - h^*(s,D)}} = 1 . \tag{2.119}$$

The function $h^*(s, D)$ determined by this condition does not depend on c, since the latter does not appear in Eq. (2.119), and it actually depends on s and D via the combination $\tilde{s} = sD^2$. Equation (2.119) can be easily solved numerically: we report the corresponding result for $h^*(\tilde{s})$ in Fig. 2.7. Interestingly, the function $h^*(\tilde{s})$ appears to be almost linear in $\tilde{s}$. In fact, it is not difficult to compute the asymptotic behavior of $h^*(\tilde{s})$ for $\tilde{s} \to \infty$. Inserting Eq. (2.102) written up to order $O(s^{-1})$, $h_0' = h_0 - h(0)$ with h_0 and $h(0)$ defined in Eqs. (2.102) and Eq. (2.117), respectively,

$$h^*(\tilde{s}) = \tilde{s}h' + h_0' + O(\tilde{s}^{-1}) \tag{2.120}$$

into Eq. (2.118), in the large-s limit $\rho_s^*(\lambda)$ becomes a step function; in particular, imposing the correct density, we find

$$\lim_{s\to\infty} \rho_s^*(\lambda) = \begin{cases} \frac{1}{2\pi} & \text{for} \quad |\lambda| < D\pi, \\ 0 & \text{for} \quad |\lambda| > D\pi, \end{cases} \tag{2.121}$$

and therefore the simple relation $h' = 2\pi^2$ in the Tonks-Girardeau limit. The behavior of $h^*(\tilde{s})$ can be analytically studied also for $\tilde{s} \to 0$, although the computations are more involved. We do not report them in the thesis for the sake of

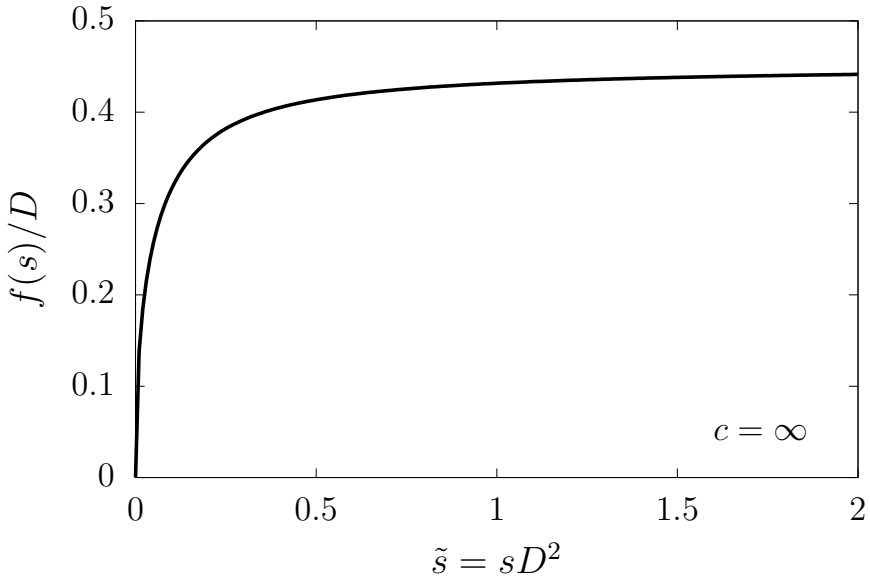

FIGURE 2.8: Scaled cumulant generating function divided by the density of bosons $f(s)/D$ as a function of $\tilde{s} = sD^2 > 0$ for quenches to infinitely repulsive interactions $c \to \infty$ (Tonks-Girardeau limit). The function approaches the origin $\tilde{s} \to 0$ with infinite slope, according to Eq. (2.124). Image taken from Ref. [2].

brevity, as they are described in detail in the Appendix of Ref. [2]. The final result reads

$$h^*(\tilde{s}) = \frac{16}{\sqrt{2\pi}}\sqrt{\tilde{s}} + O(\tilde{s})\,. \tag{2.122}$$

The expressions in Eqs. (2.120) and (2.122) allow us to obtain directly the corresponding expansions for the scaled cumulant generating function $f(s)$. First, note that in the Tonks-Girardeau limit the latter can be expressed explicitly by plugging Eq. (2.115) into Eqs. (2.79) and (2.83), finding

$$\begin{aligned} f(s) = D + \frac{D}{2}h^*(sD^2) - \frac{D^3\pi^2}{3}s \\ - \frac{1}{2}\int_{-\infty}^{\infty}\frac{\mathrm{d}\lambda}{2\pi}\ln\left(1 + \frac{4D^2}{\lambda^2}\mathrm{e}^{-2s\lambda^2 + h^*(s,D)}\right)\,. \end{aligned} \tag{2.123}$$

This expression can be easily evaluated numerically, as it amounts to a simple integral, once the function $h^*(sD^2)$ is known. Notice that, rescaling $\lambda = Dy$ in the integral of Eq. (2.123), it turns out that $f(s)/D$ is actually a function of $\tilde{s} = sD^2$ only, as it has been already noticed also for $h^*(s, D^2)$. We report the resulting data for $f(s)/D$ in Fig. 2.8. The same rescaling in terms of D does not apply to the case at finite c of Secs. 2.5.1 and 2.5.2 as one realizes by looking, e.g., at the small-s expansion in Eq. (2.96). Note also that, differently from the case of finite interactions c, the average value of the work is infinite in the Tonks-Girardeau limit. Indeed, the expansion of $f(s)/D$ near $s = 0$ differs from Eq. (2.96), as one realizes by plugging Eq. (2.122) into Eq. (2.123). The details of this calculation are

reported in detail in the Appendix of Ref. [1], where we find

$$\frac{f(s)}{D} = \alpha_{1/2}\, \tilde{s}^{1/2} + O\left(\tilde{s}\right) , \tag{2.124}$$

with

$$\alpha_{1/2} \;=\; 2\sqrt{\frac{2}{\pi}} . \tag{2.125}$$

Analogously, the asymptotic behavior of $f(s)$ for $s \to \infty$ can be derived by plugging in Eq. (2.123) the expression in Eq. (2.120) for $h^*(\tilde{s})$. The intermediate steps are reported in Appendix of Ref. [2], while the final result reads

$$\frac{f(s)}{D} = 2f_0 + \frac{f_1}{\tilde{s}} + O(\tilde{s}^{-2}) , \tag{2.126}$$

with

$$f_0 \;=\; \frac{1}{2} \ln \frac{\pi}{2} , \tag{2.127}$$

$$f_1 \;=\; \frac{1}{8\pi^2} \left[-\frac{\pi^2}{6} - \frac{1}{2} \ln^2 \left(\frac{\pi^2}{4} \mathrm{e}^{-h_0'} \right) \right] . \tag{2.128}$$

Note that the expression for f_1 in Eq. (2.128) is equal to the limit $c \to \infty$ of Eq. (2.111), as it should.

Finally, we discuss the rate function $I(w)$ in the Tonks-Girardeau limit which can be computed by numerically performing the Legendre-Fenchel transform of Eq. (2.123), displayed in Fig. 2.5(b). Given the scaling form of $f(s)/D$ as a function of sD^2, one readily obtains from Eq. (2.5) a scaling form for $I(w)/D$ as a function of the variable $\tilde{w} = w/D^3$ only. Contrary to the case of finite interactions, $I(w)/D$ never vanishes, as the average work $\overline{w}$ grows to infinity as $c \to \infty$. It is thus meaningful to study the asymptotic behavior of $I(w)/D$ for large values of w/D^3. This can be easily done by plugging into Eq. (2.82) the expansion in Eq. (2.124), finding

$$\frac{I(w)}{D} = \frac{\alpha_{1/2}^2}{4} \tilde{w}^{-1} + O\left(\tilde{w}^{-2}\right) , \tag{2.129}$$

where $\alpha_{1/2}$ is given in Eq.(2.125). Eq. (2.129) is plotted in Fig. 2.9 together with the exact numerical values of $I(w)/D$.

Before concluding this Section, we note that an analogous analysis can be done for the limit $w \to 0$ of the rate function $I(w)$, by plugging Eq. (2.126) into Eq. (2.82). In this case, we find that $I(w)$ behaves as in Eq. (2.114), showing that fluctuations for small values of w are not qualitatively affected by considering the Tonks-Girardeau regime $c \to \infty$.

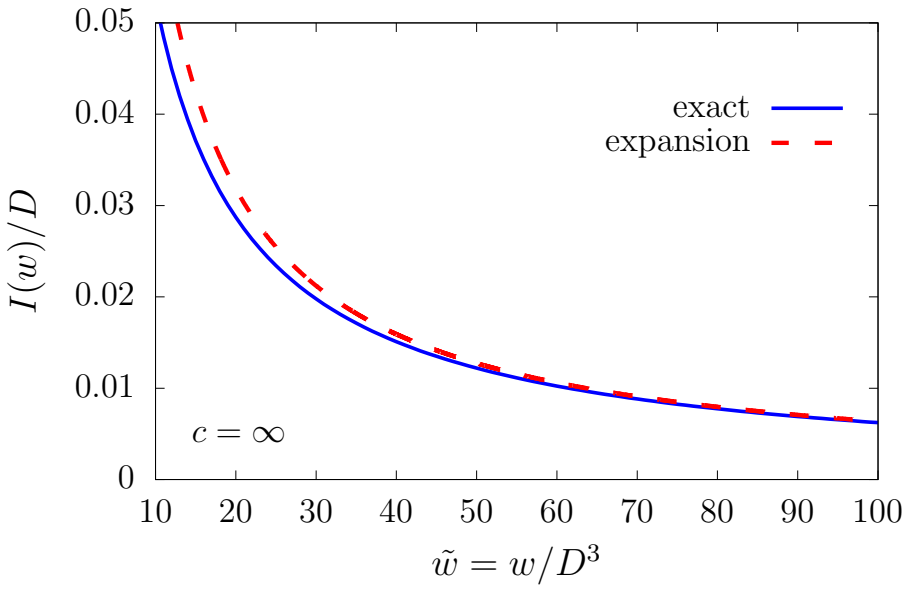

FIGURE 2.9: Asymptotic behavior of the rate function $I(w)/D$ for large values of $\tilde{w} = w/D^3$ and quenches to the Tonks-Girardeau regime $c \to \infty$. The solid line corresponds to the exact value obtained by the numerical Legendre-Fenchel transform of the function $f(s)/D$ given in Eq. (2.123), while the dashed line is the analytical expansion in Eq. (2.129). Image taken from Ref. [2].

2.6 Algebraic behavior at large w

In the previous sections we have quantitatively analyzed the rate function $I(w)$, characterizing the exponential decay of the distribution function $p(w)$ for $w < \overline{w}$ as L grows. On the other hand, for the quench considered here, we saw that $I(w)$ vanishes identically for $w > \overline{w}$, so that, in this regime, the decay of $p(w)$ as a function of L is sub-exponential. As we have anticipated in Sec. 2.5.1, assuming (for large w) a power-law decay $p(w) \sim C(L,c)\, w^{-\beta}$ one can bound the value of β based on the divergence of cumulants of w higher than the first. However, the leading behavior in L of $C(L,c)$, characterizing $p(w)$ for $w > \overline{w}$, and the value of the exponent β, can not be obtained by large deviation theory and a more sophisticated analysis has to be carried out.

In order to determine such a leading behavior, one could start from an exact expression for $p(w)$ at finite sizes, and then perform the correct asymptotic analysis. This strategy, however, appears to be unpractical, as the exact computation of $p(w)$ at finite sizes is a significant challenge. Nevertheless, in this Section we show that this problem can be solved assuming a vanishingly small density of particles. In particular, we consider the limit $L \to \infty$, with the number N of particles kept fixed. We will show that, in this regime, one can extract the exact leading dependence on L of $p(w)$ for large values of w.

From the technical point of view, the reason why the problem becomes tractable in this regime lies in the simplified structure of the solution to the Bethe equations (2.26), parametrizing the eigenstates of the Hamiltonian. Indeed, fixing the quantum numbers I_j in Eq. (2.27), one immediately obtains the following

expansion as L grows

$$\lambda_j = \frac{2\pi I_j}{L} + \sum_{n=2}^{\infty} \frac{\lambda_j^{(n)}}{L^n} = \frac{2\pi I_j}{L} + O(L^{-2}) \,, \tag{2.130}$$

with $j = 1, \dots N$. Namely, at the leading order in L, the rapidities coincide with the quasi-momenta of a free quantum gas confined within a ring of length L (with the condition $I_j \neq I_k$ for $j \neq k$). The corresponding eigenvalues of the Hamiltonian become

$$E_N = \sum_{j=1}^{N} \lambda_j^2 = \frac{4\pi^2}{L^2} \sum_{j=1}^{N} I_j^2 + O(L^{-3}) \,. \tag{2.131}$$

For simplicity, we consider below the case in which the number N of particles is odd, so that the quantum numbers I_j are integer, i.e., we choose

$$N = 2M + 1 \,. \tag{2.132}$$

A completely analogous derivation applies to the case of even N.

As a first ingredient for the computation of $p(w)$, we consider the zero-density limit of the overlap in Eq. (2.66), which has been already studied in the literature [295, 301, 302]. In particular one finds

$$\langle \{\lambda_j\} | \mathrm{BEC} \rangle \simeq \frac{\sqrt{(cL)^{-M}} \sqrt{N!}}{\prod_{j=1}^{M} \left(\frac{\lambda_j}{c} \sqrt{\frac{1}{4} + \frac{\lambda_j^2}{c^2}} \right)} \,. \tag{2.133}$$

As a consistency check, one should verify that, using Eq. (2.133) and keeping only the leading term of the rapidities $\lambda_j \simeq 2\pi I_j / L$, one obtains the correct values for the normalization and the energy of the initial state, i.e.,

$$\sum_{I_1 < I_2 < \dots I_M} |\langle \{\lambda_j\} | \mathrm{BEC} \rangle|^2 = 1 \,, \tag{2.134}$$

and

$$\sum_{I_1 < I_2 < \dots I_M} \left(\sum_{j=1}^{M} 2\lambda_j^2 \right) |\langle \{\lambda_j\} | \mathrm{BEC} \rangle|^2 = \frac{cN(N-1)}{L} \,. \tag{2.135}$$

In fact, Eq. (2.134) can be established analytically on the basis of Eq. (2.133) by using the identity (see, e.g., Ref. [303])

$$\sum_{1 \leq I_1 < I_2 < \dots I_M < \infty} \prod_{j=1}^{M} \frac{1}{I_j^2} = \frac{\pi^{2M}}{(2M+1)!} \,, \tag{2.136}$$

while we checked that also Eq. (2.135) is fulfilled by numerically performing the sum for small particle numbers.

We have now all the ingredients to determine the leading behavior of $p(w)$. Our strategy consists in a direct computation based on the definition in Eq. (2.1)

which, for the Lieb-Liniger model, reads

$$P(W) = \sum_{\{\lambda_j\}} |\langle\{\lambda_j\}|\mathrm{BEC}\rangle|^2 \delta\left(W - (E[\{\lambda_j\}] - E_0^c)\right) . \tag{2.137}$$

Let us fix the value w, so that the extensive work is $W = wL$, and let $\epsilon \ll W$ be a small energy shell (more precisely, we choose $\epsilon = \tilde{\epsilon} L$ with $\tilde{\epsilon} \ll w$). Then, the definition in Eq. (2.137) directly yields

$$\sum_{W' \in (W-\epsilon, W+\epsilon)} P(W') \sim \epsilon\, P(W) . \tag{2.138}$$

Note that since $w = O(L^0)$, we are in the regime $w \gg \overline{w}$, since in the zero-density limit $\overline{w} = O(L^{-2})$. We can then proceed to evaluate the sum over the energy shell in Eq. (2.138) and obtain the behavior of $P(W)$ and hence of $p(w)$. In order to simplify the discussion, we start by illustrating the main idea of this derivation in the simplest case where $M = 1$, i.e., $N = 3$. The generalization to an arbitrary number N of particles, which does not bear conceptual complications, is presented in Appendix 2.C. At the end of this Subsection we will report the final result of this analysis.

For $M = 1$, Eq. (2.138) can be rewritten as

$$\epsilon P(W) = \sum_{I_1 \in (I_{\min}, I_{\max})} |\langle I_1|\mathrm{BEC}\rangle|^2 , \tag{2.139}$$

where $I_{\min}$ and $I_{\max}$ are determined, via Eq. (2.131), by the boundaries of the energy shell in Eq. (2.138), i.e.,

$$I_{\min} = \frac{L}{\sqrt{8\pi}} \sqrt{W - \epsilon} , \tag{2.140}$$

$$I_{\max} = \frac{L}{\sqrt{8\pi}} \sqrt{W + \epsilon} . \tag{2.141}$$

Here we dropped the ground state energy $E_0^c \sim 1/L^2$ since it is sub-leading with respect to W. Consequently we have

$$\begin{aligned} \epsilon P(W) &= \frac{6c^2L^2}{16\pi^2} \sum_{I=I_{\min}}^{I_{\max}} \frac{1}{I_1^2(\pi^2 I_1^2 + \frac{c^2L^2}{16})} \\ &= \frac{3c^2L^2}{8\pi^2} \sum_{j=0}^{\delta I} \frac{1}{(j + I_{\min})^2(\pi^2(j + I_{\min})^2 + \frac{c^2L^2}{16})} , \end{aligned} \tag{2.142}$$

where

$$\delta I \equiv I_{\max} - I_{\min} = \frac{L\epsilon}{\sqrt{8W\pi}} + O\left(\epsilon^2\right) . \tag{2.143}$$

The series in Eq. (2.142) can be easily bounded as

$$\epsilon P_{\min} < \epsilon P(W) < \epsilon P_{\max} , \tag{2.144}$$

where

$$\begin{aligned} \epsilon P_{\min} &= \frac{3c^2L^2}{8\pi^2}\sum_{j=0}^{\delta I}\frac{1}{I_{\max}^2(\pi^2 I_{\max}^2+\frac{c^2L^2}{16})} \\ &= \frac{3c^2L^2}{8\pi^2}\frac{\delta I}{I_{\max}^2(\pi^2 I_{\max}^2+\frac{c^2L^2}{16})}\,, \end{aligned} \tag{2.145}$$

$$\begin{aligned} \epsilon P_{\max} &= \frac{3c^2L^2}{8\pi^2}\sum_{j=0}^{\delta I}\frac{1}{I_{\min}^2(\pi^2 I_{\min}^2+\frac{c^2L^2}{16})} \\ &= \frac{3c^2L^2}{8\pi^2}\frac{\delta I}{I_{\min}^2(\pi^2 I_{\min}^2+\frac{c^2L^2}{16})}\,. \end{aligned} \tag{2.146}$$

Plugging Eqs. (2.140)–(2.143) into Eqs. (2.145) and (2.146), we immediately get

$$P_{\min} = \frac{3c^2L^3}{\pi^3\sqrt{8^3W}}\frac{1}{W(\frac{c^2L^4}{128\pi^2}+\frac{WL^4}{64\pi^2})}+O(\epsilon)\,, \tag{2.147}$$

$$P_{\max} = \frac{3c^2L^3}{\pi^3\sqrt{8^3W}}\frac{1}{W(\frac{c^2L^4}{128\pi^2}+\frac{WL^4}{64\pi^2})}+O(\epsilon)\,. \tag{2.148}$$

Accordingly, at the leading order in ϵ, we find $P_{\min} = P_{\max} = P(W)$. We recall now that the probability distribution function $p(w)$ of the intensive work is related to $P(W)$ by $p(w) = L\,P(wL)$. Accordingly, from Eq. (2.148), we obtain

$$p(w) \propto \frac{c^2}{L^{5/2}}\,w^{-5/2}+O(L^{-7/2})\,. \tag{2.149}$$

which has the form anticipated in Eq. (2.90) with $C(L,c) = c^2/L^{5/2}$, $\beta = 5/2$ and clearly displays that the dependence $C(L,c)$ of $p(w)$ on L is *not* exponential. The value of β furthermore satisfies the bound $2 < \beta < 3$, anticipated in Sec. 2.5.1. Finally, we show in Appendix 2.C that the same reasoning can be repeated for an arbitrary number N of particles and that the behavior in Eq. (2.149) is valid for all N (with an N-dependent numerical prefactor). To our knowledge, this constitutes the first quantitative calculation of the power-law tail of $p(w)$, first predicted in Ref. [69], for interactive bosonic systems starting from a critical initial state. Note that, even if the result in Eq. (2.149) holds for an arbitrary finite number of particles N, its validity is still limited to the regime of vanishing density D: indeed, by construction, the large-L limit is taken while N is kept finite. In fact, in the case of finite D, while the bound $2 < \beta < 3$ continues to hold, we can not make any statement on the exact value of the exponent without further assumptions about the functional form of $p(w)$ at finite sizes.

2.7 Concluding remarks

In this Chapter we presented our results, originally reported in Ref. [2], concerning the large-deviation statistics of the intensive work w done by an interaction quench of the one-dimensional Lieb-Liniger model, focusing on the case in which the initial state is the ground state of the non-interacting gas. By means of the quench action approach, see Sec. 2.3, we have shown that, for $w < \overline{w}$, the large-deviation principle applies to the probability $p(w)$, as it depends exponentially on the system size L with $p(w) \asymp \exp[-LI(w)]$, and that the Gärtner-Ellis theorem employed in Ref. [69] can be used in order to determine the corresponding rate function $I(w)$. We have provided a fully quantitative analysis of the latter, working out analytically its behavior for small values of the intensive work w, cf. Eq. (2.114), and close to the average work $\overline{w}$, cf. Eq. (2.97). Interestingly enough, we have shown that for $w \simeq \overline{w}^-$ fluctuations are not Gaussian, in contrast to what would be expected from a direct application of the central-limit theorem. Furthermore, we analyzed the probability distribution function of the intensive work $p(w)$ for $w \gg \overline{w}$ where the large-deviation principle is violated and $p(w)$ has a sub-exponential dependence on L. Using an exact Bethe ansatz representation of the eigenstates of the Hamiltonian, we have derived the power-law decay of $p(w)$ in the regime of vanishing particle density, see Eq. (2.149), providing the first quantitative calculation of the power-law tail of $p(w)$ for interactive bosonic systems starting from a critical initial state.

Contrary to other works [70, 256, 259, 260], our approach to derive $p(w)$ is not based on the Fourier transform of the so-called Loschmidt echo evaluated at real times $s = it$. In the derivation of Sec. 2.4 the variable s is always real so that the quench action $S_{QA}[s, \rho]$ is computed at imaginary times and it can be considered a real valued functional. This is an important point, as the Loschmidt echo has proven to be especially hard to compute in real time $s = it$ [296, 297], due to the presence of points of "non-analyticity" arising in its real-time dynamics [35]. For this reason the quench action approach presented in this Chapter can be straightforwardly generalized to the calculation of the dynamical free energy $G(s)$, see Sec. 2.1, for a wide class of quantum quenches in other interacting integrable models. A particular interesting example would be the prototypical XXZ Heisenberg chain, where, for instance, the quantum-classical correspondence mentioned in Sec. 2.5.2 could be investigated in detail.

We stress that the result of Ref. [2] on which this Chapter is pivoted applies to homogeneous quantum quenches, where the initial state $|\Psi_0\rangle$ is translationally invariant. This is clearly the case for the BEC initial state of Subsec. 2.3.2, where the N bosons are uniformly distributed on the ring of length L. Current experimental realizations of one-dimensional Bose gases in cold-atomic settings [269–271, 273, 274, 276, 277] and measurements of the work statistics in non-equilibrium protocols [304–309] require, however, the system to be trapped by external potentials, breaking the translational invariance and making the space distributions of the bosons non uniform. However, we expect that our analysis can be extended to deal with these cases, because the trapping potentials generically vary on length scales which are much larger than the microscopic ones. Accordingly, one can

employ the generalized hydrodynamic approach [159, 160] to extend the thermodynamic Bethe ansatz formalism of this Chapter to these weakly inhomogenous settings. The case of inhomogeneous initial states and the generalized hydrodynamics will be the content of the following Chapters 3 and 4.

Appendix of Chapter 2

2.A Small s asymptotics of the scaled cumulant generating function

In this Appendix we derive Eqs. (2.95) and (2.96), characterizing the behavior of the scaled cumulant generating function $f(s)$ as $s \to 0$. The starting point is Eq. (2.94) in the main text and therefore the expansion in s of $\rho_s^*(\lambda)$ is needed. The latter can be obtained from the expansions in s of $a_s(\lambda)$ and $\rho_s^t(\lambda)$ that we now perform.

First, from the integral equation of $\eta_s^*(\lambda)$ we can write that for $a_s(\lambda)$, which reads

$$\ln a_s(\lambda) = -2s\lambda^2 - \ln\left[\frac{\lambda^2}{c^2}\left(\frac{\lambda^2}{c^2}+\frac{1}{4}\right)\right] + h(s) + \int_{-\infty}^{\infty}\frac{\mathrm{d}\mu}{2\pi}K(\lambda-\mu)\ln\left(1+a_s(\mu)\right). \tag{2.150}$$

As a first step, we write the formal expansions of $\ln a_s(\lambda)$ and $h(s)$ as a function of s:

$$\ln a_s(\lambda) = \ln a^{(0)}(\lambda) + s\ln a^{(1)}(\lambda) + \frac{s^2}{2}\ln a^{(2)}(\lambda) + \dots, \tag{2.151}$$

$$h(s) = h_0 + sh_1 + \frac{s^2}{2}h_2 + \dots. \tag{2.152}$$

Plugging these into Eq. (2.150), we obtain a system of integral equations, one for each successive order in the expansion in s. The order 0 gives the same quench action equations solved in Ref. [129]. To clarify the procedure we write in addition the result at first order

$$\ln a^{(1)}(\lambda) = -2\lambda^2 + h_1 + \int_{-\infty}^{+\infty}\frac{\mathrm{d}\mu}{2\pi}K(\lambda-\mu)\frac{a^{(0)}(\mu)}{1+a^{(0)}(\mu)}\ln a^{(1)}(\mu). \tag{2.153}$$

Since, for each fixed value of s, the driving term of Eq. (2.150) grows as λ^2 when $\lambda \to \infty$, it follows that $\ln a_s(\lambda)$ increases at most as λ^2 in the same limit, and therefore the following expansion as a function of λ can be written:

$$\ln a_s(\lambda) - \ln a^{(0)}(\lambda) = \beta_2(s)\lambda^2 + \beta_0(s) + \beta_{-2}\lambda^{-2}(s) + \dots, \tag{2.154}$$

where $\beta_{2j}(s) = O(s)$ and $j \leq 1$ is an integer number. In particular, one has

$$\beta_2(s) = -2s + O(s^2). \tag{2.155}$$

Accordingly, from Eq. (2.154) one has

$$a_s(\lambda) = a_0(\lambda)\mathrm{e}^{\beta_2(s)\lambda^2+\beta_0(s)+\beta_2\lambda^{-2}+\dots} = a_0(\lambda)\mathrm{e}^{\beta_2(s)\lambda^2}\sum_{n=0}^{\infty}\alpha_n(s)\lambda^{-2n}\,. \tag{2.156}$$

Since $a_s(\lambda)$ equals $a_0(\lambda)$ in $s=0$ we have that

$$\alpha_n(s) = \delta_{n,0} + O(s) \quad \text{for } s\to 0 \tag{2.157}$$

with $\delta_{n,0}$ the Kronecker delta symbol. Next, since the driving term of Bethe equations (2.34) is $1/2\pi$, with a reasoning analogous to the one done to justify Eq. (2.154) one has the asymptotic expansion for ρ_s^t for large λ

$$\rho_s^t(\lambda) = \frac{1}{2\pi} + \sum_{n=1}^{\infty}\gamma_{2n}(s)\lambda^{-2n}, \tag{2.158}$$

with suitable coefficients $\gamma_{2n}(s)$ whose explicit expression we do not need for the present calculation. We can eventually use the results in Eqs. (2.156) and (2.158) into the integral in the r.h.s. of Eq. (2.94), that we conveniently write as

$$\int_{-\infty}^{+\infty}\mathrm{d}\lambda\,\rho_s^*(\lambda)\lambda^2 = 2\int_0^1\mathrm{d}\lambda\,\rho_s^*(\lambda)\lambda^2 + 2\int_1^{+\infty}\mathrm{d}\lambda\,\rho_s^*(\lambda)\lambda^2\,. \tag{2.159}$$

Since the first integral on the r.h.s. has a finite support, one can expand $\rho_s^*(\lambda)$ in a power series in s. Each term can be integrated without divergences, so that after integration the result is expected to have the form of a power series in s. Hence, no term proportional to $\sqrt{s}$ will arise from this contribution. This is not the case for the second integral on the r.h.s. as we see in the following. First, we write it as

$$\int_1^{+\infty}\mathrm{d}\lambda\,\rho_s^*(\lambda)\lambda^2 = \int_1^{+\infty}\mathrm{d}\lambda\,\frac{a_s(\lambda)}{1+a_s(\lambda)}\left(\frac{1}{2\pi}+\sum_{n=1}^{\infty}\gamma_{2n}(s)\lambda^{-2n}\right)\lambda^2\,, \tag{2.160}$$

where we used $\rho(\lambda) = \rho^t(\lambda)a(\lambda)/(1+a(\lambda))$ for $\rho_s^*(\lambda)$ and Eq. (2.158). It is not difficult to see that substituting $a_s(\lambda)$ with $a_0(\lambda)$ in the denominator of the integrand on the r.h.s. of Eq. (2.160) leads only to corrections of order $O(s)$. As we are interested in the emergence of terms of order $O(\sqrt{s})$, we are allowed to perform this substitution. Next we can use Eq. (2.156) to express $a_s(\lambda)$ in the numerator of the resulting integrand of Eq. (2.160) and then note that [129]

$$\frac{a_0(\lambda)}{1+a_0(\lambda)} \simeq \frac{c^2D^2}{\lambda^4} + O(\lambda^{-6})\,, \tag{2.161}$$

such that Eq. (2.160) becomes

$$\int_1^{+\infty}\mathrm{d}\lambda\rho_s^*(\lambda)\lambda^2 = \int_1^{+\infty}\mathrm{d}\lambda\left(\frac{c^2D^2}{2\pi\lambda^2}+\sum_{n=2}^{\infty}z_{2n}(s)\lambda^{-2n}\right)\mathrm{e}^{\beta_2(s)\lambda^2}\,, \tag{2.162}$$

where we used Eq. (2.157) for α_0, which again leads to corrections of order $O(s)$,

while the coefficients $z_{2n}(s)$ can in principle be derived from $\alpha_{2n}(s)$ and $\gamma_{2n}(s)$ introduced in Eqs. (2.156) and (2.158), respectively. The integration in Eq. (2.162) can be performed term by term and only the first one yields a contribution $O(\sqrt{s})$ which is easily computed. Putting the latter result together with Eq. (2.88), which fixes the term linear in s, one arrives at Eq. (2.95), which we also tested numerically.

2.B Large s asymptotics of the large deviation function

In this Appendix we provide a detailed derivation of Eqs. (2.106)–(2.109) reported in the main text.

We start from the equation (2.77) for $\varepsilon_s^*(\lambda)$ which in the large-s limit reads as

$$\varepsilon_s^*(\lambda) = 2\lambda^2 - h' - \frac{h_0}{s} - \frac{h_{-1}}{s^2} + \frac{1}{s}\ln\left[\frac{\lambda^2}{c^2}\left(\frac{\lambda^2}{c^2}+\frac{1}{4}\right)\right] - \frac{1}{s}\int_{-\infty}^{\infty}\frac{\mathrm{d}^-}{2\pi}K(\lambda-\mu)\ln\left(1+\mathrm{e}^{-s\varepsilon_s^*(\mu)}\right) + O(s^{-3}), \tag{2.163}$$

where we used the large-s asymptotic of $h(s)$ in Eq. (2.102). Taking the difference between Eq. (2.163) and Eq. (2.100) we have

$$\varepsilon_s^*(\lambda) - \varepsilon_\infty(\lambda) = -\frac{h_0}{s} - \frac{h_{-1}}{s^2} + \frac{1}{s}\ln\left[\frac{\lambda^2}{c^2}\left(\frac{\lambda^2}{c^2}+\frac{1}{4}\right)\right] - \frac{1}{s}\left[\int_{-\infty}^{\infty}\frac{\mathrm{d}\mu}{2\pi}K(\lambda-\mu)\left(\ln\left(1+\mathrm{e}^{-s\varepsilon_s^*(\mu)}\right)+s\varepsilon_\infty^-(\mu)\right)\right] + O(s^{-3}), \tag{2.164}$$

where $\varepsilon_\infty^-(\lambda)$ is defined as

$$\varepsilon_\infty^-(\lambda) = \frac{1}{2}(\varepsilon_\infty(\lambda) - |\varepsilon_\infty(\lambda)|). \tag{2.165}$$

The last integral in Eq. (2.164) can be decomposed in a way similar to Eq. (2.103), namely,

$$\begin{aligned}\int_{-\infty}^{\infty}\frac{\mathrm{d}\mu}{2\pi}K(\lambda-\mu)\left(\ln\left(1+\mathrm{e}^{-s\varepsilon_s^*(\mu)}\right)+s\varepsilon_\infty^-(\mu)\right) &= -s\int_{-Q'}^{-Q}\frac{\mathrm{d}\mu}{2\pi}K(\lambda-\mu)\varepsilon_s^*(\mu) \\ &- s\int_{Q}^{Q'}\frac{\mathrm{d}\mu}{2\pi}K(\lambda-\mu)\varepsilon_s^*(\mu) - s\int_{-Q}^{Q}\frac{\mathrm{d}\mu}{2\pi}K(\lambda-\mu)\left[\varepsilon_s^*(\mu)-\varepsilon_\infty(\mu)\right] \\ &+ \int_{-\infty}^{+\infty}\frac{\mathrm{d}\mu}{2\pi}K(\lambda-\mu)\ln\left(1+\mathrm{e}^{-s|\varepsilon_s^*(\lambda)|}\right),\end{aligned} \tag{2.166}$$

with Q' and Q having the same meaning as in Sec. 2.5.2. The analysis of the integrals appearing on the right hand side is completely analogous to the one

carried out in Sec. 2.5.2 for Eqs. (2.104),(2.105) and (2.107). In conclusion from Eqs. (2.164),(2.166), $\delta\varepsilon_s^*(\lambda) = \varepsilon_s^*(\lambda) - \varepsilon_\infty(\lambda)$ satisfies the following integral equation

$$\begin{aligned}\delta\varepsilon_s^*(\lambda) = & - \frac{h_0}{s} - \frac{h_{-1}}{s^2} + \frac{1}{s}\ln\left[\frac{\lambda^2}{c^2}\left(\frac{\lambda^2}{c^2}+\frac{1}{4}\right)\right] + \int_{-Q}^{Q}\frac{\mathrm{d}\mu}{2\pi}K(\lambda-\mu)\delta\varepsilon_s^*(\mu) \\ & - \frac{\varepsilon'_\infty(Q)}{4\pi}(Q'-Q)^2(K(\lambda-Q)+K(\lambda+Q)) \\ & - \frac{\pi}{12\varepsilon'_\infty(Q)s^2}[K(\lambda-Q)+K(\lambda+Q)] + O(s^{-3})\,. \end{aligned} \tag{2.167}$$

With a reasoning analogous to the one done in Ref. [172] one can show that the term containing $(Q'-Q)^2$ is at least of order $O(s^{-2})$. Accordingly,

$$\delta\varepsilon_s^*(\lambda) = \frac{U_1(\lambda)}{s} + O(s^{-2}), \tag{2.168}$$

where the function $U_1(\lambda)$ is the solution of the integral equation

$$U_1(\lambda) = -h_0 + \ln\left[\frac{\lambda^2}{c^2}\left(\frac{\lambda^2}{c^2}+\frac{1}{4}\right)\right] + \int_{-Q}^{Q}\frac{\mathrm{d}\mu}{2\pi}K(\lambda-\mu)U_1(\mu)\,. \tag{2.169}$$

In particular, computing Eq. (2.168) for $\lambda = Q'$ and expanding it in the difference $Q'-Q$ we get

$$Q'-Q = -\frac{U_1(Q)}{s\varepsilon'_\infty(Q)} + O(s^{-2})\,. \tag{2.170}$$

Note that this result shows that $(Q'-Q)^2$ is exactly of order $O(s^{-2})$. As a consequence, in order to determine $\delta\varepsilon_s^*(\lambda)$ up to the second order in $1/s$ in Eq. (2.167) we keep the terms containing $Q'-Q$. Exploiting the first-order result reported in Eq. (2.168), we finally obtain

$$\delta\varepsilon_s^*(\lambda) = \varepsilon_s^*(\lambda) - \varepsilon_\infty(\lambda) = \frac{U_1(\lambda)}{s} + \frac{U_2(\lambda)}{s^2} + O(s^{-3})\,, \tag{2.171}$$

$$\begin{aligned} U_2(\lambda) = & \frac{[K(\lambda-Q)+K(\lambda+Q)]}{\varepsilon'_\infty(Q)}\left(-\frac{U_1^2(Q)}{4\pi} - \frac{\pi}{12}\right) - h_{-1} \\ & + \int_{-Q}^{Q}\frac{\mathrm{d}\mu}{2\pi}\,K(\lambda-\mu)U_2(\mu)\,, \end{aligned} \tag{2.172}$$

completing the derivation of Eqs. (2.106)–(2.109) in the main text.

2.C Algebraic behavior of $p(w)$ at large w: arbitrary particle number

In this Appendix we show how to extend by induction the computation presented in Sec. 2.6 for $N = 3$ to an arbitrary number N of particles. In order to simplify the discussion we will first present the explicit example $M = 2$ ($N = 5$),

and then treat the general case. As a result of the analysis of this Appendix, we conclude that Eq. (2.149) holds for arbitrary values of N.

In the case $M = 2$, Eq. (2.138) reads

$$\begin{aligned} \epsilon P(W) &= \sum_{W' \in (W-\epsilon, W+\epsilon)} |\langle I_1, I_2 | \mathrm{BEC} \rangle|^2 \\ &= \sum_{I_1, I_2 \in \mathcal{D}} |\langle I_1, I_2 | \mathrm{BEC} \rangle|^2, \end{aligned} \tag{2.173}$$

where the domain $\mathcal{D}$ of the double sum is determined, via Eq. (2.131), by the boundaries of the energy shell in Eq. (2.173) and the fact the two quantum numbers I_1 and I_2 have to be different. In particular

$$I_1, I_2 \in \mathcal{D} \Leftrightarrow \begin{cases} I_1^2 + I_2^2 \in \frac{L^2}{8\pi^2}(W-\epsilon, W+\epsilon) \\ 0 < I_1 < I_2, \end{cases} \tag{2.174}$$

corresponding to the region highlighted in blue in the $I_1 - I_2$ plane shown in Fig. 2.C.1. For convenience we will neglect from the start the contribution of the domain $\mathcal{D}$ where $I_1 > I_1^{\max} = L\sqrt{(W-\epsilon)}/(4\pi)$, depicted in red in Fig. 2.C.1, which provides a contribution $O(\epsilon^2)$. Then, from Eqs. (2.173),(2.130) and (2.133)

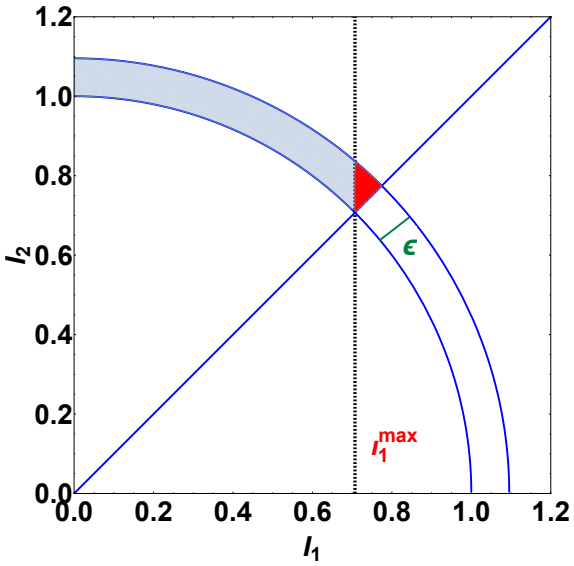

FIGURE 2.C.1: Pictorial representation of the summation domain $\mathcal{D}$ of Eq. (2.174) in blue and red shaded areas. The latter one is of order ϵ^2, with ϵ the thickness of the shell, and can therefore be neglected to order ϵ. The intercept of the vertical black dashed line with the horizontal I_1 axis is given by $I_1^{\max} = L\sqrt{(W-\epsilon)}/(4\pi)$. Image taken from Ref. [2].

one has

$$\epsilon P(W) = \frac{5! c^4 L^4}{(16\pi^2)^2} \sum_{I_1=1}^{I_1^{\max}} \frac{1}{I_1^2(\pi^2 I_1^2 + \frac{c^2 L^2}{16})} \sum_{I_2 = I_2^{\min}(I_1)}^{I_2^{\max}(I_1)} \frac{1}{I_2^2(\pi^2 I_2^2 + \frac{c^2 L^2}{16})}, \tag{2.175}$$

where $I_2 = I_2^{\min}(I_1)$ and $I_2^{\max}(I_1)$ are obtained from the on-shell condition in Eq. (2.174), in analogy with the case $M = 1$, and read

$$\begin{aligned} I_2^{\min}(I_1) &= \sqrt{\frac{L^2}{8\pi^2}W - \epsilon - I_1^2}, \\ I_2^{\max}(I_1) &= \sqrt{\frac{L^2}{8\pi^2}W + \epsilon - I_1^2}, \\ \delta I(I_1) &\equiv I_2^{\max}(I_1) - I_2^{\min}(I_1) = \frac{L^2\epsilon}{8\pi^2\sqrt{\frac{L^2W}{8\pi^2} - I_1^2}} + O\left(\epsilon^2\right). \end{aligned} \tag{2.176}$$

The sum $\mathcal{S}(I_1)$ over I_2 in Eq. (2.175) can be bounded using the same argument as the one presented in Sec. 2.6 for the case $M = 1$ to get Eqs. (2.145) and (2.146); in particular at leading order in ϵ

$$\begin{aligned} \mathcal{S}(I_1) &\equiv \sum_{I_2=I_2^{\min}(I_1)}^{I_2^{\max}(I_1)} \frac{1}{I_2^2(\pi^2 I_2^2 + \frac{c^2L^2}{16})} \\ &= \sum_{j=0}^{\delta I(I_1)} \frac{1}{[j + I_2^{\min}(I_1)]^2[\pi^2(j + I_2^{\min}(I_1))^2 + \frac{c^2L^2}{16}]} \\ &= \frac{L^2\epsilon}{8\pi^2\sqrt{L^2W/(8\pi^2) - I_1^2}} \frac{1}{L^2W/(8\pi^2) - I_1^2} \frac{1}{\pi^2(L^2W/(8\pi^2) - I_1^2) + \frac{c^2L^2}{16}} + O(\epsilon^2). \end{aligned} \tag{2.177}$$

In terms of $\mathcal{S}(I_1)$ in Eq. (2.177), $\epsilon P(w)$ in Eq. (2.175) can be written as

$$\epsilon P(W) = \frac{5! c^4 L^4}{(16\pi^2)^2} \sum_{I_1=1}^{I_1^{\max}} \frac{1}{I_1^2(\pi^2 I_1^2 + \frac{c^2L^2}{16})} \mathcal{S}(I_1), \tag{2.178}$$

where $\mathcal{S}(I_1)$ can be bounded as

$$\begin{aligned} \mathcal{S}(I_1 = 1) &< \mathcal{S}(I_1) < \mathcal{S}(I_1^{\max}), \\ \mathcal{S}(I_1 = 1) &\propto \mathcal{S}(I_1^{\max}) \propto \frac{L^2\epsilon}{\sqrt{L^2W}L^2W(\frac{L^2W}{8\pi^2} + \frac{c^2L^2}{16})} + O(\epsilon^2), \end{aligned} \tag{2.179}$$

where the symbol $\propto$ henceforth indicates that we are neglecting numerical prefactors. From Eq. (2.179) it follows that

$$\epsilon P(W) \propto c^4 L^4 \frac{L^2\epsilon}{\sqrt{L^2W}L^2W(\frac{L^2W}{8\pi^2} + \frac{c^2L^2}{16})} \sum_{I_1=1}^{L\sqrt{W}/4\pi} \frac{1}{I_1^2(\pi^2 I_1^2 + \frac{c^2L^2}{16})} + O(\epsilon^2), \tag{2.180}$$

and, equivalently, for the probability density function $p(w) = LP(wL)$ of the intensive work w

$$\epsilon p(w) \propto c^4 L^5 \frac{L^2 \epsilon}{\sqrt{L^3 w} L^3 w (\frac{L^3 w}{8\pi^2} + \frac{c^2 L^2}{16})} \sum_{I_1=1}^{L\sqrt{wL}/4\pi} \frac{1}{I_1^2(\pi^2 I_1^2 + \frac{c^2 L^2}{16})} + O(\epsilon^2). \quad (2.181)$$

In order to get the leading behaviour of $p(w)$ as a function of L, as a final step, we need to estimate the asymptotic of the sum over I_1 in Eq. (2.181) for L large. We have

$$\sum_{I_1=1}^{L\sqrt{wL}/4\pi} \frac{1}{I_1^2(\pi^2 I_1^2 + \frac{c^2 L^2}{16})} = \sum_{I_1=1}^{\infty} \frac{1}{I_1^2(\pi^2 I_1^2 + \frac{c^2 L^2}{16})} - \sum_{I_1=L\sqrt{wL}/4\pi}^{\infty} \frac{1}{I_1^2(\pi^2 I_1^2 + \frac{c^2 L^2}{16})}, \quad (2.182)$$

with

$$\begin{aligned} \sum_{I_1=L\sqrt{wL}/4\pi}^{\infty} \frac{1}{I_1^2(\pi^2 I_1^2 + \frac{c^2 L^2}{16})} &\leq \frac{1}{L^3 w/(16\pi^2)} \sum_{I_1=L\sqrt{wL}/4\pi}^{\infty} \frac{1}{(\pi^2 I_1^2 + \frac{c^2 L^2}{16})} \\ &\leq \frac{16\pi^2}{L^3 w} \sum_{I_1=1}^{\infty} \frac{1}{(\pi^2 I_1^2 + \frac{c^2 L^2}{16})} = \frac{32\pi^2}{c\, w L^4} + O(L^{-5}), \end{aligned} \quad (2.183)$$

and

$$\sum_{I_1=1}^{\infty} \frac{1}{I_1^2(\pi^2 I_1^2 + \frac{c^2 L^2}{16})} = 8\pi^2 \frac{48 + c^2 L^2 - 12\, cL \coth\left(\frac{cL}{4}\right)}{3c^4 L^4} = \frac{8\pi^2}{3c^2 L^2} + O(L^{-3}) \quad (2.184)$$

as $L \to \infty$. Plugging this into Eq. (2.181) we arrive at the final result

$$\begin{aligned} p(w) &\propto c^4 L^5 \frac{L^2}{\sqrt{L^3 w} L^3 w (\frac{L^3 w}{8\pi^2} + \frac{c^2 L^2}{16})} \left[\frac{8\pi^2}{3c^2 L^2} + O(L^{-3}) \right]. \\ &\propto \frac{c^2}{L^{5/2}} w^{-5/2} + O(L^{-7/2}) \quad \text{as } L \to \infty. \end{aligned} \quad (2.185)$$

At this point it should be clear how to generalize the result in Eq. (2.185) by induction to the general case of $N = 2M + 1$ particles. Indeed, consider the expression for $P_M(W)$

$$\begin{aligned} \epsilon P_M(W) &= \sum_{I_1, I_2, \ldots I_M \in \mathcal{D}} |\langle I_1, I_2, \ldots I_M | \text{BEC} \rangle|^2 \\ &= \frac{N c^2 L^2}{16\pi^2} \sum_{I_1=1}^{I_1^{\max}} \frac{1}{I_1^2(\pi^2 I_1^2 + \frac{c^2 L^2}{16})} \left(\sum_{I_2, I_3, \ldots I_M \in \mathcal{D}'(W')} |\langle I_2, I_3, \ldots I_M | \text{BEC} \rangle|^2 \right). \end{aligned} \quad (2.186)$$

Here the sum in the first line is over the M-dimensional shell $\mathcal{D}$ defined by

$$I_1 \dots I_M \in \mathcal{D} \Leftrightarrow \begin{cases} I_1^2 + I_2^2 + \dots I_M^2 \in \frac{L^2}{8\pi^2}(W-\epsilon, W+\epsilon), \\ 0 < I_1 < I_2 \dots < I_M, \end{cases} \tag{2.187}$$

while $\mathcal{D}'$, appearing in the second line, is the same as $\mathcal{D}$ with $W \to W' = W - 8\pi^2 I_1^2/L^2$ and $I_1^{\max} = L\sqrt{(W-\epsilon)}/(\sqrt{8M}\pi)$. Then, we note that Eq. (2.186) can be written in terms of P_{M-1} as

$$\epsilon P_M(W) = \frac{Nc^2L^2}{16\pi^2} \sum_{I_1=1}^{I_1^{\max}} \frac{1}{I_1^2(\pi^2 I_1^2 + \frac{c^2L^2}{16})} \epsilon P_{M-1}(W'). \tag{2.188}$$

Exploiting now the induction hypothesis, we have

$$\epsilon P_{M-1}(W') \propto c^2L^2 \frac{L^2\epsilon}{\sqrt{L^2W}L^2W(\frac{L^2W}{8\pi^2} + \frac{c^2L^2}{16})} + O(\epsilon^2) \tag{2.189}$$

where again we neglect numerical prefactors depending on N. Then using Eqs. (2.182), (2.183) and (2.184) it follows that $p_M(w)$ displays the large-L behavior in Eq. (2.185), concluding the derivation.

Chapter 3

Inhomogeneous systems: transport in free-particle models

In this Chapter we deal with quantum transport in one-dimensional isolated quantum systems. The presence of currents describing the transport of globally conserved quantities, like the energy or the particle number, is a paradigmatic example of non-equilibrium dynamics with ubiquitous technological applications. In particular, systems reaching a non-equilibrium steady state (NESS) supporting the flow of a current are now topical. Fluctuations of current flows in non-equilibrium steady states of classical systems, as a matter of fact, can be classified via the large deviation theory, which allows for the formulation of ordering principles generalizing equilibrium thermodynamics to non-equilibrium transport [310–313]. In quantum systems, on the other hand, much less is known about the statistical properties of current flows and their universality because of the interplay of both quantum and classical fluctuations. In this respect, one-dimensional integrable systems provide an ideal framework to study quantum transport and the corresponding large deviation formalism. In fact, on the one hand, they provide an approximation amenable to analytical results of actual three-dimensional systems with strong anisotropy. On the other hand, they might display an anomalous heat conduction which violates Fourier's law because of the ballistic transport of energy [314]. Fundamentally, all these features can be probed with current cold-atomic experiments, in which, e.g., the heat current flowing between two leads kept at different temperatures can be measured [315, 316].

In order to study transport phenomena in isolated quantum systems one needs to consider *inhomogeneous* initial states, where a macroscopic imbalance e.g., of energy is initially present across the system as a function of space. The simplest inhomogeneous initial state is provided by the *partitioning protocol* [141–144], introduced in Subsec. 1.4.2, whereby an homogeneous and stationary (translationally invariant in time) NESS is generated by gluing together at time $t = 0$ two halves of the same system described by two different generalized Gibbs ensembles (GGEs). The particular case that will be addressed in this Chapter is the one of two thermal GGEs, which are identified by two different Lagrange parameters (one for each GGE) β_r and β_l coupled to the corresponding Hamiltonians H_r and H_l, according to Eq. (1.44). All the other multipliers β_i are equal to zero in the initial state. In this case, $\beta_{l,r}$ have the meaning of inverse temperatures and the two GGEs reduce to the two corresponding canonical distributions. The resulting initial state is thus described by a density matrix ρ_0 which is inhomogeneous in space because of the two different temperatures, while the subsequent dynamics

is determined by a translationally invariant Hamiltonian: accordingly, this is a prototypical instance of the so-called inhomogeneous quench.

In this Chapter we will consider the energy transport arising from the partitioning protocol initial state in non-interacting many-body systems, where freely propagating stable quasi-particles excitations can be defined, as anticipated in Subsecs. 1.3.5 and 1.4.2. In these models transport is ballistic and a NESS develops at long times after the quench[1]. In particular, we will consider the transverse field Ising chain in Eq. (1.2), which is characterized by fermionic quasi-particle excitations, and the harmonic chain, which has bosonic excitations. The aim of this Chapter is twofold. First, we show that the energy current and density in the limit of large space coordinate x along the chain and time t elapsed after the quench, with fixed ratio $v = x/t$, are described by hydrodynamic expressions with a rather universal structure, where the only model-specific data are the single-particle energy spectrum and the (Fermi-Dirac or Bose-Einstein) statistical distribution. These expressions are functions of the scaling variable v and they describe the whole space and time dynamics beyond the NESS. Second, aiming at the statistics of fluctuations beyond the mean value, we calculate exactly the scaled cumulant generating function (SCGF) of the time-integrated current $J_E = \Delta e(x,t)/t$, defined in Eq. (1.48), for the inhomogeneous partitioning protocol initial state ρ_0. The SCGF is a function of v, via the Legendre-Fenchel transform the complete evolution in space and time of the associated large deviation function $I(J_E, v)$ beyond the stationary limit is obtained. We shall see that the results for the SCGF can be naturally interpreted in terms of the semiclassical quasi-particle picture introduced in Subsecs. 1.4.2 for the case of inhomogeneous quenches.

This Chapter is organized as follows. In Sec. 3.1 we briefly report the main formulas entering in the exact solution of the Ising chain, presented in Subsec. 3.1.1, and of the chain of harmonic oscillators, in Subsec. 3.1.2. In Sec. 3.2 we review the definition of the partitioning protocol and of the ensuing NESS. Sections 3.3, 3.4 and 3.5 contain our original contributions, published in Refs. [1, 4]. In Sec. 3.3 the hydrodynamic scaling limit of the mean values of the energy current and density is computed. In Sec. 3.4 we calculate the sub-diffusive corrections to the hydrodynamic limit discussed in the previous Section. In Sec. 3.5, instead, we focus on the full statistics of the energy current and density beyond the mean value. The hydrodynamic limit of the SCGF is first defined and then we recall known facts concerning the long-time limit of this function, i.e., in the NESS. Subsection 3.5.1 presents the main result regarding the SCGF in the space-time scaling limit and the corresponding derivation. In Subsec. 3.5.2 we discuss a semi-classical picture for calculating the SCGF, in agreement with Subsec. 3.5.1. In Subsecs. 3.5.3 and 3.5.4 we specialize the general expression of Subsec. 3.5.1 to the fermionic and bosonic cases, respectively, and we determine the Legendre-Fenchel transform of the SCGF, discussing the resulting large deviation function $I(J_E, v)$ for both cases. Finally, we conclude in Sec. 3.6, while some of the technical aspects of the various calculations underlying the results of this Chapter are presented in Appendix 3.

[1] In the more general case of interacting integrable models the picture is more complex and transport is not necessarily ballistic as diffusion might be present. This aspect will be discussed in Chapter 4 when interacting integrable models will be addressed.

3.1 Basic models with free quasi-particle excitations and their exact solutions

The initial density matrix ρ_0 of the partitioning protocol [141–144] considered in this Chapter is given by

$$\rho_0 = \mathrm{e}^{-\beta_r H_r} \otimes \mathrm{e}^{-\beta_l H_l} / Z, \tag{3.1}$$

where H_r and H_l are the Hamiltonians corresponding to the two parts, conventionally referred to as right (r) and left (l) of the system (e.g., two complementary but otherwise identical semi-infinite chains) initially at thermal equilibrium at the inverse temperatures β_r and β_l, respectively, while Z is the associated partition function. In Subsection 3.1.1 we take for $H_{r,l}$ the transverse field Ising Hamiltonian, which corresponds to fermionic quasi-particle excitations, while in Subsection 3.1.2 the harmonic chain is considered, which is described by bosonic quasi-particle excitations.

3.1.1 The quantum Ising chain in a transverse field

As anticipated above, in the partitioning protocol, two originally disconnected identical chains of length N are joined at the initial time $t = 0$. The right (r) and left (l) Hamiltonians before the quench are, respectively,

$$H_r = -\frac{J}{2}\left[\sum_{n=1}^{N-1} \sigma_n^x \sigma_{n+1}^x + h \sum_{n=1}^{N} \sigma_n^z\right], \tag{3.2a}$$

$$H_l = -\frac{J}{2}\left[\sum_{n=1}^{N-1} \sigma_{-n}^x \sigma_{-n+1}^x + h \sum_{n=0}^{N-1} \sigma_{-n}^z\right], \tag{3.2b}$$

with $H_0 = H_r + H_l$ being the pre-quench Hamiltonian, $\sigma_n^{x,y,z}$ are the usual spin 1/2 Pauli matrices at lattice site n, while J and h are the microscopic parameters of the model, i.e., the strength of the ferromagnetic interaction and the transverse field, respectively. The right chain is defined on the lattice sites labeled by $\{1, 2, \ldots, N\}$, while the left one on the sites $\{-N+1, -N+2, \ldots, 0\}$. Open boundary conditions are assumed for both chains. Notice that, compared to Eq. (1.2), we have explicitly introduced in Eq. (3.2) the constant J as the characteristic energy scale of the problem. Energies and times are therefore measured in units of J and J^{-1}, respectively. With a Jordan-Wigner transformation (see, e.g., Ref. [13]) one writes the Hamiltonians $H_{r,l}$ in terms of the Jordan-Wigner lattice fermionic operators c_n at site n

$$c_n = \left(\mathrm{e}^{i\pi \sum_{m=1}^{n-1} \sigma_m^- \sigma_m^+}\right) \sigma_n^+ = \left(\prod_{m=1}^{n-1} \sigma_m^z\right) \sigma_n^+, \tag{3.3}$$

where $\sigma_m^{\pm} = (\sigma_m^x \pm i\sigma_m^y)/2$ are the spin raising and lowering operators. The Hamiltonians $H_{r,l}$ acquire the bilinear form

$$H_r = -\frac{J}{2}\sum_{n=1}^{N-1}\left(c_n^\dagger c_{n+1}^\dagger + c_n^\dagger c_{n+1} + h.c.\right) + Jh\sum_{n=1}^{N} c_n^\dagger c_n, \tag{3.4}$$

where $h.c.$ denotes the Hermitian conjugate of the preceding expression and an analogous form holds for H_l. As discussed in Ref. [75] (additional details which are not reported here for brevity can be found in Ref. [1]) Hamiltonians of this type can be diagonalized via a Bogoliubov transformation which suitably introduces two fields $\phi_{r,l}(k)$ as

$$\phi_r(k) = \sum_{n=1}^{N}\left[\omega_r^n(k)c_n + \xi_r^n(k)c_n^\dagger\right], \tag{3.5}$$

with an analogous expression for $\phi_l(k)$, but with coefficients $\{\omega_l^n(k),\, \xi_l^n(k)\}$ and $n = -N+1,\ldots,0$, whose analytic expressions is reported in Appendix 3.A. In terms of these fields one eventually finds

$$H_{r,l} = \sum_k \varepsilon(k)\phi_{r,l}^\dagger(k)\phi_{r,l}(k), \tag{3.6}$$

where the single-particle energy spectrum is given by

$$\varepsilon(k) = J\sqrt{h^2 - 2h\cos k + 1}. \tag{3.7}$$

Due to the finite length N of both (half-) chains, the set of allowed values of k in the sum of Eq. (3.6) is discrete and, as a consequence of the open boundary conditions, determined by the implicit condition

$$k_n = \frac{n\pi}{N+1} + \frac{f(k_n)}{N+1}, \quad \text{with} \quad n = 0, 1, ...N, \tag{3.8}$$

where

$$f(k) \equiv \arctan\left(\frac{\sin k}{\cos k - h}\right). \tag{3.9}$$

In the thermodynamic limit $N \to \infty$, both chains become semi-infinite, either to their right or to their left. Correspondingly, the set of allowed values k_n becomes continuous within the interval $[0, \pi]$ and, upon redefining $\Phi_{r,l}(k) = \lim_{N\to\infty}(N/\pi)^{1/2}\phi_{r,l}(k)$, the Hamiltonians take the diagonal form

$$H_{r,l} = \int_0^\pi \mathrm{d}k\; \varepsilon(k)\Phi_{r,l}^\dagger(k)\Phi_{r,l}(k), \tag{3.10}$$

where the single-particle energy spectrum $\varepsilon(k)$ is the same as in Eq. (3.7).

At time $t = 0$ the two chains are instantaneously joined in order to form a unique, homogeneous chain with Hamiltonian:

$$H \;=\; H_0 + \delta H = H_0 - \frac{J}{2}\sigma_0^x\sigma_1^x \tag{3.11}$$

with δH representing the local interaction determined by the junction of the left and right chains through their closest end points at $n = 0$ and $n = 1$, respectively. After the quench $H_0 \to H$, since there is no impurity and the two half-chains are equal, the Hamiltonian becomes translationally invariant, i.e., $[H, P_{tr}] = 0$, where P_{tr} is the translation operator

$$\sigma^{\alpha}_{n-1} = P^{\dagger}_{tr}\sigma^{\alpha}_{n}P_{tr}, \quad \text{with} \quad \alpha = x, y, z. \tag{3.12}$$

It is then possible to introduce two fermionic operators $\Psi_{R,L}(k)$, satisfying fermionic canonical anticommutation relations $[\Psi_{R,L}(k), \Psi^{\dagger}_{R,L}(k')]_+ = \delta(k - k')$, for each value of the wavevector k corresponding to right- and left-moving fermionic quasi-particles excitations, respectively, which acquire opposite phases under the action of the translation operator, i.e.,

$$P^{\dagger}_{tr}\Psi_{R,L}(k)P_{tr} = \mathrm{e}^{\mp ik}\Psi_{R,L}(k). \tag{3.13}$$

For the sake of completeness we report here the definition of $\Psi_{R,L}(k)$ in terms of the Jordan-Wigner fermions of Eq. (3.3), with the notation of Ref. [1]:

$$\Psi_{R,L}(k) = \sum_{n=-\infty}^{+\infty} \left[c_n \omega^n_{R,L}(k) + c^{\dagger}_n \xi^n_{R,L}(k) \right], \tag{3.14}$$

where

$$\omega^n_R(k) = \frac{1}{2}\frac{1}{\sqrt{2\pi}}\mathrm{e}^{-ink+k}(1 + \mathrm{e}^{-if(k)}), \quad \xi^n_R(k) = \frac{1}{2}\frac{1}{\sqrt{2\pi}}\mathrm{e}^{-ink+k}(1 - \mathrm{e}^{-if(k)}), \tag{3.15}$$

while $\omega^n_L(k)$ and $\xi^n_L(k)$ can be simply expressed in terms of the corresponding "right" functions $\omega^n_R(k)$ and $\xi^n_R(k)$ as

$$\omega^n_L(k) = \omega^n_R(-k)\,\mathrm{e}^{i(k-f(k))} \ , \ \xi^n_L(k) = \xi^n_R(-k)\,\mathrm{e}^{i(k-f(k))} \tag{3.16}$$

with $f(k)$ given in Eq. (3.9). From Eq. (3.16) it immediately follows that

$$\Psi_L(k) = \mathrm{e}^{i(k-f(k))}\Psi_R(-k), \tag{3.17}$$

i.e., right-moving quasi-particles excitations with momentum k have opposite momentum with respect to left moving ones $\Psi_L(k)$, but the same energy since $\varepsilon(k)$ in Eq. (3.7) is an even function of k. The post-quench Hamiltonian takes the diagonal form

$$H = \int_0^{\pi} dk \ \varepsilon(k) \left[\Psi^{\dagger}_R(k)\Psi_R(k) + \Psi^{\dagger}_L(k)\Psi_L(k) \right] \equiv H_R + H_L, \tag{3.18}$$

which makes explicit the free-fermionic nature of the model.

3.1.2 The quantum harmonic chain

The right (r) and left (l) Hamiltonians of the chains of harmonic oscillators are

$$H_r = \frac{1}{2}\sum_{x=1}^{N}\left(p_x^2 + m^2\phi_x^2\right) + \frac{1}{2}\sum_{x=0}^{N}\omega^2(\phi_{x+1}-\phi_x)^2, \tag{3.19a}$$

$$H_l = \frac{1}{2}\sum_{x=0}^{N-1}\left(p_{-x}^2 + m^2\phi_{-x}^2\right) + \frac{1}{2}\sum_{x=0}^{N}\omega^2(\phi_{-x+1}-\phi_{-x})^2, \tag{3.19b}$$

respectively, where the position ϕ_x and momentum p_x operators satisfy the equal-time canonical commutation relations $[\phi_x, p_y] = i\delta_{x,y}$, with all the other possible commutators vanishing, m is the "mass" of the oscillators and ω their angular frequency. As in the case of the Ising model discussed in the previous Subsection, the right chain consists of N lattice sites indexed by $\{1,2,\dots,N\}$, while the left chain is defined on the lattice sites $\{-N+1,-N+2,\dots,0\}$. For both chains we assume Dirichlet boundary conditions, which read

$$\phi_0 = \phi_{N+1} \equiv 0 \quad \text{and} \quad p_0 = p_{N+1} \equiv 0 \tag{3.20}$$

for the right chain, while $\phi_1 = \phi_{-N} \equiv 0$ and $p_1 = p_{-N} \equiv 0$ for the left one.

The first step for solving the model (here we provide some details for the right chain; the similar analysis for the left chain is reported in Appendix 3.A) is to introduce, in the thermodynamic limit $N \to \infty$, the operators $\hat{\phi}_r(k)$, $\hat{p}_r(k)$ for the right (r) chain (see, e.g., Ref. [317])

$$\hat{\phi}_r(k) = \sqrt{\frac{2}{\pi}}\sum_{x=1}^{\infty}\sin(kx)\phi_x, \quad \hat{p}_r(k) = \sqrt{\frac{2}{\pi}}\sum_{x=1}^{\infty}\sin(kx)p_x, \tag{3.21}$$

in terms of which ϕ_x and p_x are expressed as

$$\phi_x = \sqrt{\frac{2}{\pi}}\int_0^{\pi} dk\,\sin(kx)\hat{\phi}_r(k), \quad p_x = \sqrt{\frac{2}{\pi}}\int_0^{\pi} dk\,\sin(kx)\hat{p}_r(k). \tag{3.22}$$

In the thermodynamic limit the set of allowed values of k is continuous within the interval $[0,\pi]$, due to the fact that for finite N its values k_n are discrete according to the integer $n = 1,2,...N$, from the boundary condition (3.20), with

$$k_n = \frac{\pi n}{N+1}. \tag{3.23}$$

Note that, as a consequence of the presence of the sine function in Eq. (3.22), the boundary condition for ϕ_x and p_x in $x = 0$ is automatically fulfilled. In terms of the operators $\hat{\phi}_r$ and $\hat{p}_r$ the usual creation and annihilation operators can be introduced

$$\begin{aligned} A_r^{\dagger}(k_n) &= \frac{1}{\sqrt{2\Omega(k)}}\left[\Omega(k)\hat{\phi}_r(k) - i\hat{p}_r(k)\right], \\ A_r(k) &= \frac{1}{\sqrt{2\Omega(k)}}\left[\Omega(k)\hat{\phi}_r(k) + i\hat{p}_r(k)\right], \end{aligned} \tag{3.24}$$

which satisfy the canonical commutation relations $[A_r(k), A_r^\dagger(k')] = \delta(k-k')$. In terms of these operators H_r in Eq. (3.19a) then takes the diagonal form

$$H_r = \int_0^\pi dk\, \Omega(k) A_r^\dagger(k) A_r(k), \tag{3.25}$$

where $\Omega(k)$ denotes the single-particle dispersion relation given by

$$\Omega(k) = \sqrt{m^2 + 2\omega^2(1-\cos k)}, \tag{3.26}$$

which has the same qualitative dependence on k as Eq. (3.7) and becomes identical to it upon identifying $\omega \mapsto J\sqrt{h}$ and $m \mapsto J|h-1|$. Note that in Eq. (3.25) we have dropped the inconsequential zero-point energy term

$$\sum_{k_n} \frac{\Omega(k_n)}{2} \to \frac{N}{2} \int_{-\pi}^{\pi} \frac{dk}{2\pi} \Omega(k) \quad \text{for} \quad N \to \infty, \tag{3.27}$$

as it does not affect transport properties and their statistics (note that it can be anyhow removed by normal-ordering the initial Hamiltonians in Eq. (3.19)).

The quench occurring at time $t = 0$ connects the chains via their end points at site 0 resulting in the post-quench Hamiltonian $H = H_r + H_l + \delta H$, with $\delta H = -\omega^2 \phi_1 \phi_0$, and therefore

$$H = \frac{1}{2} \sum_{x=-N+1}^{N} \left(p_x^2 + m^2 \phi_x^2 \right) + \frac{1}{2} \sum_{x=-N}^{N} \omega^2 (\phi_{x+1} - \phi_x)^2, \tag{3.28}$$

with boundary conditions $\phi_{-N} = \phi_{N+1} \equiv 0$ and $p_{-N} = p_{N+1} \equiv 0$. In the thermodynamic limit $N \to \infty$, the chain becomes translationally invariant, i.e., $[H, P_{tr}] = 0$ with the translation operator P_{tr} defined similarly to the Ising case (see Eq. (3.12)) as

$$P_{tr}^\dagger \phi_x P_{tr} = \phi_{x-1}, \;\; P_{tr}^\dagger p_x P_{tr} = p_{x-1}; \tag{3.29}$$

the resulting model can solved by means of Fourier transform as in the case with periodic boundary conditions, which yields

$$H = \int_0^\pi dk \;\; \Omega(k) \;\; \left[\mathbb{A}^\dagger(k) \mathbb{A}(k) + \mathbb{A}^\dagger(-k) \mathbb{A}(-k) \right] \; = H_R + H_L,$$

where k varies continuously within the interval $[-\pi, \pi]$ and

$$\mathbb{A}(k) = \frac{1}{\sqrt{2\Omega(k)}} \left[\Omega(k) \hat{\phi}(k) + i \hat{p}(k) \right], \tag{3.30}$$

while

$$\hat{\phi}(k) = \frac{1}{\sqrt{2\pi}} \sum_{x=-\infty}^{+\infty} \mathrm{e}^{-ikx} \phi_x, \quad \hat{p}(k) = \frac{1}{\sqrt{2\pi}} \sum_{x=-\infty}^{+\infty} \mathrm{e}^{-ikx} p_x, \tag{3.31}$$

are the Fourier transformed operators. Note that by applying the definition in Eq. (3.29) to Eq. (3.30), keeping into account Eqs. (3.31), it follows that

$$P_{tr}^{\dagger}\mathbb{A}(\pm k)P_{tr} = \mathrm{e}^{\mp ik}, \tag{3.32}$$

i.e., analogously to Eq. (3.13) for the post-quench mode operators $\Psi_{R,L}(k)$ of the transverse field Ising chain, the operators $\mathbb{A}(\pm k)$ having positive/negative wave vector k can be interpreted as bosonic right/left moving quasi-particles excitations.

3.2 Partitioning protocol and the non-equilibrium steady state

As anticipated in Secs. 3 and 3.1, the NESS in the partitioning protocol is obtained by joining at time $t = 0$ two subsystems, which are initially described by two different GGEs. The junction is taken to be at point $x = 0$. Henceforth the case of two thermal GGEs identified by two different temperatures β_l and β_r will be considered and therefore the initial inhomogeneous and non-stationary density matrix ρ_0 is given by Eq. (3.1). In order to be able to access the stationary state, both the time t and the system size N must be large, the latter being always larger than the maximal distance $v_{max}t$ travelled by the fermionic excitations at time t, where v_{max} is the Lieb-Robinson velocity, which has been defined in Subsec. 1.3.5 (for the transverse field Ising chain and the harmonic chain is given, respectively, by Eqs. (3.51) and (3.65)). In this case, the steady state density matrix ρ_{stat} is formally defined by requiring that [142–146, 148]

$$\langle\mathcal{O}\rangle_{stat} \equiv \lim_{t\to\infty}\lim_{\mathrm{N}\to\infty}\mathrm{Tr}[\mathcal{O}\rho(t)] = \mathrm{Tr}[\mathcal{O}\rho_{stat}], \tag{3.33}$$

for any generic local observable $\mathcal{O}$, as discussed further below. Accordingly, ρ_{stat} can be formally expressed as

$$\rho_{stat} = S\rho_0 S^{\dagger}, \tag{3.34}$$

where the operator

$$S = \lim_{t\to\infty}\lim_{\mathrm{N}\to\infty}\mathrm{e}^{-iHt}\mathrm{e}^{iH_0 t} \tag{3.35}$$

evolves states to time $t = -\infty$ according to the dynamics of $H_0 = H_l + H_r$ and then brings them back to $t = 0$ with the dynamics prescribed by $H = H_0 + \delta H$. In order to observe the stationary behaviour, measurements have to be performed within the spatial region which has already reached a stationary state, the typical extension of which is given by $v_{max}t$, since excitations propagate ballistically, as we shall see below. As a consequence, the spatial support of the observable $\mathcal{O}$ should include points at a maximal distance ℓ from the junction between the two chains which is much smaller than the distance $v_{max}t$ within which the steady state is established at time t, i.e., $\ell \ll vt \ll N$. Under these conditions, Eq. (3.34) defines the steady state ρ_{stat} which describes the steady average of any operator $\mathcal{O}$ with a finite support. This is pictorially shown in Fig. 3.1.

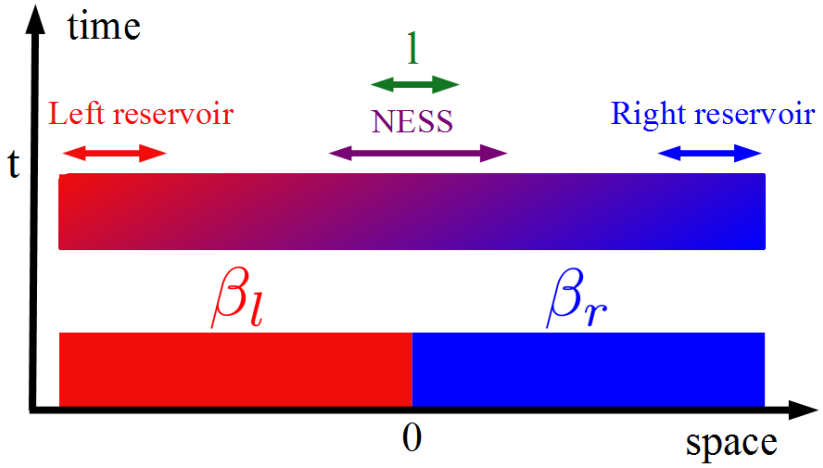

FIGURE 3.1: Pictorial representation of the partitioning protocol. At time $t = 0$ two identical subsystems at different inverse temperatures β_l, in red, and β_r, in blue, are joined at the point $x = 0$. At a later time t, the initial step at $t = 0$ is smeared out and a smoothly varying profile of energy current and density develops. The NESS extends from the junction at $x = 0$ with a width $v_{max}t$ (represented in purple in the figure). The mean value of any local observable having a support l (represented in green in the figure) within the NESS relaxes to the stationary value in Eq. (3.33). As time elapses the spatial extension of the NESS increases, determining a light-cone propagation as in Fig. 1.9. Provided that $N \gg vt$ the two regions asymptotically on the left and on the right are not affected by the dynamics and they act as effective thermal reservoirs for the rest of the system.

In particular, for the partitioning protocol initial state in Eq. (3.1), it is well-known [142–146, 148] (see also the references cited in Subsec. 1.4.2) that the stationary density matrix ρ_{stat} eventually takes the form

$$\rho_{stat} = \frac{1}{Z} e^{-\beta_r H_L} \otimes e^{-\beta_l H_R} = \frac{1}{Z} e^{-(\beta_r+\beta_l)H/2} \otimes e^{-(\beta_l-\beta_r)P/2}, \tag{3.36}$$

with $H_{L,R}$ given in Eqs. (3.18) and (3.30) for the Ising and the harmonic chain, respectively. In the second equality we have defined the operator $P = H_R - H_L$. Essentially, this tells us that the right- (viz. left-)moving excitations of the Hamiltonian are characterised by the initial temperature of the left (viz. right) chain. ρ_{stat} in Eq.. (3.33) is homogeneous and stationary since it is diagonal in the post-quench mode operators. This implies that the steady state is homogeneous, i.e., that there is no energy density gradient: however, a non-vanishing stationary current $\mathcal{J}^E_{NESS} \neq 0$ is present. As a consequence, one can conclude that transport is ballistic and Fourier law is broken. One can notice that the present discussion about the relaxation of local observables $\mathcal{O}$ in Eq. (3.33) is very similar to the one of Subsecs. 1.3.3 and 1.4.1 for homogeneous quantum quenches. It is then natural to wonder whether ρ_{stat} in Eq. (3.36) can be written in the GGE form of Eq. (1.44). In the conformal field theory limit [142–145], which can be obtained upon setting the transverse field to its critical value $h = 1$ (or $m = 0$ in Eq. (3.26) for the harmonic chain) and expanding around $k = 0$ in Eq. (3.7) $\varepsilon(k) = J|k|$, one realizes that the lattice operator P in Eq. (3.33), see also Ref [146], just reduces to the momentum conserved charge, which is local. Accordingly, for the conformal field

theory, ρ_{stat} can be written as the exponential of local conserved charges as it is the case for the GGE in non interacting models, see Subsec. 1.4.1. In non-critical systems, instead, ρ_{stat} in Eq. (3.33) is constructed in terms of the post-quench mode operators, $n(k) = \Psi_R^\dagger(k)\Psi_R(k)$ for the Ising chain and $n(k) = \mathbb{A}^\dagger(k)\mathbb{A}(k)$ for the harmonic chain, which are neither local nor extensive. Note, however, that in principle this is still consistent with the GGE in homogeneous quantum quenches in non-interacting models, where the GGE can be, indeed, equivalently written in terms of the mode operators as the latter are linearly related to the local conserved charges, see, e.g., Ref. [57]. In the case of the inhomogeneous initial partitioning protocol state, however, it has been shown in Ref. [148] for the free Klein-Gordon field theory, that the steady state ρ_{stat}, which has a form identical to Eq. (3.36), cannot be recast in terms of local conserved charges only. As a consequence, one has that ρ_{stat} in Eq. (3.36) has not the same local structure of the GGE as, instead, in the conformal field theory limit. The lack of locality of ρ_{stat} in free systems not at criticality has consequences on the large distance decay of correlation functions in the steady state. Indeed, it has been proved in Ref. [148] that the correlation functions of some operators display an algebraic decay at large distances, in contrast with the exponential decay that applies to correlation functions in the conformal field theory case [142–144].

3.3 Mean values of transport quantities in the hydrodynamic limit

In Subsec. 3.3.1 we introduce the energy current and density operators, which are the observables charaterizing the energy transport in the partitioning protocol. The hydrodynamic scaling limit of these quantities is then defined. In Subsec. 3.3.2 we specialize the discussion to the quantum Ising chain, corresponding to fermionic quasi-particles, while in Subsec. 3.3.3 we focus on the harmonic chain, corresponding to bosonic excitations.

3.3.1 The hydrodynamic limit

The quantities related to transport which we focus on in this Chapter are the energy density u_x and current j_x^E at a point x of the chain. The former is defined from the Hamiltonian of the complete chain such that

$$H = \sum_{x=-N+1}^{N} u_x. \tag{3.37}$$

The latter, instead, is defined such that

$$\frac{du_x(t)}{dt} = i[H, u_x(t)] = j_x^E - j_{x+1}^E, \tag{3.38}$$

which is the continuity equation written at the operatorial level: the time derivative of the energy density u_x equals the opposite of the discrete divergence of the energy current. This relationship ensures that the total energy H in Eq. (3.37) is

conserved in time. We emphasize here that both u_x and j^E_x are local operators, in the sense that they act non-trivially only on a finite number of sites around x. The mean values we are interested in are generically defined as

$$O(x,t) = \mathrm{Tr}[\rho_0\, o_x(t)], \tag{3.39}$$

where $o_x(t)$ is a local observable, e.g., u_x or j^E_x, at site x and evolved up to time t and ρ_0 is the partitioning protocol initial density matrix in Eq. (3.1). Note that ρ_0 is neither stationary, i.e., invariant under time evolution with the post-quench Hamiltonian H, nor homogenous, i.e., invariant under space translations according to Eqs. (3.12) or (3.29). As a consequence, $O(x,t)$ displays a non-trivial space and time dependence. In the present work we are interested in studying the dynamics of $O(x,t)$ in the so-called hydrodynamic limit [149–158] (also dubbed in the literature space-time scaling or semi-classical limit), where both x and t are much larger than the corresponding microscopic scales, with a fixed and finite ratio $v = x/t$. In formulas, the hydrodynamic limit $\mathcal{O}$ of the quantity O is defined as

$$\mathcal{O}(v) = \lim_{\substack{x,t\to\infty \\ v=x/t}} \lim_{N\to\infty} O(x,t) = \mathrm{Tr}[\rho(v)\, o_{x=0}(0)], \tag{3.40}$$

where, exploiting the definition of the translation operator in Eqs. (3.12) or (3.29) we defined

$$\rho(v) = \lim_{\substack{x,t\to\infty \\ v=x/t}} \lim_{N\to\infty} (P^\dagger_{tr})^x \mathrm{e}^{-iHt} \rho_0 \mathrm{e}^{iHt} (P_{tr})^x. \tag{3.41}$$

Accordingly, the state $\rho(v)$ fully describes the hydrodynamic limit of any local observable $o_x(t)$.

A complementary approach to Eqs. (3.40) and (3.41) for computing the hydrodynamic limit $\mathcal{O}$ consists in determining first the large space-time scaling of the operator $o(x,t)$, similarly to Eq. (3.41), and then in taking the trace over the initial density matrix ρ_0 according to Eq. (3.39). This scheme has been pursued in Refs. [1, 157] in order to compute the space-time scaling limit $\mathcal{U}(v)$, $\mathcal{J}^E(v)$ of the energy density u_x and current j^E_x, respectively. Compared to the latter, the advantage of the approach of Eqs. (3.40) and (3.41) is that, once the state $\rho(v)$ is known, the hydrodynamic limit of any local observable, not only of u_x and j^E_x, can be readily obtained from Eq. (3.40). Furthermore, the knowledge of $\rho(v)$ is fundamental for the calculation of the transferred energy scaled cumulant generating function, as shown in Section 3.5. Accordingly, in this Chapter we will proceed following Eqs. (3.40) and (3.41), as done in Ref. [4], while the calculations presented in Ref. [1] will not be discussed for the sake of brevity.

As we shall see explicitly, see Eq. (3.46) for the transverse field Ising chain and Eq. (3.61) below for the harmonic chain, the state $\rho(v)$ depends on an homogeneous and stationary combination of the post-quench mode operators $\Psi_R(k)$ and $\mathbb{A}(k)$, being the dependence on v brought in only by the coefficients. The existence of the limit in Eq. (3.40) can be considered as a consequence, in the present context, of the so-called "local entropy maximization principle" [155, 159, 162] (see also Subsec. 4.1.2 in Chapter 4), which asserts that averages of local observables $o_x(t)$ over a state ρ_0, generically inhomogenous and non-stationary, can be replaced by

averages of the same observable over the local equilibrium — and therefore homogeneous and stationary — state $\rho(x,t)$ at point x and time t. Note that, while ρ_0 characterizes *globally* the state of the system, $\rho(x,t)$ applies only *locally* at the space-time point (x,t) for the calculation of the average of local observables $o_x(t)$. Other quantities, such as the dynamical two-point functions, where the observables involve different space-time points, cannot be computed solely on the basis of the local equilibrium state $\rho(x,t)$, as we shall discuss in detail in Sec. 4.2 of Chapter 4. This principle is at the basis of the so-called generalized hydrodynamics description of interacting integrable systems out of equilibrium [159, 162], which will be discussed in Chapter 4. In Eqs. (3.40) and (3.41) we are actually anticipating, cf., Eq. (3.46) for the transverse field Ising chain and Eq. (3.61) for the harmonic chain, that in the present case of a dynamics starting from the initial state ρ_0 in Eq. (3.1), the evolved state $\rho(x,t)$ is a scaling function of $v = x/t$. The long-time limit $t \to \infty$ with x fixed and therefore $v \to 0$ corresponds, in particular, to the stationary limit $\rho(v=0) \equiv \rho_{stat}$ discussed in Sec. 3.2.

3.3.2 Energy transport in the quantum Ising chain

For the Ising chain we denote the energy density operator at site x as u_x, which from Eqs. (3.2) and (3.37) takes the form

$$u_x = -\frac{J}{4}[\sigma^x_x\sigma^x_{x+1} + \sigma^x_{x-1}\sigma^x_x] - \frac{Jh}{2}\sigma^z_x, \tag{3.42}$$

while the energy current j^E_x consequently follows from Eq. (3.38), i.e.,

$$j^E_x = \frac{J^2h}{4}(\sigma^x_x\sigma^y_{x+1} - \sigma^y_x\sigma^x_{x+1}) = \frac{ihJ^2}{2}(c^\dagger_{x+1}c_x - c^\dagger_x c_{x+1}), \tag{3.43}$$

where in the last step we used the Jordan-Wigner transformation in Eq. (3.3) to write the energy current in terms of the lattice fermionic operators. In order to compute the hydrodynamic limit of the aforementioned quantities according to Eq. (3.40) one first needs to construct the state $\rho(v)$ in Eq. (3.41). To do this we write the initial state ρ_0 in Eq. (3.1), with $H_{r,l}$ expressed in terms of the pre-quench modes $\Phi_{r,l}(k)$ according to Eq. (3.10), as a function of the post-quench modes $\Psi_R(k)$ by means of the transformation

$$\Phi_\alpha(k) = \int_{-\pi}^{\pi} dk' [\Psi_R(k')\, m^*_{+,\alpha}(k',k) + \Psi^\dagger_R(k')\, m_{-,\alpha}(k',k)], \tag{3.44}$$

with $\alpha \in \{r,l\}$; the expressions for the coefficients $m^*_{\pm,\alpha}(k',k)$ are provided in Appendix 3.A (see Eqs. (3.133) and (3.134)). In terms of the post-quench operators, using Eq. (3.13) and, remembering that under the post-quench Hamiltonian H the time evolution is trivial $e^{-iHt}\Psi_R(k)e^{iHt} = e^{i\varepsilon(k)t}\Psi_R(k)$, the space and time propagation $\rho(x,t)$ of the state ρ according to Eq. (3.41) can be determined explicitly. As detailed in Appendix 3.B, the leading space-time dependence of $\rho(x,t)$ in the

semi-classical limit of Eq. (3.41) turns out to be

$$\rho(x,t) = \frac{1}{Z}\exp\left\{-\int_{-\pi}^{\pi} dk'dk'' \Psi_R^\dagger(k')\Psi_R(k'')e^{i\varphi^+_{x,t}(k',k'')} \times \left[\beta_r I^r_{+,+}(k',k'') + \beta_l I^l_{+,+}(k',k'')\right]\right\}, \tag{3.45}$$

where the expressions of $\varphi^+_{x,t}(k',k'')$ and $I^{r,l}_{+,+}(k',k'')$ are reported in Appendix 3.B (see Eqs. (3.143) and (3.148)). The expression in Eq. (3.45) can be further simplified as $x,t \to \infty$ with fixed ratio $v = x/t$, by performing a stationary phase approximation [153] as done in Ref. [4] (in this thesis we briefly report some details in Appendix 3.B). In this limit the integral in Eq. (3.45) is determined by the values of k' and k'' within the integration domains at which the phase $\varphi^+_{x,t}(k',k'')$ in the exponential is stationary and by the possible singularities of $I^{r,l}_{+,+}(k',k'')$. Since $\varphi^+_{x,t}(k',k'')$ turns out to be stationary for $k' = k''$, the integral is then determined by the behaviour of $I^{r,l}_{+,+}(k',k'')$ for $k' \simeq k''$. Accordingly, it is convenient to introduce the variables $Q = k' - k''$ and $K = (k' + k'')/2$ and to consider the integrand in Eq. (3.45) for $Q \simeq 0$ following the procedure highlighted in Ref. [153]. Expanding the phase $\varphi^+_{x,t}$ up to first order in Q and K, the procedure turns out to be completely analogous to the one performed in Refs. [1, 157] and it leads to the result [4]

$$\rho(v) = \frac{1}{Z}\exp\left\{-\int_{-\pi}^{\pi} dk\, \beta(v,k)\varepsilon(k)\Psi_R^\dagger(k)\Psi_R(k)\right\}, \quad \text{where} \quad \beta(v,k) = \beta_r\Theta(v - v_g(k)) + \beta_l\Theta(v_g(k) - v), \tag{3.46}$$

where $v_g(k) = d\varepsilon(k)/dk$ is the group velocity of the quasi-particles excitations with energy $\varepsilon(k)$ (see Eq. (3.7)) and $\Theta(x) = 1$ if $x > 0$ and 0 otherwise, being the Heaviside step function. Since $\rho(v)$ is diagonal in terms of the post-quench mode operators $\Psi_R(k)$, and the dependence on v is brought in only by the coefficients $\beta(v,k)$, it is effectively stationary and homogeneous, as anticipated in the discussion in Sec. 3.3. One can also notice that $\rho(v)$ is indeed a function of the scaling variable $v = x/t$ as the entire space-time dependence is encoded within the Heaviside function. Moreover, in the stationary limit $v = 0$, it agrees with the known general expression of the non-equilibrium steady state density matrix of Eq. (3.36). The expression of $\rho(v)$ in Eq. (3.46) generalizes the known result for the stationary state ρ_{stat}, thereby accounting for the whole dynamics of any local observable along a ray in the space-time plane with fixed $v = x/t$. Moreover, in the stationary limit $v = 0$, it agrees with the known general expression of the non-equilibrium steady-state density matrix of Eq. (3.36). The expression of $\rho(v)$ in Eq. (3.46) generalizes the known result for the stationary state ρ_{stat}, thereby accounting for the whole dynamics of any local observable $o_x(t)$ along a ray in the space-time plane with fixed $v = x/t$. Outside the light cone, for $v > v_{max}$ ($v < -v_{max}$), $\rho(v)$ depends only on β_r (β_l), as expected. It is, however, important to emphasize that $\rho(v)$ in Eq. (3.46) does not reduce to ρ_0 outside the light cone ($|v| > v_{max}$). This is related to the fact that $\rho(v)$ is defined only locally at the space-time point (x,t), as emphasized above in Subsec. 3.3. This implies that $\rho(v)$

can be used for the calculation, in the hydrodynamic limit, of averages of local observables $\mathcal{O}(v)$ at the space-time point (x,t) according to Eq. (3.40). For $|v| > v_{max}$ the average $\mathcal{O}(v)$ reduces to the corresponding average over the initial state ρ_0 in Eq. (3.1) of the right or left chain. This can be explicitly checked in Eq. (3.49) (and Eq. (3.64) for the harmonic chain) for the energy current and density.

It is immediate to calculate the average over $\rho(v)$ of any fermionic bilinear function of the post-quench operators $\Psi_R^\dagger(k)\Psi_R(k')$, taking into account that

$$\mathrm{Tr}[\rho(v)\Psi_R^\dagger(k)\Psi_R(k')] = \delta(k-k')n^+(v,k), \tag{3.47}$$

where we introduced

$$n^+(v,k) = f^+_{\beta_r}(k)\Theta(v-v_g(k)) + f^+_{\beta_l}(k)\Theta(v_g(k)-v) \tag{3.48}$$

and $f^+_\beta(k) = 1/(\mathrm{e}^{\beta\varepsilon(k)}+1)$ denotes the Fermi-Dirac distribution at inverse temperature β. The physical meaning of $n^+(v,k)$ is simple: the state $\rho(v)$ is determined by ballistically propagating quasi-particles capable of crossing the ray in the space-time diagram with fixed $v = x/t$: for the right half chain ($x > 0$) this requires $v > v_g(k)$ while for the left one (with $x < 0$) $v_g(k) > v$. Since these quasi-particles do not experience scattering, they maintain their initial thermal distribution $f^+_{\beta_r}(k)$ for the right chain and $f^+_{\beta_l}(k)$ for the left, from which Eq. (3.48) follows. As we shall see in Chapter 5, Eq. (3.48) represents the solution for a free theory of the generalized hydrodynamics equation [159, 162] for the mode occupation $n^+(v,k)$ with the initial state of Eq. (3.1).

Accordingly, concerning the calculation of mean values, the knowledge of $\rho(v)$ allows one to determine not only the space-time scaling limit of the transport quantities introduced in Sec. 3.3, but, more generally, the hydrodynamic limit $\mathcal{O}(x,t)$ of any local observable $o_x(t)$, as dictated by Eq. (3.40). In practice, one should simply write the latter in terms of the post-quench mode operators $\Psi_R(k)$ and then use Eqs. (3.47) and (3.48). Specializing to the energy current $j^E_{x=0}$ in Eq. (3.48) and the energy density $u_{x=0}$ in Eq. (3.42), the results for the corresponding mean values $\mathcal{J}^E$ and $\mathcal{U}$ are [1, 4, 157]:

$$\mathcal{J}^E(v) = \int_{-\pi}^{\pi}\frac{dk}{2\pi}\varepsilon(k)v_g(k)n^+(v,k); \quad \mathcal{U}(v) = \int_{-\pi}^{\pi}\frac{dk}{2\pi}\varepsilon(k)n^+(v,k), \tag{3.49}$$

which can be easily shown to satisfy the continuity equation

$$\frac{\partial\mathcal{U}(x,t)}{\partial t} = -\frac{\partial\mathcal{J}^E(x,t)}{\partial x}. \tag{3.50}$$

The energy current $\mathcal{J}^E(v)$ is plotted in Fig. 3.3(a) as a function of v for $\beta_l = 2$ and $\beta_r = 5$. The profile of the current turns out to be an even function of v, i.e., $\mathcal{J}^E(v) = \mathcal{J}^E(-v)$, as it is clearly shown by the figure and by a careful inspection of Eq. (3.49). In addition, Fig. 3.2(a) shows that, because of causality and the finite maximum value v_{max} of the propagation velocity $v_g(k)$ of the excitations, there is always a region in space within which the initial state is not perturbed and, correspondingly, $\mathcal{J}^E$ vanishes. This determines a propagation of the current in

space and time in a light-cone fashion, as anticipated in Subsec. 1.4.2 (see Fig. 1.9). The edge v_{max} of the profile of $\mathcal{J}^E(v)$ for the transverse field Ising chain, is given by

$$v_{max} = J \min(h, 1) = \frac{\varepsilon_{max} - \varepsilon_{min}}{2}, \tag{3.51}$$

where we identified the maximum $\varepsilon_{max} = J(h+1)$ and the minimum $\varepsilon_{min} = J|h-1|$ of the dispersion relation $\varepsilon(k)$ in Eq. (3.7). The physical interpretation of Eq. (3.49) is clear in terms of quasi-particles produced in the initial thermal state with statistics $f^+_{\beta_l}$ and $f^+_{\beta_r}$ for the left and right chain, respectively; these excitations propagate ballistically with velocity $v_g(k)$ without experiencing scattering since the model is non-interacting and translationally invariant, and they contribute with $\varepsilon(k)v_g(k)dk$ to the flux of energy. This picture has been first proposed in Refs. [318–321] to study low-temperature correlation functions. Based on this picture, Eq. (3.49) could have been derived without the explicit calculations reported above. In fact, consider the space-time diagram in Fig. 3.2(b): the excitations with wavevector $k > 0$ produced uniformly along the chain at time $t = 0$ travel ballistically with velocity $\pm v_g(k)$ for $t > 0$ and, in particular, those with statistics $f_{\beta_r}(k)$ (blue rays in Fig. 3.2(b)) [viz. $f_{\beta_l}(k)$ (red rays)] originating from $x > 0$ [viz. $x < 0$] also propagate into the complementary part of the chain. As a result, the flux of energy (i.e., the energy current) produced by each of these modes at a point with coordinate x (e.g., $x = 1$ in Fig. 3.2(b), corresponding to the green vertical world line) vanishes for $|v_g(k)|t < |x|$ because the flux of energy carried by the particles with wavevector $+k$ cancels out the one of particles with wavevector $-k$ moving in the opposite direction and having the same statistics. This cancellation no longer occurs for $|v_g(k)|t > |x|$ because, for $x > 0$, the statistics of the excitations with velocity $-v_g(k)$ crossing the world line of the point x (in green in Fig. 3.2(b)) is given by $f_{\beta_r}(k)$ while that of the excitations with velocity $+v_g(k)$ by $f_{\beta_l}(k)$, as they were originally generated in the left part of the chain, see the sketch in Fig. 3.2(b). As a consequence, for each value of $k \in [0, \pi]$, the contribution to the energy flux is given by $\varepsilon(k)v_g(k)dk \times [f_{\beta_l}(k) - f_{\beta_r}(k)]\Theta(v_g(k)t - x)$ for $x > 0$ and $\varepsilon(k)v_g(k)dk \times [f_{\beta_l}(k) - f_{\beta_r}(k)]\Theta(v_g(k)t + x)$ for $x < 0$, which is equivalent to the integrand of Eq. (3.49). The integral over k in Eq. (3.49) can be calculated in analytic form, details are reported in Ref. [1], and therefore $\mathcal{J}^E(v)$ can be written in the form

$$\mathcal{J}^E(v) = \Theta(v_{max} - |v|)\,[\mathcal{J}_1(\beta_l, v) - \mathcal{J}_1(\beta_r, v)] \tag{3.52}$$

where

$$\mathcal{J}_1(\beta, v) = \frac{1}{2\pi\beta^2}\left\{G_1(\beta[\varepsilon_>(v) - \varepsilon_<(v)]) - G_1(\beta[\varepsilon_>(v) + \varepsilon_<(v)])\right\}, \tag{3.53}$$

with

$$G_1(x) = -\mathrm{Li}_2(-\mathrm{e}^{-x}) + x\log(1 + \mathrm{e}^{-x}). \tag{3.54}$$

In this equation Li_2 is the polylogarithm of order 2 while $\varepsilon_>(v) = \sqrt{[J\max(1,h)]^2 - v^2}$, and $\varepsilon_<(v)$ has the same expression as $\varepsilon_>$ but with max replaced by min, such that (see Eq. (3.51)) $\varepsilon_<(v) = \sqrt{v^2_{max} - v^2}$. Since $\varepsilon_{\gtrless}(v)$ and therefore $\mathcal{J}_E(v)$ depends only on v^2, the energy current in Eq. (3.52) is confirmed

to be an even function of v, as anticipated above. For $v = 0$, Eq. (3.52) reduces to the steady-state energy current $\mathcal{J}^E_{NESS}$, which has been first computed in Ref. [146]. Figure 3.2 clearly shows that $\mathcal{J}^E(v)$, upon approaching the val-

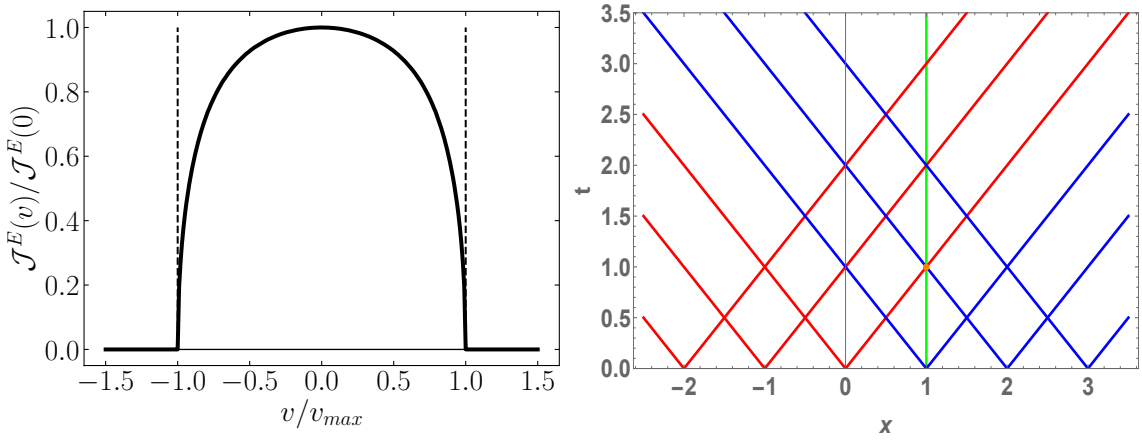

(a) (b)

FIGURE 3.2: (a) Dependence of the energy current $\mathcal{J}^E(v)/\mathcal{J}^E(0)$ at time t and point x along the Ising chain on the scaling variable $v \equiv x/t$, within the hydrodynamic scaling limit. The parameters of the chain are $h = 1.6$ and $J = 1$, with the left part $v < 0$ initially thermalised at $\beta_l = 2$ and the right part $v > 0$ at $\beta_r = 5$. (b) Space-time diagram in which the coordinate x along the chain and the time $t > 0$ are reported on the horizontal and vertical axis, respectively. Each point of the chain at time $t = 0$ acts as a source of quasiparticles with velocities $\pm v_g(k)$, with $k > 0$, energy $\varepsilon(k)$ and statistics $f_{\beta_l}(k)$ for $x < 0$ (red rays) and $f_{\beta_r}(k)$ for $x > 0$ (blue rays), respectively. These particles propagate ballistically for $t > 0$ and generate an energy current, as discussed in the main text. The green vertical line represents the "world line" of the fixed point $x = 1$ in this space-time diagram. Image adapted from Ref. [1].

ues $\pm v_{max}$ of the variable v which correspond to the edge of the propagating front, displays a non-analytic behaviour, which can be determined on the basis of Eqs. (3.52) and (3.53). In particular, for $v \to \pm v^{\mp}_{max}$ one finds, at the leading order,

$$\mathcal{J}^E(v) = C_1 \left(v^2_{max} - v^2\right)^{1/2} + \mathcal{O}((v_{max} - |v|)^{3/2}), \tag{3.55}$$

where C_1 is given in Appendix 3.B, see Eq. (3.159). Note that $\mathcal{J}^E(v)$ vanishes at the edge according to a semi-circular law, as shown in Fig. 3.2(a), and consistently with what is observed in Ref. [149] for the XX chain evolving from a domain-wall initial state and in Ref. [156] for the transverse field Ising chain in an initial domain-wall state created by the action of a local Jordan-Wigner fermion operator. However, when the transverse field h of the Ising chain is poised at its critical value $h_c = 1$, the constant C_1 in Eq. (3.55) vanishes and the approach of $\mathcal{J}^E(v)$ to the edge turns out to change qualitatively (see the discussion in Appendix 3.B after Eq. (3.159)), with

$$\mathcal{J}^E(v) = \frac{\beta_r - \beta_l}{3\pi} \left(v^2_{max} - v^2\right)^{3/2} + \mathcal{O}((v_{max} - |v|)^{5/2}). \tag{3.56}$$

The edge asymptotics of the energy density $\mathcal{U}(v)$ can be worked out similarly starting from Eqs. (3.55), (3.56) in the critical case $h = 1$, and the continuity equation (3.50). For brevity, we do not report here the results, which can be found in Ref. [1].

Based on the knowledge of the mean energy current $\mathcal{J}^E(v)$ it is immediate to determine the total energy transferred across point x in the time interval $[0, t]$, whose definition as an operator is

$$\Delta e(x,t) = \int_0^t ds\, j_x^E(s); \tag{3.57}$$

its mean $\Delta\mathcal{E}(x,t)$, in the hydrodynamic limit, is given by (see Eq. (3.49))

$$\Delta\mathcal{E}(x,t) = t\int_0^\pi \frac{dk}{2\pi}\varepsilon(k)(v_g(k) - |v|)\left[f^+_{\beta_l}(k) - f^+_{\beta_r}(k)\right]\Theta(v_g(k) - |v|). \tag{3.58}$$

Note that, as expected, the transferred energy grows extensively upon increasing time t. This property is fundamental for studying fluctuations of this observable within the large deviation theory, as shown in Sec. 3.5. In concluding this Section, we emphasize that the expression of $\rho(v)$ in Eq. (3.46) derived here will be fundamental for the determination of the fluctuations of the transferred energy in Eq. (3.57) beyond the mean value in Eq. (3.58), as discussed further below in Sec. 3.5.

3.3.3 Energy transport in the quantum harmonic chain

For the harmonic chain, the energy density u_x at lattice site x, from on Eq. (3.19b), is given by

$$u_x = \frac{1}{2}p_x^2 + \frac{1}{2}m^2\phi_x^2 + \frac{1}{4}\omega^2(\phi_{x+1} - \phi_x)^2 + \frac{1}{4}\omega^2(\phi_{x-1} - \phi_x)^2, \tag{3.59}$$

while the energy current j_x^E at site x is consequently defined according to the continuity equation in Eq. (3.38), i.e.,

$$j_x^E = \frac{\omega^2}{2}(\phi_{x-1} - \phi_x)(p_{x-1} + p_x). \tag{3.60}$$

In order to compute the hydrodynamic limit of these observables the procedure to construct the state $\rho(v)$ of Eq. (3.41) is completely analogous to the one presented above for the quantum Ising chain and therefore we report here the final result, leaving all the details of the derivation in Appendix 3.B. In the hydrodynamic limit $x, t \to \infty$ with fixed ratio $v = x/t$, one finds

$$\rho(v) = \frac{1}{Z}\exp\left\{-\int_{-\pi}^{\pi} dk\, \beta(v,k)\Omega(k)\mathbb{A}^\dagger(k)\mathbb{A}(k)\right\}, \tag{3.61}$$

where $\beta(v,k)$ has the same formal expression as in the case of the transverse field Ising chain in Eq. (3.46), but with the group velocity $v_g(k) = d\Omega(k)/dk$ determined by the dispersion relation $\Omega(k)$ in Eq. (3.26). As far as the mean of a bilinear

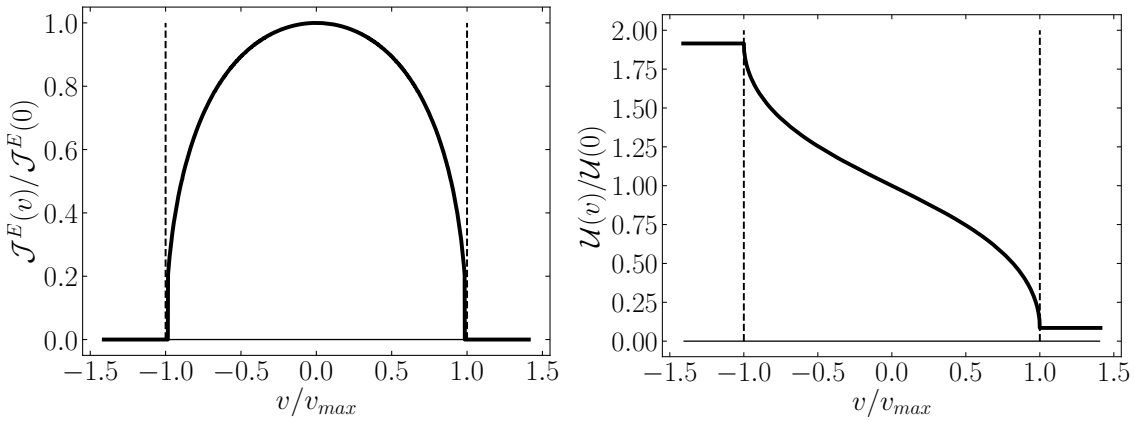

(a) (b)

FIGURE 3.3: Scaling form of (a) the energy current $\mathcal{J}^E(v)/\mathcal{J}^E(0)$ and (b) the energy density $\mathcal{U}(v)/\mathcal{U}(0)$, both have been normalized by the corresponding stationary values in $v = 0$, as functions of v/v_{max} for $\omega = 1$ and $m = 0.7$, resulting in a $v_{max} \simeq 0.71$ according to Eq. (3.65). The inverse temperatures are chosen to be $\beta_l = 2$ and $\beta_r = 5$. Image taken from Ref. [4].

function of the mode operators $\mathbb{A}^\dagger(k)$ and $\mathbb{A}(k')$ is concerned, one finds

$$\mathrm{Tr}[\rho(v)\mathbb{A}^\dagger(k)\mathbb{A}(k')] = \delta(k-k')n^-(v,k), \tag{3.62}$$

where

$$n^-(v,k) = f^-_{\beta_r}(k)\Theta(v - v_g(k)) + f^-_{\beta_l}(k)\Theta(v_g(k) - v), \tag{3.63}$$

and $f^-_\beta(k) = 1/(e^{\beta\Omega(k)} - 1)$ is the Bose-Einstein occupation, with the dispersion relation $\Omega(k)$ of the harmonic chain defined in Eq. (3.26); the important difference between Eqs. (3.61), (3.62), and (3.63) and the corresponding formulas in the fermionic case (see Eqs. (3.46), (3.47), and (3.48)) is the fact that post-quench modes $\mathbb{A}(k)$ have bosonic statistics and therefore they obey canonical commutation relations. This is also signaled by the appearance of $f^-_\beta(k)$ within the mode occupation function $n^-(v,k)$.

The hydrodynamic limit of the mean energy density $\mathcal{U}(v)$ and mean current $\mathcal{J}^E(v)$ then follows as

$$\mathcal{J}^E(v) = \int_{-\pi}^{\pi} \frac{dk}{2\pi}\Omega(k)v_g(k)n^-(v,k); \quad \mathcal{U}(v) = \int_{-\pi}^{\pi} \frac{dk}{2\pi}\Omega(k)n^-(v,k), \tag{3.64}$$

which have precisely the same form as Eq. (3.49). This shows that the form of the profile of $\mathcal{J}^E$ and $\mathcal{U}$ in the hydrodynamic limit is universal to a large extent since the only remaining microscopic ingredients characteristic of the model are the spectrum ($\varepsilon(k)$ in Eq. (3.7) for the quantum Ising chain and $\Omega(k)$ in Eq. (3.26) for the harmonic chain) and the statistics of the involved quasi-particles ($f^+_\beta(k)$ for the fermionic case and $f^-_\beta(k)$ in the bosonic one). $\mathcal{J}^E(v)$ and $\mathcal{U}(v)$ satisfy the continuity equation in Eq. (3.50) as in quantum Ising chain. The curves in Fig. 3.3 are, as expected, qualitatively similar to those corresponding to the same physical

quantities in the quantum Ising chain, see Fig. 3.2(a). The position of the singular edge at $v = v_{max}$ in the profile of $\mathcal{J}^E(v)$ is, however, a model-specific quantity depending on the microscopic parameters of the Hamiltonian in Eq. (3.19) and it is therefore different from Eq. (3.51). In the harmonic chain one has

$$v_{max} = \frac{1}{2}\left(\sqrt{m^2 + 4\omega^2} - m\right) = \frac{1}{2}(\Omega_{max} - \Omega_{min}), \tag{3.65}$$

where $\Omega_{max} = \sqrt{m^2 + 4\omega^2}$ and $\Omega_{min} = m$ are the maximum and the minimum, respectively, of the dispersion relation $\Omega(k)$ in Eq. (3.26). The integral over k in Eq. (3.64) can be calculated analytically, as detailed in Appendix 3.B, leading to

$$\mathcal{J}^E(v) = \Theta(v_{max} - |v|)[\mathcal{Y}(\beta_l, v) - \mathcal{Y}(\beta_r, v)], \tag{3.66}$$

where

$$\mathcal{Y}(\beta, v) = \frac{Y(\beta\Omega_-(v)) - Y(\beta\Omega_+(v))}{2\pi\beta^2}, \tag{3.67}$$

with

$$Y(x) = \mathrm{Li}_2(\mathrm{e}^{-x}) - x\ln(1 - \mathrm{e}^{-x}), \tag{3.68}$$

with $\Omega_\pm(v)$ given in Eqs. (3.153) in Appendix 3.B and they depend only on v^2, implying that $\mathcal{J}^E(v)$ is an even function of v as one realizes from Fig. 3.3. For $v = 0$, Eq. (3.66) reduces to the steady state current supported by the stationary state ρ_{stat} in Eq. (3.33). In this case, the expression in Eq. (3.64) agrees with the result of Ref. [322] for the steady-state energy current flowing in a translationally invariant harmonic chain as in Eq. (3.19), where the mass m and the angular frequency ω are the same at every lattice site. Note that the dispersion relation $\Omega(k)$ in Ref. [322] takes arbitrary real values, while here $\Omega(k) \in (\Omega_{min}, \Omega_{max})$ from Eqs. (3.26) and (3.65). In addition, the system considered in Ref. [322] is open, as the harmonic chain is connected to two external baths at temperatures $T_{l,r}$, which are modeled as an infinite collection of harmonic oscillators. In the present case, instead, with the partitioning protocol, the heat baths are provided by portions of the system itself, so that, as a whole, it evolves unitarily. Our result in Eq. (3.64) therefore shows the independence, in the hydrodynamic limit, of the energy current profile from the actual setting adopted to obtain the non-equilibrium steady state.

Figure 3.3 also shows that, as it happens for the transverse field Ising chain, see Eq. (3.55), the energy current $\mathcal{J}^E(v)$ approaches the edge at $v = v_{max}$ of the propagating front with a non-analytic behavior, which can be determined from Eqs. (3.66), (3.67) and (3.68): for $v \to \pm v_{max}^{\mp}$, it turns out to be identical to Eq. (3.55) with the constant C_1 in this case given in Eq. (3.159) of Appendix 3.B. Interestingly enough, when the mass m is set to zero and thus the spectrum $\Omega(k)$ in Eq. (3.26) becomes gapless, the qualitative form of the edge singularity in Eq. (3.55) is unchanged, with $C_1 = (\beta_l^{-1} - \beta_r^{-1})/\pi$. This is in stark contrast with the case of the quantum Ising chain in Eq. (3.56) for a critical transverse field $h = 1$.

The hydrodynamic limit of the total energy $\Delta e(x, t)$ flowing through point x, defined in Eq. (3.57), takes a form analogous to Eq. (3.58), i.e.,

$$\Delta\mathcal{E}(x, t) = t\int_0^\pi \frac{dk}{2\pi}\varepsilon(k)(v_g(k) - |v|)\left[f^-_{\beta_l}(k) - f^-_{\beta_r}(k)\right]\Theta(v_g(k) - |v|). \tag{3.69}$$

Accordingly, as far as the mean value of the transferred energy $\Delta\mathcal{E}(x,t)$ is concerned, a free bosonic theory is actually very similar to a free fermionic theory. In Sec. 3.5, however, we will show that the full counting statistics of the operator $\Delta e(x,t)$ — which takes into account also higher-order cumulants — strongly differs in the two cases.

3.4 Sub-diffusive behavior near the edge of the propagating front

Close to the edges $|v| \simeq v_{max}$, it has been shown in free fermionic systems [153, 154, 323] that the propagating front exhibits a finer structure within a distance Δx from the edge $x \simeq \pm v_{max} t$ which scales as $\Delta x \sim t^{1/3}$. This behavior is classified as sub-diffusive, as it grows slower than the typical diffusive scaling $\Delta x \sim t^{1/2}$. Note that in non-interacting systems, such as those considered here, diffusion does not occur, as shown in Refs. [324, 325]. The leading correction to the hydrodynamic scaling is therefore sub-diffusive with a relative width $\Delta x/x \sim t^{-2/3}$, which vanishes in the limit $t \to \infty$. These features are therefore not captured by the previous analysis and they require a separate treatment. In particular, this behavior has been shown to be described by a universal function, the Airy kernel [326]. In the following Subsection we study the emergence of the Airy kernel both in the Ising and in the harmonic chain.

3.4.1 Sub-diffusive corrections to the energy current

As discussed after Eq. (3.45) and in Appendix 3.B, the space-time scaling limit is conveniently studied by performing the change of variable $Q = k' - k''$ and $K = (k' + k'')/2$ and after expanding around $Q = 0$ up to first order in Q: this renders Eqs. (3.49) and (3.64) discussed in the previous Section. Here, instead, we are interested in the behaviour of this quantity near the edge of the propagating front, corresponding to having $|x| \simeq v_{max} t$: in this case, higher-order corrections in the expansion of the phase $\varphi^{+}_{x,t}(k',k'')$ around the stationary point become important and therefore they have to be accounted for. Namely, as $v \equiv x/t$ approaches $\pm v_{max}$, the two solutions $k_{\pm}(v)$ of the stationary phase equation (see Eq. (3.146) in Appendix 3.B for details)

$$v_g(k_{\pm}(v)) = |v| \tag{3.70}$$

merge into a unique stationary point $k_s = k_{\pm}(v_{max})$ obtained by taking $v = v_{max}$ into Eq. (3.146), at which the second partial derivatives of the phase $\varphi^{+}_{x,t}(k',k'')$ with respect to k' and k'' vanish. Accordingly, one expects non-trivial corrections due to higher-order terms in the expansion of $\varphi^{+}_{x,t}(k',k'')$ around the stationary

point k_s. In particular, the third-order correction is expected to provide the dominant contribution and, accordingly, the phase is expanded as

$$\varphi^{+}_{x,t}(k',k'') = (k'-k_s)(x-v_{max}t) + \frac{(k'-k_s)^3}{3!}v_{max}t \\ + (v_{max}t-x)(k''-k_s) - \frac{(k''-k_s)^3}{3!}v_{max}t + \mathcal{O}((k'-k_s)^4), \tag{3.71}$$

where we used the fact that $\varepsilon'''(k_s) = -v_{max}$ and $\varepsilon''(k_s) = 0$. Exploiting Eq. (3.71) and introducing the scaling variable X (the derivation is presented in Appendix 3.C)

$$X = (x - v_{max}t)\left(\frac{2}{v_{max}t}\right)^{1/3}, \tag{3.72}$$

the behavior of the energy current at the right edge $x \simeq v_{max}t$ is found to be

$$\mathcal{J}^E(X,t) = \varepsilon(k_s)v_{max}\left[n_l(X,t) - n_r(X,t)\right], \tag{3.73}$$

with

$$n_{l,r}(X,t) = \left(\frac{2}{v_{max}t}\right)^{1/3} f^{+}_{\beta_{l,r}}(k_s)K^A(X,X), \tag{3.74}$$

and $K^A(X,X)$ is the celebrated Airy kernel [326], defined as

$$K^A(X,X) = \left[\mathrm{Ai}'(X)\right]^2 - X\left[\mathrm{Ai}(X)\right]^2, \tag{3.75}$$

where $\mathrm{Ai}(X)$ is the Airy function. The same formula applies to the left edge $x \simeq -v_{max}t$ with x replaced by $-x$ in Eq. (3.72). It is important to stress that the appearance of the Airy kernel relies both from the fact that the two solutions of Eq. (3.70) merge near the edge of the light-cone into a unique saddle point k_s, where the second derivative of the dispersion relation vanishes $\varepsilon''(k_s) = 0$, and from the fact that the integrand in Eq. (3.160) (see Appendix 3.C) is singular when $k' = k''$. Since in the harmonic chain the dispersion relation $\Omega(k)$ in Eq. (3.26) has the same structure as $\varepsilon(k)$ in Eq. (3.7), the derivation just outlined applies also to the bosonic case. In particular, the sub-diffusive corrections to the energy current in Eq. (3.64) are still described by the Airy kernel, as per Eqs. (3.73), (3.74) and (3.75) upon replacing $\varepsilon(k_s) \leftrightarrows \Omega(k_s)$, $f^{+}_{\beta_{l,r}} \leftrightarrows f^{-}_{\beta_{l,r}}$, with v_{max} in Eq. (3.65). This kernel emerges rather generically in the literature concerning free spinless fermionic chains [153, 323], where it has been reported for the case of an initial state consisting of a fully occupied half chain and for a more general initial factorized Fermi sea state [154]. Equation (3.73) shows that the leading effect of an initial state with two different (finite) temperatures β_l^{-1} and β_r^{-1} is the presence of the corresponding distributions $f^{\pm}_{\beta_{l,r}}(k_s)$ as a multiplicative factor of the Airy scaling function. In passing we mention that the Airy kernel and a generalization of it emerge at the spatial edge of a system at zero and finite temperature, respectively, also in the case of a one-dimensional gas of free fermions confined by an harmonic potential [327–329]. However, in this case, the edge does not expand in time but is rather fixed by the presence of the harmonic potential which makes the fermion density

vanish beyond a certain distance from the center of the trap. Close to that edge, the correlation function is expressed as a determinantal process whose kernel can be interpreted as an extension of the Airy one. Our analysis thereby shows that for the dynamical edge of the energy current profile the appearance of the Airy kernel is not only restricted to fermionic spin chains, as in the aforementioned cases, but it carries over to bosonic models as well.

The hydrodynamic limit discussed in Subsecs. 3.3.2 and 3.3.3 — in which $v \equiv x/t \leq v_{max}$ is kept constant as $t \to \infty$ — corresponds to having $X \propto (v - v_{max})t^{2/3} \to -\infty$ here and, in fact, in this limit, Eq. (3.73) renders the behavior of $\mathcal{J}^E(v)$ close to the edge, reported in Eq. (3.55). This can be easily seen by using Eq. (3.159) in Eqs. (3.73) and (3.74) and by taking into account the asymptotic behaviour of the Airy Kernel $K^A(X, X) \to \sqrt{-X}/\pi$ [330]. This is shown in Fig. 3.4(a), where we plot on the vertical axis the rescaled energy current $\mathcal{J}^E(X, t)\,(v_{max}t/2)^{1/3}/(\varepsilon(k_s)v_{max}(f^{\pm}_{\beta_l} - f^{\pm}_{\beta_r}))$ as a function of X in Eq. (3.72) for the ballistic limit in Eq. (3.55), dashed line, and in the sub-diffusive case of Eq. (3.75), solid line. The latter displays a typical staircase structure: for a free fermionic chain starting from a domain-wall initial state this staircase has been interpreted in Ref. [323] by establishing a correspondence between the counting statistics of free fermions and the eigenvalues statistics in random matrix theory.

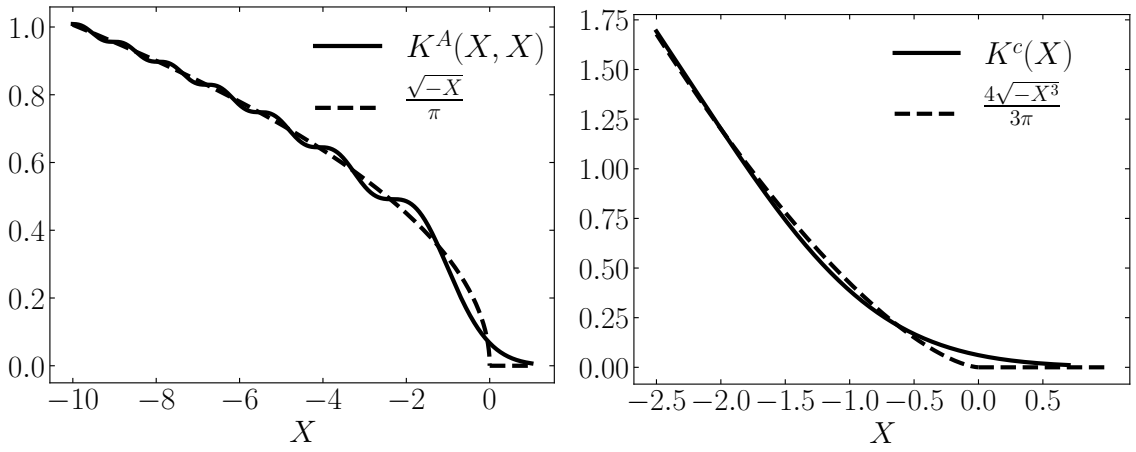

(a) (b)

FIGURE 3.4: (a) On the vertical axis the rescaled energy current $\mathcal{J}^E(X, t)\,(v_{max}t/2)^{1/3}/(\varepsilon(k_s)v_{max}(f^{\pm}_{\beta_l} - f^{\pm}_{\beta_r}))$ is plotted as a function of X. We compare the edge behavior of the energy current in Eq. (3.55) (dashed line) at the ballistic scale and the edge asymptotic in Eqs. (3.73), (3.74), and (3.75) of the same quantity including sub-diffusive corrections (solid line). The dashed line is obtained by expressing Eq. (3.55) as a function of X (see Eq. (3.72)). The solid line is the Airy kernel $K^A(X, X)$ in Eq. (3.75). Sub-diffusive corrections introduce oscillations on top of the ballistic edge profile. These oscillations vanish in the limit $X \to -\infty$ corresponding to the hydrodynamic scaling. (b) Dependence of $K^c(X)$ on the rescaled coordinate X [see Eq. (3.77)] near the edge $X = 0$, for a critical value $h = h_c = 1$ of the transverse field. The parameters are $t = 1$, $J = 1$, $\beta_l = 2$ and $\beta_r = 3$. Image taken from Ref. [1].

As we noted in Subec. 3.3.2, the behavior of the current $\mathcal{J}^E(v)$ for the Ising chain in the space-time scaling limit changes qualitatively when the transverse

field h takes its critical value $h_c = 1$. Accordingly, one expects the edge behavior to be affected as well. In fact, it is straightforward to note that $k_s \to 0$ as $h \to 1$ and, correspondingly, $\varepsilon(k_s) \to 0$ in the same limit, which makes the expression for $\mathcal{J}^E(X,t)$ in Eq. (3.73) vanish identically. In this case, within the stationary-phase approximation adopted here, one has to keep terms up to the first non-vanishing order $\propto 1/t$ in the expansion in k' and k'' around k_s. Proceeding in this way (see Appendix 3.C for details), one finds

$$\mathcal{J}^E(X,t) = \frac{1}{t}\frac{v_{max}^2(\beta_r - \beta_l)}{4} K^c(X) \tag{3.76}$$

where X in Eq. (3.73) (see Eq. (3.72)) is replaced by

$$X = (x - v_{max}t)\left(\frac{8}{v_{max}t}\right)^{1/3}, \tag{3.77}$$

and

$$K^c(X) = \frac{4}{3}\{X^2[\mathrm{Ai}(X)]^2 - \frac{1}{2}\mathrm{Ai}(X)\mathrm{Ai}'(X) - X[\mathrm{Ai}'(X)]^2\}. \tag{3.78}$$

By using the defining property of the Airy function $\mathrm{Ai}''(X) = X\mathrm{Ai}(X)$ one can easily show by differentiating the previous equation that $K^c(X)$ is related to $K^A(X,X)$ in Eq. (3.75) by

$$K^c(X) = 2\int_X^{+\infty} dY\, K^A(Y,Y). \tag{3.79}$$

As in the case $h \neq h_c$ discussed above, Eq. (3.76) renders Eq. (3.56) after taking into account the asymptotic behaviour $K^c(X \to -\infty) \simeq 4\sqrt{-X^3}/(3\pi)$ [330]. Figure 3.4(b) presents a plot of the current $J_E(X,t) \times 4t/[v_{max}^2(\beta_r - \beta_l)]$, i.e., of $K^c(X)$ (solid line) as a function of the scaling variable X, which is compared with the asymptotic behavior for $X \to -\infty$ (dashed line). One immediately notes that for $X > 0$ the critical kernel $K^c(X)$ is qualitatively similar to the non-critical one $K^A(X,X)$ and they both decay exponentially upon increasing X, as can be readily checked from the asymptotics of the Airy kernel [330]. On the contrary, for $X < 0$, the typical staircase structure of the Airy kernel $K^A(X,X)$ shown in Fig. 3.4(a) is absent in the critical case $K^c(X)$ reported in Fig. 3.4(b). Note that the novel kernel $K^c(X)$ is as "universal" as the Airy kernel, as it does not depend on the specific properties of the system under investigation, i.e., J, v_{max}, etc. and, together with the scaling function which involves it, is essentially determined by $\varepsilon'(k_s)$ and $\varepsilon^{(3)}(k_s)$. The latter quantity vanishes within the standard scaling limit in which the actual dispersion relation $\varepsilon(k)$ is replaced, at criticality, by its linear approximation $v_{max}k$. Accordingly, the effective description usually introduced in order to capture the large-distance behavior of a system and which is at the root of the emerging universality of critical phenomena cannot predict the features discussed here.

In the harmonic chain, on the contrary, the edge behavior does not qualitatively change when the mass m is set to zero. From Eq. (3.73), with $\varepsilon(k_s) \to \Omega(k_s)$

and $f^{+}_{\beta_{l,r}} \to f^{-}_{\beta_{l,r}}$, one obtains (details are provided in Appendix 3.C)

$$\mathcal{J}^{E}(X,t) = v_{max}\left(\frac{8}{v_{max}t}\right)^{1/3}\left(\frac{1}{\beta_l}-\frac{1}{\beta_r}\right)K^{A}(X,X) \tag{3.80}$$

with the scaling variable X defined as in Eq. (3.77). $\mathcal{J}^{E}(X)$ is therefore proportional to that corresponding to $m \neq 0$ (see Eq. (3.73)). Accordingly, for free bosonic systems, the edge behavior does not qualitatively change at criticality $m = 0$, in contrast with what happens in free fermionic systems.

The discussion of this Section applies to non-interacting systems where diffusion does not take place, as anticipated in Sec. 3.4, and the leading correction the ballistic hydrodynamic scaling is of sub-diffusive nature. Hence, one could wonder about the robustness of the Airy kernel with respect to the inclusion of interactions. This problem, in the framework of quantum transport arising from the partitioning protocol initial inhomogeneity, has been addressed in Ref. [169], where the XXZ spin chain initialized in two halves with opposite magnetization in the z direction is considered. In particular the findings of Ref. [169] show that in the presence of interactions the edge behavior is captured by a diffusive scaling $X \sim (x - v_{max}t)/t^{1/2}$ and therefore the appearance of the Airy kernel is hindered by the interactions.

3.5 Scaled cumulant generating function and large deviations in the hydrodynamic limit

The analysis of Secs. 3.3 and 3.4 focused on the mean value of the transferred energy operator $\Delta e(x,t)$ in Eq. (3.57) within the hydrodynamic scaling limit. However, to get information about fluctuations beyond mean values, one needs to study higher-order cumulants of this quantity. This is conveniently done by defining the scaled cumulant generating function $G(\lambda, v)$ at the hydrodynamic scale with $x, t \to \infty$ and fixed $v = x/t$. For the transferred energy $\Delta e(x,t)$ this function reads:

$$G(\lambda, v) \equiv \lim_{\substack{x,t\to\infty \\ v=x/t}} \frac{1}{t}\ln \mathrm{Tr}[\rho_0 \exp(-\lambda \Delta e(x,t))], \tag{3.81}$$

where we are anticipating the fact that $G(\lambda, v)$ depends on x and t only via the scaling variable v. Note that the operator $\Delta e(x,t)$, differently from the energy current j^{E}_{x} and the density u_x and according to its very definition in Eq. (3.57), is not local and therefore the average over ρ in Eq. (3.81) cannot be taken directly as in Eq. (3.40). Moreover, the trace in Eq. (3.81) is taken with respect to the initial density matrix ρ_0 in Eq. (3.1) which is, as already stated in Sec. 3.3, non-stationary and inhomogeneous. This causes $G(\lambda, v)$ to have a non-trivial dependence on v.

As noticed after Eq. (3.58), $\Delta\mathcal{E}(x,t)$ grows extensively upon increasing the time t and it is therefore convenient to focus on the intensive quantity $J_E = \Delta e(x,t)/t$. According to the large deviation principle, see Secs. 1.2 and 1.4.2,. the probability density function $p(J_E, v)$ for $t \to \infty$ peaks exponentially around the mean value

$\langle J_E \rangle = \Delta\mathcal{E}(x,t)/t$ as

$$p(J_E, v) \asymp \exp[-tI(J_E, v)], \tag{3.82}$$

where $I(J_E, v)$ is the rate function, which is related to $G(\lambda, v)$ via the Legendre-Fenchel transform in Eq. (1.15), i.e., as

$$I(J_E, v) = \sup_{\lambda} \left[-\lambda J_E - G(\lambda, v)\right]. \tag{3.83}$$

The Legendre duality relations in Eq. (1.16) implies

$$\frac{\partial G(\lambda, v)}{\partial \lambda} = -J_E; \quad \text{and} \quad \frac{\partial I(J_E, v)}{\partial J_E} = -\lambda. \tag{3.84}$$

To our knowledge, all the available predictions for the scaled cumulant generating function of the transferred energy $\Delta e(x,t)$ are obtained by computing the trace in Eq. (3.81) over the stationary density matrix ρ_{stat} in Eq. (3.33), i.e.,

$$G(\lambda) = \lim_{t\to\infty} \frac{1}{t} \ln \mathrm{Tr}[\rho_{stat} \exp(-\lambda \Delta e(x,t))]; \tag{3.85}$$

since ρ_{stat} is homogeneous and stationary $G(\lambda)$ does not depend, in this case, on space or time. In particular, for free-fermions models, $G(\lambda)$ can be determined via the celebrated Levitov and Lesovik formula [331–338], which, with the notation of this thesis, reads

$$G(\lambda) = \int_{\varepsilon_{min}}^{\varepsilon_{max}} \frac{d\varepsilon}{2\pi} \ln \Big\{ 1 + T(\varepsilon)[(\mathrm{e}^{-\lambda\varepsilon} - 1) f^+_{\beta_l}(\varepsilon)(1 - f^+_{\beta_r}(\varepsilon)) + (\mathrm{e}^{\lambda\varepsilon} - 1) f^+_{\beta_r}(\varepsilon)(1 - f^+_{\beta_l}(\varepsilon))] \Big\}, \tag{3.86}$$

where ε_{min} and ε_{max} have been defined after Eq. (3.51) for the Ising chain, and $T(\varepsilon)$ denotes the transmission probability of a particle from the left to the right chain and vice versa. In a similar way, $G(\lambda)$ can be computed for a free bosonic theory [322] and its analytic expression, obtained via the Keldysh formalism, turns out to have a structure similar to that of Eq. (3.86):

$$G(\lambda) = -\int_{\Omega_{min}}^{\Omega_{max}} \frac{d\Omega}{4\pi} \ln \Big\{ 1 + T(\Omega)[(\mathrm{e}^{-\lambda\Omega} - 1) \times f^-_{\beta_l}(\Omega) f^-_{\beta_r}(-\Omega) + (\mathrm{e}^{\lambda\Omega} - 1) f^-_{\beta_r}(\Omega) f^-_{\beta_l}(-\Omega)] \Big\}, \tag{3.87}$$

with Ω_{min} and Ω_{max} given in Eq. (3.65) for the harmonic chain. Remarkably, a recent expression of $G(\lambda)$ for interacting integrable models in homogenous stationary states has been found in Refs. [339, 340] on the basis of generalized hydrodynamics techniques (see Subsec. 4.3.2 in Chapter 4 for details about this result). This formula is valid for homogeneous and stationary GGEs, which include the non-equilibrium steady states of the form in Eq. (3.33) obtained from the partitioning protocol and, in fact, it renders Eqs. (3.86) and (3.87) when specialized to free fermions and bosons, respectively.

In spite of this important progress, no analytical result is available for the SCGF

of the transferred energy $\Delta e(x,t)$ for inhomogeneous states ρ_0, both in the case of non-interacting systems and of interacting integrable models. Aiming at filling this gap, we therefore begin in this Chapter by presenting in Subsec. 3.5.1 the exact calculation of the SCGF $G(\lambda, v)$ at the hydrodynamic scale in Eq. (3.81) for non-interacting models. In Subsec. 3.5.2 a simple semi-classical interpretation of these results is provided. In Subsecs. 3.5.3 and 3.5.3 the general result of Subsec. 3.5.1 is eventually specialized for the transverse field Ising chain, and the harmonic chain, respectively. The more complex case of interacting integrable systems will be addressed in Chapter 4, where an analytical formula for $G(\lambda, v)$ valid for this class of models, which extends the findings of Subsec. 3.5.1 will be derived.

3.5.1 Derivation of the SCGF in the hydrodynamic limit

The derivation of the scaled cumulant generating function presented here is similar to that of $G(\lambda)$ in Eq. (3.85) done in conformal field theory [142–144], on the lattice for the transverse field Ising chain [146], and, more recently, for interacting integrable models [339, 340] (see Subsec. 4.3.2 in Chapter 4 for more details about the latter case). In order to determine $G(\lambda, v)$ we start by taking the derivative with respect to λ of Eq. (3.81), i.e.,

$$-\frac{\partial G(\lambda,v)}{\partial \lambda} = \lim_{\substack{x,t\to\infty \\ v=x/t}} \frac{1}{t}\int_0^t ds \frac{\mathrm{Tr}[\rho_0\, j_x^E(s)\exp(-\lambda\Delta e(x,t))]}{\mathrm{Tr}[\rho_0 \exp(-\lambda\Delta e(x,t))]}. \tag{3.88}$$

By using the definition of the translation operator P_{tr} in Eq. (3.12) (or in Eq. (3.29) for the harmonic chain) and the time evolution under H we can write

$$j_x^E(s) = \mathrm{e}^{iHs}(P_{tr})^x j_0^E(0)(P_{tr}^\dagger)^x \mathrm{e}^{-iHs}, \tag{3.89}$$

and therefore, by cyclicity of the trace, Eq. (3.88) becomes

$$-\frac{\partial G(\lambda,v)}{\partial \lambda} = \lim_{\substack{x,t\to\infty \\ v=x/t}} \frac{1}{t}\int_0^t ds \frac{\mathrm{Tr}[\rho(x,s,\lambda) j_0^E(0)]}{\mathrm{Tr}[\rho(x,s,\lambda)]}, \tag{3.90}$$

where we defined

$$\rho(x,s,\lambda) \equiv \exp[-\lambda\Delta e(0;s,t)](P_{tr}^\dagger)^x \mathrm{e}^{-iHs}\rho_0 \mathrm{e}^{iHs} P_{tr}^x, \tag{3.91}$$

and

$$\exp[-\lambda\Delta e(0;s,t)] \equiv \mathrm{e}^{-iHs}\exp[-\lambda\Delta e(0,t)]\mathrm{e}^{iHs} = \exp\left(-\lambda\int_{-s}^{t-s} ds' j_0^E(s')\right). \tag{3.92}$$

Note that, for $\lambda = 0$, Eq. (3.91) reduces in the hydrodynamic limit to Eq. (3.46) for the Ising chain, and to Eq. (3.61) for the harmonic one, while Eq. (3.90) is just the hydrodynamic limit of the mean of the energy current $j_0^E(0)$ given in Eq. (3.49) for the fermionic case, and in Eq. (3.64) for the bosonic one. The physical interpretation of Eqs. (3.90), (3.91), and (3.92) is therefore that the insertion of the exponential of the time-integrated current biases the statistical measure, from $\rho(v)$ to

$\rho(x,t,\lambda)$, with respect to which the energy current is averaged. The key point to proceed in the calculation is that this λ-tilted ensemble $\rho(x,t,\lambda)$ has still the same form as Eq. (3.46) for fermions (and Eq. (3.61) for bosons) with $\beta(v,k)$ acquiring an additional dependence on λ as $\beta(v,k,\lambda)$.

To see this, we consider the hydrodynamic limit of Eq. (3.92), which can be readily determined by writing $j_0^E(0)$ in terms of post-quench mode operators $\Psi_R(k)$ for the Ising case, and $\mathbb{A}(k)$ for the harmonic oscillators (see Eq. (3.150) in Appendix 3.A); then we consider the time evolution up to time s', integrating according to Eq. (3.92) and then doing a stationary phase approximation analogous to the one done after Eq. (3.45), with x set to zero. An analogous analysis has been done for $\Delta e(0;t/2,t)$ in Ref. [146]. For the Ising model, this results in

$$\Delta e(0;s,t) = \int_{-\pi}^{\pi} dk\, \mathrm{sgn}(v_g(k))\varepsilon(k)\Psi_R^\dagger(k)\Psi_R(k), \tag{3.93}$$

(the corresponding equation for the harmonic chain can be obtained by replacing $\Psi_R(k) \rightleftarrows \mathbb{A}(k)$ and $\varepsilon(k) \rightleftarrows \Omega(k)$) with $\mathrm{sgn}(x>0) = +1$ and $\mathrm{sgn}(x<0) = -1$. By plugging Eq. (3.93) into Eq. (3.92) and then into Eq. (3.91), we get a state $\rho(x,t,\lambda) = \rho(v,\lambda)$ equal to the one in Eq. (3.46) (or Eq. (3.61) for the harmonic chain) with the replacement

$$\beta(v,k) \longrightarrow \beta(v,k,\lambda) = \beta(v,k) + \lambda\, \mathrm{sgn}(v_g(k)). \tag{3.94}$$

In Eq. (3.90), with $\rho(v,\lambda)$ determined by Eq. (3.94), one can directly calculate the average of $j_0^E(0)$ in the hydrodynamic limit, as in Eq. (3.40), since now only the local operator $j_0^E(0)$ appears inside the trace. Using the expression in Eqs. (3.49) and (3.64) into Eq. (3.88), we get

$$\frac{\partial G(\lambda,v)}{\partial\lambda} = -\frac{1}{t}\int_0^t ds \int_{-\pi}^{\pi}\frac{dk}{2\pi}\varepsilon(k)v_g(k)n^+\left(\frac{x}{s},k,\lambda\right), \tag{3.95}$$

where

$$n^+(v,k,\lambda) = f^+_{\beta_r(\lambda)}(k)\Theta(v-v_g(k)) + f^+_{\beta_l(\lambda)}(k)\Theta(v_g(k)-v), \tag{3.96}$$

with $\beta_{r,l}(\lambda) = \beta_{r,l} + \lambda\,\mathrm{sgn}(v_g(k))$. Integrating Eq. (3.95) over λ with the initial condition $G(\lambda=0,v)=0$, after simple algebraic manipulations, one obtains a final compact expression for $G(\lambda,v)$ with $v>0$ valid for both fermions and bosons

$$G(\lambda,v) = G_{\beta_r}(\lambda) - \int_{\epsilon_{min}}^{\epsilon_{max}}\frac{d\varepsilon}{2\pi}\Theta(v_g(\varepsilon)-v)\left(1-\frac{v}{v_g(\varepsilon)}\right) \\ \{[F((\beta_l+\lambda)\,\varepsilon) - F(\beta_l\,\varepsilon)] - [F((\beta_r+\lambda)\,\varepsilon) - F(\beta_r\,\varepsilon)]\}, \tag{3.97}$$

where we introduced

$$G_\beta(\lambda) = -\int_{\epsilon_{min}}^{\epsilon_{max}}\frac{d\varepsilon}{2\pi}\{[F((\beta+\lambda)\,\varepsilon) - F(\beta\,\varepsilon)] + [F((\beta-\lambda)\,\varepsilon) - F(\beta\,\varepsilon)]\}, \tag{3.98}$$

with the function $F(\varepsilon)$ depending on the statistics of the quasi-particles as

$$F(\varepsilon) = \begin{cases} -\ln(1+\mathrm{e}^{-\varepsilon}) & \text{for fermions;} \\ \ln(1-\mathrm{e}^{-\varepsilon}) & \text{for bosons.} \end{cases} \tag{3.99}$$

In the previous expressions ϵ_{min} and ϵ_{max} are the minimum and the maximum of the single-particle energy spectrum (see Eq. (3.51) for the Ising chain and Eq. (3.65) for the harmonic chain). For $v < 0$, one gets from Eq. (3.95) a formula similar to Eq. (3.97) with the replacements $v \to -v$, $l \rightleftarrows r$ and $\lambda \to -\lambda$, i.e.,

$$G(\lambda, v) = G_{\beta_l}(\lambda) - \int_{\epsilon_{min}}^{\epsilon_{max}} \frac{d\varepsilon}{2\pi} \Theta(v_g(\varepsilon) + v) \left(1 + \frac{v}{v_g(\varepsilon)}\right) \\ \{[F((\beta_r - \lambda)\,\varepsilon) - F(\beta_r\,\varepsilon)] - [F((\beta_l - \lambda)\,\varepsilon) - F(\beta_l\,\varepsilon)]\}\,. \tag{3.100}$$

One can see that for $v > v_{max}$ ($v < -v_{max}$) (where v_{max} is given in Eq. (3.51) or (3.65) depending on the model considered), the second term in Eqs. (3.97) and (3.100) vanishes and one is left with $G(\lambda, v) = G_{\beta_r}(\lambda)$ ($G_{\beta_l}(\lambda)$). The physical interpretation of this result is straightforward since outside the light-cone $v > v_{max}$ ($v < -v_{max}$) the system is described by a reservoir at inverse temperature β_r (β_l), which is not affected by the dynamics. Correspondingly, the temperature in this region is homogeneous and the mean current $\mathcal{J}^E(v)$ vanishes, while due to thermal fluctuations, its higher-order cumulants do not vanish and they are described by the SCGF of the reservoir at the initial temperature of that part of the chain. On the other hand, the NESS can be retrieved as a particular case of Eqs. (3.97) and (3.100): upon setting $v = 0$ in these expressions one finds

$$G(\lambda, v = 0) = -\int_{\epsilon_{min}}^{\epsilon_{max}} \frac{d\varepsilon}{2\pi} \{[F((\beta_l + \lambda)\,\varepsilon) - F(\beta_l\,\varepsilon)] + [F((\beta_r - \lambda)\,\varepsilon) - F(\beta_r\,\varepsilon)]\}\,. \tag{3.101}$$

In Secs. 3.5.3 and 3.5.4, we show that for non-interacting fermions and bosons Eq. (3.101) coincides with Eqs. (3.86), and (3.87) respectively, with unitary transmission coefficient, as expected from the fact that, after the quench, the Hamiltonian is translational invariant and therefore no reflection occurs at the junction. For generic values of v, Eqs. (3.97) and (3.100) provide the complete dynamics of the SCGF, and of all the cumulants of the transferred energy $\Delta e(x,t)$, in the hydrodynamic limit, extending the known results in the literature about the NESS.

Note that the expressions in Eqs. (3.97) and (3.100) for $G(\lambda, v)$ satisfy the important relation

$$\frac{\partial G(\lambda, v)}{\partial \lambda} = -\frac{1}{t}\Delta\mathcal{E}(x,t)\,\big|_{\beta_l+\lambda,\beta_r-\lambda} - \frac{1}{t}\Delta\mathcal{E}(x,t)\,\big|_{\beta_r-\lambda,\beta_r+\lambda} + \mathcal{J}^E_{NESS}\,\big|_{\beta_r-\lambda,\beta_r+\lambda}\,, \tag{3.102}$$

where we denoted by $\Delta\mathcal{E}(x,t)\,\big|_{\beta_l,\beta_r}$ the mean in Eqs. (3.58) and (3.69) of the transferred energy operator $\Delta e(x,t)$ at the hydrodynamic scale. The first subscript β_l of $\Delta\mathcal{E}(x,t)\,\big|_{\beta_l,\beta_r}$ refers to the inverse temperature of the first Fermi-Bose function $f^{+}_{\beta_{l,r}}$ appearing on the right hand side of Eqs. (3.58) and (3.69) with positive sign, while

the second subscript β_r denotes the inverse temperature of the second Fermi-Bose factor appearing in the same equations with negative sign. $\mathcal{J}^E_{NESS}\big|_{\beta_r-\lambda,\beta_r+\lambda}$ is the stationary-state energy current obtained upon setting $v = 0$ in Eqs. (3.49) and (3.64) and by replacing $\beta_l \to \beta_r - \lambda$ and $\beta_r \to \beta_r + \lambda$. In particular, for $v = 0$ the two terms on the second line of Eq. (3.102) cancel each other and one obtains

$$\frac{\partial G(\lambda, v=0)}{\partial \lambda} = -\mathcal{J}^E_{NESS}\big|_{\beta_l+\lambda,\beta_r-\lambda}\,, \tag{3.103}$$

which is known in the literature as the extended fluctuation relation; it was proved in Ref. [145] for the NESS limit of the SCGF $G(\lambda)$ in Eq. (3.85), and in particular it is known to apply to free particles models [143, 146, 338] and conformal field theory [142–144]. Our result in Eq. (3.102) therefore represents an extension of the extended fluctuation relation to the space-time scaling limit $v = x/t$ of the SCGF $G(\lambda, v)$ in Eq. (3.81). The relation in Eq. (3.102) and generalizations thereof are important for the generalization of the calculation of the cumulant generating function in Eq. (3.81) to interacting integrable models, as we shall see in Chapter 4. In the latter case, in fact, the SCGF will be computed by integrating the expression for the mean current available from the generalized hydrodynamics [159, 162] with appropriately modified Lagrange parameters β as a function of λ, thereby providing access to an expression otherwise extremely difficult to obtain.

3.5.2 Semiclassical picture of the SCGF

We have seen in Sec. 3.3, cf. Fig. 3.2, that Eqs. (3.49) and (3.64) can be simply interpreted in terms of quasi-particles excitations generated by the post-quench mode operators $\Psi^\dagger_R(k)$ or $\mathbb{A}^\dagger(k)$ in Eqs. (3.14) or (3.30) with wave-vector $k \in [0, \pi)$, which travel ballistically with velocity $\pm v_g(k)$, defined after Eqs. (3.46) and (3.61). This is not surprising since the quasi-particle picture is expected to give exact results in the hydrodynamic limit $x, t \to \infty$ at fixed $v = x/t$, as discussed in Subsec. 1.4.2. In this Section we show that this picture can be non-trivially extended in order to exactly capture the SCGF $G(\lambda, v)$ in Eq. (3.81), thereby accounting for all higher-order cumulants of the transferred energy $\Delta e(x, t)$ beyond the mean value. The possibility of accounting for fluctuations via the quasi-particle picture resides in the fact that in finite-temperature states, as in the partitioning protocol considered in this Chapter, fluctuations are dominated by classical effects, i.e., they are essentially due to the statistical distribution of the initial state. Notice, however, that these fluctuations, albeit being of classical nature, carry memory of the quantumness of the system through the function $F(\varepsilon)$ in Eq. (3.99), which encodes the quantum statistics of the underlying quasi-particle excitations.

Quasi-particles with velocity $+v_g(k)$ propagate rightwards (right movers), while those with velocity $-v_g(k)$ propagate leftwards (left movers). The occupation of each mode k is determined by the statistics of the initial state. For the one resulting from the partitioning protocol in Eq. (3.1), this occupation is thermal at inverse temperatures β_l and β_r for $y < 0$ and $y > 0$, respectively, where y is the spatial coordinate along the chain which vanishes at the junction point between the two halves. As a consequence, in order to represent in a semi-classical way the quasi-particles corresponding to the modes $\Psi^\dagger_R(k)$ and $\mathbb{A}^\dagger(k)$, one defines the

number $n_{\beta(y)}(k)$ of quasi-particles with wave vector k initially "located" at site y as a classical random variable with a probability distribution $P(n_{\beta(y)}(k))$ determined by the thermal distribution at inverse temperature $\beta(y)$. According to elementary statistical mechanics [8], for fermionic quasi-particles this distribution is given by

$$P(n_{\beta(y)}(k)=n)=\frac{\mathrm{e}^{-\beta(y)\varepsilon(k)n}}{1+\mathrm{e}^{-\beta(y)\varepsilon(k)}} \quad \text{with} \quad n=0,1, \tag{3.104}$$

while in the bosonic case

$$P(n_{\beta(y)}(k)=n)=\mathrm{e}^{-\beta(y)\Omega(k)n}(1-\mathrm{e}^{-\beta(y)\Omega(k)}) \quad \text{with} \quad n=0,1,\dots\infty, \tag{3.105}$$

and

$$\beta(y)=\beta_r\Theta(y)+\beta_l\Theta(-y). \tag{3.106}$$

The random variables $n_{\beta(y')}(k')$ and $n_{\beta(y)}(k)$ at lattice sites $y'\neq y$ and with wave vector $k'\neq k$ are taken to be independent since in free-particle models the various modes evolve independently of each other and therefore Eqs. (3.104), (3.105), and (3.106) specify completely the probability of a given configuration of the quasi-particles along the chain after the quench.

As a consequence of the independence of the variables $n_{\beta(y)}(k)$ for different values of k, one can write the scaled cumulant generating function $G(\lambda,x,t)$ of the total transferred energy $\Delta e(x,t)$ as

$$G(\lambda,x,t)=\lim_{\substack{x,t\to\infty\\ v=x/t}}\frac{1}{t}\int_0^\pi\frac{dk}{2\pi}\ln g(\lambda,x,t;k), \tag{3.107}$$

where $g(\lambda,x,t;k)$ is the moment generating function of the contribution $\Delta e(x,t;k)$ to the total transferred energy $\Delta e(x,t)$ due to the quasi-particles with wave vector k, defined as

$$g(\lambda,x,t;k)=\langle \mathrm{e}^{-\lambda\Delta e(x,t;k)}\rangle_{sc}, \tag{3.108}$$

where the subscript "sc" denotes the semi-classical average according to the mode distributions in Eqs. (3.104), (3.105), and (3.106). We emphasize that, within the semi-classical description presented here, $\Delta e(x,t;k)$ is considered as a classical random variable depending on $n_{\beta(y)}(k)$ and it is simply related to the total transferred energy $\Delta e(x,t)$ as

$$\Delta e(x,t)=\int_0^\pi\frac{dk}{2\pi}\Delta e(x,t;k). \tag{3.109}$$

This formula expresses again the fact that modes with different k contribute independently to $\Delta e(x,t)$ and therefore to $G(\lambda,x,t)$, as one can also see from Eq. (3.107).

Since the transferred energy $\Delta e(x,t;k)$ is a time-integrated observable, it is determined not only by the flux of quasi-particles with wave vector k arriving in x at time t, but also by all the excitations crossing x at times earlier than t, i.e., within the temporal interval $(0,t)$. Given that the quasi-particles propagate ballistically with velocity $\pm v_g(k)$, it is straightforward to express $\Delta e(x,t;k)$ in terms of the

random variables $n_{\beta(y)}(k)$ in Eq. (3.106). In particular, assuming $v \equiv x/t > 0$, the quasi-particles with $v_g(k) > v$ and coming from the left chain are always able to reach the point x within the time interval of interest, as sketched in Fig. 3.5(a), while those with $v_g(k) < v$ contribute to the total energy change $\Delta e(x,t;k)$ only if coming from the right chain, see Fig. 3.5(b). The semi-classical expression of

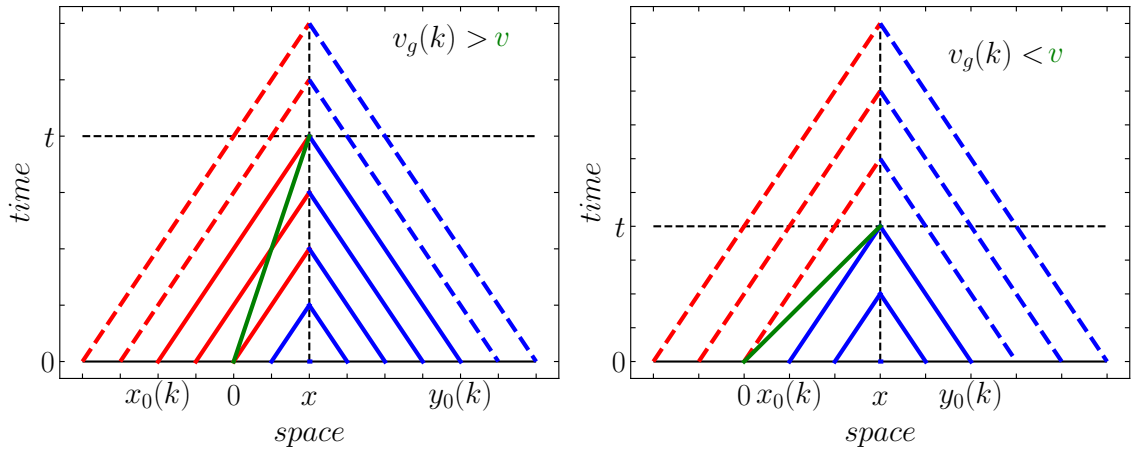

FIGURE 3.5: Quasi-particles interpretation of the transferred energy $\Delta e(x,t;k)$ determined by the mode k for a point at position $x = 2$ and time $t = 4$, corresponding to $v = x/t = 0.5$. In panel (a) we consider a value of k such that $v_g(k) > v$, choosing, as an example, $v_g(k) = 1$. The light-ray with constant $v = x/t$ is reported in green. Right-moving quasi particles with $v_g(k) > 0$ initially generated at points y with $x_0(k) \leq y \leq x$ cross the point x within the interval $[0,t]$ and therefore contribute to the statistics of $\Delta e(x,t;k)$; in the sketch, their light-rays are indicated as red or blue solid lines depending on their inverse temperature being β_l (for $y < 0$) or β_r (for $y > 0$), respectively. Quasi-particles arriving in x after time t, instead, do not contribute to $\Delta e(x,t;k)$ and the corresponding light-rays are indicated by dashed lines. Similarly, left-moving quasi particles contribute if they come from the interval $x \leq y \leq y_0(k)$. In panel (b) we consider the case $x = 3$, $t = 4$, corresponding to $v = 0.75$ and a value of k such that $v_g(k) < v$, choosing $v_g(k) = 0.5$. The same interpretation as panel (a) applies with the difference that only quasi particles coming from the right chain ($y > 0$) determine now the statistics of the transferred energy. Image taken from Ref. [4].

the energy transferred by the mode $k \in [0,\pi)$ for a generic value of v is therefore given by the difference between the flux of quasi-particles initially generated in the interval $[x_0(k),x]$ and that of the quasi-particles generated in $[x,y_0(k)]$, with $x_0(k) = x - v_g(k)t$ and $y_0(k) = x + v_g(k)t$, as shown in Fig. 3.5. In formulas,

$$\Delta e(x,t;k) = \sum_{y=x_0(k)}^{x} \varepsilon(k) n_{\beta(y)}(k) - \sum_{y=x}^{y_0(k)} \varepsilon(k) n_{\beta(y)}(k), \tag{3.110}$$

where $n_{\beta(y)}(k)$ is defined before Eq. (3.104), and the energy $\varepsilon(k)$ carried by a mode k in Eq. (3.7) for the Ising chain, while for the harmonic chain one has to replace $\varepsilon(k) \leftrightarrows \Omega(k)$, with $\Omega(k)$ given in Eq. (3.26). The moment generating function $g(\lambda,x,t;k)$ in Eq. (3.108) can be then computed (see the Appendix of Ref. [4] for

further details about the calculations), starting from Eqs. (3.110), (3.104), (3.105), and (3.106) given that

$$\begin{aligned}\langle \mathrm{e}^{-\lambda\varepsilon(k)n_{\beta(y)}(k)}\rangle_{sc} &= 1 + f^{+}_{\beta(y)}(k)(\mathrm{e}^{-\lambda\varepsilon(k)} - 1) \\ &= \exp[F(\beta(y)\varepsilon(k)) - F((\beta(y)+\lambda)\varepsilon(k))],\end{aligned} \tag{3.111}$$

for fermionic excitations, while

$$\begin{aligned}\langle \mathrm{e}^{-\lambda\Omega(k)n_{\beta(y)}(k)}\rangle_{sc} &= [1 + f^{-}_{\beta(y)}(k)(1 - \mathrm{e}^{-\lambda\Omega(k)})]^{-1} \\ &= \exp[F(\beta(y)\Omega(k)) - F((\beta(y)+\lambda)\Omega(k))] \quad \text{for} \quad \lambda > -\beta(y),\end{aligned} \tag{3.112}$$

and otherwise infinite, in the bosonic case. The function $F(\varepsilon)$ has been defined in Eq. (3.99) and it depends on the statistics of the quasi-particles. Inserting the expression of $g(\lambda, x, t; k)$ into Eq. (3.107) and after taking the space-time scaling limit, the expression for the SCGF turns out to be, as expected, a scaling function of $v = x/t$, i.e., $G(\lambda, x, t) \equiv G(\lambda, v)$ the expression of which coincides with the Eqs. (3.97), for $v > 0$, and with Eq. (3.100) for $v < 0$. In particular, the semi-classical picture provides a natural explanation for the structure of Eq. (3.102), which we have already recognized as a generalization of the extended fluctuation relation of Eq. (3.103) in the hydrodynamic limit. Indeed, in Ref. [145] such a relation has been proved under the assumption of pure transmission, i.e., assuming that the energy of left (right)-moving quasi-particles coming from the far right (left) of the system flows towards its far right (left) part without experiencing reflection. Also in the case analysed here quasi-particles do not experience scattering; however, as shown in Fig. 3.5(a), for times t comparable to the space coordinate x not only the right (left)-moving particles coming from the left (right) chain contribute to the statistics of the transferred energy $\Delta e(x, t)$, but also the right-moving particles from the space interval $[0, x]$, which result in the additional terms in the second line of Eq. (3.102). In the NESS, the contribution from particles generated within the interval $[0, x]$ vanishes and only right (left) moving particles from the left (right) chain matter, recovering the extended fluctuation relation in Eq. (3.103).

3.5.3 The quantum Ising chain: SCGF and large deviations

For the quantum Ising chain in a transverse field, the SCGF can be calculated explicitly by inserting in the general expression (3.97) the function $F(\varepsilon)$ specified in the first line of Eq. (3.99), where $\epsilon_{min} = \varepsilon_{min}$ and $\epsilon_{max} = \varepsilon_{max}$ are defined after Eq. (3.51); the final result is

$$\begin{aligned}G(\lambda, v) = G_{\beta_r}(\lambda) + \int_{\varepsilon_{min}}^{\varepsilon_{max}} \frac{d\varepsilon}{2\pi}\Theta(v_g(\varepsilon) - v)\left(1 - \frac{v}{v_g(\varepsilon)}\right) \\ \left\{\ln[1 + f^{+}_{\beta_l}(\varepsilon)(\mathrm{e}^{-\lambda\varepsilon} - 1)] - \ln[1 + f^{+}_{\beta_r}(\varepsilon)(\mathrm{e}^{-\lambda\varepsilon} - 1)]\right\},\end{aligned} \tag{3.113}$$

where

$$G_\beta(\lambda) = \int_{\varepsilon_{min}}^{\varepsilon_{max}} \frac{d\varepsilon}{2\pi} \left\{ \ln[1 + f_\beta^+(\varepsilon)(e^{-\lambda\varepsilon} - 1)] + \ln[1 + f_\beta^+(\varepsilon)(e^{\lambda\varepsilon} - 1)] \right\}, \quad (3.114)$$

for $v > 0$, while for $v < 0$ one gets from Eq. (3.100) the same result as here but with the replacements $v \to -v, l \leftrightarrows r$ and $\lambda \to -\lambda$. The general considerations done in Sec. 3.5.1 about the dependence of $G(\lambda, v)$ on v applies. In particular, for $v > v_{max}$, with v_{max} given by Eq. (3.51), $G(\lambda, v) = G_{\beta_r}(\lambda)$: after simple algebraic manipulations, it is easy to show that this expression coincides with the Levitov-Lesovik formula for non-interacting fermions in Eq. (3.86), with the two parts of the system having equal inverse temperatures set to β_r. Accordingly, $G(\lambda, v > v_{max})$ describes the energy current fluctuations in the right thermal reservoir. Upon setting $v = 0$ in Eq. (3.114), instead, we get the NESS limit of the SCGF, which for non-interacting fermions models is again provided by the Levitov-Lesovik formula in Eq. (3.86) with unitary transmission coefficient, as already noted after Eq. (3.101). From the latter equation, performing explicitly the integral over the energy spectrum one finds

$$G(\lambda, v = 0) = g^+_{\beta_l}(\lambda) - g^+_{\beta_l}(0) + g^+_{\beta_r}(-\lambda) - g^+_{\beta_r}(0), \quad (3.115)$$

where

$$g^+_\beta(\lambda) = \frac{\mathrm{Li}_2(-e^{-(\beta+\lambda)\varepsilon_{max}}) - \mathrm{Li}_2(-e^{-(\beta+\lambda)\varepsilon_{min}})}{2\pi(\beta + \lambda)}; \quad (3.116)$$

this expression agrees with the one derived (under the assumption $h > 1$) in Ref. [146], see Eqs. (33) and (34) therein, for the stationary limit of the SCGF of the transferred energy following an inhomogeneous quench of two Ising chains according to the very same protocol considered in this work and calculated by evaluating Eq. (3.85).

The plot of $G(\lambda, v)$ in Eq. (3.113) as a function of λ for various fixed values of v is reported in Fig. 3.6(a) for $v > 0$ and in Fig. 3.6(b) for $v < 0$. The corresponding large-deviation function $I(J_E, v)$, obtained by taking the Legendre-Fenchel transform of $G(\lambda, v)$, is reported in Fig. 3.7 for the same values of parameters as in Fig. 3.6. A different choice of the parameters $\beta_{l,r}$ does not alter the qualitative features of the plot, but it changes the zero of I, i.e., $I(\langle J_E \rangle, v) = 0$, where $\langle J_E \rangle = \Delta\mathcal{E}(x,t)/t$ is the mean and typical value. In particular, for $\beta_r > \beta_l$, $\langle J_E \rangle$ is positive as the typical flow of energy is from the left (hotter) to the right (colder) chain, according to the initial temperature gradient. In the opposite case, $\beta_r < \beta_l$, one has $\langle J_E \rangle < 0$ and the zero of I is consequently negative. As far as the dependence on v of $G(\lambda, v)$ and $I(J_E, v)$ is concerned, we note that the statistics of the rare fluctuations with J_E smaller (larger) than $\langle J_E \rangle$ does not depend significantly on the value of $v > 0$ ($v < 0$). This fact can be understood in terms of the quasi-particles picture sketched in Fig. 3.5: in the case $v > 0$, for instance, in order to have a current smaller than the mean one, e.g., a negative value with the current flowing against the temperature gradient, one needs a fluctuation in the number of left-moving particles coming from the right chain, in particular those initially generated within the space interval $[x, y_0(k)]$, with $y_0(k)$ defined after Eq. (3.110); given that these excitations are entirely produced in the right part

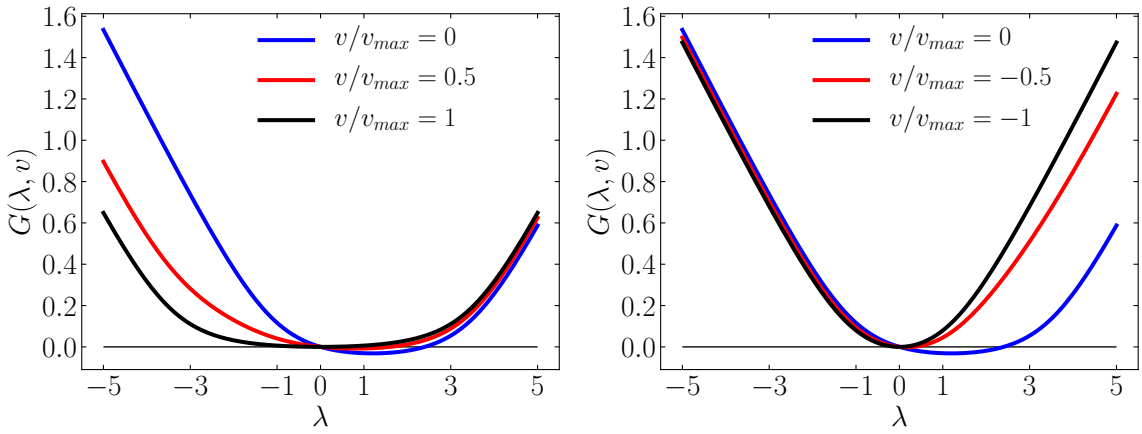

FIGURE 3.6: Scaled cumulant generating function $G(\lambda, v)$ as a function of λ and fixed v for the quantum Ising chain with $\beta_l = 1.1$, $\beta_r = 3.5$, $h = 1.3$, $J = 1$. In particular, panel (a) corresponds to positive values of $v/v_{max} = 0, 0.5, 1$ (from top to bottom) while panel (b) to negative values $v/v_{max} = 0, -0.5, -1$ (from bottom to top). v_{max} is given in Eq. (3.51). Image taken from Ref. [4].

of the chain, at inverse temperature β_r, the corresponding fluctuations are practically time-independent because the properties of the reservoir have not been affected by the dynamics. Concerning the dependence on λ, instead, the SCGF is defined over the whole real axis for all values of v and it is asymptotically linear as $\lambda \to \pm\infty$, with slopes $\mathcal{J}^E_{max}$ and $\mathcal{J}^E_{min} = -\mathcal{J}^E_{max}$, respectively, which are independent of v:

$$\mathcal{J}^E_{max} = -\frac{\partial G(\lambda, v)}{\partial \lambda}\Big|_{\lambda \to -\infty} = \frac{J^2 h}{\pi}. \tag{3.117}$$

Accordingly, by using the Legendre duality relations in Eqs. (3.84), an asymptotic linear behavior of $G(\lambda \to \pm\infty, v)$ such as that displayed by $G(\lambda, v)$ in Fig. 3.6 implies that $I(J_E, v)$ diverges for values of J_E outside the interval delimited by the slopes of $G(\lambda \to -\infty, v)$ and $G(\lambda \to \infty, v)$ and, correspondingly, the probability vanishes. This means that the values $\mathcal{J}^E_{min}$ and $\mathcal{J}^E_{max}$ identified above actually coincide with the minimal and maximal possible values, respectively, of $J_E = \Delta e(x,t)/t$. Accordingly, the rate function $I(J_E, v)$ is finite only within the interval $J_E \in [\mathcal{J}^E_{min}, \mathcal{J}^E_{max}]$, with $\mathcal{J}^E_{min}$ and $\mathcal{J}^E_{max}$ given in Eq. (3.117), while it diverges outside this interval, meaning that the corresponding values of the transferred energy cannot be observed in the system. In fact, because the transport is determined by fermionic quasi-particles, the exclusion principle requires that each mode k has at most an occupation number equal to 1 and therefore the modulus of the energy current $|\mathcal{J}^E(v)|$ in Eq. (3.49) can never exceed the value $\mathcal{J}^E_{max}$ obtained by setting all these occupation numbers to 1. This can be seen quantitatively by starting from the expression of $\mathcal{J}^E(v)$ in Eq. (3.49). Remembering that $\mathcal{J}^E(v = 0)$ is the value of the energy current in the NESS, and that $\mathcal{J}^E(v) < \mathcal{J}^E(0)$ since as time increases the current along the chain approaches the steady state value from

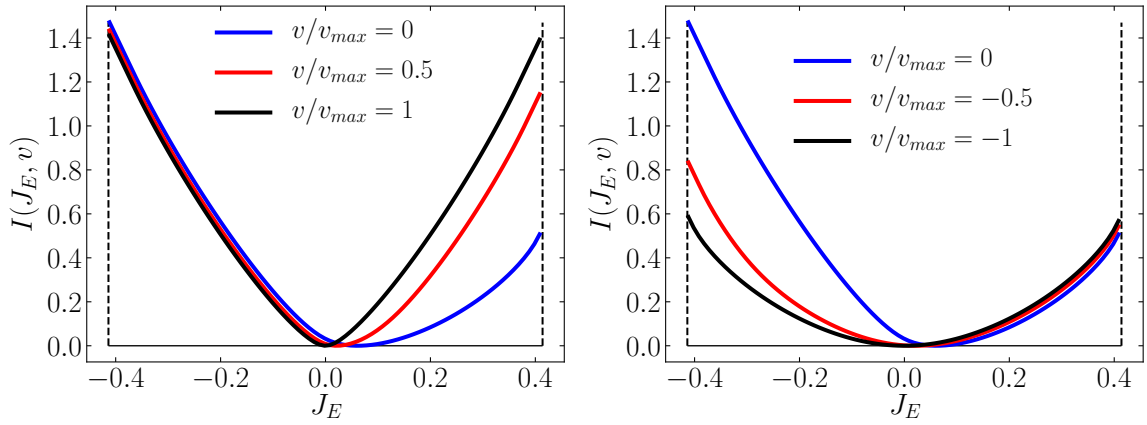

(a) (b)

FIGURE 3.7: Large deviation function $I(J_E, v)$ as a function of J_E and fixed v for the quantum Ising chain with the same values of parameters as in Fig. 3.6. In particular, panel (a) corresponds to positive values of $v/v_{max} = 0, 0.5, 1$ (from bottom to top) while panel (b) to negative values $v/v_{max} = 0, -0.5, -1$ (from top to bottom). v_{max} is given in Eq. (3.51). The vertical dashed lines correspond to the maximal and minimal values of the current $\pm\mathcal{J}^E_{max}$ in Eq. (3.117): the rate function is finite only within the interval $(-\mathcal{J}^E_{max}, \mathcal{J}^E_{max})$ while it is infinite outside it. Image taken from Ref. [4].

below since transport is ballistic, one has

$$|\mathcal{J}^E(v)| < |\mathcal{J}^E(0)| < \int_0^\pi \frac{\mathrm{d}k}{2\pi}\varepsilon(k)v_g(k)|f^+_{\beta_l}(k) - f^+_{\beta_r}(k)|. \tag{3.118}$$

By observing that, due to the fermionic statistics,

$$|f^+_{\beta_l}(k) - f^+_{\beta_r}(k)| < 1, \tag{3.119}$$

it follows that

$$|\mathcal{J}^E(v)| < \int_0^\pi \frac{\mathrm{d}k}{2\pi}\varepsilon(k)v_g(k) = \int_{\varepsilon_{min}}^{\varepsilon_{max}} \frac{\mathrm{d}\varepsilon}{2\pi}\varepsilon = \frac{J^2 h}{\pi}, \tag{3.120}$$

which is indeed the value in Eq. (3.117) of the asymptotic slope of $G(\lambda, v)$ for $\lambda \to \infty$. An analogous behavior has been found in Ref. [140, 341] in the boundary driven open XX spin chain, where the magnetization current exhibit a finite upper and lower bound determined by the asymptotic linear behavior of the SCGF.

3.5.4 The quantum harmonic chain: SCGF and large deviations

In the harmonic chain, $F(\varepsilon)$ in Eq. (3.97) is given by the second line of Eq. (3.99), while $\epsilon_{min} = \Omega_{min}$ and $\epsilon_{max} = \Omega_{max}$ are defined after Eq. (3.65). Accordingly,

Eq. (3.97) becomes

$$G(\lambda,v) = G_{\beta_r}(\lambda) - \int_{\Omega_{min}}^{\Omega_{max}} \frac{\mathrm{d}\varepsilon}{2\pi}\Theta(v_g(\varepsilon)-v)\left(1-\frac{v}{v_g(\varepsilon)}\right) \left\{\ln[1+f^-_{\beta_l}(\varepsilon)(1-\mathrm{e}^{-\lambda\varepsilon})]-\ln[1+f^-_{\beta_r}(\varepsilon)(1-\mathrm{e}^{-\lambda\varepsilon})]\right\}, \tag{3.121}$$

where

$$G_\beta(\lambda) = -\int_{\Omega_{min}}^{\Omega_{max}} \frac{\mathrm{d}\varepsilon}{2\pi}\left\{\ln[1+f^-_{\beta}(\varepsilon)(1-\mathrm{e}^{-\lambda\varepsilon})]+\ln[1+f^-_{\beta}(\varepsilon)(1-\mathrm{e}^{\lambda\varepsilon})]\right\}. \tag{3.122}$$

For $v<0$ a similar expression can be written starting from Eq. (3.100) with the replacements $v\to -v$, $\lambda\to-\lambda$ and $l\leftrightarrows r$. Similarly to the case of the Ising model, the term $G_\beta(\lambda)$ encodes thermal fluctuations of the right reservoir. Upon setting $v=0$ in Eq. (3.121) the NESS scaled cumulant generating function can obtained by directly calculating the integral over the energy spectrum Ω, which renders

$$G(\lambda,v=0) = g^-_{\beta_l}(\lambda) - g^-_{\beta_l}(0) + g^-_{\beta_r}(-\lambda) - g^-_{\beta_l}(0), \tag{3.123}$$

where

$$g^-_\beta(\lambda) = \frac{\mathrm{Li}_2(\mathrm{e}^{-\Omega_{min}(\beta+\lambda)}) - \mathrm{Li}_2(\mathrm{e}^{-\Omega_{max}(\beta+\lambda)})}{2\pi(\beta+\lambda)}. \tag{3.124}$$

The result in Eq. (3.123) is consistent with the one obtained in Ref. [322] for the SCGF of a chain of harmonic oscillators coupled to two external heat baths at temperatures T_l and T_r. In addition, it shows that the SCGF and the cumulants of the transferred energy $\Delta e(x,t)$ are independent of the protocol chosen to get the non-equilibrium steady state, as it happens for the mean value of the energy current reported after Eqs. (3.66), (3.67), and (3.68).

The plot of $G(\lambda,v)$ in Eq. (3.121) as a function of λ for various fixed values of v is reported in Fig. 3.8(a) for $v>0$ and in Fig. 3.8(b) for $v<0$. The corresponding large-deviation function $I(J_E,v)$, obtained by taking the Legendre-Fenchel transform of $G(\lambda,v)$, is reported in the two panels of Fig. 3.9 for the same values of parameters as in Fig. 3.8. As in the case of the Ising chain, the qualitative features of the plot are unaltered upon varying the values of the parameters of model, the only difference being in the sign of the mean transferred energy $\langle J_E\rangle$ which is positive for $\beta_r>\beta_l$, as it is the case for Fig. 3.9, and negative otherwise. The most important difference with respect to the SCGF of the fermionic case reported in Fig. 3.6 is that $G(\lambda,v)$ as a function of λ is defined on a finite interval, the extremes of which depend on the value of the variable v, i.e., it is finite if

$$\begin{aligned} &\lambda\in[-\min(\beta_l,\beta_r),\beta_r] \quad \text{for} \quad 0<v<v_{max},\\ &\lambda\in[-\beta_l,\min(\beta_l,\beta_r)] \quad \text{for} \quad -v_{max}<v<0, \end{aligned} \tag{3.125}$$

while it is otherwise infinite. In the non-equilibrium stationary state, corresponding to setting $v=0$, and in the cases $v>v_{max}$ and $v<-v_{max}$, with v_{max} given in

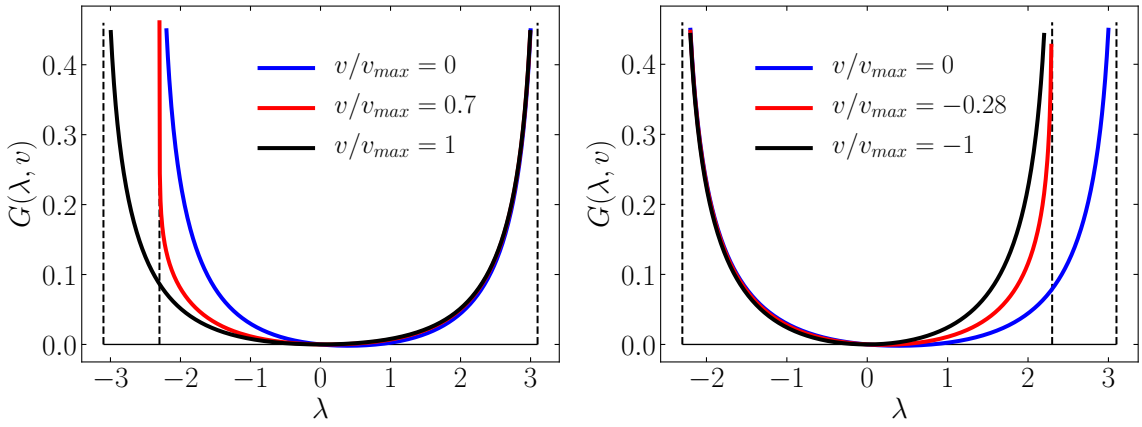

(a) (b)

FIGURE 3.8: Scaled cumulant generating function $G(\lambda, v)$ as a function of λ and fixed v for the harmonic chain with $\beta_l = 2.3$, $\beta_r = 3.1$, $m = 0.7$, $\omega = 1$, $v_{max} \simeq 0.71$ according to Eq. (3.65). In particular, panel (a) corresponds to positive values of $v/v_{max} = 0, 0.7, 1$ (from top to bottom) while panel (b) to negative values $v/v_{max} = 0, -0.28, -1$ (from bottom to top). The vertical dashed lines correspond to the boundaries of the domain of $G(\lambda, v)$ according to Eqs. (3.125) and (3.126). Image taken from Ref. [4].

Eq. (3.65), the domain of the SCGF is, instead,

$$\begin{aligned} &\lambda \in [-\beta_r, \beta_r] \quad \text{for} \quad v \geq v_{max}, \\ &\lambda \in [-\beta_l, \beta_l] \quad \text{for} \quad v \leq -v_{max}, \\ &\lambda \in [-\beta_l, \beta_r] \quad \text{for} \quad v = 0. \end{aligned} \tag{3.126}$$

In particular, the dependence of the domain of $G(\lambda, v)$ on v, as we can see from Fig. 3.8, turns out to be discontinuous; namely in the case $v > 0$ of Fig. 3.8(a) the domain is $\lambda \in [-\beta_l, \beta_r]$ for $0 < v < v_{max}$ since $\beta_r > \beta_l$, while, in the case $v > v_{max}$ it becomes the one of the the SCGF of the right reservoir in Eq. (3.122), i.e., $\lambda \in [-\beta_r, \beta_r]$. Similarly, for $v < 0$, the domain is $\lambda \in [-\beta_l, \beta_l]$ for $-v_{max} < v < 0$ while it changes to the domain of the NESS scaled cumulant generating function $\lambda \in [-\beta_l, \beta_r]$ for $v = 0$. In terms of the large deviation function $I(J_E, v)$ and due to the Legendre duality expressed in Eq. (3.84), the presence of these domains translates into asymptotically linear behaviours for large $|J_E|$, with the slopes determined by the boundaries of the domain of the SCGF, given in Eqs. (3.125) and (3.126). This is shown in Fig. 3.9(a) for $v > 0$ and in Fig. 3.9(b) for $v < 0$.

The peculiar behavior of the domain of the SCGF in Eq. (3.125) can be again understood in terms of the quasi-particles picture sketched in Fig. 3.5. Consider, for example, the case $v > 0$: since the transferred energy operator $\Delta e(x, t)$ in Eq. (3.57) is a time-integrated quantity one has to consider the flux of quasi-particles arriving in x within the time interval $(0, t)$, as already noted after Eq. (3.107). Left movers contributing to the expression in Eq. (3.121) are generated initially only within the interval $(x, y_0(k)]$ along the chain, with inverse temperature β_r. The

contribution of right-moving excitations, instead, comes from those initially generated within the intervals $(x_0(k), 0]$ and $(0, x]$ along the chain, with different inverse temperatures β_l and β_r, respectively, where $x_0(k)$ and $y_0(k)$ are defined after Eq. (3.110). In each of these intervals there is a finite probability of generating an arbitrarily large number of bosons in the initial state for each mode k, according to Eq. (3.105). Therefore each interval can behave as an effective reservoir at the corresponding temperature, in the sense that it is able to inject an arbitrarily large number of quasi-particles in the system. The domain of the SCGF is then determined by the reservoir of left moving excitations, at inverse temperature β_r, and by the reservoir of those moving rightwards, with the temperature of the latter being determined by the largest between the temperatures at which the particles in the intervals $(x_0(k), 0]$ and those in $(x, y_0(k)]$ are initially generated, in accordance with Eq. (3.125). This is the physical interpretation of the origin of the behaviour displayed in Fig. 3.9(a): a similar argument can be repeated for $v < 0$ in order to explain the features of Fig. 3.9(b). In particular, due to the fact $\Delta e(x, t)$ is a time-integrated observable, one can conclude that $G(\lambda, v)$ in Eq. (3.81) as a function of v can be discontinuous in $v = 0$ or at the edges $v = \pm v_{max}$ whenever the Hilbert space for each mode k of the excitations is infinite, as it is the case for bosons. If, on the contrary, for every wave vector k the Hilbert space has a finite dimension, as in the fermionic case in Sec. 3.5.3, these discontinuities are absent.

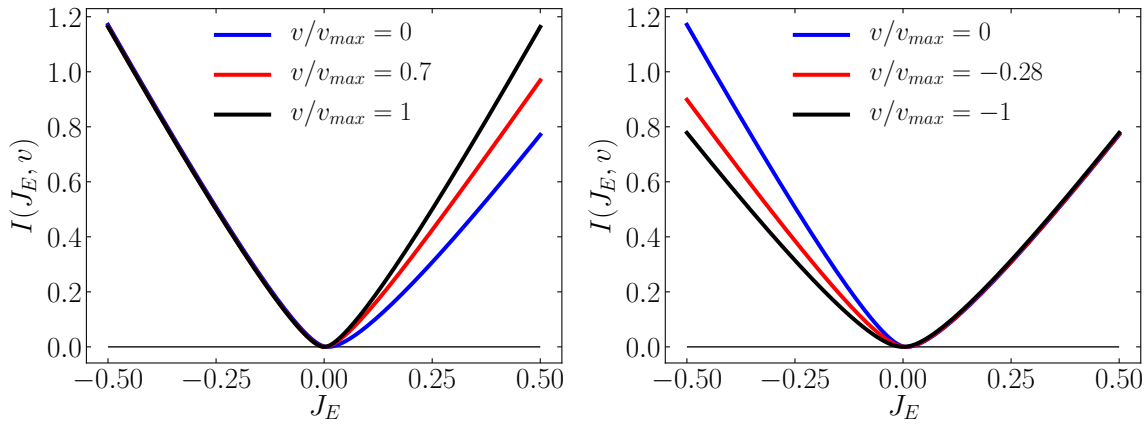

FIGURE 3.9: Large deviation function $I(J_E, v)$ as a function of J_E and fixed v for the quantum harmonic chain with the same values of parameters as in Fig. 3.8. In particular, panel (a) corresponds to positive values of $v/v_{max} = 0, 0.7, 1$ (from bottom to top) while panel (b) to negative values $v/v_{max} = 0, -0.28, -1$ (from top to bottom). Image taken from Ref. [4].

The bosonic large deviation function $I(J_E, v)$ is therefore defined as a function of J_E over the whole real axis for all values of v, and fluctuations of the transferred energy $J_E = \Delta e(x, t)/t$ can in principle be arbitrarily large; the physical reason is clear since in this case each mode k is not restricted to be populated by one or zero particles, as in the fermionic case, and as a consequence no bound as in Eq. (3.119) can be determined. In particular, the asymptotic linear behaviour of the rate function shown in Fig. 3.9, according to Eq. (3.82), causes the tails of the probability

density $p(J_E, v)$ of the transferred energy to be exponentially distributed according to

$$p(J_E, v) \sim \exp[-t\,\beta(v)|J_E|], \tag{3.127}$$

with $\beta(v)$ depending on v consistently with Eqs. (3.125) and (3.126). In the steady state, corresponding to setting $v = 0$, one has

$$\beta(v = 0) = \beta_l \Theta(J_E) + \beta_r \Theta(-J_E), \tag{3.128}$$

in agreement with Ref. [322], where identical exponential tails have been observed for the probability distribution of the energy current flowing in an harmonic chain connected to two thermal reservoirs at inverse temperatures β_l and β_r.

3.6 Concluding remarks

In this Chapter we considered quantum transport in non-interacting models in the partitioning protocol setup, see Sec. 3.2, where two halves described by two different GGEs are instantaneously joined at the point $x = 0$. In particular, we have considered the thermal transport occurring when two thermal ensembles at two different temperatures β_r and β_l, as in Eq. (3.1), are joined (with all the other Lagrange parameters of the two GGEs in Eq. (1.44) initially set to zero). We focused on the exactly solvable cases of the quantum Ising chain in a transverse field and of the harmonic chain, introduced in Sec. 3.1, which are characterized, respectively, by the fermionic and bosonic excitations in Eqs. (3.14) and (3.30). In Sec. 3.3 we have discussed the calculation of the energy current $\mathcal{J}^E(v)$ and density $\mathcal{U}(v)$ (see Eqs. (3.49) and (3.64)) in the space-time scaling/hydrodynamic limit $x, t \to \infty$ with fixed $v = x/t$. These quantities propagate along the chain ballistically in a light-cone fashion, as anticipated in Fig. 1.9, travelling with the characteristic velocity v_{max}, in Eq. (3.51) for the Ising and in Eq. (3.65) for the harmonic chain. The expressions of the energy current $\mathcal{J}^E(v)$ and density $\mathcal{U}(v)$ in the hydrodynamic limit turn out to have a rather universal structure, in the sense that the only appearing model-specific information is the single-particle energy spectrum and the Fermi-Dirac ($f^+_\beta(k)$) or Bose-Einstein ($f^-_\beta(k)$) statistics of the quasi particles. In Sec. 3.4 we have shown that the sub-diffusive corrections to the profile $\mathcal{J}^E(v)$ around the edge $x \simeq v_{max}t$ acquire a "universal" behavior, conveniently expressed in terms of the celebrated Airy kernel in Eqs. (3.73), (3.74) and (3.75) both in the fermionic case, as it was already known in many other cases [153, 154, 323, 327–329], and in the bosonic one, where it has been first established. For the quantum Ising chain, as the transverse field takes its critical value $h_c = 1$, a novel scaling form $K^c(X)$ emerges, see Eqs. (3.76), (3.78) and (3.79), which lacks the staircase structure characterising the Airy kernel.

In Sec. 3.5 we turned our attention to the study of fluctuations of transport. In Subsec. 3.5.1 the scaled cumulant generating function (SCGF) $G(\lambda, v)$ in the hydrodynamic limit, see Eq. (3.81), has been determined, with the result reported in Eqs. (3.97) and (3.100). The calculation is based on an exponential tilting $\rho(v, \lambda)$ of the density matrix according to the exponential of the time integrated current, as shown by Eqs. (3.90), (3.91), and (3.92). Equations (3.97) and (3.100) express the

SCGF as a function of v, therefore extending known results for the Ising chain (see Ref. [146]) and for the harmonic oscillators (see Ref. [322]) concerning the stationary limit of this function, corresponding to $v = 0$. In particular, in Eq. (3.102) we have derived a generalization of the so-called extended fluctuation relation [145], which allows us to calculate the SCGF $G(\lambda, v)$ via an integration over λ of the energy current $\mathcal{J}^E(v)$, with suitably modified inverse temperatures $\beta(\lambda)$. In Subsec. 3.5.2 we have provided a simple semi-classical derivation of Eqs. (3.97) and (3.100) in terms of quasi-particles which ballistically propagate along the chain. Via the Legendre-Fenchel transform in Eq. (3.83), the large deviation function $I(J_E, v)$ of the transferred energy $\Delta e(x,t)/t$ (see Eq. (3.82)) has been obtained. As far as the large deviation function is concerned, bosons and fermions behave rather differently. For fermions, see Subsec. 3.5.3 for the Ising chain, $I(J_E, v)$ as a function of J_E is finite only on the closed interval $[-\mathcal{J}^E_{max}, \mathcal{J}^E_{max}]$ (see Eq. (3.117)), while it is infinite outside it, meaning that $\Delta e(x,t)/t$ cannot exceed the maximum value $\mathcal{J}^E_{max}$. For bosons, see Subsec. 3.5.4, instead, $I(J_E, v)$ as a function of J_E is defined on the whole real axis and it shows linear tails (see Eqs. (3.127) and (3.128)), which imply that the probability density of the rare fluctuations is exponentially distributed.

As a future perspective it would be interesting to generalize the calculation of the SCGF to systems admitting quasi-particle excitations possessing some internal quantum number, e.g., the spin, as done in Refs. [342, 343]. The transport of the spin in these case does not happen along straight lines, as in the case of the energy in Subsec. 3.5.2, as the spin is not purely transmitted during the scattering among quasi-particles. It is then interesting to account for fluctuations of the time-integrated spin current within the large deviation approach pursued in this Chapter. In the next Chapter 4 we will address the case of inhomogeneous initial states in the more complex scenario of interacting integrable systems within the generalized hydrodynamics formalism [159, 162]. Namely, we will extend the findings of Sec. 3.5 to general inhomogeneous initial states both for classical and quantum integrable models.

Appendix of Chapter 3

3.A Non interacting models: details of their solutions

In this Appendix, we provide for completeness the expressions of the operators entering in the exact solution of the models introduced in Sec. 3.1.

In particular, for the quantum Ising chain the pre-quench mode operators $\Phi_{r,l}(k)$ in Eq.(3.5) can be eventually expressed in terms of the post-quench ones $\Psi_R(k)$, according to Eq. (3.44): we report here only the final results, more details can be found in Ref. [1]. The functions $\omega^n_{r,l}$ and $\xi^n_{r,l}$ in Eq. (3.5) are defined as

$$\omega^n_{r,l}(k) = \frac{A^n_{r,l}(k) + B^n_{r,l}(k)}{2}, \quad \xi^n_{r,l}(k) = \frac{A^n_{r,l}(k) - B^n_{r,l}(k)}{2}, \tag{3.129}$$

and

$$A^n_r(k) = \sqrt{2/\pi}\,\sin(nk - f(k)), \quad B^n_r(k) = \sqrt{2/\pi}\,\sin(nk), \tag{3.130}$$

where $f(k)$ is defined in Eq. (3.9). The functions A^n_l and B^n_l for the left chain are simply related to those of the right chain as

$$A^n_l(k) = B^{1-n}_r(k) \quad \text{and} \quad B^n_l(k) = A^{1-n}_r(k). \tag{3.131}$$

In order to express the operators $\Phi_{r,l}$ in Eq. (3.5) in term of $\Psi_R(k)$, we fist need to write the lattice fermionic operators c_n in terms of the post-quench modes as

$$c_n = \int_{-\pi}^{\pi} \mathrm{d}k \, \left[\Psi_R(k)(\omega^n_R(k))^* + \Psi^\dagger_R(k)\xi^n_R(k)\right], \tag{3.132}$$

where ω^n_R and ξ^n_R have been defined in Eqs. (3.15). By inserting Eq. (3.132) into Eq. (3.5), we get Eq. (3.44), where the sums over lattice sites can be computed as a geometric series resulting into the coefficients $m_{\pm,\alpha}(k,k')$, with $\alpha \in \{l,r\}$. The latter have been first computed in Ref. [146] and are listed here for completeness

$$m_{\pm,l}(k,k') = \frac{1}{4\pi i}\left\{\frac{\mathrm{e}^{-i[f(k)+f(k')]} \pm 1}{1 - \mathrm{e}^{i(k+k'+i\delta)}} - \frac{\mathrm{e}^{i[f(k')-f(k)]} \pm 1}{1 - \mathrm{e}^{i(k-k'+i\delta)}}\right\}, \tag{3.133}$$

for the left chain, and

$$m_{\pm,r}(k,k') = \frac{1}{4\pi i}\left\{\frac{\mathrm{e}^{i[k-f(k')]} \pm \mathrm{e}^{i[k-f(k)]}}{1 - \mathrm{e}^{i(k'-k+i\delta)}} - \frac{\mathrm{e}^{i[k+f(k')]} \pm \mathrm{e}^{i[k-f(k)]}}{1 - \mathrm{e}^{-i(k+k'-i\delta)}}\right\}, \tag{3.134}$$

for the right one.

For the harmonic chain, the exact solution of the left Hamiltonian in Eq. (3.19b) can be obtained by following the same procedure as for the right one with the definition, in the thermodynamic limit, of the operators $\hat{\phi}_l(k)$, $\hat{p}_l(k)$, where

$$\begin{aligned} \hat{\phi}_l(k) &= -\sqrt{2/\pi} \sum_{x=-\infty}^{0} \sin(k(x-1))\, \phi_x, \\ \hat{p}_l(k) &= -\sqrt{2/\pi} \sum_{x=-\infty}^{0} \sin(k(x-1))\, p_x, \end{aligned} \tag{3.135}$$

as a function of which the original lattice operators ϕ_x, p_x can be written as

$$\begin{aligned} \phi_x &= -\sqrt{2/\pi} \int_0^{\pi} \mathrm{d}k\, \sin(k(x-1))\, \hat{\phi}_l(k), \\ p_x &= -\sqrt{2/\pi} \int_0^{\pi} \mathrm{d}k\, \sin(k(x-1))\, \hat{p}_l(k). \end{aligned} \tag{3.136}$$

In particular, we emphasize that ϕ_x and p_x in Eq. (3.136) automatically satisfy the boundary conditions for the left chain $\phi_1 = p_1 \equiv 0$ reported right after Eq. (3.20). From the operators $\hat{\phi}_l(k)$ and $\hat{p}_l(k)$ in Eq. (3.135), the bosonic annihilation and creation operators $A_l(k)$ and $A_l^\dagger(k)$, respectively, for the left chain can be introduced in the same way as in Eq. (3.24), i.e.,

$$A_l(k) = \frac{1}{\sqrt{2\Omega(k)}} \left[\Omega(k)\hat{\phi}_l(k) + i\hat{p}_l(k)\right], \tag{3.137}$$

and the Hamiltonian then takes the diagonal form

$$H_l = \int_0^{\pi} \mathrm{d}k\, \Omega(k)\, A_l^\dagger(k) A_l(k). \tag{3.138}$$

For the harmonic chain the dynamics can be studied according to the same strategy as the quantum Ising chain, i.e., it is useful to write the pre-quench modes $A_{r,l}(k)$ in terms of the post-quench ones $\mathbb{A}(k)$ in Eq. (3.30). This can be done by inserting Eq. (3.21) (or Eq. (3.135) for the left chain) into Eq. (3.24) (or Eq. (3.137) for the left Hamiltonian) and then by writing the lattice operators ϕ_x and p_x as in Eq. (3.31). The sum over the lattice coordinate can be again computed as a geometric series, with the following result:

$$\begin{aligned} A_r(k) &= \int_{-\pi}^{\pi} \mathrm{d}k' \left[-\mathbb{A}^\dagger(k')\, m_{-,r}(k',k) + \mathbb{A}(k')\, m^*_{+,r}(k',k)\right], \\ A_l(k) &= \int_{-\pi}^{\pi} \mathrm{d}k' \left[\mathbb{A}^\dagger(k')\, m_{-,l}(k',k) + \mathbb{A}(k')\, m^*_{+,l}(k',k)\right], \end{aligned} \tag{3.139}$$

with the following expressions for the coefficients $m_{\pm,l,r}(k,k')$

$$m_{\pm,l}(k,k') = \pm\frac{1}{4\pi i}\left[\frac{e^{ik'}}{1-e^{i(k+k'+i\delta)}} - \frac{e^{-ik'}}{1-e^{i(k-k'+i\delta)}}\right]\left[\sqrt{\frac{\Omega(k')}{\Omega(k)}} \pm \sqrt{\frac{\Omega(k)}{\Omega(k')}}\right],$$
$$m_{\pm,r}(k,k') = \frac{1}{4\pi i}\left[\frac{e^{i(k'-k)}}{1-e^{i(k'-k+i\delta)}} - \frac{e^{-i(k+k')}}{1-e^{-i(k+k'-i\delta)}}\right]\left[\sqrt{\frac{\Omega(k)}{\Omega(k')}} \pm \sqrt{\frac{\Omega(k')}{\Omega(k)}}\right]. \tag{3.140}$$

It is also possible to invert Eq. (3.139) in order to express $\mathbb{A}(k)$ as a function of $A_{r,l}(k)$

$$\mathbb{A}(k) = \int_0^\pi dk' \left[m_{-,l}(k,k')A_l^\dagger(k') + m_{+,l}(k,k')A_l(k') + m_{-,r}(k,k')A_r^\dagger(k') + m_{+,r}(k,k')A_r(k')\right]. \tag{3.141}$$

3.B Calculation of the energy current in the hydrodynamic limit

In this Appendix we report the calculations in the hydrodynamic limit underlying Eqs. (3.61) and (3.64) for the harmonic chain. The corresponding derivation of Eqs. (3.46) and (3.49) for the quantum Ising model are analogous and therefore will not be reported for brevity. Details can be found in Refs. [1, 4, 157].

We start by writing the left and right Hamiltonians H_α, with $\alpha \in \{l,r\}$, in Eqs. (3.25) and (3.138), determining the initial state ρ_0 of Eq. (3.1), as a function of the post-quench modes via Eq. (3.139). In terms of the operators $\mathbb{A}(k)$, the space and time evolution of Eq. (3.40) can be easily calculated, because for them it is simply given by Eq. (3.32) and $e^{iHt}\mathbb{A}(k)e^{-iHt} = e^{-i\Omega(k)t}\mathbb{A}(k)$, resulting in

$$(P_{tr}^\dagger)^x e^{-iHt} H_\alpha e^{iHt}(P_{tr})^x = \int_{-\pi}^{\pi}dk'\int_{-\pi}^{\pi}dk''\Big[e^{-i\varphi^+_{x,t}(k',k'')}I^\alpha_{--}(k',k'')\mathbb{A}(k')\mathbb{A}^\dagger(k'') + e^{i\varphi^+_{x,t}(k',k'')}I^\alpha_{++}(k',k'')\mathbb{A}^\dagger(k')\mathbb{A}(k'') - e^{i\varphi^-_{x,t}(k',k'')}I^\alpha_{-+}(k',k'')\mathbb{A}(k')\mathbb{A}(k'') - e^{-i\varphi^-_{x,t}(k',k'')}I^\alpha_{+-}(k',k'')\mathbb{A}^\dagger(k')\mathbb{A}^\dagger(k'')\Big], \tag{3.142}$$

with the phases $\varphi^\pm_{x,t}(k',k'')$ defined as

$$\varphi^\pm_{x,t}(k',k'') = [\Omega(k'') \mp \Omega(k')]t \pm x(k' \mp k''), \tag{3.143}$$

and the coefficients $I^{\alpha}_{\pm,\pm}(k',k'')$ given by integrals of the overlaps in Eq. (3.140) as follows

$$\begin{aligned} I^{\alpha}_{++}(k',k'') &= \frac{1}{2}\oint_{C_1} \frac{\Omega(-i\ln(z))\, m_{+,\alpha}(k',-i\ln(z))\, m^{*}_{+,\alpha}(k'',-i\ln(z))}{iz}, \\ I^{\alpha}_{+-}(k',k'') &= \frac{1}{2}\oint_{C_1} \frac{\Omega(-i\ln(z))\, m_{+,\alpha}(k',-i\ln(z))\, m_{-,\alpha}(k'',-i\ln(z))}{iz}, \end{aligned} \tag{3.144}$$

while $I^{\alpha}_{-\pm}$ can be obtained from $I^{\alpha}_{+\pm}$ by taking the complex conjugate and exchanging $m_{+,\alpha} \leftrightarrows m_{-,\alpha}$. Note that in Eq. (3.144) we have first extended the integrals from $(0,\pi)$ to $(-\pi,\pi)$ by exploiting the properties $m_{\pm,\alpha}(k',k) = -m_{\pm,\alpha}(k',-k)$, $\Omega(-k) = \Omega(k)$. Then we have performed the change of variable $z = \mathrm{e}^{ik}$, which transforms the original integral into one along a circle with unit radius C_1 centered at the origin of the complex plane. In the space-time scaling limit of Eq. (3.40) each of the four integrals appearing in Eq. (3.142) is dominated by the regions in the (k',k'') plane where the phases $\varphi^{\pm}_{x,t}$ are stationary and by the singularities of the integrands $\{I^{\alpha}(k',k'')\}$ occurring in correspondence to these stationary points. In particular, the stationary-phase condition for $\varphi^{\pm}_{x,t}(k)$ is

$$\begin{cases} \dfrac{\partial \varphi^{\pm}_{x,t}(k',k'')}{\partial k'} = \mp v_g(k')t \pm x = 0, \\ \dfrac{\partial \varphi^{\pm}_{x,t}(k',k'')}{\partial k''} = v_g(k'')t - x = 0, \end{cases} \tag{3.145}$$

where $v_g(k)$ is the group velocity defined after Eq. (3.46). Each of this stationary phase conditions has two solutions $k_{\pm}(v)$ if $x/t = v < v_{max}$ (where v_{max} is given by Eq. (3.65) for the harmonic chain) such that

$$\cos(k_{\pm}(v)) = \frac{v^2}{\omega^2} \pm \sqrt{\frac{v^4}{\omega^4} - \frac{v^2 m^2}{\omega^4} - \frac{2v^2}{\omega^2} + 1} = \frac{v^2}{\omega^2} \pm \frac{1}{\omega^2}\sqrt{(v^2_{max} - v^2)(y^2 - v^2)}, \tag{3.146}$$

where

$$y = \frac{m + \sqrt{m^2 + 4\omega^2}}{2}; \tag{3.147}$$

accordingly, the system in Eq. (3.145) admits four pairs of solutions (k_+,k_+), (k_-,k_-), (k_-,k_+), and (k_+,k_-). The integrands $I^{\alpha}_{\pm\pm}(k',k'')$ are, however, singular only for the stationary points $(k',k'') = (k_+,k_+)$ and (k_-,k_-), at which $k' = k''$. Accordingly, the integrals in Eq. (3.142) can be computed, in the hydrodynamic limit, by expanding the integrand around $k' \simeq k''$. The singular part of $I^{\alpha}_{++}(k',k'')$ as $k' \to k''$ can be extracted from Eq. (3.144), with the residue theorem, finding that

$$\beta_l\, I^{l}_{++}(k',k'') + \beta_r\, I^{r}_{++}(k',k'') = \frac{\beta_l}{4\pi i}\frac{\Omega(k)+\Omega(k')}{k''-k'-2i\delta} - \frac{\beta_r}{4\pi i}\frac{\Omega(k)+\Omega(k')}{k''-k'+2i\delta} + \ldots, \tag{3.148}$$

where $\ldots$ represent terms that are regular as $k' \to k''$ and that we omit as they are

sub-leading in the space-time scaling limit. The integrals $I^{\alpha}_{+-}(k',k'')$, $I^{\alpha}_{-+}(k',k'')$, and $I^{\alpha}_{--}(k',k'')$ can be neglected for the same reason as these regular terms, as they are not singular for $k' \to k''$. Notice that the singularities of the matrix elements $m_{\pm,\alpha}(k,k')$, in Eq. (3.140) for the harmonic chains, are identical to those of the same coefficients in Eqs. (3.133) and (3.134) for the Ising chain. The stationary-phase analysis for the fermionic case of the integral in Eq. (3.142) proceeds therefore in the same way as in the bosonic case outlined here and the expression for I^{α}_{++} is identical to that in Eq. (3.148) upon replacing $\Omega(k) \leftrightarrows \varepsilon(k)$, in agreement with the result of Refs. [1, 157]. By inserting Eq. (3.142) for the right and left Hamiltonians into Eq. (3.1) and by taking into account that the only singular contribution as $k' \to k''$ comes from Eq. (3.148), one obtains Eq. (3.45) (with the replacement $\mathbb{A}(k) \leftrightarrows \Psi_R(k)$ for the harmonic chain) for the leading space-time dependence $\rho(x,t)$ of the density matrix in the hydrodynamic limit. The rest of the calculation, as outlined in the main text, follows by changing variables to $Q = k' - k''$ and $K = (k' + k'')/2$ in the double integral in Eq. (3.45). Expanding $\varphi^{+}_{x,t}(k',k'')$ around $Q = 0$, i.e.,

$$\varphi^{+}_{x,t}(k',k'') = \varphi^{+}_{x,t}(K + Q/2, K - Q/2) = Q(x - v_g(K)\,t) + O(Q^2), \tag{3.149}$$

with the integral definition $\Theta = \lim_{\delta\to 0^+} \int_{-\infty}^{\infty} \frac{\mathrm{d}y}{2\pi i} \frac{\mathrm{e}^{ixy}}{y - i\delta}$ of the Heaviside step function, the result in Eqs. (3.46) and (3.61) for the time-evolved density matrix $\rho(v)$ in the hydrodynamic limit is eventually found.

Similarly, the calculation of the energy current can be done by writing the operator j^{E}_{0} in Eq. (3.60) in terms of the post-quench operators $\mathbb{A}(k)$ by using Eqs. (3.30) and (3.31), i.e.,

$$\begin{aligned} j^{E}_{0} = \frac{i\omega^2}{4} \int_{-\pi}^{\pi} \mathrm{d}k \int_{-\pi}^{\pi} \frac{\mathrm{d}k'}{2\pi} \sqrt{\frac{\Omega(k')}{\Omega(k)}} (\mathrm{e}^{-ik} - 1)(\mathrm{e}^{-ik'} + 1) \\ \Big[\mathbb{A}(k)\mathbb{A}^{\dagger}(-k') - \mathbb{A}(k)\mathbb{A}(k') + \mathbb{A}^{\dagger}(-k)\mathbb{A}^{\dagger}(-k') - \mathbb{A}^{\dagger}(-k)\mathbb{A}(k')\Big], \end{aligned} \tag{3.150}$$

and then by exploiting Eqs. (3.47) and (3.62) together with

$$\mathrm{Tr}[\rho(v)\,\mathbb{A}(k)\,\mathbb{A}(k')] = \mathrm{Tr}[\rho(v)\,\mathbb{A}^{\dagger}(k)\,\mathbb{A}^{\dagger}(k')] = 0, \tag{3.151}$$

for expressing the average over $\rho(v)$ of bilinears in the post-quench modes. The very same procedure applies to the energy density operator u_0 and it is not reported here for brevity. The expression of $\mathcal{J}^{E}(v)$ in Eqs. (3.63) and (3.64) with a change a variable $k \to \Omega(k)$ can be written as

$$\begin{aligned} \mathcal{J}^{E}(v) &= \int_{\Omega_{min}}^{\Omega_{max}} \frac{\mathrm{d}\Omega}{2\pi}\, \Omega\, (f^{-}_{\beta_l}(\Omega) - f^{-}_{\beta_r}(\Omega))\Theta(v_g(\Omega) - |v|) \\ &= \int_{\Omega_{-}(v)}^{\Omega_{+}(v)} \frac{\mathrm{d}\Omega}{2\pi}\, \Omega\, (f^{-}_{\beta_l}(\Omega) - f^{-}_{\beta_r}(\Omega)), \end{aligned} \tag{3.152}$$

where

$$\Omega_{\pm}(v) = \Omega(k_{\mp}(v)) = \sqrt{m^2 + 2(\omega^2 - v^2) \pm 2\sqrt{(\omega^2 - v^2 + mv)(\omega^2 - v^2 - mv)}},$$
$$= \sqrt{m^2 + 2(\omega^2 - v^2) \pm 2\sqrt{(v_{max}^2 - v^2)(y^2 - v^2)}}, \qquad (3.153)$$

and $k_{\pm}(k)$ is defined in Eq. (3.146) as the roots of the stationary-phase equations in Eq. (3.145). Integrating the expression in Eq. (3.152), the results reported in Eqs. (3.66) and (3.67) are eventually recovered by introducing the integral representation of the function $\Upsilon(x)$ in Eq. (3.68) [330]

$$\Upsilon(x) = \int_x^{\infty} \mathrm{d}y \frac{y}{\mathrm{e}^y - 1}. \qquad (3.154)$$

In order to determine the edge asymptotic of $\mathcal{J}^E(v)$ in Eqs. (3.66), (3.67) and (3.68) as $v \to \pm v_{max}^{\mp}$ we start by noting that $\Omega_+(v)$ and $\Omega_-(v)$ tend to coalesce in this limit to the value

$$\Omega(k_s) = \Omega_{\pm}(v_{max}) = \sqrt{m\sqrt{m^2 + 4\omega^2}}, \qquad (3.155)$$

where $k_s = k_{\pm}(v_{max})$ has been defined after Eq. (3.70). Therefore

$$\Omega_-(v) - \Omega_+(v) = -2\sqrt{v_{max}^2 - v^2} + \mathcal{O}\left((v_{max} - |v|)^{3/2}\right); \qquad (3.156)$$

correspondingly, for the function $\mathcal{Y}(\beta, v)$ in Eq. (3.67), one can write

$$\mathcal{Y}(\beta, v) = -\frac{1}{2\pi\beta^2}\beta[\Omega_+(v) - \Omega_-(v)]\Upsilon'(\beta\Omega(k_s)) + \mathcal{O}\left((v_{max} - |v|)^{3/2}\right)$$
$$= \frac{1}{2\pi}[\Omega_+(v) - \Omega_-(v)]\,\Omega_0\, f_{\beta}^{-}(\Omega(k_s)) + \mathcal{O}\left((v_{max} - |v|)^{3/2}\right), \qquad (3.157)$$

where the last step follows from the integral representation of $\Upsilon(x)$ in Eq. (3.154). Inserting Eq. (3.156) into Eq. (3.157) and eventually into Eq. (3.66), the result in Eq. (3.55) is obtained, i.e.,

$$\mathcal{J}^E = C_1\sqrt{v_{max}^2 - v^2} + \mathcal{O}\left((v_{max} - |v|)^{3/2}\right), \qquad (3.158)$$

with C_1 for the harmonic chain given by

$$C_1 = \frac{\Omega(k_s)}{\pi}[f_{\beta_l}^{-}(\Omega(k_s)) - f_{\beta_r}^{-}(\Omega(k_s))] = \frac{\Omega(k_s)}{\pi}\left(\frac{1}{\mathrm{e}^{\beta_l\Omega(k_s)} - 1} - \frac{1}{\mathrm{e}^{\beta_r\Omega(k_s)} - 1}\right). \qquad (3.159)$$

For the Ising chain C_1 in Eq. (3.55) is given by the same formula as Eq. (3.159) with the replacements $\Omega(k_s) \to \varepsilon(k_s)$ and $f_{\beta}^{-} \to f_{\beta}^{+}$. In this case when the transverse field approaches its critical value $h = h_c = 1$, as discussed in Subsecs. 3.3 and 3.4.1, $k_s \to 0$ and $\varepsilon(k_s) \to 0$. In the same limit, the Fermi-Dirac function approaches a finite value $f_{\beta}^{+}(k_s) \to 1/2$ and therefore C_1 vanishes. The leading edge

behavior can then be obtained by expanding the function $\mathcal{J}_1$ in Eq. (3.53) up to order $(v_{max}-v)^{3/2}$, as shown in Ref. [1], and it leads to Eq. (3.56). For the harmonic chain, instead, when the mass m is set to zero, the edge behavior is still expressed by Eq. (3.55): indeed, from Eq. (3.55), we see that $f^-_\beta(\Omega(k_s)) \to 1/(\beta\Omega(k_s))$ as $m \to 0$ and therefore Eq. (3.55) remains valid with $C_1 = 1/\pi(1/\beta_l - 1/\beta_r)$.

3.C Fine structure of the edge of the propagating front

In this Appendix we report the main steps about the calculations underlying the results of Subsec. 3.4.1 for the sub-diffusive corrections to the ballistic profiles of the energy current $\mathcal{J}^E$. In the following calculations we will refer to the harmonic chain, but the procedure for the Ising chain is analogous. At the end of the Section, instead, we will highlight the differences that are present when discussing the critical case, where for the Ising model the novel scaling form $K^c(X)$ in Eq. (2.35) emerges. The detailed calculations are in Ref. [1]. Based on the approach of the latter the hydrodynamic limit is taken directly by evolving in space and time the energy current operator, in Eq. (3.48) for the Ising and (3.60) for the harmonic chain, and eventually taking the trace over the initial state ρ_0 in Eq. (3.1). The final result result reads as

$$\mathcal{J}^E(x,t) = \int_{-\pi}^{\pi} \mathrm{d}k \int_{-\pi}^{\pi} \frac{\mathrm{d}k'}{2\pi}\, \mathrm{e}^{\varphi^+_{x,t}(k,k')} \left[I^r_{++}(k,k') + I^l_{++}(k,k') \right] g(k,k'), \tag{3.160}$$

where we have defined for brevity

$$g(k,k') = \frac{i\omega^2}{4}\left((\mathrm{e}^{-ik}-1)(\mathrm{e}^{ik'}+1)\sqrt{\frac{\Omega(k')}{\Omega(k)}} - (\mathrm{e}^{ik'}-1)(\mathrm{e}^{-ik}+1)\sqrt{\frac{\Omega(k)}{\Omega(k')}} \right), \tag{3.161}$$

and $I^{r,l}_{++}$ are given by Eq. (3.148) after replacing $\Omega(k)$ and $\Omega(k')$ in the numerator with $f^-_{\beta_{r,l}}(k)$ and $f^-_{\beta_{r,l}}(k')$, respectively:

$$I^l_{++}(k,k') = \frac{1}{4\pi i}\frac{f^-_{\beta_l}(k) + f^-_{\beta_l}(k')}{k'-k-2i\delta} \quad \text{and} \quad I^r_{++}(k,k') = -\frac{1}{4\pi i}\frac{f^-_{\beta_r}(k) + f^-_{\beta_r}(k')}{k'-k+2i\delta}. \tag{3.162}$$

From the previous expression, introducing the variables $Q = k - k'$, $K = (k + k')/2$ and expanding the phase $\varphi^+_{x,t}$ to first order in Q as in Eq. (3.149), one readily obtains Eqs. (3.64) and (3.152) as detailed in Appendix 3.B. Here, however, we are interested in the behavior of $\mathcal{J}^E(x,t)$ for $x \simeq v_{max}t$. In this case, Eq. (3.146) has a unique solution $k_s = k_\pm(v_{max})$ as $x \simeq v_{max}t$, as observed after Eq. (3.70), where the group velocity is maximum $v_g(k_s) = v_{max}$. The second derivative of $\varphi^+_{x,t}$ therefore vanishes and the leading correction to the ballistic profile is obtained by expanding to the third order in $k - k_s$ as in Eq. (3.71). In order to evaluate the integral in Eq. (3.160), with $\varphi^+_{x,t}$ expanded as in Eq. (3.71), from a saddle-point approximation around k_s we extend the integrals in Eq. (3.160) to the whole real line as the regions where k and k' are far away from k_s do not contribute. Since

the cubic term in Eq. (3.71) is expected to be the dominant one, it is convenient to introduce the variables

$$K = \left(\frac{v_{max}t}{2}\right)^{1/3}(k-k_s), \quad Q = \left(\frac{v_{max}t}{2}\right)^{1/3}(k'-k_s), \tag{3.163}$$

and the scaling variable X in Eq. (3.72). For the first contribution on the r.h.s. of Eq. (3.160) we find, after expanding the integrand around the saddle-point k_s,

$$\left(\frac{2}{v_{max}t}\right)^{1/3}\int_{-\infty}^{\infty}\frac{\mathrm{d}K}{2\pi}\int_{-\infty}^{\infty}\frac{\mathrm{d}Q}{2\pi}\frac{\mathrm{e}^{iKX+iK^3/3-iQX-iQ^3/3}g(K,Q)[f^-_{\beta_l}(K)+f^-_{\beta_l}(Q)]}{2i\,(Q-K-2i\delta)} = \left(\frac{2}{v_{max}t}\right)^{1/3}\Omega(k_s)v_{max}\,f^-_{\beta_l}(k_s)K^A(X,X), \tag{3.164}$$

where we have used the integral representation of the Airy kernel [326]

$$K^A(X,Y) = \int_{-\infty}^{\infty}\frac{\mathrm{d}K}{2\pi}\int_{-\infty}^{\infty}\frac{\mathrm{d}Q}{2\pi}\frac{\mathrm{e}^{iKY+iK^3/3-iQX-iQ^3/3}}{i(Q-K-i\delta)}. \tag{3.165}$$

For the second contribution, instead, a bit more care is needed: in fact, one can notice that the sign of the infinitesimal displacement δ in the integrand is opposite to that present in the definition of the Airy kernel in Eq. (3.165). The k' integral in Eq. (3.160) therefore avoids the pole at $k' = k$ from above and, by using the residue theorem, one can pull the integration contour below the pole, thereby changing the sign of δ in Eq. (3.160), at the price of subtracting the residue at $k' = k$. The latter is easily computed to be

$$-\int_{-\pi}^{\pi}\frac{\mathrm{d}k}{2\pi}\omega^2\sin(k)f^-_{\beta_r}(k) = -\int_{-\pi}^{\pi}\frac{\mathrm{d}k}{2\pi}\Omega(k)v_g(k)f^-_{\beta_r}(k) = 0, \tag{3.166}$$

and corresponds to the equilibrium value of the energy current for $v > v_{max}$, which is zero because, in the initial equilibrium state in Eq. (3.1), the current vanishes. This fact applies also to other physical quantities, for example the energy density, and the residue of the integral at $k = k'$ gives the equilibrium value of the observable outside the light-cone; this constant has to be added to the Airy kernel to give the correct edge-profile. Accordingly, the second contribution in Eq. (3.160) can be analyzed in the same way as we did for the first one in Eq. (3.164):

$$\left(\frac{2}{v_{max}t}\right)^{1/3}\int_{-\infty}^{\infty}\frac{\mathrm{d}K}{2\pi}\int_{-\infty}^{\infty}\frac{\mathrm{d}Q}{2\pi}\frac{\mathrm{e}^{iKX+iK^3/3-iQX-iQ^3/3}g(K,Q)[f^-_{\beta_r}(K)+f^-_{\beta_r}(Q)]}{2i\,(Q-K-2i\delta)} = \left(\frac{2}{v_{max}t}\right)^{1/3}\Omega(k_s)v_{max}\,f^-_{\beta_r}(k_s)K^A(X,X). \tag{3.167}$$

Inserting Eqs. (3.164) and (3.167) into Eq. (3.160), the results in Eqs. (3.73), (3.74), and (3.75) of the main text immediately follow (with the usual replacements $\varepsilon(k_s) \to \Omega(k_s)$ and $f^+_\beta \to f^-_\beta$). The derivation of the Airy kernel for the edge asymptotics of the Ising chain is totally analogous.

As outlined in Subsec. 3.4.1, on the contrary, in the quantum Ising chain when h approaches $h_c = 1$ Eq. (3.73) vanishes and a separate treatment is needed. Accordingly, one has to expand Eq. (3.160) up to the first non-vanishing order. For the Ising chain the usual replacements $\Omega(k) \to \varepsilon(k)$ and $f_\beta^- \to f_\beta^+$ have to be done in Eq. (3.160) and the function $g(k,k')$ is

$$g(k,k') = \frac{ihJ^2}{2}\left(\mathrm{e}^{-ik'} - \mathrm{e}^{ik}\right). \tag{3.168}$$

In particular, for $h = h_c$, the stationary point k_s of the phase $\varphi^+_{x,t}(k,k')$ turns out to be at $k = k' = k_s = 0$, approached from above for $x \simeq v_{max}t$ and from below for $x \simeq -v_{max}t$ (with $v_{max} = J$ from Eq. (3.51)). Correspondingly, the odd derivatives of the dispersion relation $\varepsilon(k)$ become discontinuous at $k = 0$ because $\varepsilon(k) = 2v_{max}|\sin(k/2)|$, and therefore one has to consider the proper limits, i.e.,

$$\lim_{k\to 0^\pm} \varepsilon'(k) = v_g(0^\pm) = \pm v_{max} \quad \text{and} \quad \lim_{k\to 0^\pm} \varepsilon^{(3)}(k) = \mp v_{max}/4, \tag{3.169}$$

while all the even derivatives vanish. As a consequence, by expanding up to third order in the phase $\varphi^+_{x,t}(k,k')$, for $x \simeq v_{max}t$, one finds (instead of Eq. (3.71) with $k_s = 0$)

$$\begin{aligned}\varphi^+_{x,t}(k,k') &= (k-k')(v_{max}t - x) - \frac{1}{3!}\frac{v_{max}}{4}(k^3 - k'^3)t + \mathcal{O}(k^5) \\ &= -\frac{1}{3}(K^3 - Q^3) - X(K-Q) + \mathcal{O}\left(t^{-2/3}\right),\end{aligned} \tag{3.170}$$

where we defined $k = (v_{max}t/8)^{-1/3}K$ and the scaling variable X in Eq. (3.77) which is analogous to Eq. (3.72), except for a numerical factor due to the fact that $\varepsilon^{(3)}(k_s)$ at the critical point is no longer $-v_{max}$ as in the non-critical case, but it is given by Eq. (3.169). The function $g(k,k')$ in Eq. (3.168) must be expanded up to first order in K and Q, since it vanishes identically at the lowest order,

$$g(k,k') = \frac{iJ^2}{2}\left(\mathrm{e}^{-ik'} - \mathrm{e}^{ik}\right) = \frac{J^2}{2}(K+Q)(v_{max}t/8)^{-1/3} + \mathcal{O}\left(t^{-2/3}\right), \tag{3.171}$$

Similarly, in order to determine the first non-vanishing order, one needs to expand the Fermi-Dirac distributions

$$\begin{aligned}f_{\beta_l}(k) + f_{\beta_l}(k') - f_{\beta_r}(k) - f_{\beta_r}(k') = [f'_{\beta_l}(0^+) - f'_{\beta_r}(0^+)](K+Q)(v_{max}t/8)^{-1/3} \\ + \mathcal{O}\left(t^{-2/3}\right)\end{aligned} \tag{3.172}$$

with $f_\beta(0^+) = -\beta v_{max}/4$. By inserting Eqs. (3.170), (3.171) and (3.172) into Eq. (3.160) one eventually finds Eq. (3.76) where

$$K^c(X) = \int_{-\infty}^{+\infty}\frac{\mathrm{d}K}{2\pi}\int_{-\infty}^{+\infty}\frac{\mathrm{d}Q}{2\pi}\frac{(Q+K)^2\,\mathrm{e}^{-iKX - iK^3/3}\mathrm{e}^{iQX + iQ^3/3}}{i(K-Q-2i\delta)}. \tag{3.173}$$

One can make the expression of K^c more explicit by taking a derivative with respect to X and then by using the integral representation of the Airy function

$$\mathrm{Ai}(X) = \int \frac{\mathrm{d}K}{2\pi} \mathrm{e}^{iKX + iK^3/3}, \tag{3.174}$$

and (3.75) in order to show that

$$\frac{\partial K^c(X)}{\partial X} = -2K^A(X, X). \tag{3.175}$$

The latter equation renders Eqs. (3.79) and, by integration, Eq. (3.78).

For the harmonic chain, instead, when the mass m is set to zero, as mentioned at the end of Appendix 3.B, $f_\beta^-(\Omega(k_s)) \to 1/(\beta\Omega(k_s))$ and Eq. (3.80) is obtained, with the scaling variable X in Eq. (3.77) as a consequence of the fact that for $m = 0$

$$\lim_{k \to 0^\pm} \Omega^{(3)}(k) = \mp v_{max}/4. \tag{3.176}$$

The qualitative shape of the kernel describing the sub-diffusive corrections is therefore in this case not altered upon setting $m = 0$.

Chapter 4

Inhomogeneous systems: Interacting integrable models

In the Chapter 3 the dynamics in the presence of inhomogeneous initial states was investigated and understood for non-interacting systems. Due to the breaking of translational invariance in the initial state, however, most of the techniques which apply to homogeneous quenches in interacting integrable systems do not carry over in the inhomogeneous realm. For example, no application of the quench action approach, introduced in Sec. 2.3 of Chapter 2, has been so far developed for initial inhomogeneous states. The analytic description of transport in isolated systems has been therefore initially limited to non-interacting systems, as in Chapter 3, conformal field theory and Luttinger liquids [344–347] (see also the references cited in Subsec. 1.4.2). Truly interacting systems were studied, so far, only numerically [348–352].

In this context the introduction of the *generalized hydrodynamics* (GHD) in Refs. [159, 160] has been a groundbreaking advancement. This theory is an extension of hydrodynamics to integrable systems: while Euler (Navier-Stokes) hydrodynamics describes fluids with a finite number of conservation laws, i.e., the energy, the number of particles, and the momentum, the generalized hydrodynamics concerns integrable systems, where an infinite number of conserved charges is present in the thermodynamic limit (see Subsec. 1.4.3). As a consequence, the generalized hydrodynamics is based on the generalized Gibbs ensemble, instead of the canonical Gibbs ensemble. In this perspective being the GHD an hydrodynamic theory, it describes situations where the inhomogeneity varies on length scales which are much larger than the microscopic ones, the latter being related to the mean distance among the microscopic constituents of the system. Under this condition, the system consists of locally homogeneous fluid-cells located at space-time points (x, t) exhibiting only small variations compared to their neighbouring cells. Within these cells the microscopic dynamics establishes local relaxation at time-scales faster than the global dynamics, whereby the system remains in a quasi-stationary state. Thus, the GGE and the thermodynamic Bethe ansatz, introduced in Subsec. 2.2.2 of Chapter 2, locally apply at every fluid cell, with the root density $\rho(\lambda)$ upgraded to be space and time dependent $\rho(\lambda) \to \rho(x, t, \lambda)$. The dynamics of the system is then efficiently studied by solving a set of differential equations for $\rho(x, t, \lambda)$, which have a form similar to that of the Euler (or Navier-Stokes) hydrodynamics equations. Since its introduction at the end of 2016 in Refs. [159, 160] the GHD formalism has been applied to a huge variety of non-equilibrium contexts, like systems with local defects [155, 353, 354], diffusive

effects [325, 355–357], and to open systems experiencing non-unitary dynamics [358, 359] (see also the references in Subsec. 1.4.3). Remarkably, the formalism applies also to non-integrable systems provided the integrability breaking term varies on large enough length scales [173, 360, 361].

In this Chapter we discuss two applications of GHD, which, as we shall see, are strongly intertwined. First, we study dynamical correlation functions, which measure the correlations between observables at different space-time points. We will focus on correlation functions emerging in a very general class of many-body states which are inhomogeneous and non-stationary. For this class of states, general expressions of dynamical correlation functions have been obtained in Ref. [177] exploiting the fluctuation-dissipation theorem in combination with GHD. The final result takes the form of a quite involved set of nonlinear integral equations, which, so far, were neither solved numerically, nor tested against microscopic simulations. In this Chapter, we will carry out these two necessary steps by numerically calculating the dynamical two-point correlations, in the generic theory of Ref. [177]. In particular we will investigate the propagation of correlations from inhomogeneous states in the Lieb-Liniger model, the relativistic sinh-Gordon model, and the classical hard-rod gas. In addition, we first compare our results against microscopic Monte Carlo simulations of the hard-rod model and we examine the time required to reach the hydrodynamic-limit of correlations. Second, for the same class of inhomogeneous and non-stationary states, we study the scaled cumulant generating function of the time-integrated current associated to some ballistically transported conserved charge. In the specific case, the conserved charge is the energy and the initial inhomogeneity is the partitioning protocol state: this problem can be considered the extension, in the more complex scenario of interacting systems, of the calculation presented in Sec. 3.5 of Chapter 3. As anticipated in Chapter 3, so far, the expression of the SCGF in this setup for *interacting* integrable systems has been derived only in homogeneous and stationary GGEs in Refs. [339, 340]. The analysis of the SCGF for inhomogeneous and non-stationary states has been so far limited to the results of Ref. [4] presented in Sec. 3.5 of the previous Chapter 3, which regards non-interacting systems. Our study of the SCGF thereby generalizes deeply the analysis of Refs. [339, 340] and of Ref. [4] by accounting for inhomogeneous situations and interactions, respectively. Given the universality of GHD, the expression obtained for the SCGF is applicable to any integrable model obeying the hydrodynamic equations, both classical and quantum.

This Chapter is organized as follows. In Sec. 4.1 we review the basic concepts of GHD that will be needed for our analysis. In Sec. 4.2 we first briefly review the expressions of the dynamical two-point functions in inhomogeneous and non-stationary states derived in Ref. [177] (Subsec. 4.2.1) and then we present our results from Ref. [3] regarding two-point correlation functions, see Subsecs. 4.2.2, 4.2.3, 4.2.4, and 4.2.5. In Sec. 4.3 we first define in Subsec. 4.3.1 the SCGF of the time-integrated current and then we review in Subsec. 4.3.2 the findings from Refs. [339, 340] for the SCGF in homogeneous and stationary states. The original results of Ref. [5] for the SCGF in interacting integrable models in inhomogeneous states are then presented in Subsecs. 4.3.3, 4.3.4, 4.3.5, 4.3.6. In Sec. 4.4 we draw our conclusions. Some technical aspects are in Appendix 4.

4.1 An introduction to the generalized hydrodynamics

In this Section we review the basic concepts underlying the generalized hydrodynamics theory that will be needed for the presentation of our results, that will follow in Secs. 4.2 and 4.3. Reference [173] and the lecture notes in Ref. [362] provide a very good review on the subject. In Subsec. 4.1.1 we recall the basic identities regarding the description of the GGE in the thermodynamic Bethe ansatz formalism. In Subsec. 4.1.2 we define the Euler-scaling limit for a generic local observable. In Subsec. 4.1.3 we briefly recall the derivation of the main GHD equations. In Subsec. 4.1.4 we specialize the discussion to the classical integrable hard-rod gas and we recall the main ingredients of its thermodynamic Bethe ansatz description. This model, being classical, can be simulated in a relatively easier way than quantum systems and therefore it represents an ideal benchmark to test the GHD equations. In Subsec. 4.1.5 we show how the partitioning protocol, discussed in Chapter 3, can be exactly solved in interacting integrable systems within the GHD theory.

4.1.1 Thermodynamic Bethe ansatz description of the GGE

We consider interacting integrable models in one spatial dimension, where, in the thermodynamic limit, an infinite number of local conserved charges $\{Q_i\}$ exists, with $[Q_i, Q_j] = 0$ and $i, j = 1, 2 \dots \infty$ (see also the introductory presentation in Subsec. 1.4.1). Since the charges Q_i are local, they can be written as $Q_i = \int \mathrm{d}x\, q_i(x)$, where the density q_i associated to the conserved charge Q_i obeys a continuity equation with the current density j_i, corresponding to the current $J_i = \int \mathrm{d}x\, j_i(x)$, written in the form[1]

$$\partial_t q_i(x) + \partial_x j_i = 0. \tag{4.1}$$

The GGE density matrix in Eq. (1.44) can be written as

$$\rho_{GGE} = \frac{\mathrm{e}^{-W}}{Z_{GGE}}, \qquad \text{where} \qquad W = \sum_i \beta^i Q_i. \tag{4.2}$$

For the Lagrange parameters in this Chapter we are using the superscript notation $\{\beta^i\}$ following the notation of Refs. [339, 340], but the superscript i has not to be confused with an exponent. Notice that the present discussion applies both to classical and quantum models. In the former case ρ_{GGE} is a statistical distribution in the phase-space, while in the latter is a density matrix. The TBA description introduced in Subsec. 2.2.2 for a thermal ensemble easily generalize to the GGE, which is then uniquely identified by the knowledge of the so-called pseudoenergy function $\varepsilon(\lambda)$, which, in turn, is determined by the non-linear integral equation

$$\varepsilon(\lambda) = w(\lambda) + \int \mathrm{d}\mu\, T(\lambda, \mu)\, F(\varepsilon(\mu)), \tag{4.3}$$

[1] We use in this Section the continuum space notation just for simplicity, but the discussion carries over to discrete lattice models, e.g., spin chains.

where $T(\lambda,\mu) = K(\lambda,\mu)/2\pi$ and $K(\lambda,\mu)$ is the differential two-body scattering phase. For the Lieb-Liniger, for example, $K(\lambda,\mu)$ is given in Eq. (2.35). $F(\varepsilon)$ is named free energy function and it depends on the statistics of the quasi-particles of the theory. $F(\varepsilon)$ has been already defined in Eq. (3.99) for fermions (as it is the case for the Lieb Liniger, see Eq. (2.45)) and for bosons. For classical particles, instead, $F(\varepsilon) = -\mathrm{e}^{-\varepsilon}$ (as for the hard-rod gas of Subsec. 4.1.4); $w(\lambda)$ is named source term and it is given by

$$w(\lambda) = \sum_i \beta^i h_i(\lambda), \tag{4.4}$$

where $h_i(\lambda)$ is the single particle eigenvalue of the conserved charge Q_i and β^i are the parameters of the GGE in Eq. (4.2). For the Lieb-Liniger model, for instance, they have been defined in Eq. (2.30) (we have changed the notation from $q_i(\lambda)$ to $h_i(\lambda)$ to avoid confusion with the density in Eq. (4.1)). We emphasize that the TBA description introduced in this Subsection is not restricted to the Lieb-Liniger model, which we have just used as a prototypical example to introduce the formalism, but it applies to all the models that can be solved by the Bethe ansatz. The only model-specific quantities in Eqs. (4.3) and (4.4) are the single-particle eigenvalues $h_i(\lambda)$, the scattering phase $T(\lambda,\mu)$, the free energy function $F(\varepsilon)$, and the spectral space $\int \mathrm{d}\mu$. The latter, as commented in Subsec. 4.1.1, in the cases where multiple quasi-particle species n are present, has to be enlarged to $\sum_n \int \mathrm{d}\mu$. In this Chapter only models with one type of quasi-particles will be considered. In the case of the repulsive Lieb-Liniger model, for example, the integration in μ in Eq. (4.3) ranges in $(-\infty,\infty)$, as already seen in Sec. 2.2 of Chapter 2. The source term $w(\lambda)$ of the integral equation in Eq. (4.3) uniquely fixes $\varepsilon(\lambda)$, with the thermal case corresponding to $w^{(th)}(\lambda) = \beta\lambda^2/2$. In an equivalent way, the GGE is identified by the root density $\rho(\lambda)$, or, equivalently, by the mode occupation function $\vartheta(\lambda)$ (see Eq. (2.36)), since the knowledge of the latter determines the average value of all the conserved charges $\{Q_i\}$ of the model, as we have seen in Subsec. 2.2.2. As a consequence, in the following, we will the denote the average of a local operator $\mathcal{O}(x,t)$ at point x and time t over the GGE in Eq. (4.2) as $\langle\mathcal{O}(x,t)\rangle_\vartheta = \langle\mathcal{O}(0,0)\rangle_\vartheta$, where the second equality follows from the fact that the GGE is homogeneous and stationary. The dependence of ϑ on λ will be omitted to simplify the notation.

4.1.2 The Euler scale

In this Chapter we consider the case in which an integrable system is initialized in some state ρ_0 which is inhomogeneous and non-stationary. The average of a local operator $\mathcal{O}(x,t)$ over a generic inhomogeneous state ρ_0 will be denoted as $\langle\mathcal{O}(x,t)\rangle$. In order to derive the hydrodynamic description of integrable systems evolving from an inhomogeneous initial state ρ_0 two assumptions are necessary

- Local relaxation or "local maximization of entropy principle" (an excellent book on this is Ref. [161]). This assumption amounts at considering inhomogeneities which slowly vary in space, such that the system locally relaxes to

a GGE:

$$\langle \mathcal{O}(x,t)\rangle \simeq \langle \mathcal{O}(0,0)\rangle_{\vartheta(x,t)}. \tag{4.5}$$

The space-time dependence is recovered, in the spirit of a local-density approximation, by promoting the GGE Lagrange multipliers $\{\beta^i\} \to \{\beta^i(x,t)\}$, and the mode occupation function $\vartheta \to \vartheta(x,t)$, to be dependent on the space-time point (x,t) where the operator is located.

- The existence of a continuity equation for each density $q_i(x)$ and the corresponding current $j_i(x)$, as in Eq. (4.1). Exploiting the continuity equation, the function $\vartheta(x,t)$, and therefore the GGE, can be evolved as a function of space and time.

Equation (4.5) becomes exact in the limit of infinite length scale of the variation of the inhomogeneity. In the case of large, but finite, length scales for the variation in space and time of the inhomogeneity, instead, Eq. (4.5) is only approximate. The limit where Eq. (4.5) becomes exact is usually named "Euler-scaling limit" or simply "Euler scale". Henceforth we will use both the names interchangeably. Let us emphasize that proving the validity of Eq. (4.5) is a formidably difficult task and it is similarly difficult to identify the microscopic parameters controlling the approximation in Eq. (4.5). Surely, the mean inter-particle distance should matter, but, in general, there is currently no proof for interacting deterministic systems of their large scale emergent hydrodynamic description. The only exception is provided by the hard-rod gas (see Subsec. 4.1.4), where Eq. (4.5) has been proved in Refs. [363, 364] (see also Chapter 3 of Ref. [161]) for a broad class of initial states and the emergence of the hydrodynamic equations has been established with mathematical rigor.

To make the discussion more concrete, here we introduce a particular class of inhomogeneous and dynamical initial states, which generalize the GGE in Eq. (4.2), which are given by

$$\rho_0 = \frac{1}{Z}\exp\left(-\sum_i \int_{\mathbb{R}} \mathrm{d}x\, \beta^i(x/z,0)\, q_i(x,0)\right). \tag{4.6}$$

In this expression z is a characteristic length scale which has to be large enough such that the Lagrange parameters $\{\beta^i\}$ are smooth functions of the position x. In the case the multipliers $\{\beta^i\}$ do not depend on space, the state ρ_0 is equivalent to the GGE in Eq. (1.44). For this reason, we will refer henceforth to ρ_0 as *inhomogeneous GGE*. In this Chapter, we will denote $\langle \dots \rangle_{\mathrm{inh},z}$ the averages over ρ_0 in Eq. (4.6). In the case of ρ_0 in Eq. (4.6) the Euler-scaling limit can be achieved by taking the limit where the length scale of the inhomogeneity $z \to \infty$ is infinite. In order not to have a trivial, homogeneous and stationary, limit, the space-time point (x,t) where the operator $\mathcal{O}$ is computed has to be rescaled by the same factor z. In formulas

$$\begin{aligned}\langle \mathcal{O}(0,0)\rangle_{\vartheta(x,t)} &= \lim_{z\to\infty} \langle \mathcal{O}(zx,zt)\rangle_{\mathrm{inh},z} \\ &= \lim_{z\to\infty} \frac{1}{Z}\mathrm{Tr}\left[\mathcal{O}(zx,zt)\exp\left(-\sum_i \int_{\mathbb{R}} \mathrm{d}x \beta^i(x/z,0) q_i(x,0)\right)\right].\end{aligned} \tag{4.7}$$

In Eq. (4.7) we have used for convenience the quantum-mechanical trace notation, for classical systems it has to be replaced by an integral in phase space. When one-point functions at (x,t) are considered, we will use the subscript $\vartheta(x,t)$ to denote averages over the homogeneous GGE (4.2) at (x,t) as done in Eqs. (4.5) and (4.7), consistently with the notation introduced in the previous Subsec. 4.1.1. In the original work presented in Secs. 4.2 and 4.3 we will consider initial inhomogeneous and dynamical states of the form of Eq. (4.6).

4.1.3 Hydrodynamical equations

Once the Euler-scaling limit in Eqs. (4.5) and (4.7) is assumed, it is rather simple to derive the hydrodynamic equations ruling the evolution of the system. In particular, the charge density in Eq. (4.1) is given by the TBA description (cf. Eqs. (2.37) and (2.38) in Subsec. 2.2.2 for the energy and the density of particles)

$$\begin{aligned}\langle q_i(x,t)\rangle \simeq \langle q_i(0,0)\rangle_{\vartheta(x,t)} &= \int \mathrm{d}\lambda\, h_i(\lambda)\rho(x,t,\lambda)\\ &= \int \frac{\mathrm{d}\lambda}{2\pi}\, h_i(\lambda)\vartheta(x,t)1^{\mathrm{dr}}(x,t,\lambda),\end{aligned} \tag{4.8}$$

where the dressing operation has been defined in Eq. (2.53), and we used Eq. (2.36) with $\rho^t(\lambda) = 1^{\mathrm{dr}}(\lambda)/(2\pi)$ from Eq. (2.34), together with, in the second equality, the following useful relation valid for an arbitrary function $g(\lambda)$ of the rapidity

$$\int \mathrm{d}\lambda g(\lambda)\vartheta(\lambda)h^{\mathrm{dr}}(\lambda) = \int \mathrm{d}\lambda g^{\mathrm{dr}}(\lambda)\vartheta(\lambda)h(\lambda). \tag{4.9}$$

In particular, all dressed quantities become functions of space and time, being determined by $\vartheta(x,t)$ via Eq. (2.51). The expression of the current in Eq. (4.1) has been first discovered in Refs. [159, 160] and it reads as

$$\begin{aligned}\langle j_i(x,t)\rangle \simeq \langle j_i(0,0)\rangle_{\vartheta(x,t)} &= \int \mathrm{d}\lambda\, v^{\mathrm{eff}}(x,t,\lambda)\rho(x,t,\lambda)h_i(\lambda)\\ &= \int \frac{\mathrm{d}\lambda}{2\pi}\,(E')^{\mathrm{dr}}(x,t,\lambda)\vartheta(x,t)h_i(\lambda),\end{aligned} \tag{4.10}$$

where $E(\lambda)$ is the bare single-particle energy eigenvalue and the effective velocity v^{eff} is given by

$$v^{\mathrm{eff}}(x,t,\lambda) = \frac{(E')^{\mathrm{dr}}(x,t,\lambda)}{1^{\mathrm{dr}}(x,t,\lambda)} = \frac{(E')^{\mathrm{dr}}(x,t,\lambda)}{(P')^{\mathrm{dr}}(x,t,\lambda)}, \tag{4.11}$$

where in the last equality we used that for non-relativistic models $P(\lambda) = \lambda$ (see, e.g., Eq. (2.28) for the Lieb Liniger). Keep in mind, however, that the second relation in Eq. (4.11) holds also for more general parametrizations of the momentum as a function of the rapidity. The effective velocity v^{eff} is a generalization of the group velocity v_g (see Chapter 3), which takes into account the interactions among the quasi-particles via the dressing operation. v^{eff} has been first defined

in Ref. [83] in the context of the light-cone spreading of correlations in homogeneous quantum quenches. Its physical meaning can be best understood in the "flea gas" algorithm of Ref. [365], where $v^{\rm eff}$ emerges as the effective velocity of a quasi-particle as the latter travels through the medium of the other quasi-particles, taking into account the shift the quasi-particle experiences during each scattering event. We stress that Eq. (4.10) falls outside of the historically developed TBA approach and it has been first proved in relativistically invariant quantum field theories in Ref. [160] and numerically tested in quantum spin chains in Ref. [159]. Later, it has been proved in a variety of contexts including quantum spin chains and classical models [366–372].

Inserting Eqs. (4.8) and (4.10) into the continuity equation (4.1), and assuming the completeness of the set of local (or quasi-local) charges $h_i(\lambda)$, the final GHD evolution equation turns out to be [159, 160]

$$\partial_t \rho(x,t,\lambda) + \partial_x [v^{\rm eff}(x,t,\lambda)\rho(x,t,\lambda)] = 0. \tag{4.12}$$

This equation can be equivalently written for the filling function (see Refs. [159, 160] for the details) as

$$\partial_t \vartheta(x,t,\lambda) + v^{\rm eff}(x,t,\lambda)\partial_x \vartheta(x,t,\lambda) = 0. \tag{4.13}$$

Equations (4.12) and (4.13) are the most important results of Refs. [159, 160] and are at the basis of the GHD theory. They express the fact that, at the Euler scale, the system is described by quasi-particles having a density in rapidity space $\rho(x,t,\lambda)$ and propagating with velocity $v^{\rm eff}$. Generalizations of Eqs. (4.12) and (4.13) to account for the presence of trapping potentials [173], diffusive corrections [325], space-time variations of the interaction terms of the Hamiltonian [360] and Markovian coupling to an external bath [358] have been further developed. For the deriving our results in Secs. 4.2 and 4.3 the form in Eqs. (4.12) and (4.13) will be sufficient.

As a final piece of introduction we mention that Eq. (4.13) admits a solution by the characteristic function, $\mathcal{U}(x,t,\lambda,t_0)$, encoding the position at time t_0 of the characteristic curve $x(\mathcal{U},t,\lambda,t_0)$ of the quasi-particle with rapidity λ that at time t is in x. The latter is defined as the curve tangent to the effective velocity $v^{\rm eff}$ in Eq. (4.11)

$$\partial_t x(\mathcal{U},t,\lambda,t_0) = v^{\rm eff}(x(\mathcal{U},t,\lambda,t_0)t,\lambda), \quad x(\mathcal{U},t_0,\lambda,t_0) = \mathcal{U}. \tag{4.14}$$

The function $\mathcal{U}(x,t,\lambda,t_0)$ is defined by inverting $x(\mathcal{U},t,\lambda,t_0)$ with the respect to the initial position $\mathcal{U}$, see Refs. [176, 183] for a detailed discussion. From Eq. (4.13), it is simple to see that the filling function $\vartheta(x,t,\lambda)$ is constant along the characteristic $\mathcal{U}(x,t,\lambda,t_0)$

$$\vartheta(x,t,\lambda) = \vartheta(\mathcal{U}(x,t;\lambda,t_0),t_0,\lambda)\ . \tag{4.15}$$

The characteristic function follows the same hydrodynamical equation as the filling function in Eq. (4.13)

$$\partial_t \mathcal{U}(x,t,\lambda,t_0) + v^{\rm eff}(x,t,\lambda)\partial_x \mathcal{U}(x,t,\lambda,t_0) = 0\ , \quad \mathcal{U}(x,t_0,\lambda,t_0) = x. \tag{4.16}$$

The characteristic function also solves a system of nonlinear integral equations [176] where time enters as a fixed parameter. The characteristic equation in Eqs. (4.15) and (4.16) is at the basis of the exact expression for Euler-scale dynamical correlation functions, which will be the object of Sec. 4.2. In the next Subsection, to make the discussion more concrete, we introduce the (classical) hard-rod gas as an example of a system whose hydrodynamics description is captured by the GHD.

4.1.4 The hard-rod gas

This model describes a set of N classical particles of rods $a > 0$ with positions $x_i \in \mathbb{R}$, corresponding to the center of the rods, and momenta $p_i \in \mathbb{R}$, with $i = 1, 2 \dots N$. The rods propagate freely in one spatial dimension except for elastic collisions, during which the two colliding particles exchange their velocities. The mass m of the rods will be henceforth set equal to 1, so that for p_i the names momentum and velocity will be interchangeably used. The concept of quasi particle is in this case very simple: a quasi particle with momentum p is a "label" which jumps from one rod to another during the collisions such that its velocity is conserved. For this reason, in this context, quasi-particles are also named velocity tracers; they follow linear trajectories in the space-time diagram (x, t) punctuated by instantaneous jumps of length a when a collision occurs. This is shown schematically in Fig. 4.1. Consequently, for a set of N rods there are N conserved

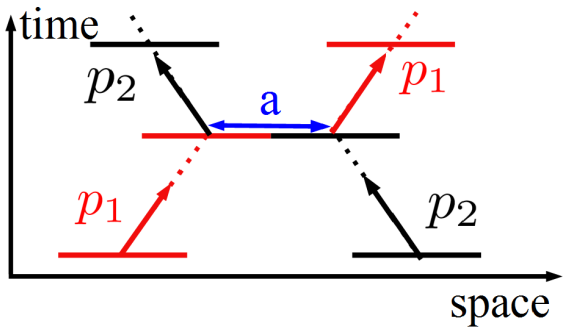

FIGURE 4.1: Schematic representation of the hard-rod dynamics. Two rods with momenta p_1, in red, and p_2, in black, upon colliding exchange their momenta. Quasi-particles can be considered as velocity tracers moving along linear trajectories punctuated by jumps of size equal to the rod length a (in blue in the figure). The trajectory of the quasi-particle with momentum p_1 is shown by the red-dashed, while the one of the quasi-particle with momentum p_2 by the black dashed.

quantities which corresponds to the quasi particles' velocities (assuming they are all different), whose values are fixed by the initial conditions of the rods. We can therefore define $n(x, \lambda, t)$

$$n(x, \lambda, t) = \sum_{i=1}^{N} \delta(x - x_i(t))\delta(\lambda - p_i), \tag{4.17}$$

whence $n(x, \lambda, t)dxd\lambda$ is the number of quasi-particles in the phase space volume element $(x, x + dx) \times (\lambda, \lambda + d\lambda)$. This quantity is conserved by the dynamics,

and, together with the associated current $j(x,v,t)$,

$$j(x,\lambda,t) = \sum_i \frac{\mathrm{d}x_i(t)}{\mathrm{d}t}\,\delta(x - x_i(t))\delta(\lambda - p_i), \tag{4.18}$$

it satisfies the continuity equation

$$\partial_t n(x,\lambda,t) + \partial_x j(x,\lambda,t) = 0. \tag{4.19}$$

Notice that the variable λ labels the continuity equation in the same way as the index i in Eq. (3.50). One can see that the present discussion has big similarities with the one in Subsec. 4.1.1 for Bethe ansatz integrable models, since stable quasi-particles with velocity p can be defined and an infinite number of conservation laws arise in the thermodynamic limit. As a matter of fact the hard-rod gas can be described with the TBA formalism, as first shown in Refs. [162, 179]. The TBA data of the model in particular are

$$E(\lambda) = \frac{\lambda^2}{2}, \quad p(\lambda) = \lambda, \quad T(\lambda,\mu) = -\frac{a}{2\pi}, \tag{4.20}$$

where $T(\lambda,\mu)$, defined in Eq. (4.3), has the meaning of the shift the quasi particle trajectory experiences during a two-body scattering (see again Fig. 4.1). The parametrization of the single-particle eigenvalues of the energy $E(\lambda)$ and of the momentum $p(\lambda)$ is simply the one of a classical Galilean gas of particles (with unit mass). Additional details about the TBA description of the hard-rod gas, and the expressions for its thermal distribution are provided in Appendix 4.A.

As anticipated in Subsec. 4.1.2, the emergence of the hydrodynamic equations for the hard rods has been rigorously proved in Refs. [363, 364] for a large class of initial states, see also Ref. [161] for a very detailed and clear analysis. In particular, in the Euler-scaling limit $\langle n(x,\lambda,t)\rangle = \rho(x,t,\lambda)$ and $\langle j(x,\lambda,t)\rangle = \rho(x,t,\lambda)v^{\mathrm{eff}}(x,t,\lambda)$ and Eqs. (4.8), (4.10), and (4.12) are recovered upon setting $h_0(\lambda) = 1$[2], since the particle current is considered. Moreover, in the case of Galilean invariant models, i.e., models invariant under the Galilean transformations of the rapidities, such as the hard-rod gas, it is simple to realize that Eqs. (4.8) and (4.10) coincide with the Euler equation of standard hydrodynamic when the number of particles and the momentum conserved charges are considered, as shown in Ref. [173]. In fact, for this class of models, $\langle j_0\rangle = \langle q_1\rangle$, which expresses the equality between the particle current and the momentum density. By defining the fluid velocity v, the mass density ρ_{fl} and the pressure $\mathcal{P}$

$$\langle q_0\rangle = \rho_{fl}, \quad \langle j_0\rangle = v\langle q_0\rangle, \quad \mathcal{P} = \langle j_1\rangle - \rho_{fl}v^2, \tag{4.21}$$

[2]We are keeping the same convention adopted for the the Lieb-Liniger model, cf. Eq. (2.30), to indicate by q_0, q_1 and q_2, respectively, the number, momentum and energy charges.

after some algebraic manipulations the difference between $\partial_t \langle q_1 \rangle + \partial_x \langle j_1 \rangle = 0$ and $\partial_t \langle q_0 \rangle + \partial_x \langle j_0 \rangle = 0$ can be written as

$$\partial_t v + v\, \partial_x v = -\frac{1}{\rho_{fl}} \partial_x \mathcal{P}. \tag{4.22}$$

The latter is just the Euler equation, which expresses the conservation of the mass and the momentum of the fluid. We remark that the Euler equation describes ideal fluids, where viscosity is absent. When the latter is included in Eq. (4.22) the Navier-Stokes equation is attained. The inclusion of viscosity terms into Eq. (4.12) can be accomplished by studying diffusive corrections to the Euler-scaling limit in Subsec. 4.1.2 when the length scale of the inhomogeneities is large, but finite. This has been performed in Refs. [325, 355–357]. Our results presented in Secs. 4.2 and 4.3 applies to the Euler scale description and we will not address diffusive corrections in this Chapter. Note, however, that diffusion is not prohibited in integrable systems and it has been, indeed, observed in a variety of contexts, e.g., in spin and charge transport in spin chains [342, 373–377]. It has been also argued in Ref. [378] that diffusion distinguishes interacting models from free ones, where it is absent as commented in Sec. 3.4. The diffusion in the hard-rod gas has been investigated in Refs. [161, 162, 364].

The advantage of considering the hard-rod gas is first that its TBA description is much simpler than the one of other integrable models, e.g., the Lieb-Liniger, since its two-body scattering shift T in Eq. (4.20) is independent of λ and μ. This simplifies the analysis of the TBA integral equations and eventually allows to prove a number of results, which can only be conjectured in other TBA solvable models. Second, the hard-rod fluid, being a classical system, is relatively simple to simulate and therefore it can be used as a benchmark to numerically test various predictions of the GHD theory. The latter aspect will be relevant for the analysis of Sec. 4.2, where the hard-rod gas will be exploited in order to test the GHD predictions for dynamical two-point correlation functions.

4.1.5 The first application: the partitioning protocol

We briefly review here the solution of evolution within the partitioning protocol, introduced in Chapter 3, available from GHD. The partitioning protocol has been the first application of the generalized hydrodynamics in the original Refs. [159, 160], and later it has been extensively studied both in spin chains [166–172], in relativistic models [163] and in classical systems [162, 165] (see also the references in Subsec. 1.4.3 of Chapter 1). The corresponding initial state ρ_0 is given by Eq. (4.6) with the generalized inverse temperatures chosen as

$$\beta^i(x,0) = \beta^i_r\, \Theta(x) + \beta^i_l\, \Theta(-x), \tag{4.23}$$

where $\Theta(x)$ is the Heaviside step function, with the same notation of Chapter 3. The thermal inhomogeneity discussed in Chapter 3 corresponds to having only a non-vanishing $\beta^2(x,0)$ coupled to the Hamiltonian H. All the other Lagrange parameters are initialized to zero. Notice that the inhomogeneity in Eq. (4.23) is not at all smooth and therefore one may wonder about the validity of the Euler-scaling

limit of Subsec. 4.1.2. However, as time increases, the flow of quasi-particles from one half of the system to the other smoothens the initial step inhomogeneity and smooth profiles of the densities and of the currents develop (see Figs. 3.2 and 3.3 in the case of non-interacting systems). At sufficiently long times, the Euler scale is therefore reached and the hydrodynamic description applies. The initial filling function $\vartheta(x,0,\lambda)$ corresponding to Eq. (4.23) is given by

$$\vartheta(x,0,\lambda) = \vartheta_r(\lambda)\,\Theta(x) + \vartheta_l(\lambda)\,\Theta(-x), \tag{4.24}$$

where $\vartheta_{l,r}$ are fixed by the boundary conditions one imposes on the left and right reservoirs. In the thermal case of Chapter 3, for example, $\vartheta_{l,r}$ is obtained as the solution of the Yang-Yang equation in Eq. (2.45) with Eq. (2.36). The initial fluid state in Eq. (4.24) can be propagated in time via Eq. (4.13). The solution, as detailed in Refs. [159, 160], is a set of states $\vartheta(\xi,\lambda)$ dependent on the ray $\xi = x/t$, given by[3]

$$\vartheta(\xi,\lambda) = \vartheta_r(\lambda)\,\Theta(\xi - v^{\rm eff}(\xi,\lambda)) + \vartheta_l(\lambda)\,\Theta(v^{\rm eff}(\xi,\lambda) - \xi). \tag{4.25}$$

Equation (4.25) in the non-interacting limit, in which the dressing is absent and $v^{\rm eff}(\xi,\lambda) = v_g(\lambda)$, reduces to Eqs. (3.48) (or (3.63) for bosonic quasi particles) for an initial thermal inhomogeneity. In this case, indeed, $\vartheta_{l,r}(\lambda)$ is simply given by the Fermi-Dirac (or Bose-Einstein) distribution at the corresponding temperature. For interacting systems, the evaluation of Eq. (4.25) is more difficult since $v^{\rm eff}(x,t,\lambda)$ depends on $\vartheta(x,t,\lambda)$ itself because of the dressing procedure in Eq. (4.11). Accordingly, Eq. (4.25) is therefore more conveniently solved iteratively starting from the initial bare expression $v_g(\lambda)$ of the velocity. This expression is then used in order to evaluate ϑ in Eq. (4.25). In turn, this value of ϑ is used to update the expression of the effective velocity in Eq. (4.11) and so forth. This procedure has been first tested in Refs. [159, 160] and it has been checked that it converges after few iterations. The expression for the charge and current densities are obtained by inserting $\vartheta(x,t,\lambda)$ in Eqs. (4.8) and (4.10). In order to give a concrete example we will use the hard-rod gas introduced in Subsec. 4.1.4. The solution in Eq. (4.25) has been derived for the hard-rod gas in Ref. [162], where it has been shown that it can be further simplified as

$$\vartheta(\xi,\lambda) = \vartheta_r(\lambda)\,\Theta(\lambda < \lambda_*(\xi)) + \vartheta_l(\lambda)\,\theta(\lambda > \lambda_*(\xi)), \tag{4.26}$$

with $\lambda_*(\xi) = g^{-1}(\xi)$ and g^{-1} the inverse of the function

$$g(x) = \lambda - a\left(\int_x^\infty {\rm d}\lambda\,\lambda\vartheta_l(\lambda) + \int_{-\infty}^x {\rm d}\lambda\,\lambda\vartheta_r(\lambda)\right) + a\lambda\left(\int_x^\infty {\rm d}\lambda\vartheta_l(\lambda) + \int_{-\infty}^x {\rm d}\lambda\vartheta_r(\lambda)\right). \tag{4.27}$$

In Fig. 4.2 we compare with the numerical simulations of the hard-rod fluid the exact Euler-scale solution for the particle density $n(x,t)$ and the associated current $\mathcal{J}_0$, obtained by solving Eqs. (4.26) and (4.27) and plugging the result into Eqs. (4.8) and (4.10) with $h_0(\lambda) = 1$. The left and right filling functions $\vartheta_{l,r}$ correspond to the thermal case at temperatures $\beta_{l,r}$. The corresponding expressions

[3] We have changed notation compared to Chapter 3 where we were using $v = x/t$ just to conform to the standard notation adopted in the generalized hydrodynamics literature.

are provided in Appendix 4.A, while details about the simulations of the hard-rod gas will be presented in Subsec. 4.2.3 and in Appendix 4.B. As one can see from Fig. 4.2, already at time $t = 1$ the Euler scale is reached and the dynamics is very accurately described by the generalized hydrodynamics. This is caused by the fact that the length-scale z where the density and the current are inhomogeneous at time $t = 1$ is of order $z \sim 200$; this value is much larger than the ones of the microscopic length-scales in the plot, i.e., the mean inter-particle distance and the rod length (see the caption of Fig. 4.2 for the numerical values).

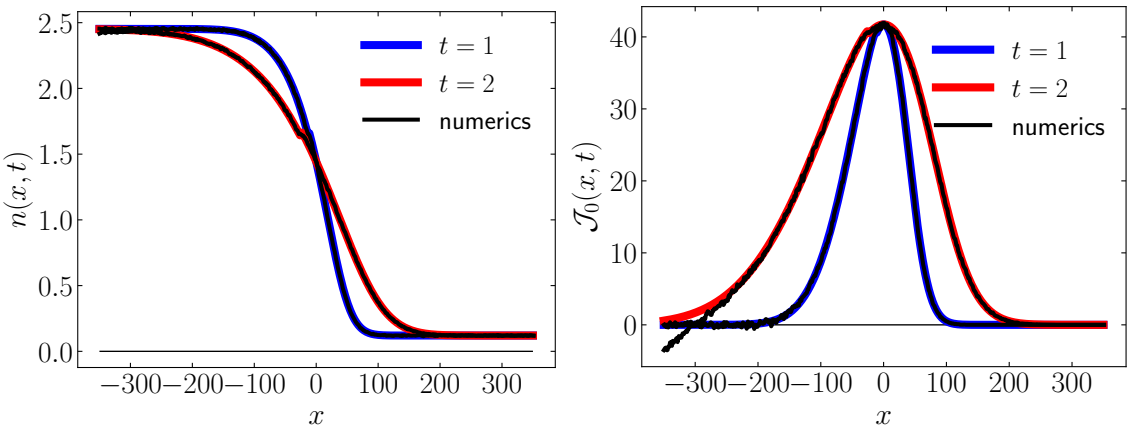

(a) (b)

FIGURE 4.2: (a) particle density $n(x,t)$ and (b) current $\mathcal{J}_0(x,t)$ are plotted as a function of space x for times $t = 1, 2$. The coloured lines are the exact Euler-scale profiles obtained by solving Eqs. (4.26) and (4.27) and plugging the result into Eqs. (4.8) and (4.10). In black the numerical simulations (see Appendix 4.B). The asymptotic states on the left and the right are thermal (see Appendix 4.A) at inverse temperatures $\beta_l = 0.001$ and $\beta_r = 10$ and densities $n_l(x,0) \simeq 2.45$ and $n_r(x,0) \simeq 0.12$. The rod length is $a = 0.2$. At time $t = 2$ the discrepancies between the exact and the numerical solution, as in the particle current profile close to $x \sim -300$, are due to finite-size effects of the simulations. Notice that the profiles are asymmetric as a function of x because the distribution of the velocities of the rods depends on $\beta_{l,r}$ and it is thereby inhomogeneous.

4.2 Dynamical correlations in inhomogeneous states

In this Section we present our findings from Ref. [3] for Euler-scale two-point correlation functions in inhomogeneous and non stationary states. Our results represent the first numerical evaluation of the exact expressions of Ref. [177]. These equations encode both the correlations due to fluid modes propagating along the flow, as well as subtle, "indirect" corrections resulting from the non-linearity of the fluid equations, which are present if the model is interacting. All aspects of the predicted correlations are reproduced by our numerical analysis, including the subtle indirect corrections. Moreover, we also provide the first numerical demonstration of the validity of the Euler-scale formulas in Ref. [177] by comparing them with Monte Carlo simulations of the microscopic hard-rod dynamics finding an excellent agreement.

In Subsec. 4.2.1 we review the main aspects of the corresponding derivation: in particular, we emphasize that the two-point correlation function decomposes into the sum of a *direct* term and an *indirect* one, where the latter encodes the inhomogeneity of the initial state. To demonstrate properties of correlations at the Euler scale we examine three different scenarios, whose hydrodynamical properties have already been well studied. First, in Subsec. 4.2.2, we calculate the spreading of correlations in a homogeneous system. The absence of inhomogeneities drastically simplifies the problem, as the indirect contribution to the correlations vanish. Next, in Subsec. 4.2.3, we consider the bump-release protocol and we study how the corresponding correlations spread in the classical hard-rod model. As already seen in Subsec. 4.1.5, this model is particularly convenient to simulate via numerical simulations which are close in spirit to Monte Carlo simulations, thus providing the opportunity to test the equations for Euler-scale correlations against simulations of the microscopic dynamics. In Subsec. 4.2.4, we examine reconsider the partitioning protocol. Although partial analytic predictions for the correlations in such a setup were made in Ref. [177], these in fact contain inaccuracies. Our numerical analysis unveils the full dynamics even at short time scales. Lastly, in Subsec. 4.2.5, we compare the light-cone spreading of correlations between a relativistic quantum field theory, the sinh-Gordon, and the non-relativistic Lieb-Liniger. For both the models a bump-release protocol is considered. The numerical evaluation of the dynamical two-point correlation functions has been performed via iFluid, an open-source framework for GHD calculations described in Ref. [379]. The code for calculating the propagator and two-point correlations has been integrated as a standalone module in the framework [380]. For brevity we do not report here the additional technical details about the numerical scheme for computing the correlation function, which can be found in Ref. [3]. Some details on the numerical simulations of the hard-rod gas are, instead, reported in Appendix 4.B.

4.2.1 Exact Euler scale correlations

The discussion of Sec. 4.1 focused on the Euler scaling of one-point functions (mean values) of local observables. Since for weak inhomogeneities the system is composed by locally homogeneous space-time fluid cells, one-point functions at the space-time point (x,t) can be computed based on the knowledge of their expression $\langle \mathcal{O} \rangle_{\vartheta(x,t)}$ in the local homogeneous GGE at (x,t) according to Eq. (4.7) (cf. also the discussion after Eqs. (3.41) and (3.46) in Chapter 3 regarding non-interacting models). Euler-scale connected correlation functions are, instead, harder to compute as they depend on the whole inhomogeneous state ρ_0 characterizing the initial state of the system, and not only on the homogeneous GGE on a specific fluid cell. The Euler-scaling limit of dynamical correlation functions can accessed via the frameworks of linear and nonlinear fluctuating hydrodynamics [381], and the theory of hydrodynamic projections [161, 179]. By focusing on the Euler-scale hydrodynamic equations and the propagation of long-lived modes, these methods allow one to extract exact asymptotic expressions for correlation functions along the propagation of such modes. However, these standard methods, as developed until now, are limited to correlation functions in homogeneous

and stationary states: they are based on (non)linear response mechanisms with respect to such states. Yet, out of equilibrium, the state of the many-body system is often inhomogeneous and non-stationary as we have seen.

A main feature of GHD is the quasi-stationary fluid state, implying that at every time slice at time t, fluid cells at separate space points are described by different GGEs and they are therefore uncorrelated. Thus, all equal-time, space-separated connected correlation functions vanish (that is, decay exponentially fast upon increasing the distance with a microscopic-scale correlation length). However, over time the propagation of quasi-particles causes quantities in separated fluid cells to become correlated in a non-trivial manner. Hence, dynamical connected correlations at the Euler scale can be viewed as initial delta-functions correlations, which over time ballistically spread and propagate throughout the system. In Ref. [177], an exact expression for such correlations in the inhomogeneous initial states of the form in Eq. (4.6) has been obtained.

The derivation is long and technical, but at least we want to convey the main ideas behind it. Consider a small perturbation of one Lagrange parameter $\beta_j(y,0) \to \beta_j(y,0) + \delta\beta_j(y,0)$ in the initial state ρ_0 in Eq. (4.6). The response of the system to the small perturbation of $\beta_j(y,0)$ is related to the connected correlation function involving the associated density $q_j(y,0)$. Consider the average of some other density $q_i(x,t)$ over ρ_0 in Eq. (4.6): the functional derivative of this average with respect to $\beta_i(y,0)$ is

$$-\frac{\delta}{\delta\beta_j(y,0)}\langle q_i(x,t)\rangle^{\mathrm{Eul}}_{\vartheta_0} = \langle q_i(x,t)q_j(y,0)\rangle^{c,\mathrm{Eul}}_{\vartheta_0},$$

with the Euler-scaling limit for the connected correlator defined as

$$\langle q_i(x,t)q_j(y,0)\rangle^{c,\mathrm{Eul}}_{\vartheta_0} = \lim_{z\to\infty} z\Big(\langle q_i(z\,x,z\,t)q_j(zy,0)\rangle_{\mathrm{inh},z} - \langle q_i(z\,x,z\,t)\rangle_{\mathrm{inh},z}\,\langle q_j(z\,y,0)\rangle_{\mathrm{inh},z}\Big). \tag{4.28}$$

In $\langle q_i(x,t)q_j(y,0)\rangle^{c,\mathrm{Eul}}_{\vartheta_0}$ the subscript ϑ_0 denotes the filling function which characterizes globally, as a function of space, the inhomogeneous state ρ_0 in Eq. (4.6) at the time slice $t = 0$ in the Euler-scaling limit $z \to \infty$. For the partitioning protocol initial state, for example, ϑ_0 is given in Eq. (4.24). This notation, where time appears as a lower index, stresses the fact that two-point correlation functions depend on the whole initial inhomogeneous state ϑ_0 of the system and not only on the homogeneous GGE $\vartheta(x,t)$ at a specific space-time fluid cell (x,t). For one-point functions, instead, we have denoted with $\langle q_i(x,t)\rangle^{\mathrm{Eul}}_{\vartheta_0} = \langle q_i(0,0)\rangle_{\vartheta(x,t)}$ the average over ρ_0 in Eq. (4.6) in the limit $z \to \infty$ according to Eq. (4.7) and in agreement with the notation introduced in Subsecs. 4.1.1 and 4.1.2. [One-point functions of the charge densities and of the associated currents are given in Eqs. (4.8) and (4.10), respectively.]

We emphasize that, for some specific models, the Euler-scale limit of two-point correlation functions requires additional care and $q_i(zx,zt)$, $q_j(zy,0)$ in the r.h.s. of Eq. (4.28) have to be averaged over space-time fluid-cells, as explained in Ref. [177] and shown in Ref. [163] for the classical sinh-Gordon field theory. For

the classical hard-rod gas considered in Ref. [3], instead, fluid-cell averaging is not necessary and the Euler-scale predictions for the two-point function are simply obtained by averaging in space.

Equation (4.28) represents an extension of the fluctuation-dissipation theorem of statistical mechanics [8] to the framework of GHD, where infinitely many conserved charges are present. The validity of Eq. (4.28) for classical systems is clear as it simply amounts to differentiation of the exponential function. For quantum systems additional care is required as additional terms related to the non-vanishing commutators $[q_i(x,0), q_j(x,0)]$ between the conserved densities are present. However, it has been shown in Ref. [173], that $[q_i(x,0), q_j(x,0)]$ can be expanded in terms of derivatives of local operators, which give a subleading contribution in the Euler-scaling limit. Indeed, the GGE density matrix enables the exact calculation of thermodynamic averages, but contains information only of the conserved charges, Q_i. Thus, the conserved charge densities, q_i, from which the Euler-scale two-point correlation functions are derived, are defined only up to a total spatial derivative of a local observable. However, in the Eulerian scaling limit any derivative corrections to q_i are expected to be vanishingly small, since the large-scale limit only probes long wavelengths (see Refs. [173, 177] for more details). From Eq. (4.28) an expression for the two-point connected correlation function $\langle q_i(x,t)q_j(y,0)\rangle^{c,\mathrm{Eul}}_{\vartheta_0}$ can then be derived exploiting the fact that the expression of the one point function on the l.h.s is known in Eq. (4.8), as shown in Ref. [177]. The latter result can then be extended to the connected two-point function of any pair of local observables $\langle \mathcal{O}(x,t)\mathcal{O}'(y,0)\rangle^{c,\mathrm{Eul}}_{\vartheta_0}$ via hydrodynamic projections [179]. The main idea of the latter is that at the Euler scale correlations are determined by the ballistically propagating conserved charges. Correlations can then be determined by "expanding" the operator $\mathcal{O}(x,t)$ of interest in the basis of the local (or quasi-local) conserved charges

$$\mathcal{O}(x,t) = \sum_{jk} q_j(x,t) \left(\mathsf{C}_{[\vartheta(x,t)]}\right)^{-1}_{jk} \langle q_k|\mathcal{O}\rangle_{\vartheta(x,t)}, \tag{4.29}$$

where the scalar product $\langle q_k|\mathcal{O}\rangle_{\vartheta(x,t)}$ is computed at the space-time point (x,t) of the observable as

$$\langle \mathcal{O}|q_k\rangle_{\vartheta(x,t)} = -\frac{\partial}{\partial\beta_k(x,t)}\langle\mathcal{O}\rangle_{\vartheta(x,t)} = \int \mathrm{d}\lambda\, \rho(x,t,\lambda) f(x,t,\lambda) V^{\mathcal{O}}(x,t,\lambda) h^{\mathrm{dr}}_k(x,t,\lambda)\,. \tag{4.30}$$

$f(x,t,\lambda)$ is dubbed statistical factor of the model. For models with fermionic quasi-particle statistics $f(x,t,\lambda) = 1-\vartheta(x,t,\lambda)$ (the case of Lieb-Liniger and sinh-Gordon), while for classical particle models $f(x,t,\lambda) = 1$. $V^{\mathcal{O}}$ in Eq. (4.30) is named one-particle-hole form factor of the operator $\mathcal{O}$, it a functional of the filling function defined such that Eq. (4.30) holds. It must be worked out for every operator individually. For charge densities and the associated currents they are very simple [179]

$$V^{q_i} = h^{\mathrm{dr}}_i \quad \text{and} \quad V^{j_i} = v^{\mathrm{eff}} h^{\mathrm{dr}}_i\,, \tag{4.31}$$

however, other observables, such as the vertex operators in the sinh-Gordon model have form factors with more complicated expressions (see Refs. [80, 177]

and Appendix 4.C). $C^{-1}_{\vartheta(x,t)}$ in Eq. (4.30) is the inverse of the correlation matrix (cf. Eq. (4.30) and Eq. (4.31) for V^{q_i})

$$(C_{\vartheta(x,t)})_{ij} = \langle q_i | q_j \rangle_{\vartheta(x,t)} = \int \mathrm{d}\lambda\, \rho(x,t,\lambda) f(x,t,\lambda) h_i^{\mathrm{dr}}(x,t,\lambda) h_j^{\mathrm{dr}}(x,t,\lambda). \quad (4.32)$$

The factor $C^{-1}_{\vartheta(x,t)}$ is introduced in Eq. (4.29) because the densities $\{q_i\}$ are not orthonormal under the scalar product $(C_{\vartheta(x,t)})_{ij} = \langle q_i | q_j \rangle_{\vartheta(x,t)}$ given in Eqs. (4.29) and (4.30). We will not attempt to justify the hydrodynamic projection identity in Eq. (4.29), a detailed and rigorous treatment is provided in Ref. [179]. For our purpose, it is sufficient to say that an exact formula for two-point correlations of generic local observables $\langle \mathcal{O}(x,t)\mathcal{O}'(y,0)\rangle^{c,\mathrm{Eul}}_{\vartheta_0}$ can be derived using Eq. (4.29) and the result for the two-point correlator of charge densities. The formula reads as

$$\langle \mathcal{O}(x,t)\mathcal{O}'(y,0)\rangle^{c,\mathrm{Eul}}_{\vartheta_0} = \int \mathrm{d}\lambda\, \rho(x,t,\lambda) f(x,t,\lambda) V^{\mathcal{O}}(x,t,\lambda) \left[\Gamma_{(y,0)\to(x,t)} V^{\mathcal{O}'}(y,0)\right](\lambda). \quad (4.33)$$

The square brackets in Eq. (4.33) denote the contraction

$$\left[\Gamma_{(y,0)\to(x,t)} h\right](\lambda) = \int \mathrm{d}\mu\, \Gamma_{(y,0)\to(x,t)}(\lambda,\mu) h(\mu)\,. \quad (4.34)$$

The propagator, $\Gamma_{(y,0)\to(x,t)}(\lambda,\mu)$, describes how the local quantity $V^{\mathcal{O}'}(y,0)$ travels through the system on a given trajectory, until it reaches the location x at time t. The propagator itself can be split into two terms

$$\Gamma_{(y,0)\to(x,t)}(\lambda,\mu) = \delta(y - \mathcal{U}(x,t,\lambda,0))\,\delta(\lambda-\mu) + \Delta_{(y,0)\to(x,t)}(\lambda,\mu)\,, \quad (4.35)$$

where each term has a clear physical interpretation. The first term is named *direct* propagator, it describes the motion of the quasi-particles along the characteristic curve $\mathcal{U}(x,t,\lambda,0)$ (see Eqs. (4.15) and (4.16) in Subsec. 4.1.3). Thus, of all the quasi-particles found at (x,t), only those with the suitable rapidity have arrived from the point $(y,0)$. Meanwhile, the second term is dubbed the *indirect* propagator, as it describes modifications to the correlations due to modifications of the quasi-particle trajectories from the inhomogeneity at $(y,0)$. Hence, all rapidities can in principle contribute to the indirect correlations. The indirect propagator encodes subtle effects, which are due to the presence of interactions and which come from the nonlinearity of the fluid equations. One of the goals of the analysis of Subsec. 4.2.3 is to confirm that these effects are present and correctly described by the indirect propagator. Inserting Eq. (4.35) into the two-point correlation formula of Eq. (4.33) yields

$$\begin{aligned}\langle \mathcal{O}(x,t)\mathcal{O}'(y,0)\rangle^{c,\mathrm{Eul}}_{\vartheta_0} = &\sum_{\gamma\in\lambda_\star(x,t,y)} \frac{\rho^t(x,t,\gamma)\vartheta(y,0,\gamma)f(y,0,\gamma)}{|\partial_\lambda \mathcal{U}(x,t,\gamma,0)|} V^{\mathcal{O}}(x,t,\gamma) V^{\mathcal{O}'}(y,0,\gamma) \\ &+ \int \mathrm{d}\lambda\, \rho(x,t,\lambda) f(x,t,\lambda) V^{\mathcal{O}}(x,t,\lambda) \left[\Delta_{(y,0)\to(x,t)} V^{\mathcal{O}'}(x,t)\right](\lambda),\end{aligned} \quad (4.36)$$

where the set $\lambda_\star(x,t,y,0) = \{\lambda : \mathcal{U}(x,t,\lambda,0) = y\}$ over which the sum on the first line runs contains only the rapidities of quasi-particles directly propagating the correlations. Following the therminology introduced after Eq. (4.35), the term on the first line of the r.h.s of Eq. (4.36) is named *direct correlator*, while the second term is dubbed *indirect correlator*. While the direct term is relatively simple to evaluate, the indirect term poses more of a challenge. The indirect propagator satisfies the linear integral equation

$$\left[\Delta_{(y,0)\to(x,t)}V^{\mathcal{O}'}\right](x,t,\lambda) = 2\pi\mathcal{D}(\mathcal{U}(x,t,\lambda,0),\lambda)\Bigg(\left[W_{(y,0)\to(x,t)}V^{\mathcal{O}'}\right](\lambda) + \\ + \int_{x_0}^{x}\mathrm{d}z\left(\rho^t(z,t)f(z,t)\left[\Delta_{(y,0)\to(z,t)}V^{\mathcal{O}'}(z,t)\right]\right)^{*\mathrm{dr}}(\lambda)\Bigg), \tag{4.37}$$

where the field $\mathcal{D}$ encodes the degree of inhomogeneity of the initial state (it is the "effective acceleration" of Ref. [173]), i.e.,

$$\mathcal{D}(x,\lambda) = \frac{\partial_x\vartheta(x,0,\lambda)}{2\pi\rho(x,0,\lambda)f(x,0,\lambda)}\,, \tag{4.38}$$

while the so-called source term reads

$$\left[\mathrm{W}_{(y,0)\to(x,t)}V^{\mathcal{O}'}\right](\lambda) = -\Theta(\mathcal{U}(x,t,\lambda,0)-y)\left(\rho^t(y,0)f(y,0)V^{\mathcal{O}'}\right)^{*\mathrm{dr}}(y,0,\lambda) \\ + \int_{x_0}^{x}\mathrm{d}z\sum_{\gamma\in\lambda_\star(z,t,y,0)}\frac{\rho^t(z,t,\gamma)\vartheta(y,0,\gamma)f(y,0,\gamma)}{|\partial_\lambda\mathcal{U}(z,t,\gamma,0)|}T^{\mathrm{dr}}(z,t,\lambda,\gamma)V^{\mathcal{O}'}(\gamma). \tag{4.39}$$

Note that, if the initial state is homogeneous $\vartheta(x,0,\lambda) = \vartheta(\lambda)$ and $\mathcal{D}$ in Eq. (4.38) vanishes, thus eliminating any indirect correlations. In the equations above $h^{*\mathrm{dr}}(\lambda) = h^{\mathrm{dr}}(\lambda) - h(\lambda)$ and $\Theta(x)$ is the Heaviside function, while x_0 is an *asymptotically stationary point*, which must be chosen such that $\vartheta_s(x;\lambda) = \vartheta_0(x;\lambda)$ for $x < x_0$ and $s \in [0,t]$ [176]. Accordingly, x_0 denotes the boundary for which disturbances of correlations have yet to spread within the time t. One could think of $x_0 = -\infty$, although for numerical simulations it is set as the first spatial gridpoint, which much be chosen sufficiently far away from the point y or any inhomogeneities. Note that in Eqs. (4.33)-(4.39) we have placed for convenience the operator $\mathcal{O}'(y,0)$ at the space-time point $(y,0)$. However, the very same formulas apply for the operator $\mathcal{O}'(y,t_0)$ at a generic time $t_0 \neq 0$ upon replacing $\mathcal{U}(x,t,\lambda,0)$ with $\mathcal{U}(x,t,\lambda,t_0)$, according to Eqs. (4.15) and (4.16), and similarly for all TBA quantities evaluated at the time 0. In particular, Eqs. (4.33)-(4.39) apply also in the case $t < 0$, where the operator $\mathcal{O}(x,t)$ is computed at a time earlier than $\mathcal{O}(y,0)$, and time ordering is not needed. This is a consequence of the fact that the Euler-scale equations (4.12) and (4.13), on which Eqs. (4.33)-(4.39) are based, are time reversible.

Solving Eq. (4.36) requires mostly the knowledge of quantities already available from the TBA and GHD frameworks, however, no numerical solution of

Eq. (4.37) and (4.39) have been currently shown. In Ref. [3] we give details about the iterative scheme for calculating the indirect propagator, while in the following Subsections, for brevity, we report only the results of our numerical analysis.

4.2.2 The homogeneous case

The spreading of Euler-scale correlations in a homogeneous system, $\vartheta(x,t,\lambda) = \vartheta(\lambda)$, is particularly simple because, correspondingly, $\mathcal{D} = 0$, causing the indirect propagator in Eq. (4.37) to vanish. Furthermore, the velocity of the quasi-particles does not depend on space, whereby the characteristic solution to Eq. (4.13) becomes $\mathcal{U}(x,t,\lambda,0) = x - v^{\mathrm{eff}}(\lambda)t$. Therefore, the the full propagator in Eq. (4.35) reduces to

$$\Gamma_{(y,0)\to(x,t)}(\lambda,\mu) = \delta(x-y-v^{\mathrm{eff}}(\lambda)t)\,\delta(\lambda-\mu)\,, \tag{4.40}$$

and the dynamic two-point correlation function of the zeroth charge density, $q_0 = n$, for $y = 0$ becomes

$$\begin{aligned}\langle n(x,t)n(0,0)\rangle^{c,\mathrm{Eul}}_{\vartheta_0} &= \int \mathrm{d}\lambda\, \delta(x-v^{\mathrm{eff}}(\lambda)t)\rho(\lambda)f(\lambda)h_0^{\mathrm{dr}}(\lambda)h_0^{\mathrm{dr}}(\lambda)\\ &= t^{-1}\sum_{\lambda\in\lambda_\star(\xi)}\frac{\rho(\lambda)f(\lambda)}{|\partial_\lambda v^{\mathrm{eff}}(\lambda)|}h_0^{\mathrm{dr}}(\lambda)h_0^{\mathrm{dr}}(\lambda)\,.\end{aligned} \tag{4.41}$$

In Eq. (4.41), $\lambda_\star(\xi)$ is the set of solutions to the equation $v^{\mathrm{eff}}(\lambda) = \xi = x/t$. Thus, the correlations spread at the same velocity as the quasi-particles move, while they diminish over time as t^{-1}. This formula was obtained in Ref. [179], and follows from a direct application of hydrodynamic projection methods. The decay in t^{-1} upon increasing t is a consequence of the continuum of hydrodynamic modes (parametrised by λ) on which the projection occurs – and thus this is a special property found in integrable models. Note, in models like the Lieb-Liniger, the sinh-Gordon model and the hard-rod gas, $v^{\mathrm{eff}}(\lambda)$ is a monotonically increasing function of λ. Hence, for any combination (x,t) the set $\lambda_\star(\xi)$ will contain only one element.
Computing the dynamical two-point correlation functions via Eq. (4.41) is remarkably straightforward, as the expression can be evaluated using only information available from the TBA without performing any hydrodynamical evolution of the system.

In Fig. 4.3, the density-density correlations calculated via the full formula in Eq. (4.36) and the simplified formula (4.41) are compared. The simulation was carried out for the Lieb-Liniger model in an homogeneous thermal state at inverse temperature $\beta = 1$, interaction strength $c = 1$, and chemical potential tuned to have a particle density of $\langle n(x,t)\rangle = 0.5$ (see Subsecs. 2.2.1 and 2.2.2 for the definition of the Lieb-Liniger model). Figure 4.3(a) depicts $\langle n(x,t)n(0,0)\rangle^{c,\mathrm{Eul}}_{\vartheta_0}$ and illustrates the aforementioned interpretation of the Euler-scale dynamic correlations; an initial delta function which spreads ballistically throughout the system. Since the quasi-particles move with the same velocity regardless of position and time, the solutions of the hydrodynamic equation (4.13) are constant on the ray

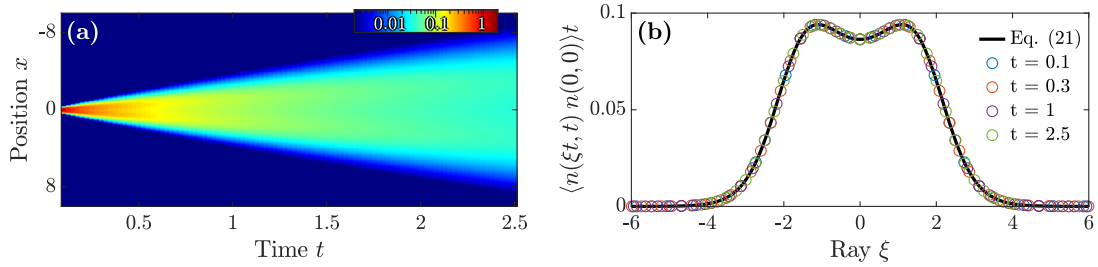

FIGURE 4.3: Two-point density correlation function in an homogeneous thermal state at inverse temperature $\beta = 1$ in the Lieb-Liniger model with interaction coupling $c = 1$. (a) Evolution of $\langle n(x,t)n(0,0)\rangle^{c,\mathrm{Eul}}_{\vartheta_0}$ evaluated via Eq. (4.36) and plotted using a logarithmic color axis. (b) Time-scaled correlations at selected times t plotted as circles against the ray ξ. The direct evaluation of Eq. (4.41) is plotted as a solid line and shows excellent agreement with the numerical implementation of the full formula from the homogeneous state. Simulation parameters can be found in the main text. Image taken from Ref. [3].

with fixed $\xi = x/t$, even at short timescales. This is exemplified in Fig. 4.3(b), where the two-point correlation function scaled by the time, t, is plotted as function of the ray, ξ. Here, correlations calculated via the full and the simplified formula overlap perfectly, as one would expect. The shape of the two-point correlation profile features a dip towards the center originating from the statistical factor $f(\lambda)$. In the TBA of the repulsive Lieb-Liniger model, the quasi-particles are fermions (despite the model describing a Bose gas). Hence, the statistical factor reads $f(\lambda) = 1 - \vartheta(\lambda)$ and the filling function is capped at one. For sufficiently low temperatures, a Fermi sea of quasi-particles can form at low rapidities, creating a barrier for other quasi-particles trying to pass through. While the system studied here is not cold enough to form a full Fermi sea, its filling function at low rapidities is still somewhat close to unit. Therefore, the propagation of correlations at lower rapidities (and by extension low values of ξ) is limited, causing the dip visible in Fig. 4.3(b).

4.2.3 Bump release and comparison with the hard-rod gas

Next, we study the spreading of correlations in the classical hard-rod model, introduced in Subsec. 4.1.4. As anticipated in Subsec. 4.1.4, and as already shown in Subsec. 4.1.5 for the partitioning protocol, thanks to its classical properties, this model is useful to test the GHD predictions against simulations of the microscopic dynamics. In this Subsection we directly compute the spreading of connected correlation functions via classical Monte Carlo simulations and therefore compare them with the Euler-scale formulas in Eq. (4.36).

For this demonstration, we turn to another well-studied protocol, namely the release of a density bump. In this protocol, a density accumulation (the bump) initially located around $x = 0$ is created by an inhomogeneous temperature profile. The density bump is then released at time $t = 0$ so that it expands in space. In addition, we also consider the more intricate case of the release of two bumps on top of a thermal background that initially do not overlap. Both setups are akin to what was studied experimentally in Ref. [184]. In Appendix 4.B further results

for the release of two density bumps are presented. The initial state of the system is a thermal inhomogeneous GGE, see Eq. (4.6), identified by the source term $w^{(th)}(x,\lambda) = \beta(x)\lambda^2/2$, cf. Eqs. (4.3), (4.4) and $h(\lambda) = \lambda^2/2$ the single particle energy eigenvalue of a Galilean invariant model in Eq. (2.51), where $\beta(x)$ for the two bumps problem is given by

$$\beta(x) = \beta_{as} + (\beta_{in} - \beta_{as})\, \mathrm{e}^{-((x-x_0)/z)^2}\Theta(x) + (\beta_{in} - \beta_{as})\, \mathrm{e}^{-((x+x_0)/z)^2}\Theta(-x); \tag{4.42}$$

for the single bump case a single Gaussian profile is considered:

$$\beta(x) = \beta_{as} + (\beta_{in} - \beta_{as})\, \mathrm{e}^{-(x/z)^2}. \tag{4.43}$$

In the expressions above z, cf. Eq. (4.6), is the length-scale of the inhomogeneity and it controls the smoothness of the space dependence of the bumps, $\pm x_0$ are the bumps positions (for simplicity we take them symmetric with respect to the origin), and β_{as}, β_{in} are the thermal background and the bump inverse temperatures, respectively. The thermal root density $\rho^{(th)}$ of the initial state at time $t = 0$ reads

$$\rho^{(th)}(x,0,\lambda) = \frac{\exp[(-w^{(th)}(x,\lambda) - W(a\, d(\beta(x)))]}{2\pi[1 + W(a\, d(\beta(x)))]}\,, \tag{4.44}$$

where $d(\beta) = 1/\sqrt{2\pi\beta}$, whereby the initial linear density of particles $n(x,0) = q_0(x,0)$ ($h(\lambda) = 1$ in Eq. (2.51)) is

$$\langle n(x,0)\rangle^{\mathrm{Eul}}_{\vartheta_0} = \int_{-\infty}^{\infty} \mathrm{d}\lambda'\, \rho^{(th)}(x,0,\lambda') = \frac{W(ad(\beta(x)))}{a[1 + W(ad(\beta(x)))]}. \tag{4.45}$$

Here $W(z)$ is the Lambert W function on its principal branch [330]. In the Monte Carlo simulations, at the initial time $t = 0$ rods are distributed in space according to Eq. (4.45) starting from some initial point $-L$ ($L > 0$), while the velocity of each rod is drawn from a Gaussian distribution with variance $1/\beta(x)$ dependent on the point x where the rod is initially located, according to Eqs. (4.42) (or (4.43)) and (4.44). From this initial condition, we then run the deterministic classical dynamics of the hard-rod gas. For each sample of the initial condition, the particle density $\langle n(x,t)\rangle_{\mathrm{MC}}$, and the density-density connected correlation function $t\,\langle n(x,t)n(0,0)\rangle^{c}_{\mathrm{MC}}$ multiplied by time t are acquired in the simulations by counting for each space point x the number of particles in an interval $(x - l/2, x + l/2)$ of length l both at time 0 and after some time t. The average of the aforementioned quantities with respect to many independent realizations of the initial rods' positions and velocities is eventually computed. We stress that only the initial configuration of the particles is random, while the dynamics is completely deterministic. More details about the Monte Carlo simulations are provided in Appendix 4.B.

The parameter z has to be chosen large enough such that $\rho^{(th)}(x,0,\lambda)$ is smooth and a sufficiently large number of rods is contained within the bump. In this way one can then expect that the hydrodynamic assumption of Subsec. 4.1.2 applies and the root density $\rho^{(th)}(x,0,\lambda)$ in Eq. (4.44) can be propagated in time according to the GHD equation (4.13). The bumps positions x_0 are consequently to be

taken large so that the two bumps do not initially overlap. The bump inverse temperature β_{in} is fixed so that the density close to the bumps at $x \sim \pm x_0$ is high and rods are densely distributed, thereby making interactions among the particles relevant for the dynamics. The thermal background density is set by β_{as} and is needed to avoid to consider space regions with no particles, which could cause deviations from the Eulerian limit of Subsec. 4.1.2. In particular, β_{as} is taken larger than β_{in} in order for the background density to be smaller than the bump density. Furthermore, since the variance of the rods velocity distribution is $1/\beta(x)$, particles from the background density intervals move slower than the ones initially located in the bumps and the dynamics is therefore characterized by the propagation of the particles from the hot high-density bump regions to the cold low-density background. In particular, for short times each of the two density peaks evolves independently of the other, while for large enough times the density in the central background region, around $x = 0$, increases as a consequence of the arrival of the rods from both the bumps, thereby inducing correlations among the particles coming from the left and the right density peak.

For the single-bump the parameters used in the Monte Carlo simulations are the following: $N = 200$, $z = 200$, $\beta_{in} = 1$, $\beta_{as} = 10$, $a = 0.1$, $L = 460$ and $l = 10$. The number of samples M is $1.5 \cdot 10^6$ for $t = 15$, $5 \cdot 10^6$ for $t = 30$ and $12 \cdot 10^6$ for $t = 45$. Meanwhile, the parameters of the double bump release read: $x_0 = 300$, $\beta_{as} = 10$, $z = 120$, $\beta_{in} = 0.2$ and $a = 1$. The number of rods used in the Monte Carlo simulations is $N = 210$, $L = 660$ and $l = 10$. For $t = 15$ and $t = 30$ we use $2 \cdot 10^6$ samples, while for $t = 70$ and 90, since the noise in the simulations increases, the sampling is enlarged to $7 \cdot 10^6$ and $8 \cdot 10^6$ samples, respectively.

The results are shown in Fig. 4.4, where they are compared against GHD predictions for various values of time t. One can see in Fig. 4.4 that the time evolution $\langle n(x,t) \rangle$ of the density from the initial condition (4.42) ((4.43)) with (4.45) matches the GHD predictions for all the times t values displayed in the figure. For the two-point correlations, on the other hand, for short times ($t = 15$ in Fig. 4.4(b) and $t = 15, 30$ in Fig. 4.4 (d)) discrepancies between the Monte Carlo simulations and Euler-scale results are evident. These differences are absent for longer time scales ($t = 30, 45$ in Fig. 4.4(b) and $t = 70, 90$ Fig. 4.4(d)) so that correlations are well reproduced by their Euler scale limit. The discrepancies can be quantified by looking at the relative distance σ between the results of the two methods

$$\sigma = \frac{\left[\int \mathrm{d}x \, \left(t \, \langle n(x,t)n(0,0)\rangle^{c,\mathrm{Eul}}_{\vartheta_0} - t \, \langle n(x,t)n(0,0)\rangle^{c}_{\mathrm{MC}}\right)^2\right]^{1/2}}{\left[\int \mathrm{d}x \, \left(t \, \langle n(x,t)n(0,0)\rangle^{c,\mathrm{Eul}}_{\vartheta_0}\right)^2\right]^{1/2}}, \tag{4.46}$$

which is reported in Fig. 4.4(b),(d).

A subtle aspect of Eq. (4.36) is the presence of the indirect propagator (4.37). As mentioned, the direct propagator, the first term in Eq. (4.36), represents the direct contribution of the normal modes (the quasi-particles), where correlations are due to the direct transport of quasi-particle along their trajectories within the inhomogeneous, non-stationary state. The indirect propagator is a correction to this, and is due to nonlinearity of the GHD equations: in a linear-response picture

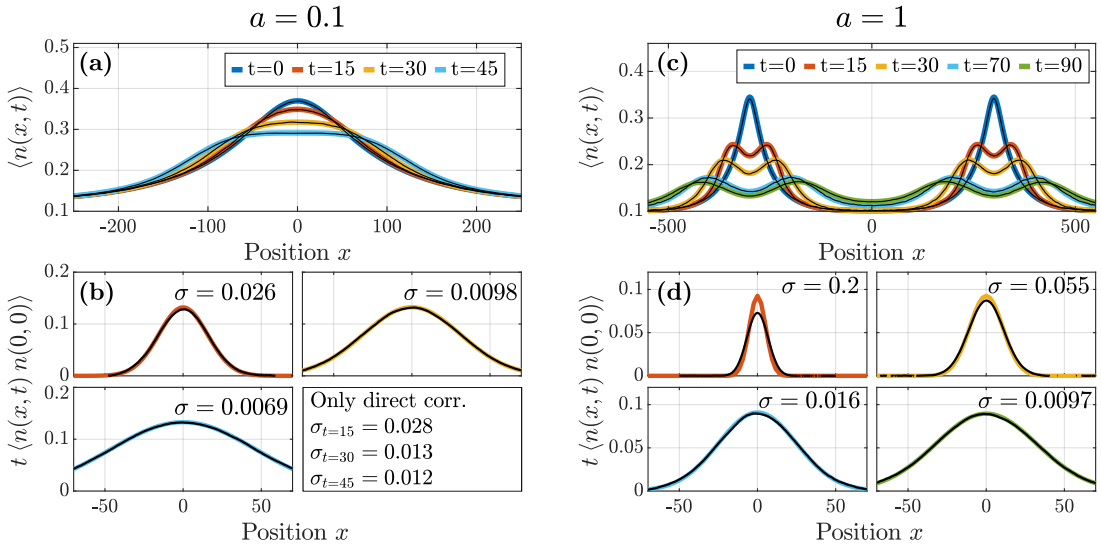

FIGURE 4.4: Bump releases in the classical hard-rod model for two different rod lengths $a = 0.1$ ($a = 1$). Panels (a) and (b) refer to the single bump case, while panels (c) and (d) to the two bumps setup. Results were calculated using GHD (colored lines) and Monte Carlo methods (black lines). Parameters of the Monte Carlo simulations are specified in the main text. (a,c) Comparison of the evolution of the density. (b,d) Comparison of two-point connected correlation function $t\,\langle n(x,t)n(0,0)\rangle$ for various values of time ($t = 15, 30, 45$ in the single bump protocol and $t = 15, 30, 70, 90$ in the two bumps setup) along with the distance σ in Eq. (4.46) between the two methods. The additional panel shows the distances when only accounting for the direct correlations (see Eqs. (4.35) and (4.36)). Image taken from Ref. [3].

of the correlation function, it encodes the effects of the local disturbance of normal mode λ on normal mode λ'. In our numerical analysis, we observe that this correction is extremely small, the dominant part of the correlation function coming from direct propagation. However, the correction is nonzero, and, as we report in Fig. 4.4(b), neglecting it renders the agreement with the simulation slightly worse. The subtle effect of indirect propagation is therefore explicitly observed.

We stress that this is the first comparison against numerical simulations of the formulas for the inhomogeneous Euler-scale correlation functions in Eqs. (4.36), (4.37) and (4.39) of Subsec. 4.2.1. In the simpler homogeneous thermal framework, Euler-scale correlation functions have been compared in Ref. [163] against Monte Carlo simulations for the classical sinh-Gordon field theory. In the latter case, results of the simulations oscillate at all times around the GHD predictions and fluid cell averaging is necessary in order to integrate them out. In the present study, on the contrary, the agreement between the classical simulations of the dynamics and the hydrodynamic expression of correlation functions become evident at larger times without the need of any further averaging procedure.

4.2.4 The partitioning protocol

We now turn our attention to the partitioning protocol, where two homogeneous, semi-infinite systems are joined together at the point $x = 0$ at time $t = 0$.

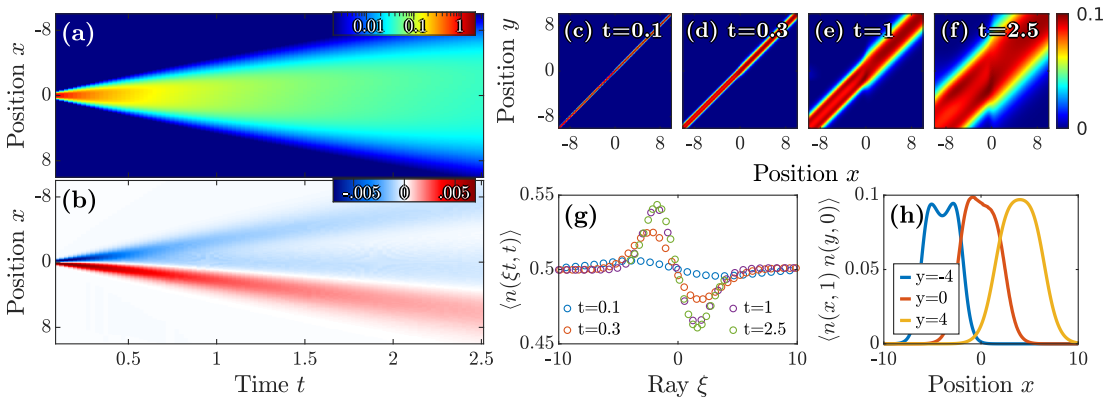

FIGURE 4.5: Two-point density correlation function of partitioning protocol in the Lieb-Liniger model. (a) *Direct*, dynamical two-point correlations for $y = 0$ plotted on logarithmic color axis. (b) *Indirect*, dynamical two-point correlations for $y = 0$. (c-f) Time-scaled correlation matrices, $t\,\langle n(x,t)n(y,0)\rangle^{c,\mathrm{Eul}}_{\vartheta_0}$, at selected times. (g) Linear density as function of the ray $\xi = x/t$ at selected times, t. (h) Cuts of the correlation matrix at $t = 1$ for different values of y. The value of the various parameters used in the simulations are reported in the main text. Image taken from Ref. [3].

In this protocol the two subsystems have different initial root densities causing a flow of charges between the two subsystems once they are joined together. This protocol has been discussed within the GHD formalism in Subsec. 4.1.5, where we have also shown an example of the corresponding dynamics in the hard-rod fluid, see Fig. 4.2. The initial fluid state ϑ_0 is given in Eq. (4.24). In this Subsection, instead, we study the partitioning protocol in the Lieb-Liniger model, where two thermal states at different inverse temperatures $\beta_l = 1$ and $\beta_r = 0.5$, but equal particle density $\langle n\rangle_l = \langle n\rangle_r = 0.5$ and interaction strength $c = 1$, are merged. As we have seen in Subsec. 4.1.5, the temperature difference alone causes a net flow from the hot side (right) towards the cold (left), as quasi-particles in the hot side are generated according to a distribution different than that characterizing the quasi-particles on the cold half. The standard partitioning protocol features an abrupt transition between the two subsystems, however, this setup is not suitable for numerical calculation of correlations, as the initial inhomogeneity $\mathcal{D}$ of Eq. (4.38) is evaluated via finite difference. Instead, we employ a softened transition achieved via a steep hyperbolic tangent temperature profile. Meanwhile, the chemical potential was adjusted in order to maintain a constant linear density across the system.

In Fig. 4.5 we have plotted several quantities showing the propagation of density-density correlations, $\langle n(x,t)n(y,0)\rangle^{c,\mathrm{Eul}}_{\vartheta_0}$. Subfigures 4.5(a) and 4.5(b) depict the spreading of the direct and indirect correlations for $y = 0$ respectively. Starting with the *direct* correlations, they appear very similar to the correlations in the homogeneous setup showcased in Fig. 4.3. This is somewhat expected, as the partitioning setup is (initially) piece-wise homogeneous with linear densities equal of the system in Sec. 4.2.2. Upon closer inspection of Fig. 4.5(a), one might notice slightly higher correlations at the negative side (seen more clearly in Fig. 4.5(h)). This asymmetry reflects the net flow of quasi-particle from right to left,

which is further exemplified in Fig. 4.5(g) showing the formation of the distinct, self-similar density profile as function of the ray, ξ. Moving on to the *indirect* correlations, we observe that the indirect correlations initially are antisymmetric around $x = 0$. As time passes, the indirect correlations become more asymmetric due to the flow of particles.

The partitioning protocol is interesting from the point of correlations, since the inhomogeneities are very localized around $x = 0$, where the subsystems are joined. Therefore, it is interesting to vary y such that it is not necessarily centered on the inhomogeneity. Subfigs. 4.5(c-f) display the time-scaled correlation matrices, $t\,\langle n(x,t)n(y,0)\rangle^{c,\mathrm{Eul}}_{\vartheta_0}$. Here, one clearly sees how the correlations start as delta functions, whereafter the propagate ballistically throughout the system. As the quasi-particles from the hot subsystem in general move faster, so do the correlations in that side propagate more rapidly. We see this in the correlation matrices, where one half of the correlations extend farther. Furthermore, towards the edges of the correlation matrices the correlations appear homogeneous, whereas around $x, y \approx 0$ a transition occurs. These three regions: the left side, the center, and the right side, are further explored in Subfig. 4.5(h), where $\langle n(x,1)n(y,0)\rangle^{c,\mathrm{Eul}}_{\vartheta_0}$ is plotted for $y = -4, 0, 4$. The $y = 0$ profile we have already discussed: it is skewed toward the left due to the particle flow. Meanwhile, the remaining two profiles are the result of placing the point y within the homogeneous subsystems. The left subsystem exhibit a correlation profile very similar to the homogeneous system in Sec. 4.2.2, as the two systems have identical temperatures. Again, the visible dip in correlations in the center of the profile is due to the high filling factor at lower rapidities present in the colder system. Conversely, the right profile exhibit no dip, as the subsystem is too hot to form any Fermi-sea-like quasi-particle distribution, whereby correlations can propagate freely even at low rapidity.

4.2.5 Comparing the light-cones of different models

In this Subsection we illustrate the difference in the spreading of correlations between a relativistic quantum field theory, the sinh-Gordon model (see Appendix 4.C for the basic definitions regarding this model), and the non-relativistic Lieb-Liniger model. The initial state in Eq. (4.6) in this case has a finite homogeneous inverse temperature β and it presents an inhomogeneity in the chemical potential multiplier $\beta^0(x) = \mu(x)$ coupled to the density of particles q_0. For the Lieb-Liniger model, the chosen value of the inverse temperature is $\beta = 0.25$, the coupling is $c = 1$, and the chemical potential $\mu(x) = 2 - 2x^2$ (we are slightly changing notation here since in the Lieb Liniger model we denoted the chemical potential with h in Eq. (2.45) of Chapter 2). For the sinh-Gordon model the value of the inverse temperature is $\beta = 0.25$, and we have $\alpha = 0.0369$, $m = 0.9989$, and $\mu(x) = 2 - 2x^2$. The inhomogeneous chemical potentials $\mu(x)$ determine an initial inhomogeneous profile with a bump centred in the origin $x = 0$, as shown in panel (c) and (g) of Fig. 4.6. At time $t = 0$ the chemical potential is suddenly set to zero so that the system evolves according to an homogeneous Hamiltonian and therefore with the GHD equation in Eq. (4.12). Hence, Fig. 4.6 displays the correlations from a bump release in the two models. In the Lieb-Liniger model, the quasi-particle group velocity is directly proportional to its rapidity. Thus, the

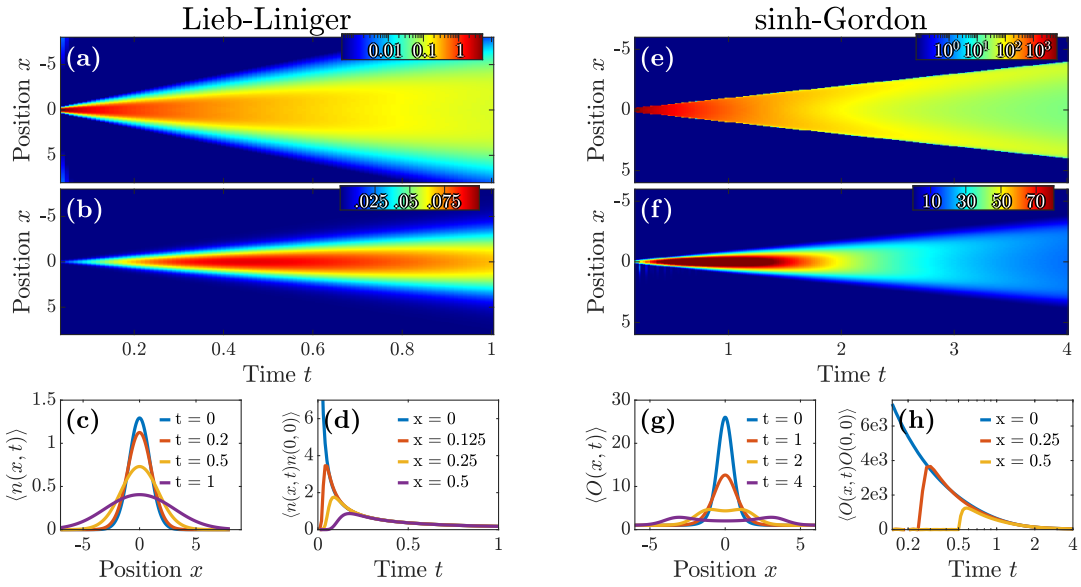

FIGURE 4.6: Two-point correlations, $\langle \mathcal{O}(x,t)\mathcal{O}'(0,0)\rangle^{c,\mathrm{Eul}}_{\vartheta_0}$, of bump releases in the Lieb-Lininger and sinh-Gordon model. The chosen operators of the Lieb-Liniger model are $\mathcal{O} = \mathcal{O}' = n$, while they for the sinh-Gordon are $\mathcal{O} = \mathcal{O}' = \mathrm{e}^{2g\phi}$. (a,e) *Direct*, dynamical two-point correlations plotted on logarithmic color axis. (b,f) *Indirect*, dynamical two-point correlations. (c,g) Evolution of the operator expectation value. (d,h) Evolution of the full correlations at various points in space. Image taken from Ref. [3].

quasi-particles have a spectrum unbounded from above and there is no maximum velocity, causing the emerging light cone of the direct correlations to have a smooth edge. Meanwhile, the group velocity in the relativistic sinh-Gordon model is bounded, as it scales a $v_g(\lambda) \sim \tanh\lambda$. Thus, the light cone of its direct correlations has a characteristic sharp edge. This is related to the discussion of Subsec. 1.3.5 of Chapter 1 and in particular to the findings of Ref. [91], where smoothened light-cone effects have been observed for an homogeneous quench of the interaction constant in the Lieb-Liniger model. Similar effects have been observed also in Ref. [92] for a local quench, where a localized defect at $x = 0$ between two identical non-relativstic free fermionic field theories is considered. Interestingly, the indirect correlations of the two models are fairly similar, and do not reflect the quasi-particle velocities to the same extent. Instead, the indirect correlations are mainly determined by the inhomogeneity of the system, which is fairly similar in the two cases (both are bump releases). Unlike the direct correlations, the indirect correlations do not decrease monotonically but in fact increase at first. We can understand this from the definition of the indirect correlations, in Eqs. (4.35), (4.37) and (4.39), namely how they are a consequence of the change in quasi-particle trajectories due to inhomogeneity. Over time, more and more particle will cross the point $y = 0$, thus increasing the indirect correlations. Meanwhile, as the correlations disperse, they start trailing of as $\sim t^{-1}$. These two competing effect produces the light cones observed in Fig. 4.6.

4.3 The SCGF for inhomogeneous states

In this Section we consider the calculation of the scaled cumulant generating function of time-integrated currents of ballistically transported conserved quantities for interacting integrable models (both classical and quantum). The analysis applies to the class of inhomogeneous and non-stationary GGEs in Eq. (4.6). As we shall see, this computation can be seen as a direct application of the results of Sec. 4.2 for the inhomogeneous two-point correlation functions, in the sense that once the validity of the latter is proved, the SCGF can be readily expressed in terms of the propagator $\Gamma_{(y,0)\to(x,t)}$ in Eq. (4.35). The calculation of the SCGF, as a matter of fact, is based on the biasing of the measure of the initial state by the exponential of the time-integrated current, in a similar way as the procedure followed in Refs. [339, 340]. The biasing of the measure is shown to be fixed by the knowledge of two-point correlation functions in inhomogeneous GGEs, discussed in Sec. 4.2. Our derivation accordingly shows that the study of two-point correlation functions in GHD [177–179] is tightly related to the large-deviation theory of current fluctuations. The biasing technique developed in Ref. [340], generalised here to inhomogeneous, dynamical situations, is in principle applicable to a wide class of hydrodynamic systems, integrable or not. In this Section, however, we concentrate on integrable systems, where all the necessary technical tools are available for the technique to lead to calculable results. At the same time, the expression of the SCGF allows to extend the analysis of Sec. 4.2 to account for n-point correlation functions through the cumulant expansion.

In Subsec. 4.3.1 we first define the Euler-scaling limit as $z \to \infty$ of the SCGF $G(s,x,t)$ for initial inhomogeneous GGEs states as in Eq. (4.6). In Subsec. 4.3.2 we then start by reviewing the results from Refs. [339, 340] regarding homogeneous and stationary states, since they will be important for our analysis. In Subsec. 4.3.3 we state the main result from Ref. [5] of this Section regarding the derivation of an exact expression for $G(s,x,t)$ in inhomogeneous and non-stationary GGEs, see Fig. 4.7. The result applies to any interacting integrable model admitting a TBA description, thereby encompassing quantum field theories (sinh-Gordon, Lieb Liniger), classical gases (hard-rods) and quantum spin chains (XXZ). We report here just the final results and all the formulas necessary for the numerical evaluation of $G(s,x,t)$. In Subsec. 4.3.4 we present the derivation of this result. In Subsec. 4.3.5 we present the results regarding the cumulants expansion of the SCGF. In Subsec. 4.3.6 we particularize the general result of Subsec. 4.3.3 to non-interacting systems. In the latter case we show that when energy transport is considered the result of Sec. 3.5 in Chapter 3 is eventually recovered.

4.3.1 Definition of the SCGF for inhomogeneous GGEs in the Euler-scaling limit

Considering the continuity equation in Eq. (4.1), each conserved density satisfies, for a particular density q_{i_*} denoted by the subscript i_* we define the time-integrated current

$$\Delta q_{i_*}(x,t) = \int_0^t \mathrm{d}\tau\, j_{i_*}(x,\tau). \tag{4.47}$$

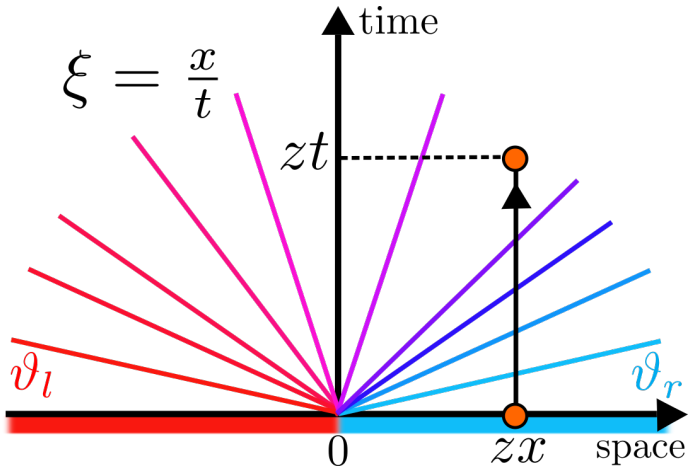

FIGURE 4.7: Schematic representation of the fluctuations of the time-integrated current in the Euler-scaling limit. In the Figure we consider, as an example, the partitioning protocol inhomogeneous state, discussed in Subsec. 4.1.5. We consider the time integral $\Delta q_{i_*}(zx,zt) = \int_0^{zt} \mathrm{d}\tau\, j_{i_*}(zx,\tau)$ of the current j_{i_*}, associated to the conserved charge q_{i_*}, flowing across the point zx over the time interval $(0,zt)$. The fluctuations of $\Delta q_{i_*}(zx,zt)$ in the Euler-scaling limit are encoded in the SCGF $G(s,x,t) = \lim_{z\to\infty} 1/(zt) \ln \langle \exp(s\,\Delta q_{i_*}(zx,zt))\rangle_{\mathrm{inh},z}$. In the case depicted in the Figure, the average $\langle \dots \rangle_{\mathrm{inh},z}$ is taken over the partitioning protocol inhomogeneous state. We emphasize, however, that the formula for $G(s,x,t)$ derived in this Section applies more generally to a wide class of inhomogeneous and dynamical states varying at large scales z. Image taken from Ref. [5].

q_{i_*} could denote, for example, the energy, the particle or any other density of the model. For the energy charge one has $q_{i_*} = q_2$ and $\Delta q_2(x,t) = \Delta e(x,t)$, defined in Eq. (1.48) of Chapter 1. As we have seen in Chapter 3, for ballistic motion, these quantities are expected to obey the large deviation principle. Here, as we are interested in the Euler-scaling limit, the SCGF is defined as

$$G(s,x,t) = \lim_{z\to\infty} \frac{1}{zt} \ln \langle \exp(s\,\Delta q_{i_*}(zx,zt))\rangle_{\mathrm{inh},z} = \sum_{k=1}^{\infty} \frac{s^k}{k!} c_k(x,t). \tag{4.48}$$

The average is taken over the rescaled inhomogeneous state ρ_0 in Eq. (4.6). Note that in the particular case where ρ_0 is taken as the partitioning protocol initial state considered in Chapter 3 in Eq. (3.1), then Eq. (4.48) coincides with Eq. (3.81). Equation (4.48) thereby generalizes the analysis of Chapter 3 by accounting for fluctuations from a broader class of inhomogeneous and dynamical GGEs states (which include the partitioning protocol initial step inhomogeneity as a particular case) and for interactions. Equation (4.48) serves to define the meaning of the probability $p(J_{i_*})$, with $J_{i_*} = \Delta q_{i_*}/t = J_2 = J_E$ in Eq. (1.49) of Chapter 1, which depends on the initial state, and therefore in particular on z; it is the scaling in z as per Eq. (4.48) that gives rise to the asymptotic equality represented by "$\asymp$" in the large deviation principle in Eq. (1.49). From the knowledge of $G(\lambda,x,t)$

in Eq. (4.48), one can obtain by Taylor expansion the cumulants $\{c_k\}$ of the time-integrated current, which are defined as

$$c_k(x,t) = \lim_{z\to\infty} \frac{1}{zt} \langle [\Delta q_{i_*}(zx,zt)]^k \rangle^c_{\text{inh},z} = \frac{1}{t} \int_0^t \mathrm{d}t_1 \cdots \int_0^t \mathrm{d}t_k \, \langle j_{i_*}(x,t_1) \dots j_{i_*}(x,t_k) \rangle^{c,\text{Eul}}_{\vartheta_0}, \tag{4.49}$$

where the Euler-scaling limit of the k-point connected correlation function $\langle \mathcal{O}(x_1,t_1) \dots \mathcal{O}(x_k,t_k) \rangle^{c,\text{Eul}}_{\vartheta_0}$ of a local observable $\mathcal{O}$ is defined in a similar way as in Eq. (4.28) for the two-point function [177][4]:

$$\langle \mathcal{O}(x_1,t_1) \dots \mathcal{O}(x_k,t_k) \rangle^{c,\text{Eul}}_{\vartheta_0} = \lim_{z\to\infty} z^{k-1} \langle \mathcal{O}(zx_1,zt_1) \dots \mathcal{O}(zx_k,zt_k) \rangle^c_{\text{inh},z}. \tag{4.50}$$

The validity of the large deviation principle in Eq. (1.49) implies that all that the connected correlation functions $\{\langle [\Delta q_{i_*}(zx,zt)]^k \rangle^c_{\text{inh},z}\}$ scale as z, with the cumulants $\{c_k\}$ being therefore finite and the series expansion in Eq. (4.48) being valid in some interval of s around the origin.

4.3.2 The SCGF for homogeneous GGEs: review of the result

In Refs. [339, 340] a general approach has been developed to compute $G(s,x,t)$ in Eq. (4.48) in the case the state ϑ_0 is the *homogeneous* GGE in Eq. (4.2). In this case, because of the homogeneity of the GGE, $G(s,x,t) = G(s)$, similarly to the case discussed in Eq. (3.85) of Chapter 3. The following discussion in this Subsection applies to the calculation of $G(s)$ in this homogeneous setup.

The analysis of Refs. [339, 340] relies on the GHD description of the Euler scale hydrodynamics. In particular, we need to introduce the so-called *flux jacobian* matrix, A^j_i

$$A^j_i = \frac{\partial \langle j_i \rangle}{\partial \langle q_j \rangle}. \tag{4.51}$$

with i the row index and j the column one (the notation is borrowed from Ref. [362]), which will play an important role in the analysis of this Section. This matrix describes how the average currents depends on the average densities and therefore it depends on the equation of state of the model. In the case of integrable systems, where the averages in Eq. (4.51) are computed over the homogeneous GGE in Eq. (4.2) as per Eqs. (4.8) and (4.10), an expression for the matrix elements of A^j_i can be given by means of the hydrodynamic projection formalism, as shown in Ref. [179]. In the basis of the single-particle eigenvalues $\{h_i(\lambda)\}$ the matrix A^j_i reads

$$A^j_i = \int \mathrm{d}\lambda \, h^{\text{dr}}_i(\lambda) \, v^{\text{eff}}(\lambda) \, h^j_{\text{dr}}(\lambda), \tag{4.52}$$

[4] As in the case of two-point functions, at the Euler scale, time-ordering is not necessary in the definition of k-point connected correlations. Fluid-cell averaging might, instead, be needed in Eq. (4.50), as discussed after Eq. (4.28).

with the effective velocity $v^{\rm eff}(\lambda)$ given in Eq. (4.11). $h^i_{\rm dr}(\lambda)$ denotes the orthonormal conjugate function of $h^{\rm dr}_i(\lambda)$, which satisfies the orthogonality and completeness relations

$$\begin{aligned}\int {\rm d}\lambda\, h^j_{\rm dr}(\lambda)\, h^{\rm dr}_i(\lambda) &= \delta^j_i,\\ \sum_j h^j_{\rm dr}(\lambda)\, h^{\rm dr}_j(\lambda') &= \delta(\lambda-\lambda'),\end{aligned} \tag{4.53}$$

respectively. Notice that the matrix A^j_i in integrable systems is infinite-dimensional, yet it can be formally defined. Moreover, for the following analysis the relations in Eqs. (4.52) and (4.53) will be sufficient. From Eqs. (4.52) and (4.53) the eigenvalue equation for A^j_i readily follows as

$$\sum_j A^j_i\, h^{\rm dr}_j(\lambda) = v^{\rm eff}(\lambda)\, h^{\rm dr}_i(\lambda), \tag{4.54}$$

which shows that the flux jacobian has a continuous spectrum indexed by the rapidity λ with eigenvalue the effective velocity $v^{\rm eff}(\lambda)$. In order to compute $G(s)$ one then biases the GGE measure in Eq. (4.2) by multiplying it by the exponential of the time-integrated current appearing in Eq. (4.48). Averages over this tilted measure become dependent on the parameter s conjugate to the time-integrated current $\langle\mathcal{O}\rangle_{\vartheta(0;s)}$. In Subsec. 4.3.4 we will explain this procedure in more details, for the moment we just report the main result for the *flow equation* from Ref. [339, 340]. The flow equation describes how the state ϑ_0, which for this Section is the homogeneous GGE in Eq. (4.2), is modified by the insertion of the exponential of the time-integrated current. Fundamentally, the s modified state $\vartheta(0;s)$ is still an homogeneous GGE, yet with Lagrange parameters $\{\beta^n\}$ dependent on s. This aspect is captured by the flow equation, which can be written as

$$\frac{\partial\beta^n(s)}{\partial s} = -{\rm sgn}\,(A(s))^n_{i_*}\,, \tag{4.55}$$

where the sign of the flux jacobian is obtained by diagonalizing the latter and by taking the sign of its eigenvalues. For interacting integrable systems, from Eq. (4.52), this implies

$${\rm sgn}\,(A)^j_i = \int {\rm d}\lambda\, h^{\rm dr}_i(\lambda)\, {\rm sgn}(v^{\rm eff}(\lambda))\, h^j_{\rm dr}(\lambda). \tag{4.56}$$

By inserting Eq. (4.55) into Eq. (4.3) and by taking the derivative with respect to s, the flow equation can be recast in a form where the dependence of the pseudoenergy $\varepsilon(\lambda;s)$ on s is exposed

$$\frac{\partial\varepsilon(\lambda;s)}{\partial s} = -{\rm sgn}(v^{\rm eff}(\lambda;s))h^{\rm dr}_{i_*}(\lambda;s). \tag{4.57}$$

Notice that, as a consequence of Eq. (4.55), all the dressed quantities, which depend on the GGE state, acquire an additional dependence on the parameter s.

Exploiting Eqs. (4.55), and equivalently (4.57), the SCGF $G(s)$ can be eventually computed as

$$G(s) = \int_0^s \mathrm{d}s' \langle j_{i_*}(0,0)\rangle_{\vartheta(0,0;s')}, \tag{4.58}$$

where we stress that the current expectation on the r.h.s. is taken over the homogeneous GGE and it is thereby given by Eq. (4.10). In Eq. (4.58) we have extended the notation introduced after (4.5) for the average over the local, homogeneous GGE $\vartheta(0,0;s')$ at the space-time point $(0,0)$ by including the additional dependence on s because of the biasing of the measure. Equations (4.55) (or equivalently Eq. (4.57)) and (4.58) are two main results of Refs. [339, 340] and they are the necessary equations to compute $G(s)$. First one has to solve numerically Eq. (4.57) to fix the dependence of the state on s, and then the result must be plugged into Eq. (4.58) to get $G(s)$. This procedure has been carried on in Ref. [339] for the classical hard-rod gas and for the quantum Lieb-Liniger model, where $G(s)$ has been computed in the homogeneous steady state developing at long times in the partitioning protocol. In the classical hard-rod fluid, moreover, the cumulants obtained from the series expansion of $G(s)$ in Eq. (4.58) have been compared against Monte-Carlo simulations, analogous to the ones discussed in the previous Subsec. 4.2, finding an excellent agreement and thus corroborating the validity of the approach. In concluding this Subsection we mention that the flow equation in Eq. (4.55) can be proved, as shown in Ref. [340], solely on the basis of linear fluctuating hydrodynamics and hydrodynamics projections [161, 381] without the need of using any tool coming from integrability. Only in deriving the form in Eq. (4.57) the TBA machinery is exploited. The expression for $G(s)$ in Eq. (4.58) together with Eq. (4.55) is therefore expected to apply more generically to any system, integrable or not integrable, displaying ballistic transport. However, so far, no confirmation of Eqs. (4.55) and (4.58) has been carried on for non-integrable models, the only specific cases addressed so far are the integrable Lieb-Liniger and the hard-rod gas, as discussed above.

4.3.3 The SCGF for inhomogeneous GGEs: statement of the result

When ϑ_0 in Eq. (4.48) corresponds to the *inhomogeneous* and *non-stationary* GGEs, as in Eq. (4.6), the evaluation of $G(s,x,t)$ is much more difficult and has not been considered before. In this Subsection we report the results from Ref. [5], which provides the first expression for the SCGF for inhomogeneous and non-stationary states in the form of ρ_0 in (4.6) in the Euler-scaling limit $z \to \infty$ as in Eq. (4.48). The derivation will be detailed in the next Subsec. 4.3.4.

Consider the inhomogeneous state ρ_0 in Eq. (4.6), $G(s,x,t)$ defined in Eq. (4.48) can be computed as

$$G(s,x,t) = \frac{1}{t}\int_0^s \mathrm{d}s' \int_0^t \mathrm{d}\tau\, \langle j_{i_*}(0,0)\rangle_{\vartheta(x,\tau;s')}\,, \tag{4.59}$$

where the average current, following the notation introduced in Sec. 4.2, is evaluated on the homogeneous GGE $\vartheta(x,\tau;s')$ in Eq. (4.2) and it is therefore given

by Eq. (4.10). The fundamental difference with respect to the homogeneous case, using the same extension of the notation introduced for Eq. (4.58), is that the GGE $\vartheta(x,\tau;s')$ depends not only on the parameter s' as a consequence of the biasing of the measure in Eq. (4.6) via the exponential of the time-integrated current, but also on the (scaled) space-time coordinates (x,τ) of the fluid cell, because, for every deformation parameter s', the state is inhomogeneous and non-stationary.

To be accurate, the bias of the measure by the exponential of the time integral of the current as in Eq. (4.48), depends not only on s, but also on the parameters x, t characterising the (scaled) space-time position of the integration interval (see, for instance, Fig. 4.7). Therefore, an average at the fluid cell (x',t') in the deformed state should be denoted as $\langle\dots\rangle_{\vartheta(x',t';x,t,s)}$. For lightness of notation, we keep implicit the x,t dependence of the bias itself in the fluid-cell average notation; these can be considered as fixed parameters throughout. The dependence on s is important, as for instance this is integrated over in Eq. (4.59).

As in the homogeneous case, the s dependence is described by a flow equation for $\beta^n(x',t';s)$, which in the inhomogeneous case is however significantly more complex than Eq. (4.55)

$$\frac{\partial\beta^n(x',t';s)}{\partial s} = -\int_0^t \mathrm{d}\tau\,\mathrm{d}\lambda\,\left[\Gamma_{(x,\tau)\to(x',t')}V^{j_{i_*}}(x,\tau;s)\right](\lambda)\;h^n_{\mathrm{dr}}(x',t',\lambda;s), \tag{4.60}$$

where the propagator Γ has been defined in Eq. (4.35) and we are using the notation introduced in Eq. (4.34). The one-particle form factor $V^{j_{i_*}}$ of the current j_{i_*} is given in Eq. (4.31). The flow equation for the pseudo-energy ε directly follows upon differentiating the left and the right hand side of Eq. (4.3) with respect to s

$$\begin{aligned}\frac{\partial\varepsilon(x',t',\lambda;s)}{\partial s} &= \sum_n \frac{\partial\beta^n(x',t';s)}{\partial s}h_n(\lambda) + \int \mathrm{d}\mu\, T(\lambda,\mu)\vartheta(x',t',\mu;s)\frac{\partial\varepsilon(x',t',\mu;s)}{\partial s}\\ &= \sum_n \frac{\partial\beta^n(x',t';s)}{\partial s}\left(h_n(\lambda) + \int \mathrm{d}\mu\, T(\lambda,\mu)\vartheta(x',t',\mu;s)h^{\mathrm{dr}}_n(x',t',\mu;s)\right)\\ &= \sum_n \frac{\partial\beta^n(x',t';s)}{\partial s}h^{\mathrm{dr}}_n(x',t',\lambda;s),\end{aligned} \tag{4.61}$$

where in the first line we have used the chain rule and the relation $\vartheta(\varepsilon) = \mathrm{d}F(\varepsilon)/\mathrm{d}\varepsilon$. In the second line we have again used the chain rule and the identity $h^{\mathrm{dr}}_n(\lambda) = \partial\varepsilon/\partial\beta^n$, which follows upon differentiating with respect to β^n Eq. (4.3) and by recognizing the integral equation in Eq. (2.53) defining the dressing operation. Upon inserting Eq. (4.60) into the last equality in Eq. (4.61) one obtains the flow equation for the pseudo-energy ε:

$$\frac{\partial\varepsilon(x',t',\lambda;s)}{\partial s} = -\int_0^t \mathrm{d}\tau\,\left[\Gamma_{(x,\tau)\to(x',t')}V^{j_{i_*}}(x,\tau;s)\right](\lambda), \tag{4.62}$$

where we have used the completeness relation in Eq. (4.53). Using the decomposition of the propagator Γ in Eq. (4.35), the last equation can be written as

$$\frac{\partial \varepsilon(x',t',\lambda;s)}{\partial s} = -\sum_{\delta\in\tau^\star(x',t',\lambda,x)} \mathrm{sgn}(v^{\mathrm{eff}}(x,\delta,\lambda;s))h^{\mathrm{dr}}_{i_*}(x,\delta,\lambda;s) - \int_0^t \mathrm{d}\tau \left[\Delta_{(x,\tau)\to(x',t')} V^{j_{i_*}}(x,\tau;s)\right](\lambda), \tag{4.63}$$

where we have defined the set of times $\tau_\star(x',t',\lambda,x) = \{\tau : \mathcal{U}(x',t',\lambda,\tau) = x\}$, with the characterstic curve defined in Eqs. (4.15) and (4.16). Notice that if the state ϑ_0 is homogeneous, the inhomogeneous propagator Δ vanishes, as already pointed out after Eq. (4.39). The characteristic curve in this case is simply given by $\mathcal{U}(x',t',\lambda,\tau) = x' - v^{\mathrm{eff}}(\lambda)(t'-\tau)$, the set $\tau_\star$ is composed by one element only and Eq. (4.63) reduces to Eq. (4.57). In the same limit, the time-integral in Eq. (4.59) trivializes, as the current average value is independent on time, and Eq. (4.58) is re-obtained. One can therefore realize that Eqs. (4.60) and (4.63) generalize the results of Refs. [339, 340], recalled in the previous Subsec. 4.3.2, by including non-stationarity and inhomogeneous situations, when motion occurs at the Euler scale of hydrodynamics. The result in Eqs. (4.59) and (4.63) are based on the knowledge of the propagator $\Gamma_{(x,\tau)\to(x',t')}$ which, as we have seen in Sec. 4.2, describes the motion of the quasi-particles between (x,τ) and (x',t') in the inhomogeneous fluid background. It is consequently clear that the Euler-scale expression for $G(s,x,t)$ is expected to apply in the same limit where the expression for the two-point correlator of Subsec. 4.2.1 does. In particular, based on the findings of Subsec. 4.2.3, where the formulas for two-point functions have been tested again numerical simulations of the microscopic hard-rod dynamics, we expect the expression for $G(s,x,t)$ in Eqs. (4.59) and (4.63) to apply for smooth initial inhomogeneities, large enough z and long times. The actual verification of this statement by comparing the predictions coming from Eqs. (4.59) and (4.63) against simulations of the hard-rod gas is part of the future developments of the present thesis and it will be addressed in a future publication, together with the evaluation of $G(s,x,t)$ for some specific quantum models, e.g., the Lieb-Liniger and the sinh-Gordon. In this Chapter, we will solely present the general theory based on Eqs. (4.59) and (4.63) describing the large deviation theory of ballistically transported conserved quantities.

We conclude this Subsection by noting that, if the state ϑ_0 is invariant under simultaneous rescaling of space and time $(x,t) \to (ax,at)$, and therefore $\beta^n(ax',at';0) = \beta^n(x',t';0)$ with $a > 0$ an arbitrary positive constant (e.g., the partitioning protocol initial state in Eq. (4.24)), then the expression in Eq. (4.59) becomes a function of the scaling variable $\xi = x/t$. As a matter of fact, using the property of the propagator Γ, valid if $\beta^n(ax',at';0) = \beta^n(x',t';0)$ for every n,x' and t',

$$\Gamma_{(x,\tau)\to(x',t')} = a\,\Gamma_{(ax,a\tau)\to(ax',at')}, \tag{4.64}$$

which directly follows from the definitions in Eqs. (4.35) and (4.37), the following scaling property can be proved for the Lagrange multipliers $\beta^n(x',t';s)$ for

arbitrary values of s by using Eq. (4.64) in Eq. (4.62)

$$\beta^n(ax', at'; s) = \beta^n(x', t'; s). \tag{4.65}$$

Eq. (4.65) in turn implies that the same scaling property holds also for the pseudo energy $\varepsilon(x', t', \lambda; s)$ and any dressed quantity $h^{\rm dr}_{i_*}(x', t', \lambda; s)$:

$$\begin{aligned} \varepsilon(ax', at', \lambda; s) &= \varepsilon(x', t', \lambda; s) \\ h^{\rm dr}_{i_*}(ax', at', \lambda; s) &= h^{\rm dr}_{i_*}(x', t', \lambda; s). \end{aligned} \tag{4.66}$$

Exploiting the last identity, the expression for $G(s, x, t)$ can be eventually written in the form

$$G(s, \xi) = \int_0^s {\rm d}s' \int_0^1 {\rm d}t' \, \langle j_{i_*}(0,0)\rangle_{\vartheta(\xi,t';s')}. \tag{4.67}$$

Eq. (4.67) closely resembles Eq. (3.90) of Chapter 3, where indeed we observed for non-interacting systems that the SCGF for the partitioning protocol becomes a function of $\xi = x/t$. In Subsec. 4.3.6 we will indeed show that Eq. (4.67) renders the result in Sec. 3.5 of Chapter 3 in the limit of vanishing interaction. Before doing this, in the next Subsection, we provide the derivation of the main results in Eqs. (4.59) and (4.63).

4.3.4 The SCGF for inhomogeneous GGEs: derivation of the main result

We start by defining the s-tilted ensemble as that obtained by biasing the measure of the inhomogeneous GGE in Eq. (4.6) with the time-integrated current in Eq. (4.47). Averages over the s-tilted ensemble will be denoted as $\langle \dots \rangle^{(s)}_{{\rm inh},z}$, with $\langle \dots \rangle^{(0)}_{{\rm inh},z} = \langle \dots \rangle_{{\rm inh},z}$ by construction. Namely, for a local operator $\mathcal{O}(zx', zt')$ at the space-time point (zx', zt') the s-tilted ensemble is defined as

$$\langle \mathcal{O}(zx', zt')\rangle^{(s)}_{{\rm inh},z} = \frac{\langle \mathcal{O}(zx', zt') \exp(s\Delta q_{i_*}(zx, zt))\rangle_{{\rm inh},z}}{\langle \exp(s\Delta q_{i_*}(zx, zt))\rangle_{{\rm inh},z}}, \tag{4.68}$$

where Δq_{i_*} is given in Eq. (4.47). From the definition (4.68) one also has

$$\frac{\partial \langle \mathcal{O}(zx', zt')\rangle^{(s)}_{{\rm inh},z}}{\partial s} = \int_0^t {\rm d}\tau \, z \langle \mathcal{O}(zx', zt') j_{i_*}(zx, z\tau)\rangle^{c,(s)}_{{\rm inh},z}, \tag{4.69}$$

with the integrand on the r.h.s. denoting the two-point connected correlation function over the s-tilted ensemble with the notation of Eq. (4.68).

It is crucial to note that, although the s-tilting involves an integral over time, this *does not affect the dynamics*. The bias is to be understood as a modification of the measure, that is, of the distribution of states at time 0, or on any chosen time slice. According to (4.68), the measure is modified by a weight which is evaluated by evolving the observables in time (or equivalenty, evolving the distribution of states in time), and evaluating the exponential of the time-integrated current. The dynamics is still given by the original, homogeneous and time-independent

Hamiltonian of the model under consideration, and thus, at the Euler scale, time slices are related to each other by the original GHD equation (4.13) of the model. This is important, as we can then use, below, the results for correlations in inhomogeneous and dynamical states reviewed in Subsec. 4.2.1, which, as emphasised, are based on the assumption of an homogeneous and time-independent dynamics.

The definition of the s-tilted measure in Eq. (4.69) is widely known in the context of large deviations in classical stochastic systems, see, e.g., Refs. [382, 383], and in open quantum systems. In the latter framework it is named "s ensemble", see, e.g., Refs. [45, 46, 48], where the approach consists in relating the bias in s, because of the exponential of the time-integrated current, to a modification of the Lindbladian ruling the evolution of the system. This operation can be done via the so-called "quantum Doob" transformation, as shown in Refs. [139, 341, 384–386], and it amounts to a biasing of the probability measures which makes rare events typical. The approach we pursue here is complementary to the quantum Doob transform, in the sense that here we relate the insertion of the exponential of the time-integrated current to a change of the inhomogeneous GGE measure. Fundamentally, the latter modification still produces an inhomogeneous GGE, whose s-dependence can be determined exactly in terms of the flow equation in Eqs. (4.60) and (4.63).

We now show that the biasing procedure in Eqs. (4.68) and (4.69) defines a flow in the manifold of the inhomogeneous GGEs. Since, by construction, the dynamics is unchanged, we may think of the manifold of inhomogenenous GGEs as described by a space-dependent GGE on any given time slice, $\{\beta^n(x',t';s)\}_{x',n}$. Let us choose the time slice $t'=0$. One can adapt the argument developed in Ref. [340] for the homogeneous case, summarized in Subsec. 4.3.2. Namely, one defines the Lie derivative $\mathcal{L}$ at the point $\langle ...\rangle^{\rm Eul}_{\vartheta_0}$ in the manifold of inhomogeneous GGEs as

$$\mathcal{L}\langle \mathcal{O}(x',0)\rangle^{\rm Eul}_{\vartheta_0} = \int_0^t {\rm d}\tau\, \langle \mathcal{O}(x',0) j_{i_*}(x,\tau)\rangle^{c,{\rm Eul}}_{\vartheta_0}. \tag{4.70}$$

Using Eq. (4.33) with τ as initial time for the propagator $\Gamma_{(x,\tau)\to(x',t')}$, and Eqs. (4.30) and (4.31), the Lie derivative can be written as

$$\mathcal{L}\langle \mathcal{O}(x',0)\rangle^{\rm Eul}_{\vartheta_0} = -\sum_n \frac{\partial\langle\mathcal{O}\rangle_{\vartheta(x',0)}}{\partial\beta^n(x',0)} \int_0^t {\rm d}\tau\, {\rm d}\lambda \left[\Gamma_{(x,\tau)\to(x',0)} V^{j_{i_*}}(x,\tau)\right](\lambda) h^n_{\rm dr}(x',0,\lambda). \tag{4.71}$$

Equation (4.71) shows that the Lie derivative lies on the tangent space to the manifold of inhomogeneous GGEs identified by the Lagrange multipliers $\{\beta^n(x',0)\}_{x',n}$. Comparing Eqs. (4.70) and (4.71) with (4.69), and remembering the definition of the Euler-scaling limit of two-point correlation functions in Eq. (4.28), one realizes that the s-tilted measure defines a flow directed along the Lie derivative as $z\to\infty$. Accordingly, from Eq. (4.69), infinitesimal s modifications lie on the tangent space to that manifold, and given that at $s=0$ the state $\langle\dots\rangle^{(0)}_{{\rm inh},z}$ is an inhomogeneous GGE and lies on that manifold, then it remains so even after the s-tilting. As a consequence, one has for the Euler-scaling limit $z\to\infty$ of Eq. (4.68) that

$$\lim_{z\to\infty}\langle \mathcal{O}(zx',zt')\rangle^{(s)}_{{\rm inh},z} = \langle \mathcal{O}(x',t')\rangle^{\rm Eul}_{\vartheta_0(s)} = \langle \mathcal{O}(0,0)\rangle_{\vartheta(x',t';s)}, \tag{4.72}$$

where in the second equality we have used the local relaxation assumption (4.5) thereby expressing the average of the local operator $\mathcal{O}$ over the local homogeneous GGE in Eq. (4.2) at the fluid cell $(x', t'; s)$. It is also worth to remark that in the second equality of (4.72) we have extended the notation introduced after (4.28) for the mode-occupation function $\vartheta_0(s)$, corresponding to the state ρ_0 in Eq. (4.6) as $z \to \infty$, by exposing the additional dependence on s due to the biasing of the measure.

In order to fix the additional dependence on s due to the tilting in Eq. (4.68) one further needs to specify the flow equation. To do this we start from (4.69) together with Eq. (4.72) by choosing the local observable $\mathcal{O}(x', t')$ as some conserved density $q_n(x', t')$ of the model

$$\frac{\partial \langle q_n(x',t')\rangle^{\text{Eul}}_{\vartheta_0(s)}}{\partial s} = \int_0^t \mathrm{d}\tau\, \langle q_n(x',t') j_{i_*}(x,\tau)\rangle^{c,\text{Eul}}_{\vartheta_0(s)}. \tag{4.73}$$

The homogeneous GGE at every fluid cell (x', t') is specified by the Lagrange multipliers $\{\beta^n(x', t'; s)\}_{x',n}$ or, equivalently, by the average conserved densities $\langle q_n(x', t')\rangle^{\text{Eul}}_{\vartheta_0(s)} = \langle q_n(0,0)\rangle_{\vartheta(x',t';s)}$ in Eq. (4.8). Equation (4.73) can therefore be considered as the "equation of motion" of the state coordinates $\langle q_n(0,0)\rangle_{\vartheta(x',t';s)}$ for their trajectory, parametrized by s, in the manifold of inhomogeneous GGEs. For convenience, we express these coordinates on an arbitrary time slice t'.

As a matter of fact, Eq. (4.73) relates the tangent vector of the trajectory, the l.h.s., to a function of the coordinate itself, the r.h.s.. Since the expression of the correlator on the r.h.s. is known, from Eq. (4.36) in Subsec. 4.2.1, the equation of motion is well defined and it fixes the flow of the inhomogeneous GGE in Eq. (4.6) as a function of s. Indeed we now show that Eq. (4.73) is equivalent to the flow equation (4.60). Exploiting the chain rule one has

$$\begin{aligned}\frac{\partial \langle q_n(x',t')\rangle^{\text{Eul}}_{\vartheta_0(s)}}{\partial s} &= \int \mathrm{d}y \sum_j \frac{\delta \langle q_n(x',t')\rangle^{\text{Eul}}_{\vartheta_0(s)}}{\delta \beta^j(y,t';s)} \frac{\partial \beta^j(y,t';s)}{\partial s} \\ &= -\sum_j (C_{\vartheta(x',t';s)})_{nj} \frac{\partial \beta^j(x',t';s)}{\partial s} = -\left[\frac{\partial \beta(x',t';s)}{\partial s} C_{\vartheta(x',t')}\right]_n,\end{aligned} \tag{4.74}$$

where in the last step we used vector-matrix notation and the symmetry of the correlation matrix $C_{\vartheta(x',t')}$, defined in Eq. (4.32). Notice that in Eq. (4.74) we have further exploited the fluctuation dissipation relation in Eq. (4.28)

$$-\frac{\delta \langle q_i(x',t')\rangle^{\text{Eul}}_{\vartheta_0(s)}}{\delta \beta^j(y,t';s)} = \langle q_i(x',t') q_j(y,t')\rangle^{\text{c,Eul}}_{\vartheta_0(s)} = \delta(x'-y)(C_{\vartheta(x',t';s)})_{ij}, \tag{4.75}$$

where the second equality comes from the fact that for equal-time connected correlation functions the propagator $\Gamma_{(y,t')\to(x',t')}(\lambda,\mu) = \delta(x'-y)\delta(\lambda-\mu)$. The latter equality simply expresses that at the Euler scale fluid cells on the same time

slice separated in space are uncorrelated, as shown in Ref. [177]. The inverse matrix $C^{-1}_{\vartheta(x',t';s)}$ can be defined by means of the functions $h^j_{\rm dr}$ in Eq. (4.53) as

$$(C^{-1}_{\vartheta(x',t';s)})^{jn} = \int {\rm d}\lambda\, \rho_p^{-1}(x',t',\lambda;s) f^{-1}(x',t',\lambda;s) h^n_{\rm dr}(x',t',\lambda;s) h^j_{\rm dr}(x',t',\lambda;s), \tag{4.76}$$

Multiplying Eq. (4.74) by $C^{-1}_{\vartheta(x',t';s)}$ in Eq. (4.76) and equating with the r.h.s of Eq. (4.73), where the connected correlator is given by Eq. (4.36), one eventually obtains the flow equation for the Lagrange parameter $\beta^n(x',t';s)$ in Eq. (4.60). The flow equation for $\varepsilon(x',t',\lambda;s)$ (4.62), (4.63) follows from Eq. (4.60) according to the steps reported in Eq. (4.61).

Once the flow equation is established, proving Eq. (4.59) for the SCGF is simple. By applying a derivative with respect to s to $G(s,x,t)$ in Eq. (4.48), with ρ_0 as given by Eq. (4.6), one obtains

$$\begin{aligned}\frac{\partial G(s,x,t)}{\partial s} &= \frac{1}{t}\int_0^t {\rm d}\tau \lim_{z\to\infty} \langle j_{i_*}(zx,z\tau)\rangle^{(s)}_{{\rm inh},z} = \frac{1}{t}\int_0^t {\rm d}\tau\, \langle j_{i_*}(x,\tau)\rangle^{\rm Eul}_{\vartheta_0(s)} \\ &= \frac{1}{t}\int_0^t {\rm d}\tau\, \langle j_{i_*}(0,0)\rangle_{\vartheta(x,\tau;s)},\end{aligned} \tag{4.77}$$

where in the first equality we have used the definition in Eq. (4.68) for the average over the s-tilted ensemble, while Eq. (4.72) has been exploited in the second and third equality. Integrating in s, and exploiting the fact that $G(s=0,x,t)=0$, from the definition in Eq. (4.48) of the SCGF, one can see that Eq. (4.77) reduces to Eq. (4.59).

In concluding this Subsection, we emphasize that the present derivation of $G(s,x,t)$ is strongly based on the result of Ref. [177], recalled in Subsec. 4.2.1, for two-point functions in inhomogeneous and dynamical GGEs. Accordingly, Equations (4.59), (4.60) and (4.63) are restricted to integrable models, differently from the results in Eqs. (4.55) and (4.58) for homogeneous GGEs. The calculation of the scaled cumulant generating for inhomogeneous and dynamical states in generic, not necessarily integrable, models is an unexplored and challenging problem which goes beyond the analysis of the present Chapter.

4.3.5 Analysis of the cumulants

We report here the first three cumulants, which can be obtained from the series expansion in Eqs. (4.48) and (4.49) of the general expression given by Eqs. (4.59) and (4.63). We write here the first three cumulants that can be obtained from the series expansion in Eq. (4.59). These cumulants provide important information about the shape of the probability distribution of $J_{i_*} = \Delta q_{i_*}/t$ and they are the easiest to access experimentally. Higher cumulants can be in principle derived as well, even if the derivation becomes combinatorially more cumbersome as the order increases.

The first cumulant is trivial from Eq. (4.59) and it is just the time integral of the GHD expression of the current in Eq. (4.10)

$$\frac{\partial G(s,x,t)}{\partial s}\Big|_{s=0} = c_1 = \frac{1}{t}\int_0^t \mathrm{d}\tau \int \frac{\mathrm{d}\lambda}{2\pi}(E')^{\mathrm{dr}}(x,\tau\lambda)\vartheta(\lambda,x,\tau)h_{i_*}(\lambda). \tag{4.78}$$

For higher-order cumulants we need the useful relation, with $X^{\mathrm{dr}}(x',t',\lambda;s)$ a generic dressed quantity (we drop for brevity all the independent variables),

$$\partial_s X^{\mathrm{dr}} = \frac{\partial\varepsilon}{\partial s} f\, X^{\mathrm{dr}} - \left(\frac{\partial\varepsilon}{\partial s} f\, X^{\mathrm{dr}}\right)^{\mathrm{dr}}, \tag{4.79}$$

which directly follows upon differentiating with respect to s Eq. (2.51). $\partial\varepsilon/\partial s$ is specified by the flow equation (4.62) and (4.63). The second cumulant is related to the Gaussianity of the distribution close to the mean value and, from Eqs. (4.59) and (4.79), its expression reads

$$c_2 = -\frac{1}{t}\int_0^t \mathrm{d}\tau \int \frac{\mathrm{d}\lambda}{2\pi} v^{\mathrm{eff}}(x,\tau,\lambda)\rho(x,\tau,\lambda)\frac{\partial\varepsilon}{\partial s}\Big|_{s=0} f(x,\tau,\lambda)h^{\mathrm{dr}}_{i_*}(x,\tau,\lambda)h^{\mathrm{dr}}_{i_*}(x,\tau,\lambda), \tag{4.80}$$

which, using (4.62) turns out to be

$$\begin{aligned} c_2 &= \frac{1}{t}\int_0^t \mathrm{d}\tau \int_0^t \mathrm{d}\tau' \,\langle j_{i_*}(x,\tau) j_{i_*}(x,\tau')\rangle^{c,\mathrm{Eul}}_{\vartheta_0}, \\ &= \frac{1}{t}\int_0^t \mathrm{d}\tau \int_0^t \mathrm{d}\tau' \int \mathrm{d}\lambda\, [\Gamma_{(x,\tau')\to(x,\tau)} V^{j_{i_*}}(x,\tau')](\lambda)\,\rho(x,\tau,\lambda) f(x,\tau,\lambda) V^{j_{i_*}}(x,\tau,\lambda), \end{aligned} \tag{4.81}$$

that is in agreement with the expression for the connected current-current two point correlation function one obtains from Eq. (4.36), therefore providing an important consistency check of Eq. (4.59). The expression of the third cumulant c_3 is related to the asymmetry or skewness of the distribution. Its expression was not known before and it is given by

$$\begin{aligned} c_3 &= \frac{1}{t}\int_0^t \mathrm{d}\tau \int_0^t \mathrm{d}\tau' \int_0^t \mathrm{d}\tau' \,\langle j_{i_*}(x,\tau) j_{i_*}(x,\tau') j_{i_*}(x,\tau'')\rangle^{c,\mathrm{Eul}}_{\vartheta_0} \\ &= -\frac{1}{t}\int_0^t \mathrm{d}\tau \int \mathrm{d}\lambda v^{\mathrm{eff}}(x,\tau,\lambda)\rho(x,\tau,\lambda) f(x,\tau,\lambda)\times \\ &\qquad \times \left[2\,\frac{\partial\varepsilon}{\partial s}\Big|_{s=0}\left(\frac{\partial\varepsilon}{\partial s}\Big|_{s=0} f h^{\mathrm{dr}}_{i_*}\right)^{\mathrm{dr}} - h^{\mathrm{dr}}_{i_*}\left(\frac{\partial^2\varepsilon}{\partial s^2}\Big|_{s=0} + \left(\frac{\partial\varepsilon}{\partial s}\right)^2\Big|_{s=0}\tilde{f}\right)\right], \end{aligned} \tag{4.82}$$

with

$$\tilde{f} = \frac{\mathrm{d}f}{\mathrm{d}\varepsilon}\frac{1}{f} + f. \tag{4.83}$$

We notice that both Eq. (4.80) for c_2 and Eq. (4.82) for c_3 are written in terms of $\partial\varepsilon/\partial s$, which is given by the flow equation (4.62) and (4.63). Once the latter is numerically solved, also the cumulants can be therefore evaluated numerically.

We note that in the cases where the initial state ϑ_0 is invariant under the rescaling $(x,t) \to (ax,at)$, with $a > 0$ an arbitrary constant, and therefore Eqs. (4.64)-(4.67) apply, the cumulants $c_k(\xi)$ in Eq. (4.49) of the time integrated current are scaling function of ξ, i.e., the connected correlation functions $\langle [\Delta q_{i_*}(x,t)]^k \rangle^{c,\mathrm{Eul}}_{\vartheta_0}$ become scaling functions of ξ once they are rescaled by t. We have numerically checked, by simulating the hard-rod gas dynamics (see Subsec. 4.2.3 and Appendix 4.B for the details about the numerical simulations) from an initial step inhomogeneity in the inverse temperature $\beta^2(x,0)$ as in Eqs. (4.23) and (4.24), that the first three cumulants $c_k(\xi)$, with $k \leq 3$, of the particle flow ($h_0(\lambda) = 1$) are functions of ξ. In this case, we have observed a linear growth as a function of t of the connected correlation functions, $\langle [\Delta q_0(\xi t,t)]^k \rangle^c_{\mathrm{inh},z}$ with ξ fixed and $k \leq 3$, which implies that the cumulants are finite (the same scaling behavior is expected also for higher cumulants with $k > 3$) and the large deviation principle applies, as commented after Eq. (4.50). In the homogeneous and stationary limit of the results in Eqs. (4.59), (4.60) and (4.63), the same scaling behavior as a function of t for the cumulants was already observed in Ref. [339]. The fineteness of the cumulants in integrable models implies that there is no divergence in the derivatives of $G(s,x,t)$ w.r.t. s and therefore no dynamical phase transition in the time-integrated current J_{i_*} statistics, see, e.g., Refs. [387–389]. The understanding of the precise reason behind the absence of divergences in the s-derivatives of $G(s,x,t)$ in integrable systems is still under investigation and it will not be addressed in this manuscript.

4.3.6 The non-interacting limit

In this Subsection we show how to specify the general result in Eqs. (4.59) and (4.60) to non-interacting systems. In the particular case of the partitioning protocol (see Subsec. 4.1.5 and Eq. (4.23) therein), with an initial thermal inhomogeneity (i.e., $\beta^i(x,0) = 0$ for $i \neq 2$) we show that the result is equivalent to that of Sec. 3.5 of Chapter 3, as it must be.

The fundamental simplification happening in non-interacting systems is that no dressing is present since the kernel $K(\lambda,\mu)$ in Eq. (2.51), or equivalently $T(\lambda,\mu)$ in Eq. (4.3), vanishes identically. The flow equation in Eq. (4.60) therefore simplifies drastically. Specifically, the propagator $\Gamma_{(x,\tau)\to(x',t')}(\lambda,\mu)$ for free models is uniquely given by the homogeneous contribution

$$\Gamma_{(x,\tau)\to(x',t')}(\lambda,\mu) = \frac{1}{|v_g(\lambda)|}\delta\left(\frac{x'-x}{v_g(\lambda)} - (t'-\tau)\right)\delta(\lambda-\mu), \tag{4.84}$$

where $v^{\mathrm{eff}}(x,t,\lambda) = v_g(\lambda) = \mathrm{d}E(\lambda)/\mathrm{d}\lambda$ is the group velocity since there is no dressing. We observe that for the calculation of $G(s,x,t)$ in Eq. (4.59), where the mean current $\langle j_{i_*}(0,0)\rangle_{\vartheta(x,\tau;s')}$ is evaluated on fluid cells at the fixed space point x and times $\tau \in (0,t)$, one has to specialize the propagator to equal space points $x' = x$, i.e., $\Gamma_{(x,\tau)\to(x,t')}(\lambda,\mu)$. Note that in interacting systems the indirect propagator $\Delta_{(x,\tau)\to(x',t')}(\lambda,\mu)$ vanishes as a consequence of the fact that the quasiparticles trajectories do not depend on the state. Inserting Eq. (4.84) into Eq. (4.60),

with $t' - (x' - x)/v_g(\lambda) < t$, one has

$$\frac{\partial \beta^n(x',t';s)}{\partial s} = -\int_0^t \mathrm{d}\tau \int \mathrm{d}\lambda\, v_g(\lambda) h_{i_*}(\lambda) h^n(\lambda)\, \delta\left(\frac{x'-x}{v_g(\lambda)} - (t'-\tau)\right) \frac{1}{|v_g(\lambda)|}$$
$$= -\int \mathrm{d}\lambda\, \mathrm{sgn}(v_g(\lambda)) h_{i_*}(\lambda) h^n(\lambda) = -\mathrm{sgn}(A)^n_{i_*}, \tag{4.85}$$

with the last step following from (4.52) without the dressing. For the same reason A^j_i is independent of s and Eq. (4.85) can be trivially integrated

$$\beta^n(x',t';s) = \beta^n(x',t') - s\,\mathrm{sgn}(A)^n_{i_*}. \tag{4.86}$$

In order to further simplify Eq. (4.85) we briefly recall some basic identities about the Lagrange mulipliers $\{\beta^n\}$. As already commented after Eq. (4.73), the GGE state can be equivalently described in terms of the Lagrange parameters $\{\beta^n(x',t')\}_{x',n}$ or with the densities $\langle q_n(0,0)\rangle_{\vartheta(x',t')}$. As a matter of fact, it simple to see that the multipliers satisfy an hydrodynamic equation similar to the one the densities fulfill, as shown in details in Refs. [159, 160],

$$\partial_t \beta^n(x',t') + \sum_j \partial_{x'} \beta^j(x',t') A^n_j(x',t') = 0. \tag{4.87}$$

Since A^j_i in the absence of dressing is independent of space and time, Eq. (4.87) is linear. Accordingly, one can introduce the normal mode function $\mathcal{N}(x',t',\lambda)$ via a simple linear combination of the $\{\beta^n(x',t')\}_{x',n}$, i.e.,

$$\mathcal{N}(x',t',\lambda) = \sum_n \beta^n(x',t')\, h_n(\lambda), \tag{4.88}$$

where h_n are the bare single-particle eigenvalues, see Eq. (4.4). Plugging Eq. (4.88) into Eq. (4.87) and exploiting the eigenvalue equation for A^j_i in Eq. (4.54) one has

$$\partial_{t'} \mathcal{N}(x',t',\lambda) + v_g(\lambda)\, \partial_{x'} \mathcal{N}(x',t',\lambda) = 0. \tag{4.89}$$

Note that Eq. (4.89) generalizes to the interacting case upon replacing $v_g(k) \to v^{\mathrm{eff}}(x',t',\lambda)$. As a matter of fact, one can notice that Eq. (4.89) has the very same structure as Eq. (4.13). Indeed, the function $\vartheta(x',t',\lambda)$ can be considered as the normal mode function associated to the conserved densities $\langle q_n(0,0)\rangle_{\vartheta(x',t',\lambda)}$, in the same way as $\mathcal{N}$ is the mode function of the Lagrange parameters $\{\beta^n\}$. The fundamental point, specific of free systems, is that $\mathcal{N}$ is linearly related to the $\{\beta^n\}$, according to Eq. (4.88). In the case of interactions, as a consequence of the nonlinearity of Eq. (4.12), the simple relation in Eq. (4.89) does not hold, see Refs. [159, 160] for a complete discussion. Inserting Eq. (4.88) into Eq. (4.86) and remembering Eq. (4.54) one has

$$\mathcal{N}(x',t',\lambda;s) = \mathcal{N}(x',t',\lambda) - s\,\mathrm{sgn}(v_g(k))\, h_{i_*}(\lambda). \tag{4.90}$$

Let us now specialize the discussion to the partitioning protocol presented in Chapter 3. In this case, the solution of Eq. (4.89) is readily found to be

$$\mathcal{N}(\xi',\lambda) = \mathcal{N}_l(\lambda)\Theta(v_g(\lambda)-\xi') + \mathcal{N}_r(\lambda)\Theta(\xi'-v_g(\lambda)), \tag{4.91}$$

with $\xi' = x'/t'$, while $\mathcal{N}_{l,r}(\lambda)$ are fixed by the initial conditions for the left and right half of the system. Let us then consider the case analyzed in Chapter 3, in which a thermal inhomogeneity is present, with $\beta^2(x',0)$ given by the step profile in Eq. (4.23) and all the other Lagrange parameters initially set to zero. Then from Eq. (4.88) computed at time $t'=0$,

$$\mathcal{N}(x',0,\lambda) = \beta^2(x',0)\, h_2(\lambda) = \beta_r\, h_2(\lambda)\Theta(x') + \beta_l\, h_2(\lambda)\,\Theta(-x'), \tag{4.92}$$

we identify

$$\mathcal{N}_r(\lambda) = \beta_r\, h_2(\lambda), \qquad \mathcal{N}_l(\lambda) = \beta_l\, h_2(\lambda). \tag{4.93}$$

Notice that in the transverse field Ising chain $h_2(\lambda) = \varepsilon(\lambda)$ in Eq. (3.7), while for the harmonic chain $h_2(\lambda) = \Omega(\lambda)$ in Eq. (3.26). Moreover $i_* = 2$ in Eq. (4.90) since we are considering energy transport. Inserting Eqs. (4.91) and (4.93) into Eq. (4.90) and diving both sides by $h_2(\lambda)$ one eventually has

$$\beta(\xi',\lambda;s) = \beta(\xi',\lambda) - s\,\mathrm{sgn}(v_g(\lambda)), \tag{4.94}$$

where we defined $\beta(\xi',\lambda) = \mathcal{N}(\xi',\lambda)/h_2(\lambda)$. We observe that for the partitioning protocol initial state $\beta(\xi',\lambda)$ depends on x' and t' through the scaling variable $\xi' = x'/t'$, and therefore the Lagrange multipliers are invariant upon simultaneous rescaling of space and time $\beta^n(ax',at') = \beta^n(x',t')$ for every n, x' and t'. Accordingly, Eq. (4.65) is satisfied, as one can explicitly see from Eq. (4.94), and $G(s,x,t) = G(s,\xi)$, with $\xi = x/t$ according to the discussion before Eq. (4.67). Upon using Eq. (4.94) into Eq. (4.59) one can see that for non-interacting systems the biasing of the measure necessary to compute the SCGF can be simply obtained by performing a linear shift of the inverse temperatures $\beta_{l,r}$ characterizing the initial partitioning protocol state in Eq. (3.1). This is indeed equivalent to the findings we obtained in Sec. 3.5 in Eqs. (3.94) and (3.95) using a stationary phase approach. As we have already commented after Eq. (3.103), this result constitute a generalization as a function of ξ of the extended fluctuation relation of Ref. [145] (see also the discussion after Eqs. (3.102) and (3.103) in Chapter 3). In other words, in non-interacting systems, the statistical properties of the time-integrated current are directly determined by the fluctuations of the initial state, since the quasi-particle trajectories do not depend on the surrounding state where the quasi-particles propagate. This is at the basis of the quasi-particle interpretation of the SCGF provided in Subsec. 3.5 of Chapter 3. The derivation of Eq. (4.90) presented in this Subsection is, instead, based on Euler-scale hydrodynamics and applies more generally to any initial state ρ_0 having the form in Eq. (4.6). Only in Eqs. (4.91)-(4.94) the result has been specialized to the partitioning protocol state with a step profile of $\beta^2(x,0)$. More importantly, the Euler-scale hydrodynamics allows for the exact treatment of interactions, as we have seen in Subsecs. 4.3.3 and 4.3.4. In interacting systems, on the contrary, quasi-particles trajectories are modified by the dynamical inhomogeneous background within which they move.

Accordingly, fluctuations become dependent on the whole motion of the quasiparticles through the inhomogeneous background between time 0 and t, as expressed by the time integral in Eqs. (4.62) and (4.63).

4.4 Concluding remarks

In this Chapter we have considered the dynamics of interacting integrable systems with inhomogeneous initial states in the framework of the generalized hydrodynamics. In Sec. 4.1 we have briefly reviewed the theory, originally proposed in Refs. [159, 160], emphasizing how it represents an extensions of ordinary hydrodynamics to integrable models, where an infinite number of conserved charges is present. In particular, we have introduced the Euler-scaling limit, where inhomogeneities are smooth and vary on a very large (ideally infinite) length scale. This is the regime where the GHD applies, and it allows one to describe locally, at every space-time point (x, t), the system as if it was homogeneous via the thermodynamics Bethe ansatz and the generalized Gibbs ensemble.

Then, we have explained in Sec. 4.2 our results from Ref. [3] about dynamical correlation functions connecting observables lying at different space-time point. We have numerically evaluated the correlation propagator, cf. Eqs. (4.33), (4.35), (4.36) and (4.37), necessary for the calculation of exact, dynamical two-body correlation functions in the Eulerian limit, first obtained in Ref. [177]. We have addressed three different inhomogeneous setups, whose transport properties have already been well-studied, namely a homogeneous system in Sec. 4.2.2, a bump release in Secs.4.2.3 and 4.2.5, and a partitioning protocol in Sec. 4.2.4. Furthermore, the universality of GHD enables our scheme to be applied to most integrable models. Then, we have studied the spreading of correlations in the Lieb-Liniger model, the classical hard-rod model, and the relativistic sinh-Gordon model. In Sec. 4.2.3, by comparing for the classical hard-rod model with the results obtained via Monte-Carlo simulations (see Fig. 4.4 and also Appendix 4.B), we have provided the first demonstration of the validity of the formulas derived in Ref. [177] for non-stationary and inhomogeneous states. Crucially, we succeeded in explicitly confirming the subtle effect of indirect propagation of correlations – correlations due to the nonlinearity of GHD, and not directly interpreted as coming from the propagation of normal modes along their curved trajectories in the moving GHD fluid. From this comparison we are able to observe the onset of the Eulerian limit at longer time scales, while for short times discrepancies between the classical microscopic simulations and the generalized hydrodynamic predictions for correlation functions are observed. We expect that these discrepancies at shorter time scales can be accounted by considering diffusive terms into the GHD equation (4.13). Although the effect of diffusive corrections on one-point functions is by now well understood [325, 355–357], for dynamical two-point correlators in inhomogeneous and non-stationary states, instead, no analytical result is currently available. It would be interesting to investigate this point further in the future.

In Sec. 4.3 we have shown our results from Ref. [5] regarding the scaled cumulant generating function of the time-integrated current associated to ballistically transported conserved quantities, which we have defined in the Euler-scaling limit in Subsec. 4.3.1. We have extended the analysis of Refs. [339, 340] for the

calculation of the SCGF in homogeneous and stationary states, which we have reviewed in Subsec. 4.3.2, to the more complex and interesting case of inhomogeneous states. Our results, detailed in Subsec. 4.3.3 and proved in Subsec. 4.3.4, express the SCGF as an integral of the mean value of the current, see Eq. (4.59). The crucial point is that the mean value is computed over a biased inhomogeneous measure according the exponential of the time-integrated current. All quantities which depend on the inhomogeneous fluid state acquire, as a consequence, an additional dependence on the parameter s, coupled to the time integral of the current. This s-dependence can be determined by solving the flow equation, see Eqs.(4.57), (4.60) and (4.63), which describes exactly how the initial measure is affected by the tilting procedure in terms of a flow, parametrized by s, in the manifold of GGEs. The flow equation is based on the knowledge of the inhomogeneous two-point correlator, whose expressions we have numerically tested in Subsec. 4.2.3 for the hard-rod gas. In Subsec. 4.3.5 we have provided the expression of the first three cumulants. We have further numerically checked with Monte-Carlo simulations of the hard-rod fluid, in an initial inhomogeneous state with an inverse temperature $\beta^2(x,0)$ profile as in Eqs. (4.23) and (4.24) and in Fig. 4.7, that the first three cumulants c_k of the particle current, with $k \leq 3$, are finite (higher cumulants are similarly expected to be finite). The numerical check of the finiteness of the cumulants is methodologically fundamental since it confirms, a posteriori, that the time integrals in Eqs. (4.78), (4.80)-(4.82) for the cumulants are convergent, that the series expansion in Eqs. (4.48) and (4.49) is well defined and that therefore the large deviation principle in Eq. (1.49) applies. The comparison between the expression in Eq. (4.82) and numerical simulations of the hard-rod model will be addressed in a future study, where we plan to specialize the general expressions in Eq. (4.59) and (4.63) to specific classical and quantum models (Lieb-Liniger, hard rods, sinh-Gordon). In Subsec. 4.3.6 we have concluded by analyzing the non-interacting limit of the general formulas in Eqs. (4.59) and (4.60). In this case, due to the linearity of the hydrodynamic equations, the flow equation drastically simplifies and it reduces to a shift of the Lagrange parameters characterizing the initial state, see Eq. (4.94). For the partitioning protocol, we have further checked the the results obtained in this way reproduce those obtained in Sec. 3.5 of Chapter 3 via stationary-phase methods. As a future perspective, it would be very interesting to extend the results of Sec. 4.3 beyond the Euler-scaling limit thereby accounting for diffusive corrections. In the specific case of classical models, like the hard-rod gas, this should somehow connect to the Macroscopic Fluctuation Theory, see Refs. [310–313], which is also based on diffusive hydrodynamics. We surely plan to carry out this study in the future.

Appendix of Chapter 4

4.A The thermal distribution of the hard-rod gas

For classical models, such as the hard-rod model, the statistical factor $f(\lambda)$ introduced after Eq. (4.30) is merely

$$f(\lambda) = 1\,. \tag{4.95}$$

The filling function for a thermal state can be easily written in terms of the source term $w^{(th)}(\lambda) = \beta\lambda^2/2$ as outlined in Appendix D of Ref. [339]

$$\vartheta^{(th)}(\lambda) = \mathrm{e}^{-\varepsilon^{(th)}(\lambda)} = \mathrm{e}^{-w^{(th)}(\lambda) - W(a\,d(\beta))}, \tag{4.96}$$

with the thermal pseudoenergy $\varepsilon^{(th)}(\lambda)$ being the solution of Eq. (4.3) with the source term $w^{(th)}(\lambda)$

$$\varepsilon^{(th)}(\lambda) = w^{(th)}(\lambda) + W(a\,d(\beta)), \tag{4.97}$$

while $d(\beta)$ has been defined after (4.44) and $W(a\,d(\beta))$ is the Lambert-W function [330], which is defined as the solution of the equation

$$W = a\,d\,\mathrm{e}^{-W}. \tag{4.98}$$

Similarly

$$\rho^{t,(th)}(\lambda) = \frac{1}{2\pi(1 + W(a\,d(\beta)))}, \tag{4.99}$$

whence, together with Eqs. (4.96) and (2.36) the expression for the thermal root density $\rho^{(th)}(\lambda)$ in (4.44) immediately follows. From the latter the thermal linear density distribution of rods is constructed in the Monte Carlo simulations as explained in Subsec. 4.2.3 of main text and in the following paragraph. In particular the initial filling function ϑ_0 in Eq. (4.45) is given by Eq. (4.96) with the inhomogeneity $\beta(x)$ given in Eq. (4.43) for the single bump and in Eq. (4.42) for the two bumps case.

4.B Numerical simulations of the hard-rod gas

We present here additional details about the Monte Carlo simulations presented in Subsec. 4.1.5 (see Fig. 4.2) and in Subsec. 4.2.3 (see Figs. 4.4 and 4.B.1). In our simulations we fix the initial point $-L$ ($L > 0$) whence rods are distributed in space and the number N of particles. The initial position L_M of the rightmost rod

is therefore fluctuating for each different realization of the initial rods' configuration. The number N of particles is chosen such that it is larger than the average number $\langle N \rangle$ of rods contained in the interval $[-L, L]$ (we take it symmetric for simplicity) where we want to compute the dynamics of the density $\langle n(x,t) \rangle$:

$$N > \langle N \rangle = \int_{-L}^{L} \mathrm{d}x \, \langle n(x,0) \rangle_{\vartheta_0}^{\mathrm{Eul}} , \tag{4.100}$$

where the initial density $\langle n(x,0) \rangle_{\vartheta_0}^{\mathrm{Eul}}$ used in the simulations is given in Eq. (4.45). In the case of the partitioning protocol, $\beta(x)$ in Eq. (4.45) is given by a step function as per Eq. (4.23). In the cases analyzed in Subsecs. 4.2.3, $\beta(x)$ is given in Eq. (4.43) for the single bump and by Eq. (4.42) for the two bumps case. As a consequence $L_M > L$. The simulations are performed in infinite volume, however, the initial rods' distribution is zero outside the interval $[-L, L_M]$ and there are two depletion zones that move inwards as time elapses in proximity of which the GHD solution does not hold anymore (see the caption of Fig. 4.2). Velocities are drawn from a Gaussian distribution with variance $1/\beta(x)$ according to Eqs.(4.42) and (4.45). Notice that one can account for boosted thermal distributions by replacing $\lambda \to \lambda - \mu$ in Eq. (4.45). In all the simulations presented in the manuscript we have set for simplicity $\mu = 0$. The density and the two-point correlation function are computed by averaging over the number M of independent sampled initial conditions

$$\langle n(x,t) \rangle_{\mathrm{MC}} = \frac{1}{M} \sum_{i=1}^{M} \frac{N_i(x,t)}{l}, \tag{4.101}$$

$$\langle n(x,t) n(x,0) \rangle_{\mathrm{MC}}^{\mathrm{c}} = \frac{1}{M} \sum_{i=1}^{M} \frac{N_i(x,t) N_i(0,0)}{l^2} - \left(\frac{1}{M} \sum_{i=1}^{M} \frac{N_i(x,t)}{l} \right) \left(\frac{1}{M} \sum_{i=1}^{M} \frac{N_i(0,0)}{l} \right), \tag{4.102}$$

where $N_i(x,t)$ and $N_i(0,0)$ denote the number of rods at time t in the interval $(x - l/2, x + l/2)$ and at time 0 in $(-l/2, l/2)$ respectively, for the $i = 1, 2 ... M$ realization of the initial rods' positions and velocities.

The results obtained for a double thermal bump release on top of a constant thermal background for rod length $a = 0.1$ and inverse temperature profile $\beta(x)$ as per Eqs. (4.42) and (4.45) are further reported in Fig. 4.B.1 for completeness. The parameters are as follows: $x_0 = 300$, $\beta_{as} = 10$, $z = 120$, $\beta_{in} = 0.4$ and $a = 0.1$. The number of rods used in the Monte Carlo simulations is $N = 270$, $L = 660$ and $l = 10$. For $t = 15$ and $t = 30$ we use $2 \cdot 10^6$ samples, while for $t = 70$ and 90, since the noise in the simulations increases, the sampling is enlarged to $7 \cdot 10^6$ and $8 \cdot 10^6$ samples respectively. Similarly to the cases analyzed in the main text, for the density dynamics $\langle n(x,t) \rangle$ an excellent agreement with the GHD results is obtained for all the times shown ($t = 15$, 30, 70 and 90). As long as correlation functions are concerned, instead, for $t = 15$, 30 a deviation with the Euler scale expression is present, for longer times $t = 70$, 90 an excellent agreement is again attained. This aspect is witnessed by the relative distance σ between the two methods, that for $t = 15$ is significantly larger than the one for the values $t = 30$, 70 and 90. In the latter cases, σ is solely determined by the noise in the Monte Carlo sampling.

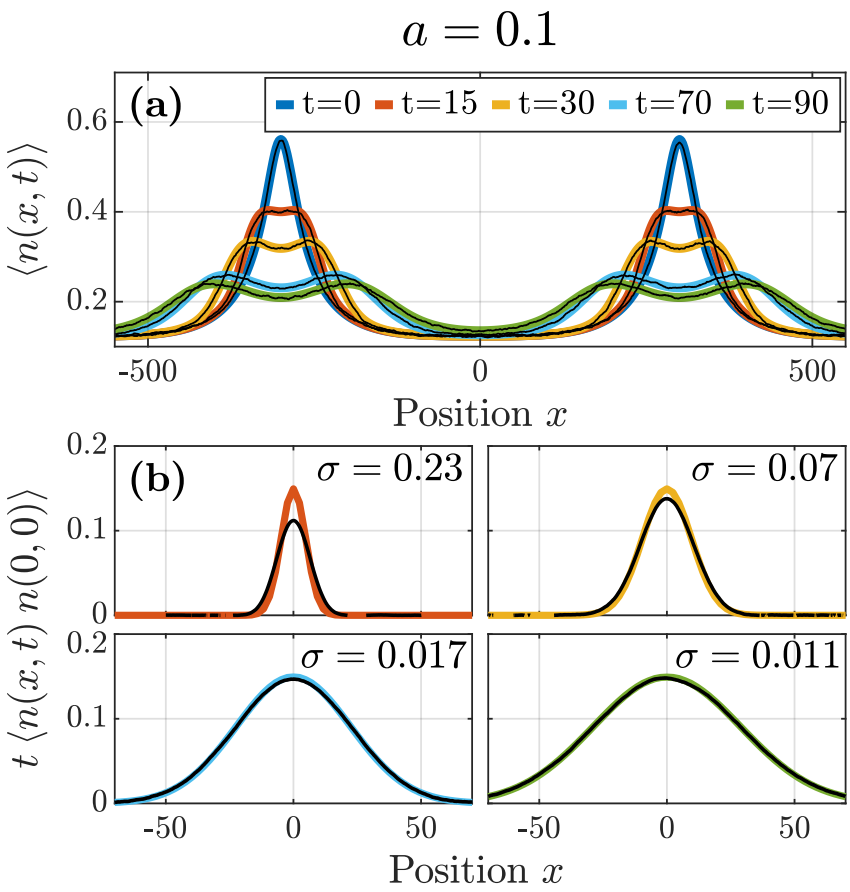

FIGURE 4.B.1: Release of a double density bump in the hard-rod model calculated using GHD (colored lines) and Monte Carlo (black lines). Parameters of the Monte Carlo simulations are specified in the text. **(a)** Comparison of the evolution of the linear density. **(b)** Comparison of two-point correlation $t\,\langle n(x,t)n(0,0)\rangle$ multiplied by time t and the relative distance between the approaches, σ. Image taken from Ref. [3].

4.C Relativistic sinh-Gordon model

The sinh-Gordon model is a relativistic quantum field theory, which is integrable. It is described by the Hamiltonian [80, 390]

$$H = \int \mathrm{d}x \left\{ \frac{\pi^2(x)}{2} + \frac{1}{2}\left[\partial_x \phi(x)\right]^2 + \frac{\beta^2 c^2}{g^2} : \cosh[g\phi(x)] : \right\} , \tag{4.103}$$

where we have set $\hbar = 1$ and $\phi(x)$ is a real scalar field. The parameters

$$m^2 = \beta^2 \frac{\sin(\alpha\pi)}{\alpha\pi} \quad \text{and} \quad \alpha = \frac{cg^2}{8\pi + cg^2} . \tag{4.104}$$

denote the mass m of the field and the dimensionless coupling constant α, respectively. In Eq. (4.103), c is the speed of light and $: \cdots :$, in the last term of the Hamiltonian, denotes the normal ordering with respect to the ground state. The

momentum operator $\pi(x,t)$ is given by

$$\pi(x,t) = \frac{1}{c^2}\frac{\partial\phi(x,t)}{\partial t}, \tag{4.105}$$

and it satisfies the canonical equal-time commutation relations with the field $\phi(x,t)$, i.e., $[\phi(x,t),\pi(x',t)] = i\delta(x-x')$. The explicit presence of the speed of light c is useful in order to study the non-relativistic limit of the sinh-Gordon in Eq. (4.103), as shown in Refs. [391, 392]. In all the following formulas, and in Subsec. 4.2.5, we set $c = 1$ since we will not consider the non-relativistic limit of Eq. (4.103). Like the in the repulsive Lieb-Liniger model, the thermodynamic Bethe ansatz is determined by a single quasi-particle species with fermionic statistics. The TBA functions of the model read

$$E(\lambda) = m\cosh\lambda - \mu,\;\; p(\lambda) = m\sinh\lambda,\;\; T(\lambda,\lambda') = \frac{1}{\pi}\frac{\sin(\pi\alpha)\cosh(\lambda-\lambda')}{\sin^2(\pi\alpha)+\sinh^2(\lambda-\lambda')}, \tag{4.106}$$

where we have added a chemical potential, μ, to the energy function. Since the quasi-particles of the sinh-Gordon model are fermions one has

$$f(\lambda) = 1 - \vartheta(\lambda)\,. \tag{4.107}$$

In Subsec. 4.2.5, see Fig. 4.6, we have considered correlation functions of vertex operators of the field ϕ. For these operator exact result for the one-point functions in a GGE ϑ are known from Refs. [80, 393, 394]

$$\langle \mathrm{e}^{kg\phi}\rangle_\vartheta = \prod_{j=0}^{k-1} H_j\,, \tag{4.108}$$

where $k \in \mathbb{N}$ and

$$H_k = 1 + 4\sin(\pi\alpha(2k+1))\int\frac{\mathrm{d}\lambda}{2\pi}\,\mathrm{e}^{\lambda}\,\vartheta(\lambda)\varepsilon_k^-(\lambda)\,, \tag{4.109}$$

and

$$\varepsilon_k^\pm(\lambda) = \mathrm{e}^{\pm\lambda} + \int\frac{\mathrm{d}\lambda'}{2\pi}\,2\,\mathrm{Im}\left(\frac{\mathrm{e}^{2ki\pi\alpha}}{\sinh(\mp(\lambda-\lambda')-i\pi\alpha)}\right)\vartheta(\lambda')\varepsilon_k^\pm(\lambda')\,. \tag{4.110}$$

Exploiting the latter result, the one-particle form factor $V^{(k)}(\lambda)$, defined in Eq. (4.30), of the vertex operator in Eq. (4.108) can be computed (see Ref. [177] for the details)

$$V^{(k)}(\lambda) = \frac{2}{\pi\,\rho^t(\lambda)}\sum_{j=0}^{k-1}\sin(\pi\alpha(2j+1))\varepsilon_j^+(\lambda)\varepsilon_j^-(\lambda)\prod_{i=0,i\neq j}^{k-1} H_l\,. \tag{4.111}$$

The expression in Eq. (4.111) for $V^{(2)}(\lambda)$ has been used in Fig. 4.6 for the correlators.

Part II

Inhomogeneous dynamics with confinement

Chapter 5

Dynamics in systems with confined quasi-particle excitations

In this Chapter we still focus on the dynamics of many-body systems having inhomogeneous initial states, as in Chapters 3 and 4, but we consider the complementary cases in which the quasi-particle excitations experience confining interactions. In this respect, the models that will be studied in this Chapter are fundamentally different from those addressed in Part I of the thesis, because they are non-integrable. At the technical level, both the thermodynamic Bethe ansatz and the quench action, introduced in Chapter 2 and largely used to derive all the results presented in Part I of the thesis, do not apply in this case. The Generalized hydrodynamics, as already commented at the beginning of Chapter 4, can be extended to account for integrability breaking terms, provided they vary on length scales larger than the microscopic ones. However, in the cases that will be addressed in this Chapter, inhomogeneities are not smooth in any sense and they are not smoothed out by the dynamics, thereby preventing any hydrodynamic approach (at least within the numerically accessible time scales). Accordingly, our analysis of systems exhibiting confinement of excitations will be mostly based on perturbation theory. Our analytical predictions are then compared with numerical simulations based on matrix product states.

As we have seen in Subsec. 1.5.1, non-integrable systems are particularly interesting for the studying the approach to thermal equilibrium and for testing the validity of the Eigenstate Thermalization Hypothesis (ETH), see Subsec. 1.3.3. In this context, the study of confinement in one-dimensional quantum statistical systems, e.g., in the quantum Ising chain in Eq. (1.50), is of paramount importance since it can lead to a slow relaxation dynamics. As a matter of fact, it has been shown that in homogeneous quantum quenches, the presence of confined quasi-particle excitations in the spectrum of the post-quench Hamiltonian are signalled by severe suppression of quantum correlation spreading, of entanglement growth, long-time persistence of spatial inhomogeneities, and extraordinaly long-lived coherent oscillations of local observables around non-thermal values, as shown in Refs. [6, 7, 224–232]. Based on extensive numerical work, it has been also suggested in Refs. [233, 234] that the Ising chain Hamiltonian in Eq. (1.50) is characterized by a pattern of atypical energy eigenstates with non-thermal features carrying over to the thermodynamic limit, which violate the eigenstate thermalization hypothesis. In this light, the aforementioned anomalous features may represent a dynamical manifestation of this phenomenon.

The study of the dynamics in the presence of confinement in statistical systems can also shed light on the similar slow relaxation behavior observed in lattice gauge theories (LGTs, see the references in Subsec. 1.5.1). Their equilibrium phase diagrams have been successfully investigated via imaginary-time path-integral Monte Carlo simulations in a wide range of parameters [395–397]. Non-equilibrium properties, however, cannot be accessed with these equilibrium Monte-Carlo simulations, as they are affected by severe sign problems [398]. In this respect, recent years have witnessed a great interest in developing *quantum simulators* of lattice gauge theories via ultra-cold atomic systems and trapped ions. Albeit, currently, there is no efficient way for simulating non-Abelian LGTs in $(3+1)$ dimensions, for Abelian LGTs in $(1+1)$ dimensions many proposals for their experimental realization via cold-atomic systems have been put forward, see, e.g., Refs. [246, 399–403]. For example, the Schwinger model, which will be discussed in this Chapter, has been realized with a system of four trapped ions in Ref. [404].

The aim of this Chapter is then twofold. First, we aim at discussing the dynamical signatures of confinement in the case of inhomogeneous quenches, which we have extensively discussed in Chapter 3 and 4. In the latter case, we have seen that when the quasi-particles ballistically propagate the initial inhomogeneity is rapidly smeared out by the dynamics and a smooth hydrodynamics description emerges. Based on the aforementioned findings about the dynamics ensuing from homogeneous quenches, we expect that the confinement of quasi-particles dramatically modifies this picture. Indeed, we show that the paradigmatic Ising chain in Eq. (1.50), initially prepared in a domain-wall states of the longitudinal magnetization with a finite energy gradient, can exhibit suppression of energy transport within the whole range of numerically accessible time scales. Second, we show that the Ising Hamiltonian in Eq. (1.50) can be exactly mapped onto a $(1+1)$ Abelian lattice gauge theory. In terms of this mapping we give a unified picture of the slow relaxation dynamics observed both in one-dimensional quantum chains and in LGTs for a rather generic set of inhomogeneous initial states.

This Chapter is organized as follows. In Sec. 5.1, we first briefly review the equilibrium physics of statistical systems with confinement and the corresponding spectral properties, and then we present our results from Ref. [7] which show how the occurence of confinement in the Ising chain in Eq. (1.2) can be understood via a mapping to an Abelian lattice gauge theory. In Sec. 5.2, we first briefly discuss the anomalous dynamics determined by the confinement of the quasi-particle excitations in homogeneous quenches, and then we detail our results from Ref. [6] for the energy transport from an inhomogeneous domain-wall initial state. In Sec. 5.3, we show, on the basis of Ref. [7], the fundamental mechanisms at the root of the slow relaxation behavior due to confined excitations. Section 5.4 presents our conclusions, while additional technical details are consigned to Appendix 5.

5.1 Confinement in one-dimensional quantum statistical models

In this Section we review how confinement of excitations arises in two important classes of one-dimensional many body systems, which will be the main subject of the investigation in Secs. 5.2 and 5.3. In Subsec. 5.1.1 we discuss one-dimensional quantum spin chains taking the Ising chain in a transverse and longitudinal field as an example. We explain how the presence of a longitudinal field non perturbatively changes the spectrum of the model, determining an effective attractive linear potential among pairs of quasi-particles, which therefore form spatially confined bound states. The spectral properties of the Hamiltonian in a longitudinal field are also discussed. In Subsec. 5.1.2 we briefly present the one-dimensional Schwinger model, which describes the quantum elecrodynamics in $(1+1)$ dimensions. In Subsec. 5.1.3 we review the lattice regularization of the same model. From the latter, Abelian quantum link models are further introduced upon replacing the gauge degrees of freedom with spin operators. In Subsec. 5.1.4 we eventually show that, by integrating out the gauge field, an effective linear Coulomb potential among the charges arises, which is responsible for their confinement. In Subsec. 5.1.5 we present our result from Ref. [7], which provides a unifying explanation of the emergence of confinement in these two classes of systems. Namely, we show that the Ising chain in a transverse field can be exactly mapped onto a LGT with local $U(1)$ symmetry.

5.1.1 Confinement in the one-dimensional quantum Ising chain

We consider the ferromagnetic quantum Ising chain, already introduced in Eq. (1.50), with a transverse and a longitudinal magnetic field, g and h, respectively; the corresponding Hamiltonian is

$$H(g,h) = -J\sum_i \sigma_i^z\sigma_{i+1}^z - g\sum_i \sigma_i^x - h\sum_i \sigma_i^z. \tag{5.1}$$

Here $\sigma_i^{x,y,z}$ are the Pauli matrices acting on the site i. Note that, compared to Eq. (1.50), we explicitly reintroduced the ferromagnetic exchange parameter $J>0$. Furthermore, in order to conform to the notation of Ref. [7], we have exchanged the role of x and z and we have renamed the fields as $h_x \to h$ and $h_z \to g$. In Subsec. 3.1.1 of Chapter 3 we have discussed in detail the exact solution of the model for $h=0$ from Ref. [75] (for open boundary conditions). As discussed in Sec. 1.1, $H(g,0)$ is invariant under $\mathbb{Z}_2$ transformations, which amount to rotations of the spins by an angle π around the z axis. In the ferromagnetic phase with $|g|<J$, the $\mathbb{Z}_2$ symmetry is spontaneously broken and the free fermionic quasi-particle excitations physically correspond to freely moving domain-walls (or kinks) connecting the two oppositely magnetized ground states with $\langle\sigma_j^z\rangle = (1-(g/J)^2)^{1/8}$. At $g=J$, a quantum phase transition separating the ferromagnetic phase from the paramagnetic one takes place. $H(g,0)$ at the quantum critical point is described by a conformal field theory of free Majorana fermions with central charge $c=1/2$

[14], as anticipated in Sec. 1.1. A finite $h \neq 0$ causes a non-perturbative modification of the spectrum of the elementary excitations: it selects as a ground state the one with $\langle \sigma_j^z \rangle$ along h and raises the energy of configurations with domains of reversed spins by an amount proportional to their extension. This corresponds to a linear, V-shaped interaction potential between two consecutive kinks delimiting a domain, which therefore become *confined* into composite objects called *mesons*, in analogy with the low-energy limit of gauge theories (see the next Subsec. 5.1.2). Within the same terminology, the kinks correspond to *quarks*, the ground state of $H(g,0)$ favoured by the longitudinal field h is named *vacuum*, while the ground state oppositely magnetized with respect to h is dubbed *false vacuum*. The confinement of pair of kinks-quarks into a meson is shown pictorially in Fig. 5.1. This modification of the spectrum has been originally studied in Refs. [203, 205,

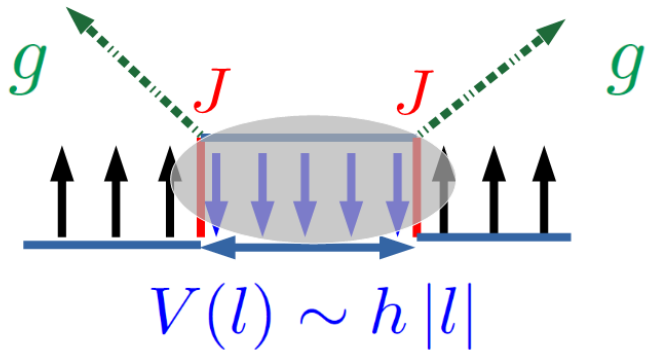

FIGURE 5.1: Pictorial representation of the confinement of a pair of kinks (in red) in the Ising chain with longitudinal (in blue) and transverse (in green) field in Eq. (5.1). In the presence of a longitudinal field h, which in the figure is assumed to point upwards, a domain of spins pointing downwards acquire with respect to the ground state configuration (all the spins pointing upwards) an additional energy proportional to its length l. This induces an effective linear attractive potential $V(l) \sim hl$ between the two kinks delimiting the region where the magnetization is oppositely polarized with respect to the longitudinal field h. The energy associated to this domain is given by the sum of the energy associated to the boundaries, $\propto J$ (in red), plus the one associated to its interior $\propto hl$ (in blue). This picture is clearly heuristic as we are dealing with a quantum model. As a matter of fact, in the presence of a transverse field, g quantum fluctuations on top of the aforementioned description are present. Kinks are no longer eigenstates of σ^z and they can propagate. Differently from the non-interacting case, $h = 0$, however, the kinks do not move freely, i.e., ballistically as they cannot get infinitely far apart from each other and form a bound state, named meson (shown by the grey area in the figure).

209, 212–216] in the vicinity of the critical point $g \to 1$ exploiting the field-theory description of the model. In particular, in the weak confinement regime $h \ll g$ the masses M_n, with $n = 1, 2 \ldots$, of the mesons are discrete and fill the interval $(2m, \infty)$, with $m = 2|J - g|$. The latter approach to compute the masses M_n of the mesons is perturbative in h and it is based on the projection of the many-body Schr$'$odinger equation onto the two-kinks (fermions) subspace, obtaining the so-called Bethe-Salpeter equation. The effects coming from multi-kink processes are then taken into account perturbatively by considering the possible transition from the two to the four and larger kinks subspaces. In particular, mesons with masses $M_n > 4m$ are unstable since they can decay into pairs of lighter mesons. The decay

rate has been computed in Ref. [216] and it scales, as a function of the longitudinal field h, as h^3. Later, the energy spectrum of the mesons has been also determined far away from criticality, for the lattice model in Eq. (5.1), still in the regime of weak confinement, in Ref. [218]. The extension of the aforementioned result for the decay of heavier mesons to the lattice model is not at all simple and it has not been pursued so far. We mention that the calculation of the meson energies can be done, in a complementary way, perturbatively in the transverse field g, as shown in Ref. [405]. In this case, the unperturbed energies are simply expressed in the "classical" basis of the eigenstates of σ^z

$$E(k,n) = E_0 + 2Jk + 2n\,h, \tag{5.2}$$

where E_0 is the ground-state energy, obtained when all the spins are aligned in the direction of h, k is the number of kinks and n the number of reversed spins with respect to the longitudinal field. In the perturbative limit $J \gg g, h$, transitions between states with a different number of kinks are characterized by the dimensionless quantity g/J, i.e., by the ratio between the coupling g and the energy gap (proportional to) J between the states connected by the transition induced by g. Accordingly, in the limit $J \gg g, h$, transitions between states with a different number of kinks are suppressed. The energy of single meson states, corresponding to having $k = 1$ in Eq. (5.2), can be exactly computed perturbatively in $J \gg g, h$, but at any order in the ratio g/h. We will come back to this analysis in Sec. 5.3 when we will derive an effective-Hamiltonian description for the longitudinal field Ising chain in the regime $J \gg g, h$. The very same description can be given of other quantum spin chains [219] and to spin ladders [220, 231]. For example, the antiferromagnetic XXZ model with $J > 0$ in a staggered field h and in the massive phase $\Delta > 1$, with Hamiltonian

$$H(\Delta, h) = J \sum_i \left(\sigma_i^x \sigma_{i+1}^x + \sigma_i^y \sigma_{i+1}^y + \Delta \sigma_i^z \sigma_{i+1}^z \right) + h \sum_i (-1)^i \sigma_i^z, \tag{5.3}$$

displays confinement of the excitations, as shown in Ref. [219]. In fact, in the limit $\Delta \gg 1$ the two degenerate ground states of $H(0, h)$ are simply expressed in the basis of the eigenstates $|\uparrow_i\rangle_z$ of σ_i^z as the antiferromagnetic Néel state $|\uparrow_i \downarrow_{i+1} \uparrow_{i+2} \downarrow_{i+3} \ldots\rangle_z$ and the anti-Néel one $|\downarrow_i \uparrow_{i+1} \downarrow_{i+2} \uparrow_{i+3} \ldots\rangle_z$. The staggering field h breaks the symmetry between the two ground states and confines pair of kinks, which in this case are interpreted as consecutive spins pointing in the same direction, into mesons, in complete analogy with the discussion we have done for the Ising chain. In Secs. 5.2 and 5.3 the discussion will be focused on the Ising chain in Eq. (5.1), but the results apply to the staggered XXZ chain as well. Further details for the latter model, which we do not report here for brevity, can be found in Appendix of Ref. [7] (see also the final comments in Appendix 5.B). In concluding this Section, we mention that it has been shown recently, in Refs. [233, 234], based on numerical analysis at finite sizes, that one-meson (two-kinks) states of the Ising Hamiltonian in Eq. (5.1) have non-thermal expectation values, in contrast to widespread expectation of the Eigenstate Thermalization Hypothesis (cf. Eq. (1.36) in Subsec. 1.3.3). As a consequence of this, one-meson states are claimed to be stable even above the inelastic threshold $M_n > 4m$ and they are supposed

to be responsible for the non-thermal dynamics observed in many quenches of the Ising chain in a longitudinal field (see Subsec. 5.2.1). It is, however, important to say that the extrapolation to the thermodynamic limit of the results presented in Refs. [233, 234] is not established beyond doubt. Indeed, the earlier analytical studies of Ref. [210], in the perturbative regime $h \ll g$, indicate the existence in the very same model of a decay of the false vacuum which occurs with a rate which is exponentially small as $1/h$ increases: this could make thermalization unaccessible to numerical calculations. Accordingly, we can certainly state that the eventual lack of thermalization in the confined phase is still a largely open field of research. In Sec. 5.3 we will not address the problem of the possible lack of thermalization at infinite times. However, we will show, in the perturbative regime $J \gg h, g$, that thermalization is suppressed until times which are exponentially long as J increases. We will elucidate the physical reasons behind this slow dynamical behavior.

5.1.2 The Schwinger model of quantum electrodynamics

The Schwinger model [237, 238] describes quantum electrodynamics in $(1+1)$ dimensions. The Lagrangian of the model is

$$\mathcal{L} = -\frac{1}{4} F^{\mu\nu} F_{\mu\nu} + \bar{\Psi}(i\partial\!\!\!/ - eA\!\!\!/ - m)\Psi, \tag{5.4}$$

where $A_\mu = (A_0, A_1)$ (the time component is labelled by 0, while the space component by 1) is the electromagnetic potential, $F_{\mu\nu}$ is the field strength tensor

$$F_{\mu\nu} = \partial_\mu A_\nu - \partial_\nu A_\mu, \tag{5.5}$$

and m is the mass of the fermionic two-components Dirac quantum field $\Psi = (\Psi_q, \Psi_{\bar{q}})$. The first component Ψ_q of the spinor represent the particles, while $\Psi_{\bar{q}}$ the antiparticles. In the following we will refer to the particle as positron and to the antiparticle as electron. In Eq. (5.4) we are adopting the Feynman slash notation $A\!\!\!/ = A^\mu \gamma_\mu$ ($\partial\!\!\!/ = \partial^\mu \gamma_\mu$), which amounts to contract with the gamma matrices γ_μ. The latter in chiral representation [202] are given by the Pauli matrices $\gamma^0 = \sigma^z$ and $\gamma^1 = i\sigma^y$, with $\bar{\Psi} = \Psi^\dagger \gamma^0$. In Eq. (5.4) we are assuming natural units $\hbar = c = 1$, with $e > 0$ the charge of the positron (and $-e$ the one of the electron). In the temporal gauge $A^0 = 0$, $A^1 = A$ is the vector potential, the Hamiltonian associated to the Schwinger Lagrangian in Eq. (5.4) is

$$H = \int \mathrm{d}x \left[-i\bar{\Psi}(x)\gamma^1(\partial_1 - ieA(x))\Psi(x) + m\bar{\Psi}(x)\Psi(x) + \frac{E^2(x)}{2} \right]. \tag{5.6}$$

E is the electric field operator, which is canonically conjugate to the vector potential

$$[A(x), E(x')] = -i\delta(x - x'). \tag{5.7}$$

The Abelian $U(1)$ gauge symmetry is expressed by the invariance of the Lagrangian $\mathcal{L}$ under the combined transformations of the matter $\Psi(x)$ and the gauge

field $A(x)$

$$\Psi'(x) = \exp[-i\,e\,\alpha(x)]\Psi(x), \quad A'(x) = A(x) - \partial_1\alpha(x). \tag{5.8}$$

5.1.3 The lattice Schwinger and quantum link models

In order to provide the lattice regularization of the Schwinger model we introduce the lattice spacing a, such that the spatial coordinate is discrete and takes the values $x_j = ja$ with $j \in \mathbb{Z}$ the lattice site. Then we adopt the staggered fermions approach of Refs. [237, 406], where a single fermionic operator ϕ_j at site j is used to represent the Dirac spinor $\Psi(x)$. The particle component $\Psi_q(x_j)$ of the spinor is placed on even lattice sites, while the antiparticle one $\Psi_{\bar{q}}(x_j)$ one the odd sites:

$$\Psi_q(2j\,a) = \frac{\phi_{2j}}{\sqrt{a}}, \quad \Psi^\dagger_{\bar{q}}((2j+1)a) = \frac{\phi_{2j+1}}{\sqrt{a}}. \tag{5.9}$$

As a consequence, particles reside on occupied even lattice sites, while antiparticles sit on empty odd sites. When the term of the Hamiltonian in Eq. (5.6) involving the partial derivative w.r.t. to the space coordinate is discretized, it produces an hopping term of the form $\phi^\dagger_j\phi_{j+1}$ (together with its Hermitean conjugate). To preserve the gauge invariance in Eq. (5.8) in the lattice model, one is then led to introduce the *parallel transporter* $U(x,y)$

$$U(x,y) = \exp\left[-ie\int_x^y \mathrm{d}x' A(x')\right], \tag{5.10}$$

and the corresponding discrete-lattice version

$$U_{j,j+1} = U(x_j = ja, x_{j+1} = (j+1)a) \simeq \exp\left[-ieaA(x_j = ja)\right] = \exp\left[-ieaA_{j,j+1}\right], \tag{5.11}$$

which is defined on the edges of the lattice. The discrete form of Eq. (5.7) reads as

$$[A_{j,j+1}, E_{j',j'+1}] = -\frac{i}{a}\delta_{j,j'}. \tag{5.12}$$

Since the gauge field $A_{j,j+1}$ will enter in the lattice Hamiltonian only through the parallel transporter $U_{j,j+1}$, it follows from Eq. (5.11) that the variable

$$0 \le \theta_{j,j+1} < 2\pi, \quad \text{with} \quad \theta_{j,j+1} = eaA_{j,j+1}, \tag{5.13}$$

has a compact representation in the interval $(0, 2\pi)$. Introducing the operator $L_{j,j+1}$ such as the commutation relation

$$[\theta_{j,j+1}, L_{j',j'+1}] = i\delta_{j,j'} \tag{5.14}$$

holds, from Eq. (5.12) one identifies $L_{j,j+1} = -E_{j,j+1}/e$. From Eqs. (5.13) and (5.14) $L_{j,j+1}$ has integer spectrum

$$L_{j,j+1} = 0, \pm 1, \pm 2, \ldots, \tag{5.15}$$

and the Hilbert space of the gauge degrees of freedom is infinite dimensional. The minimal coupling between the gauge field and the fermionic matter then corresponds to (see, e.g., Refs. [9, 237, 399])

$$H = -w \sum_{j=1}^{L-1} (\phi_j^\dagger U_{j,j+1} \phi_{j+1} + \phi_{j+1}^\dagger U_{j,j+1}^\dagger \phi_j) + m \sum_{j=1}^{L} (-1)^j \phi_j^\dagger \phi_j + J \sum_{j=1}^{L-1} L_{j,j+1}^2. \quad (5.16)$$

The couplings w and J are set as

$$w = \frac{1}{2a}, \quad J = \frac{ae^2}{2}, \quad (5.17)$$

so that Eq. (5.16) effectively renders Eq. (5.6) in the continuum limit $a \to 0$. Notice that, from Eq. (5.7) (discretized on the lattice) and Eq. (5.11), the electric field $E_{j,j+1}$ and the parallel transporter $U_{j,j+1}$ satisfy the following commutation relation

$$[E_{j,k}, U_{j',k'}] = \delta_{j,j'} \delta_{k,k'} U_{j,k}, \quad [E_{j,k}, U_{j',k'}^\dagger] = -\delta_{j,j'} \delta_{k,k'} U_{j,k}^\dagger. \quad (5.18)$$

The $U(1)$ invariance in Eq. (5.8) corresponds to the invariance of the Hamiltonian in Eq. (5.16) on the lattice under the following unitary transformation V

$$VHV^\dagger = H, \quad V = \prod_j \exp(-ie\alpha_j G_j), \quad (5.19)$$

where G_j is the generator of the transformation

$$G_j = L_{j,j+1} - L_{j-1,j} - Q_j, \quad Q_j = \phi_j^\dagger \phi_j - \frac{1 - (-1)^j}{2}, \quad (5.20)$$

which by construction commutes with the Hamiltonian $[H, G_j] = 0$. The operator G_j gives rise to the Gauss law within the neutral gauge sector [9]

$$G_j |\Psi\rangle \equiv 0. \quad (5.21)$$

This equation asserts that the variation of the electric field $L_{j,j+1}$ across the lattice site j is equal to the charge Q_j (measured in units of e) present on that lattice site. The set of states $|\Psi\rangle$ in Eq. (5.21) satisfying the Gauss law is usually named gauge-invariant subspace. Henceforth we shall always restrict to states within the neutral gauge sector in Eq. (5.21).

An alternative formulation of lattice gauge theories is then provided by *quantum link* models, first proposed in Refs. [407, 408], which have the advantage of representing the gauge degrees of freedom via spin operators acting on a finite-dimensional Hilbert space. This can be achieved with the simple substitution

$$U_{j,j+1} = S_{j,j+1}^x + iS_{j,j+1}^y = S_{j,j+1}^+, \quad E_{j,j+1} = S_{j,j+1}^z, \quad (5.22)$$

where S^α, with $\alpha = \{x, y, z\}$, are spin operators. Since the spin operators satisfy the $SU(2)$ algebra, $[S^z, S^+] = S^+$, the operators $U_{j,j+1}$ and $E_{j,j+1}$ in Eq. (5.22) still satisfy the commutation relations in Eq. (5.18). This, in turn, ensures that

the gauge transformations in Eq. (5.19), the gauge generator G_j in Eq. (5.20) and the Hamiltonian in Eq. (5.16) keep the very same form they have in the case where the gauge degrees of freedom are represented with operators acting on an infinite-dimensional Hilbert space. Quantum link models are particularly useful for the purpose of building quantum simulators of lattice gauge theories with ultra-cold atoms, as shown in Ref. [402]. In Subsec. 5.1.5 the spin 1/2 quantum link representation will be used to show the equivalence between the one-dimensional Ising chain in a longitudinal field, in Eq. (5.1), and one-dimensional Abelian LGTs.

5.1.4 Confinement in one-dimensional lattice gauge theories

In the gauge invariant subspace $G_j|\Psi\rangle = 0$ the configuration of the charges and of the gauge field are strongly related. Consider the basis of states labelled by the eigenvalues at every lattice site j of the number of fermions $\{n_j = \phi_j^\dagger \phi_j\}$ and of the electric field $\{L_{j,j+1}\}$, defined in Eq. (5.15). These states can be used as a basis for the gauge-invariant states by requiring that they satisfy the Gauss law at every lattice point. In the absence of quantum fluctuations, i.e., with $w = 0$ in Eq. (5.16), the Hamiltonian is diagonal in this basis. The use of both matter and gauge degrees of freedom, however, provide a redundant description of the state of the system. As a matter of fact, once the configuration of the charges $\{n_j\}$ is given, the set of values of the electric field $\{L_{j,j+1}\}$ is automatically fixed by the Gauss law. The converse is also true. It is then clear, that the many-body state of the system can be identified solely in terms of the eigenvalues of the charges $\{n_j\}$, or in terms of those of the electric field. It is then possible to describe the system via an effective Hamiltonian containing only matter, or gauge, degrees of freedom. In this Section we focus on the case when the gauge fields are integrated out. This can be achieved by performing the Jordan-Wigner transformation together with a gauge transformation, as first shown in Ref. [409],

$$\phi_j = \prod_{l=1}^{j-1} \left(\sigma_l^z U_{l,l+1}^\dagger \right) \sigma_j^- , \tag{5.23}$$

so that the Hamiltonian becomes

$$H = -w \sum_{j=1}^{L-1} (\sigma_j^+ \sigma_{j+1}^- + \sigma_j^- \sigma_{j+1}^+) + m \sum_{j=1}^{L} (-1)^j \sigma_j^z + J \sum_{j=1}^{L-1} L_{j,j+1}^2 . \tag{5.24}$$

Let us now focus on the last term in this equation containing the electric field $L_{j,j+1}^2$, which we denote by H_g. This can be further simplified by integrating the Gauss law in Eq. (5.20)

$$L_{j,j+1} = \sum_{l=1}^{j} Q_l + \varepsilon_0, \quad Q_j = \frac{\sigma_j^z + (-1)^j}{2}, \tag{5.25}$$

where ε_0 can be interpreted as a constant background electric field. Upon inserting Eq. (5.25) into the gauge term H_g of Eq. (5.24) one obtains

$$H_g = -J \sum_{j=1}^{L-1} \sum_{k=j+1}^{L} (k-j) Q_j Q_k - 2J\varepsilon_0 \sum_{j=1}^{L} j Q_j, \tag{5.26}$$

where we used the fact that we are working in the neutral gauge sector with

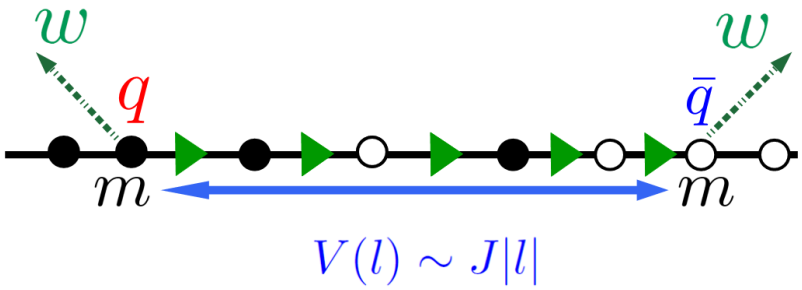

FIGURE 5.2: Pictorial representation of the confinement of a quark and antiquark pair in the lattice Schwinger model. The staggered fermion approach is used in the figure. The quark has charge $q = e > 0$ (in red) and mass m, while the antiquark $\bar{q} = -e$ (in blue) and the same mass. The pair is created on top of the vacuum (the Dirac sea), where no particles are present and the electric field is zero everywhere. As a consequence of the Gauss law in Eq. (5.20), the presence of a quark and an antiquark generates a string of electric field in between the pair (indicated by the green horizontal arrows in the picture). The value of the electric field in the string satisfies the Gauss law. The energy associated to the pair is given by the sum of the masses of the two particles, $2m$, plus the electrostatic energy $\propto Jl$ due to the electric field string. The hopping w introduces quantum fluctuations on top of this picture allowing for the movement of the particle and antiparticle pair with the consequent creation and annihilation of other pairs. As a consequence of the string of electric flux an effective attraction $V(l) \sim J|l|$ develops between q and $\bar{q}$, which causes the confinement of the pair.

$\sum_{j=1}^{L} Q_j = 0$ from Eq. (5.21). The second term in Eq. (5.26) represents the interaction of the charges Q_j with a constant electric field proportional to ε_0. The first term, instead, is the Coulomb interaction between pairs of charges. In one-dimension, indeed, the Coulomb potential associated to a charge Q located at a point x_0 increases linearly with the distance from x_0 as $V(x) \sim -Q|x - x_0|$. Consequently, the energy cost of pulling a pair of oppositely charged particles, e.g., a quark and an antiquark, at a distance l increases linearly upon increasing l, causing the confinement of the pair. The origin of this effective attraction between the charges lies in the fact that a couple of charges, as a consequence of the Gauss law, encloses a string of electric field which raises the energy, compared to the vacuum, by an amount which is proportional to the length of the string itself. This is pictorially shown in Fig. 5.2. It is evident that the confinement of pairs of quarks and antiquarks in the lattice Schwinger model presents striking similarities with the same phenomenon in the Ising chain in a longitudinal field, presented in Subsec. 5.1.1. In the next Subsection, we indeed show that by integrating out the matter degrees of freedom, in a complementary way with respect to the approach

pursued in this Subsection, an exact mapping between these two classes of models can be derived.

5.1.5 Equivalence between one-dimensional LGTs and the quantum Ising chain

The correspondence between the Ising chain in Eq. (5.1) and $U(1)$ gauge lattice gauge theories is based on the interpretation of the spin polarization operator $s_j^z \equiv \sigma_j^z/2$ as a local "electric flux", which leads one to introduce fictitious fermionic matter degrees of freedom on the sites of the dual chain (i.e., on the bonds of the original chain [1]), and local dynamical constraints that associate a kink (antikink) in the spin configuration with the presence of a "positron" ("electron") on the corresponding bond, as described in Fig. 5.3. These constraints are enforced by $U(1)$ gauge-invariant matter-field interactions, and are interpreted as a discrete Gauss law.

To make this explicit, we define two species of fermions, positively (p) and negatively (e) charged, respectively, residing on the bonds (denoted as half-integer sites), with corresponding creation operators $(c_{j+1/2}^{p,e})^\dagger$ and occupation numbers $n_{j+1/2}^{p,e} = (c_{j+1/2}^{p,e})^\dagger c_{j+1/2}^{p,e}$. We introduce a spin-1/2 $U(1)$-quantum link model, see the final part of Subsec. 5.1.3,

$$H_{U(1)} = H_{\rm m} + H_{\rm g} + H_{\rm int}\,, \tag{5.27}$$

with

$$H_{\rm m} = m\sum_j (n_{j+1/2}^p + n_{j+1/2}^e) + \mathcal{U}\sum_j n_{j+1/2}^p n_{j+1/2}^e\,, \tag{5.28}$$

$$H_{\rm g} = \frac{\tau}{2}\sum_j \sigma_j^z\,, \tag{5.29}$$

$$H_{\rm int} = w\sum_j \left\{ [(c_{j-1/2}^p)^\dagger + c_{j-1/2}^e]\sigma_j^+ [c_{j+1/2}^p + (c_{j+1/2}^e)^\dagger] + \text{h.c.} \right\}, \tag{5.30}$$

where $\sigma_j^\pm = (\sigma_j^x \pm i\sigma_j^y)/2$ act as $U(1)$ parallel transporters, according to Eq. (5.22). $H_{\rm m}$ encodes the fermion mass and the onsite Hubbard-like interaction, while $H_{\rm g}$ can be interpreted as the energy shift caused by a background field, in a similar way as ϵ_0 does in Eq. (5.26). In $H_{\rm int}$, the various terms describe hopping and pair creation/annihilation of fermions. The $U(1)$ gauge invariance of these interactions is expressed, analogously as in Eqs. (5.20) and (5.21) in the lattice Schwinger model, by the local symmetries $[H, G_j] = 0$ with $G_j = \sigma_{j+1}^z/2 - \sigma_j^z/2 - (n_{j+1/2}^p - n_{j+1/2}^e)$. As well as in Secs. 5.1.3 and 5.1.4 we work in the neutral gauge sector $G_j \equiv 0$.

[1] Note that our convenient choice is opposite to the prescription for lattice regularization of gauge theories used in Subsecs. 5.1.3 and 5.1.4, whereby matter and gauge degrees of freedom are placed on lattice sites and bonds respectively. In one-dimensional chains, though, sites and bonds are actually interchangeable.

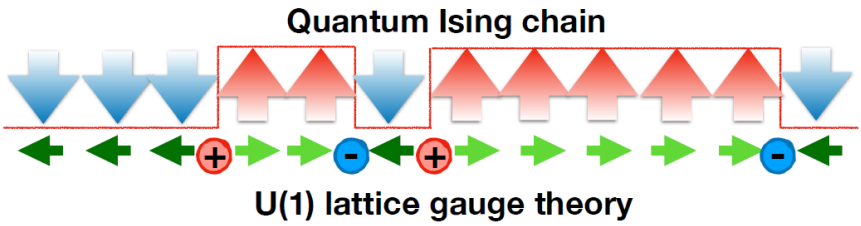

FIGURE 5.3: Cartoon of the mapping of a quantum spin chain (here, the quantum Ising chain) onto a $1+1$-dimensional lattice gauge theory. Kinks, i.e., changes upwards of the local longitudinal magnetization σ_j^z, are mapped to positively charged particles (positrons, in red in the figure), while antikink, i.e., jumps downwards of σ_j^z, to negatively charged ones (electrons, in blue in the figure). The infinite Hubbard repulsion prevents positrons and electrons to sit on the same edge. The ferromagnetic interaction J is therefore mapped to the mass m of the particles. The longitudinal field h is mapped to the electric field τ, which weights an electric field string (in green in the figure) with an energy linearly increasing with the length of the string itself. The transverse field g allows for spin flip transitions and is mapped into the matter-gauge coupling w. The picture shows the equivalent origin behind the emergence of the confinement of quantum excitations in the Ising model and in Abelian $U(1)$ lattice gauge theories. Image taken from Ref. [7].

In the presence of a strong Hubbard repulsion $\mathcal{U} \to \infty$, each "classical configuration" of the gauge field (eigenstate of all σ_j^z operators) fully determines a unique configuration of the matter particles via the Gauss law. This allows one to eliminate the redundant matter degrees of freedom [247, 410] and write the model in terms of a *locally* self-interacting gauge field. We note that this approach is complementary to the one followed in Subsec. 5.1.4, where we considered the elimination of gauge degrees of freedom thereby obtaining an Hamiltonian written solely in terms of the matter degrees of freedom. In this case, all matrix elements of the Hamiltonian (5.27) between two classical gauge-field configurations coincide with the corresponding matrix elements of the quantum Ising chain in the σ^z-basis, upon identifying $m = 2J$, $\tau = -2h$, $w = -g$, and up to an overall energy shift (see Appendix 5.A for details). Within this LGT picture, the longitudinal field h in the quantum Ising chain plays the role of the electrostatic string tension τ, leading to particle confinement. Before concluding, we mention that the Ising chain can also be mapped onto a $\mathbb{Z}_2$-LGT. The details of this mapping are presented in Appendix of Ref. [7], but we do not report them in this thesis for brevity. It is interesting to finally comment on the gauge-integrated version of the above lattice gauge theory, where the gauge field is eliminated following the same steps performed in Subsec. 5.1.4 for the lattice Schwinger model. By solving the Gauss law, in the case of the Hamiltonian in Eq. (5.27), the result is a model of charges subject to a constant electric field and to the constraint of sign alternation along the chain. The latter makes the particles interacting, as made explicit by the strong on-site Hubbard repulsion. The confinement between the quasi particles can thus be connected with the Wannier-Stark localization of charged particles moving in a crystal subject to a constant electric field [411–413]. We will get back

to the Wannier-Stark localization in Subsec. 5.3.3 when discussing the propogation velocities of the mesons.

5.2 Dynamical effects of confinement

After the discussion of the equilibrium and spectral properties of systems with confined quantum excitations, we move to the discussion of their real-time non-equilibrium dynamics. In Subsec. 5.2.1 the focus is on the homogeneous quench dynamics, where the initial state is translationally invariant. In this framework we briefly review some fundamental results from the literature, which are useful for comparison with our original results. In Subsec. 5.2.2 we present our findings from Ref. [6] for the Ising chain in Eq. (5.1) in an initial domain-wall state along the longitudinal direction. The energy transport, in the same spirit of Chapters 3 and 4, is considered. The analysis of more general initial inhomogeneous states including a finite number of mesons (or strings in the gauge theory language) will be considered in Sec. 5.3.

5.2.1 Homogeneous quantum quenches

In the context of homogeneous quantum quenches the initial state $|\Psi_0\rangle$ is usually taken as the bare vacuum of the theory, i.e., the vacuum with zero matter-gauge field coupling ($g = 0$ in Eq. (5.1) and $w = 0$ in Eq. (5.16)). By quenching to a non-vanishing value of the coupling, the non-equilbrium time evolution is eventually obtained. Both the quantum Ising model in a transverse and longitudinal field in Eq. (5.1) and the lattice Schwinger model are non-integrable and the initial state $|\Psi_0\rangle$ presents, in general, a finite energy density on top of the post-quench ground state. As a consequence, based on the discussion in Subsec. 1.3.3, one expects the averages of local observables to relax to thermal values. This expectation is, however, not met in many cases when the post-quench Hamiltonian displays confinement of the quasi-particle excitations. Some results providing evidence of this statement from Refs. [223, 226, 239] are here reported.

In particular, in Fig. 5.4(a) we report the result of Ref. [223] for the dynamics of the order parameter σ^x after a quench of both the transverse g and the longitudinal h field (the values of the parameters are reported in the figure and in the corresponding caption) in the ferromagneti phase of the Ising chain, corresponding to $g < 1$. Even for fairly small times, the dynamics is completely different from the one in the integrable case, $h = 0$, shown by the dashed line. The order parameter average does not relax to any stationary value and it displays persistent oscillations. The dynamics of the order parameter of the same model is also shown in Fig. 5.4(b), taken from Ref. [226]. The initial state and the post-quench parameters h and g (see the caption of the figure) are different from the ones used in Fig. 5.4(a), yet the same qualitative behavior is observed with persistent oscillations, in this case around the thermal expectation value. The latter behavior implies that the average value of the order parameter relaxes to the thermal steady value only after it is integrated in time. This phenomenon has been first observed in Ref. [224], where it has been named "weak thermalization". In Fig. 5.5, from Ref. [239], a

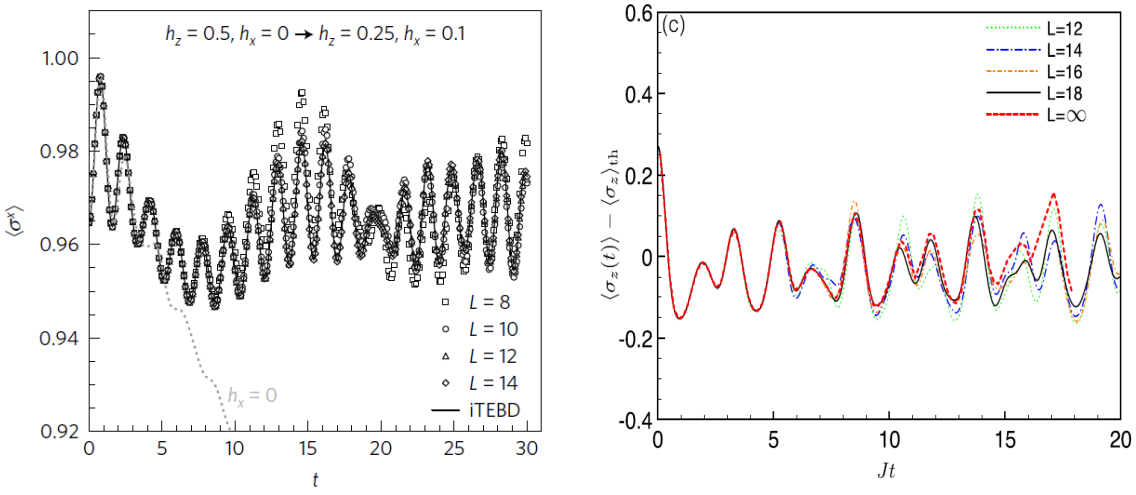

FIGURE 5.4: Dynamics of the expectation value of the longitudinal spin component in the Ising chain in Eq. (5.1), with $J = 1$ in the plot. In panel (a), taken from Ref. [223], the system is initialized in the ground state for $(g = 0.5, h = 0)$. The post-quench parameters are $(g = 0.25, h = 0.1)$. In panel (b), taken from Ref. [226], the system is initially in the ground state for $g = 0$ (the bare vacuum). The post-quench parameters are $(g = -1.05, h = 0.5)$. In (a) we are therefore in the regime of weak confinement, while in (b) a deep quench of the transverse and longitudinal field is done and we are very far from the perturbative limit. Neverthless, in both the cases, the initial state has a small energy density w.r.t. the post-quench ground state, which can be therefore described with few quasi-particles having zero momentum. In the case (a) the quasi-particles are the mesons introduced in Subsec. 5.1.1.

quench of the background electric field, ϵ_0 in Eq. (5.25), in the lattice Schwinger model is shown. Also in this case extraordinarily long-lived oscillations are observed. The common feature of the results in Figs. 5.4 and 5.5 is that the initial state of the system has a small energy density on top of the post-quench ground state. As a consequence, it can be described in terms of a small amount of quasi-particles, according to the picture introduced in Subsec. 1.3.5, having zero momentum, i.e., $k = 0$. Quasi-particles therefore do not propagate along the chain and local observables keep oscillating as a function of time. In the cases of the quenches in the ferromagnetic phase considered in Ref. [223], the excitations produced by the quench can be identified with the mesons, the bound states of pair of kinks we discussed in Subsec. 5.1.1. This fact has been explicitly shown in Ref. [223] by comparing the oscillation frequencies in Fig. 5.4(a) with the masses of the mesons, which can be computed according to the method of Ref. [218] (see Subsec. 5.1.1). In the case of Fig. 5.4(b), quasi-particles have a different nature with respect to the mesons, being the regime of parameter of the quench completely different from the one in Fig. 5.4(a). Their energies have been computed in Ref. [226] using the perturbative Schrieffer-Wolff transformation, which will be discussed in detail in Subsec. 5.3.1. In order to further show the dramatic effects that the confinement of quasi-particles might have on the homogeneous quench dynamics, in Fig. 5.6

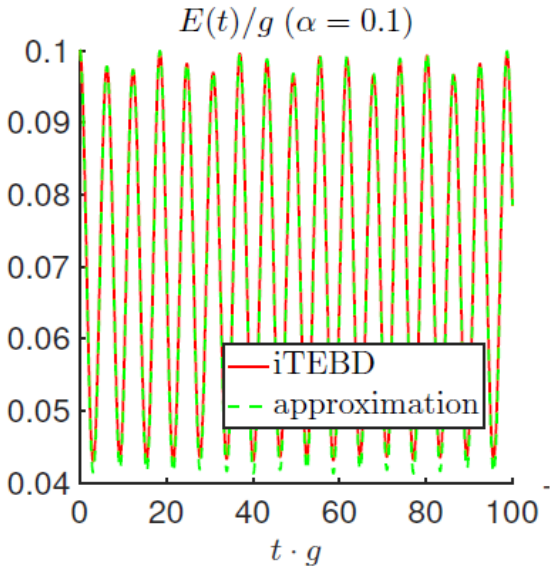

FIGURE 5.5: Dynamics of the electric field $E(t)$ after an homogeneous quench of the background field α (with our notation ϵ_0 in Eq. (5.25)) of the Schwinger model. $g > 0$ denotes the electron charge (e in our notation). The initial state is the ground of the Schwinger model for $\alpha = 0$. Image taken from Ref. [239].

we report the results of Ref. [223] for the equal-time connected correlation function of the longitudinal spin and for the bipartite entanglement entropy (defined in Eq. (1.40)). One can see that as soon a very small h is present in the post-quench Hamiltonian, the correlation spreading and the entanglement growth get severely suppressed with respect to the case where the quasi-particles freely propagate, see Figs. 1.5 and 1.6 in Subsec. 1.3.5 for comparison.

In Chapters 3 and 4 we have, however, seen that the quasi-particle picture is tremendously important also for the analysis of inhomogeneous quenches, where the initial state breaks translational invariance. It is then natural to wonder about the effect that confinement of quantum excitations might have in the dynamics starting from an inhomogeneous initial state. We start addressing this issue in the next Subsection by considering the energy transport in the Ising chain in Eq. (5.1).

5.2.2 Inhomogeneous initial state: suppression of energy transport

In order to investigate transport processes, the simplest inhomogeneous initial state we can consider in this framework is a domain-wall with a single kink in the middle of the chain. For this Subsection (and only in this Subsection) we invert the role of x and z in Eq. (5.1) to better adhere to the notation of Ref. [6]

$$H(g,h) = -J\sum_i \sigma_i^x \sigma_{i+1}^x - g\sum_i \sigma_i^z - h\sum_i \sigma_i^x. \tag{5.31}$$

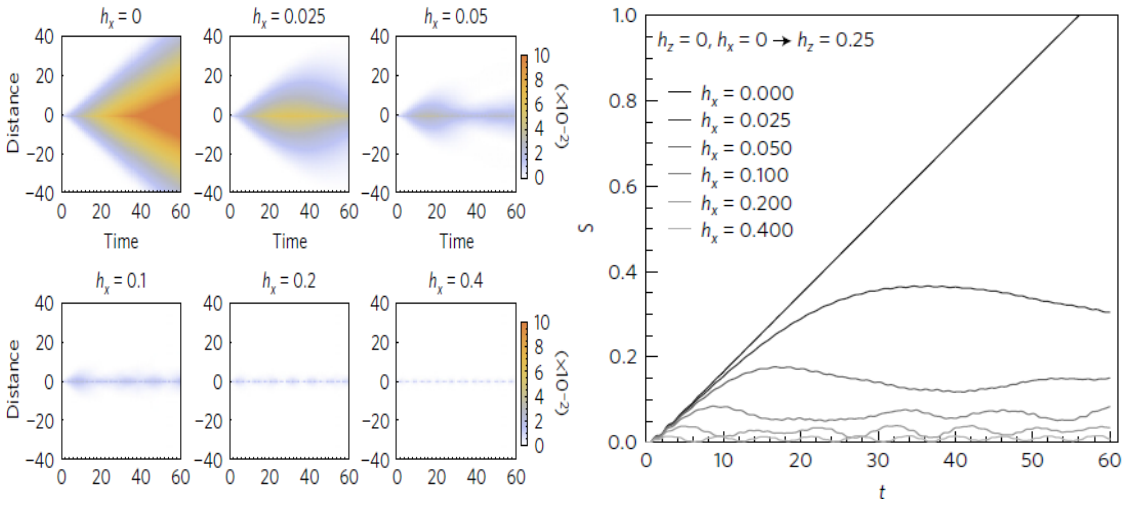

(a) (b)

FIGURE 5.6: Dynamics of the equal-time connected correlation function of the longitudinal spin component and of the bipartite entanglement entropy in the longitudinal field Ising chain. Notation: $g \to g$ and $h \to h$. The initial state is the ground state for $g = 0$. The transverse field is quenched to the value $g = 0.25$, while for h different values, reported in the figure, are considered ranging from 0 to 0.4. Image taken from Ref. [223].

This domain-wall state reads, in terms of the eigenstates $|\uparrow\rangle_j$ and $|\downarrow\rangle_j$ of σ_j^x, as

$$|\Psi_0\rangle = \bigotimes_{j=1}^{L/2} |\uparrow\rangle_j \bigotimes_{j=L/2+1}^{L} |\downarrow\rangle_j \equiv |\uparrow\uparrow \dots \uparrow\uparrow\downarrow\downarrow \dots \downarrow\downarrow\rangle. \tag{5.32}$$

$|\Psi_0\rangle$ is also an eigenstate of $H(0,h)$. At time $t > 0$, the transverse field $g \neq 0$ is suddenly switched on and we study the non-equilibrium evolution of the energy density profile $\langle \mathcal{H}_j(t) \rangle$ as a function of j, where

$$\mathcal{H}_j = -J\sigma_j^x\sigma_{j+1}^x - \frac{g}{2}\left(\sigma_j^z + \sigma_{j+1}^z\right) - \frac{h}{2}\left(\sigma_j^x + \sigma_{j+1}^x\right). \tag{5.33}$$

The associated current density $\langle \mathcal{J}_j(t) \rangle$, is

$$\mathcal{J}_j = Jg\left(\sigma_{j-1}^x\sigma_j^y - \sigma_j^y\sigma_{j+1}^x\right), \tag{5.34}$$

which is independent of the longitudinal field h and it is equal to the current in Eq. (3.43) of Chapter 3 (apart from a constant coming from the different normalization of the Ising Hamiltonian in Eq. (3.2) as compared to Eq. (5.31)). Since $H(g,h)$ is non-integrable, the Hamiltonian is the only (trivial) conserved charge of the model. As a consequence, $\mathcal{J}_i$ is the only current density that can be defined in this model from the continuity equation in Eq. (3.50). Notice that the non-equilibrium protocol we are following in this Subsection is different from the partitioning protocol of Chapters 3 and 4 since, at time $t = 0$, the global term of the Hamiltonian coupled to the transverse field g, is quenched from zero to a finite value. For

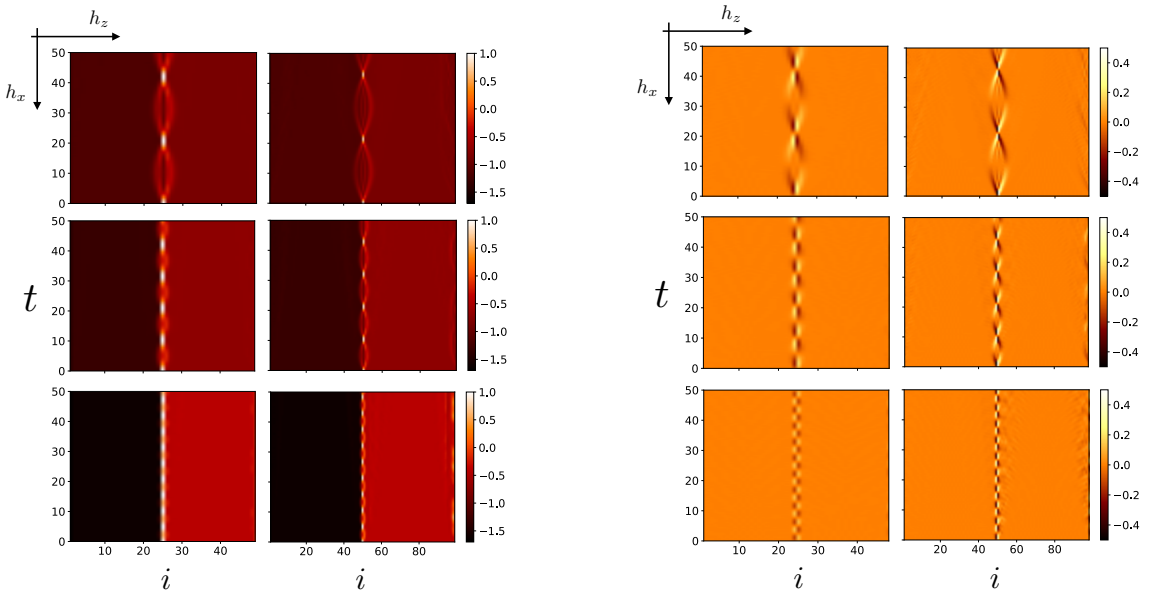

(a)

FIGURE 5.7: Evolution of the energy density $\langle \mathcal{H}_i(t) \rangle$ (left panel) and of the energy current density $\langle \mathcal{J}_i(t) \rangle$ (right panel) profiles, governed by the Hamiltonian (5.31), with the replacements in the figure $h_z \to g$ and $h_x \to h$, starting from the inhomogeneous domain-wall state (5.32), obtained from TEBD simulations, for a range of increasing field values $g = 0.2$ ($L = 50$), 0.4 ($L = 100$) and $h = 0.15, 0.3, 0.6$, varying as indicated by the axes. (Units are fixed such that $J = 1$.) The same qualitative behavior as that illustrated here persists up to long times $t = 10^3$. Note the oscillations of the profiles around the junction, with spatial amplitude $\propto g/h$ and frequency $\propto h$, while there is no evidence for the activation of transport. Image taken from Ref. [6].

$h = 0$, the initial energy density $\langle \mathcal{H}_j(0) \rangle$ is equal on the two sides of the junction, due to the $\mathbb{Z}_2$ symmetry. However, in the presence of a non-vanishing $h > 0$, the chain acquires an initial macroscopic energy imbalance between the left ("cold") part and the right ("hot") part. Transport is therefore expected to happen, similarly as in the cases analyzed in Chapters 3 and 4, leading to a smoothening of the initial imbalance after a transient (cf. Figs. 3.3 and 4.2). In the following we provide compelling evidence against this expectation.

Numerical simulations of the non-equilibrium evolution of the chain have been performed with the time-evolving block decimation (TEBD) algorithm [414–417]. It turns out that the entanglement grows slowly up to moderate values of the field $g \lesssim 0.4J$, which allows us to extend the simulations to long times $t_{\mathrm{M}} = 10^3 J^{-1}$ with modest computational efforts, as in the case of Ref. [223]. The results of the simulations are illustrated in Fig. 5.7 only up to times $t = 50 J^{-1}$, as no qualitative differences are observed up to t_{M}. In both the "strong" ($h \gg g$) and "weak" ($h \lesssim g$) confinement regime, energy transfer between the two halves of the chain is suppressed even at late times. As shown in Fig. 5.7, the main dynamical effect of switching on g is given by pronounced oscillations of the profiles around the position $j = L/2$ of the junction, with characteristic emergent amplitudes and frequencies which depend on the values of the fields. In particular, the

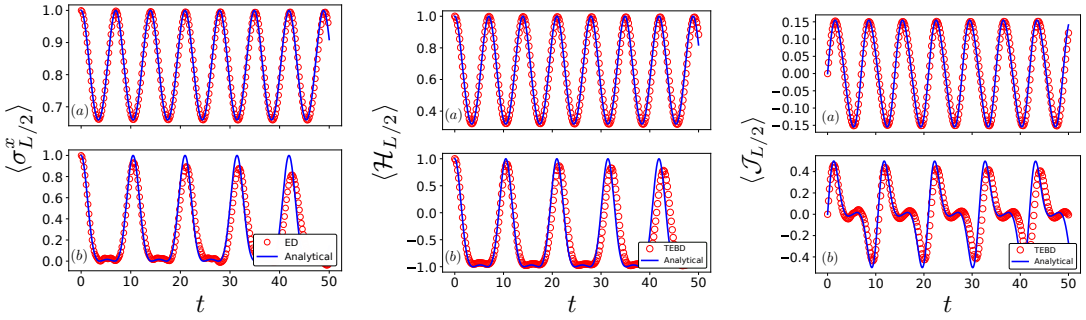

FIGURE 5.8: Comparison between the numerical results $\langle \sigma^x_{L/2}(t) \rangle$, $\langle \mathcal{H}_{L/2}(t) \rangle$, $\langle \mathcal{J}_{L/2}(t) \rangle$ (symbols), and the analytical results $m_{L/2}(t)$, $e_{L/2}(t)$, $j_{L/2}(t)$ (solid lines) for the magnetization (left panel), energy density (central panel) and energy density current (right panel) respectively, at the junction $j = L/2$, as obtained from ED (with $L = 16$) or TEBD (with $L = 50$ or 100), and from the effective single-particle model, respectively. These curves refer to $h = 0.45$, $g = 0.2$ (top row), and $h = 0.3$, $g = 0.4$ (bottom row). (Units are fixed such that $J = 1$.) Note that discrepancies appear as time increases, due to the neglected multi-kink processes. The associated time scale, however, increases upon decreasing g. Image taken from Ref. [6].

energy current density is zero everywhere apart around the junction, where it oscillates between positive values (aligned with the energy gradient) and negative values (against the energy gradient). We emphasize that, within our protocol, an increase in the energy gradient between the two halves, caused by a stronger h, does not result in the activation of transport: on the contrary, it turns out that the oscillations at the junction acquire an even smaller amplitude. The oscillations of the profiles shown in Fig. 5.7 may be interpreted as the quantum motion of the isolated kink initially localized at the junction, triggered by the transverse field $g \neq 0$. In fact, the kinetic energy associated with this motion has a finite bandwith $\sim g$ on the lattice, and therefore, because of energy conservation, the kink quasi-particle can travel, in the linear confining potential $V(l) \sim -hl$, at most a distance proportional to

$$\xi_{\rm loc} = \frac{g}{h} \tag{5.35}$$

(which we shall call henceforth confinement or localization length), before bouncing back and oscillating. This phenomenon is analogous to the Wannier-Stark localization [411–413] or Bloch oscillations, which we already mentioned at the end of Subsec. 5.1.5. In order to give an effective quasi-particle description to the aforementioned oscillations, we use an approach similar to one adopted in Ref. [226]. We map the motion of the isolated kink onto the problem of a *single quantum particle* hopping on a one-dimensional lattice, by projecting the many-body Hilbert space onto the single-kink linear subspace. This approach is valid perturbatively in $1/J$ as it assumes that the number of kinks is fixed. As we shall see in more detail in Subsec. 5.3.1, the effective Hamiltonian thus obtained for the single kink is nothing but the first-order term of the Schrieffer-Wolff perturbative expansion in $1/J$. The dynamics, in the limit $J \gg g, h$ can be then approximated within the single-kink subspace, spanned by the states $\{|n\rangle\}$ with a single domain-wall

located between sites n and $n+1$, with $n = 1, 2, \ldots, L-1$. The corresponding unperturbed energy eigenvalues are $E_n = 2J + 2h(L-n) + E_{\rm GS}$. The resulting matrix elements $\langle n|H(g,h)|m\rangle$ of the Hamiltonian in Eq. (5.31) read $E_{\rm GS}\delta_{n,m} + (H_{\rm eff})_{nm}$, with $E_{\rm GS} = -J(L-1) - hL$ and

$$(H_{\rm eff})_{nm} = [2J + 2(L-n)h]\,\delta_{n,m} - g(\delta_{n,m+1} + \delta_{n,m-1}). \tag{5.36}$$

We note that the off-diagonal perturbation produces an effective hopping amplitude for the kink quasi-particle. Accordingly, the effective Hamiltonian $H_{\rm eff}$ describes the dynamics in terms of a single particle hopping in a one-dimensional lattice in the presence of a linear potential, where the state of the particle is described by a vector $\{\psi_n\}$ with $n = 1, 2, \ldots, L-1$. The absolute value squared of the n-th component of the wavefunction $\psi_n(t)$ is equal to the probability that the particle is at site n at time t. Within this picture, the initial state in Eq. (5.32) maps to $\psi_n(0) = \delta_{n,L/2}$, corresponding to a particle completely localized at the junction between the two chains. Similarly, the magnetization $\langle\sigma_j^x(t)\rangle$ at site j and time t can be expressed within this single-particle picture as

$$m_j(t) \equiv 1 - 2\sum_{n=1}^{j-1} |\psi_n(t)|^2, \tag{5.37}$$

where $\psi_n(t) = \sum_m (\exp(-iH_{\rm eff}t))_{nm}\psi_m(0)$ is the time evolved state within the projected space. In particular, the expression of the wavefunction can be worked out analytically (see Appendix 5.B for more details) and it is equal to

$$\psi_n(t) = J_{n-L/2}(2\xi_{\rm loc}\sin(h_x t))\exp[in(\pi + 2ht)/2], \tag{5.38}$$

where $J_n(x)$ denotes the modified Bessel function of the first kind [330] and $\xi_{\rm loc}$ is given in Eq. (5.35). In order to test the accuracy of our approximation, we compare the dynamics obtained from the above effective single-particle problem with the exact dynamics generated by H [see Eq. (5.31)] in the full many-body Hilbert space, starting from the domain-wall initial state $|\Psi_0\rangle$ of Eq. (5.32) as obtained via both exact diagonalization (ED) and TEBD techniques [2]. The comparison between $m_{L/2}(t)$ and $\langle\sigma^x_{L/2}(t)\rangle$ is shown in Fig. 5.8. In particular, we observe that the agreement is fairly good up to moderate values of the transverse field $g \lesssim 0.4J$. Similarly, the relevant non-equilibrium profiles of the energy and energy current densities can be studied within the above effective single-particle description. This is achieved by projecting the energy density $\mathcal{H}_j$ at site j in Eq. (5.33) onto the single-kink subspace,

$$\left(\mathcal{H}_j^{\rm eff}\right)_{nm} = \frac{1}{2}\left[J(2\delta_{j,n} - 1) - h\,{\rm sgn}(n-j)\right]\delta_{n,m} - \frac{g}{2}\left(\delta_{j,m+1} + \delta_{j+1,m+1}\right)\delta_{n,m+1} + {\rm h.c.}, \tag{5.39}$$

[2] In this case, the simulations based on exact diagonalization of the Hamiltonian can be pushed until sufficiently late times because finite-size effects such as revivals are suppressed, due to the fact that excitations are confined [223]

where the sign function $\mathrm{sgn}(x)$ equals 1 for $x > 0$, -1 for $x < 0$ and 0 for $x = 0$. From the continuity equation

$$\frac{d\mathcal{H}_j^{\mathrm{eff}}}{dt} = i[H_{\mathrm{eff}}, \mathcal{H}_j^{\mathrm{eff}}] = \mathcal{J}_j^{\mathrm{eff}} - \mathcal{J}_{j+1}^{\mathrm{eff}}, \tag{5.40}$$

we can infer the corresponding effective expression for the energy current density operator $\mathcal{J}_j$ at site j, i.e.,

$$\left(\mathcal{J}_j^{\mathrm{eff}}\right)_{nm} = 2iJg\delta_{n,m+1}\,\delta_{m,j-1} - \frac{i}{2}g^2\delta_{m,j-2}\,\delta_{n,m+2} - \frac{i}{2}g^2\delta_{m,j-1}\,\delta_{n,m+2} + \mathrm{h.c.} \tag{5.41}$$

The time-dependent expectation value of the energy density at site j within this single-particle picture can therefore be simply written as

$$e_j(t) \equiv \sum_{n,m} \psi_n^*(t) \left(\mathcal{H}_j^{\mathrm{eff}}\right)_{nm} \psi_m(t), \tag{5.42}$$

with an analogous expression for the current $j_j(t)$ in terms of $\mathcal{J}^{\mathrm{eff}}$. Using the expression of the wavefunction $\psi_n(t)$ in Eq. (5.38) into Eq. (5.42) (and in the analogous expression for $j_j(t)$), an exact expression for the profile of the energy density (current) in the single-kink subspace can be obtained. The expression is reported in Appendix 5.B for brevity, see Eq. (5.75). In Fig. 5.8 we compare the time evolution of $e_{L/2}(t)$ and $j_{L/2}(t)$ with the corresponding exact quantities $\langle \mathcal{H}_{L/2}(t)\rangle$ and $\langle \mathcal{J}_{L/2}(t)\rangle$ as obtained from the TEBD simulations. It is remarkable that, in spite of the simplicity of this approach, the agreement is excellent for small values $g = 0.2J$ of the transverse field, whereas for larger values $g = 0.4J$, small quantitative discrepancies appear, still retaining a fairly good qualitative agreement.

5.3 Description of the slow relaxation behavior

In this Section we investigate the relationship between the dynamical effects of confinement discussed in Subsecs. 5.2.1 and 5.2.2 and prototypical aspects of the localization of interacting particles [97–99, 196, 418–423]. Based on the results of Ref. [7], we demonstrate that confinement causes quasilocalized dynamics of states with dilute excitations. In fact, the route towards thermalization involves the decay of these states into entropically favored many-particle states: the energy stored in confining strings (or mesons) has to be converted into mass via the creation of new pairs of excitations from the vacuum. We show in Subsec. 5.3.1 that these processes can become dramatically slow, in close analogy with the Schwinger effect, i.e., with the suppressed decay of false vacua in quantum electrodynamics [424]. In this regime, we further discuss in Subsec. 5.3.2 the characteristic propagation velocity of the mesons and then we show, in Subsec. 5.3.3, that their fast spatial propagation is prevented by their Stark localization [411–413] in the mutual confining potentials. In Subsec. 5.3.4 we eventually exhibit how these two phenomenona stabilize nonthermal behavior and low entanglement for extremely long times in a thermodynamically relevant portion of the many-body

Hilbert space. Henceforth in this Section we will often use the terminology of lattice gauge theories based on the dictionary of the mapping of Subsec. 5.1.5: strings (for mesons), particle and antiparticle (for kinks and antikinks), bare vacuum and false vacuum (for the two oppositely magnetized ground states in the absence of quantum fluctuations, $g = 0$ in Eq. (5.1)).

5.3.1 Suppression of string breaking and the Schwinger effect

When a particle and an antiparticle in the vacuum are adiabatically separated at a distance d, the energy $E(d) \sim \tau d$ associated with the gauge-field string linking them grows proportionally to d and eventually it overcomes the threshold $E_{\text{min}} \sim 2m$ for the creation of a new pair. We argue that the *dynamical* breaking of strings after a quench of the interactions takes anomalously long times for large values of the mass. The mechanism for this suppression may be essentially understood as a tunneling process across a high energy barrier. In fact, the decay process which converts the large amount of potential energy stored in long gauge-field strings into the energy of additional particle-antiparticle pairs is energetically allowed and entropically favorable, because a string state is very atypical compared to many-particle states with the same total energy. Accordingly, ther-

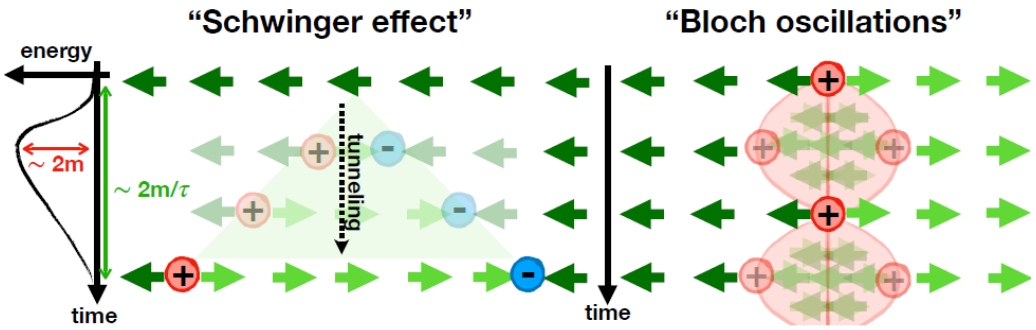

FIGURE 5.9: Schematic representation of the two key mechanisms which render the resulting dynamics slow: suppression of false vacuum decay for weak coupling ("Schwinger effect", left), and Stark-localization of particles in a linear potential ("Bloch oscillations", right. Image taken from Ref. [7].

malization requires string breaking. However, due to the energy conservation, the created particle and antiparticle of a pair must be separated at such a distance d that the energy τd they subtract from the broken string portion equals their mass, i.e., $\tau d \sim 2m$. If the string tension τ is small compared to the particle mass m, local pair creation is not possible, and virtual particles have to tunnel across a distance $d \sim 2m/\tau \gg 1$ in order for the string to decay — see the left panel of Fig. 5.9 for an illustration (here the lattice spacing is the unit length). This occurs through increasingly high-order processes in the interactions, and hence the decay is extremely slow.

The above qualitative picture is made quantitative by constructing the effective Hamiltonian in perturbation theory in $1/m$ via the Schrieffer-Wolff method, see e.g., [425]. We formally split the Hamiltonian into the mass term H_0, possessing

highly-degenerate blocks, and the rest V, which involves gauge field and interactions. H_0 defines sectors of the Hilbert space labelled by the number of particles and well-separated in energy. V may contain block-diagonal matrix elements H_1, describing particle/antiparticle energy and motion, and block-off-diagonal ones $R_1 = V - H_1$, corresponding to particle-antiparticle pair creation or annihilation. The term R_1 is eliminated through a unitary transformation e^{S_1}, with $S_1^\dagger = -S_1$ anti-Hermitean, such that

$$[S_1, H_0] + R_1 = 0. \tag{5.43}$$

This standard procedure can be carried out to any arbitrary order n in perturbation theory: The unitary transformation $e^{S_{\leq n}}$, with

$$S_{\leq n} = -S_{\leq n}^\dagger = S_1 + S_2 + \cdots + S_n, \tag{5.44}$$

is chosen in such a way that the transformed Hamiltonian commutes with H_0 up to the $n+1$-th power of the perturbation strength, i.e.,

$$H' = \mathrm{e}^{S_{\leq n}} H e^{-S_{\leq n}} = H_{\text{eff}}^{(n)} + V_{>n}, \quad [S_n, H_0] + R_n = 0, \tag{5.45}$$

with $H_{\text{eff}}^{(n)} \equiv H_0 + H_1 + \cdots + H_n$, $V_n = H_n + R_n$ and $[H_j, H_0] = 0$. The effective Hamiltonian $H_{\text{eff}}^{(n)}$ preserves the block-diagonal structure of H_0 and accounts for all transitions within each sector of H_0 occurring through up to n intermediate transitions involving states in different blocks (*virtual* particle pairs). In the case of the Ising model in Eq. (5.1) the effective Haimltonian to second order $H_{\text{eff}}^{(2)} = H_0 + H_1 + H_2$ in the expansion in Eq. (5.45) reads as

$$H_0 = -J \sum_j \sigma_j^z \sigma_{j+1}^z, \tag{5.46}$$

$$H_1 = -h \sum_j \sigma_j^z - g \sum_j \left(P_{j-1}^\uparrow \sigma_j^x P_{j+1}^\downarrow + P_{j-1}^\downarrow \sigma_j^x P_{j+1}^\uparrow \right), \tag{5.47}$$

$$\begin{aligned} H_2 = +\frac{g^2}{4J} \sum_j \Big[& + P_{j-1}^\uparrow (\sigma_j^- \sigma_{j+1}^+ + \sigma_j^+ \sigma_{j+1}^-) P_{j+2}^\uparrow + P_{j-1}^\downarrow (\sigma_j^- \sigma_{j+1}^+ + \sigma_j^+ \sigma_{j+1}^-) P_{j+2}^\downarrow \\ & - P_{j-1}^\uparrow (\sigma_j^+ \sigma_{j+1}^+ + \sigma_j^- \sigma_{j+1}^-) P_{j+2}^\downarrow - P_{j-1}^\downarrow (\sigma_j^+ \sigma_{j+1}^+ + \sigma_j^- \sigma_{j+1}^-) P_{j+2}^\uparrow - \sigma_j^z \sigma_{j+1}^z \Big], \end{aligned} \tag{5.48}$$

where $P_j^\uparrow$ ($P_j^\downarrow$) projects onto the "up" ("down") state of the j-th spin along z. Note that $H_{\text{eff}}^{(1)} = H_0 + H_1$ in Eqs. (5.46) and (5.47), once it is projected onto the subspace with one kink only, is analogous to the effective Hamiltonian we introduced in Eq. (5.39). Additional technical details, which we do not report here for brevity, about the Schrieffer-Wolff construction can be found in the Appendix of Ref. [7]. In Appendix 5.C the Schrieffer-Wolff construction for the lattice Schwinger model in Eq. (5.16) is further reported for completeness, together with the results of numerical simulations of the same model showing the suppression of string breaking. In Fig. 5.10 the allowed transitions up to second order, Eqs. (5.46), (5.47) and (5.48), are sketched. We remark that the construction presented here is similar

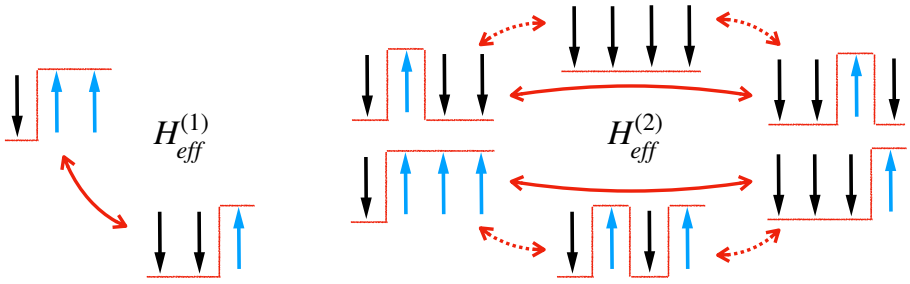

FIGURE 5.10: Cartoon of the perturbative transitions described by the effective Hamiltonian $H^{(2)}_{\rm eff}$ of the quantum Ising chain up to the second order in $1/J$. At the first order, hopping of a kink/antikink by one lattice site is the only allowed transition. At the second order, one can either have hopping by one lattice site of a string/antistring of length one (top row) or hopping of two lattice sites of a kink/antikink (bottom row). Solid arrows show the block-diagonal transitions described by the effective Hamiltonian. The intermediate states mediating the processes, indicated by dashed arrows, involve "virtual" states belonging to a different block. The amplitudes of the second-order processes are proportional to g^2/J, see Eq. (5.48). Image taken from Ref. [7].

to that of Ref. [226] for the quantum Ising chain. However, while that study is concerned with homogeneous quenches where the initial state has a low density of quasi-particle excitations above the ground state, we are here interested (see Subsecs. 5.3.3 and 5.3.4) in the effective dynamics arising from inhomogeneous states composed by dilute domain-walls, corresponding to high-energy states of the model.

The perturbative series generated by this transformation are generally divergent at finite energy density, pointing to an asymptotic hybridization of the various blocks and hence thermalization. However, by adapting the rigorous theory in Ref. [195], one finds that by truncating the series at an "optimal order" n^* that scales linearly with the particle mass m, the rest $V_{>n^*}$ can be made *exponentially* small in m. Consequently, the effect of the latter can be neglected for exponentially long times. Denoting $H^{(n^*)}_{\rm eff} \equiv H_{\rm eff}$ and $S_{\leq n^*} \equiv S$, the nonequilibrium evolution of the system is accurately described by

$$|\Psi(t)\rangle \simeq e^{-S}\, e^{-itH_{\rm eff}}\, e^{S} |\Psi(t=0)\rangle. \tag{5.49}$$

Within this transformed picture, the number of particles is exactly conserved by $H_{\rm eff}$, and hence it is approximately conserved by H in the original picture at least for exponentially long times. For the Ising model in Eq. (5.1), in the perturbative limit $J \gg g, h$ (corresponding to the large mass m limit according to the mapping of Subsec. 5.1.5), the estimates adapted from Refs. [195] lead to the quasiconservation of the spatial density of domain-walls at times $t \ll T_{\rm sb}$, where

$$T_{\rm sb} \;\geq\; g^{-1} \exp\left(\text{const} \times J/\sqrt{h^2+g^2} \right), \tag{5.50}$$

and the constant is independent of the parameters. See again the Appendix of Ref. [7] for additional details. $T_{\rm sb}$ provides a lower bound, in the perturbative regime $J \gg g, h$, on the time scale required for the thermalization of the system.

In fact, the analysis above shows that the bulk of a long gauge string, whose decay is entropically favoured and necessary for thermalization as discussed above, is stable against pair creation, since the "string-breaking" (or "vacuum-decay") time scale is exponentially long in m. From the exact mapping of Subsec. 5.1.5 this implies that heavy mesons above the inelastic threshold $M_n > 4m$ (see the discussion in Subsec. 5.1.1) are stable for exponentially long times in J. This phenomenon is reminiscent of the Schwinger effect in quantum electrodynamics [424], which describes the decay rate $\Gamma(\mathcal{E})$ per unit volume of a false vacuum into particle pairs in the presence of a background electric field $\mathcal{E}$, see Fig. 5.9. $\Gamma(\mathcal{E})$ is exponentially small in the ratio between the electron mass m and the electrostatic energy $|e\mathcal{E}| \times 1/m$ contained within a Compton length, i.e.,

$$\Gamma(\mathcal{E}) \propto (e\mathcal{E})^2 \exp\left(-\frac{\pi m^2}{|e\mathcal{E}|}\right), \tag{5.51}$$

as first shown in Ref. [424]. e denotes the electron charge and $\hbar = c = 1$ in Eq. (5.51). The non-analytical dependence on the electric field E remarks the non-perturbative origin of the Schwinger effect, as the virtual particles tunnel out of the Dirac sea. The analogy for the decay of the false vacuum (all spin reversed with respect to the direction of the longitudinal field h) is stronger and persists in the thermodynamic limit. As a matter of fact, see also the discussion in Subsec. 5.1.1, it has been show in Ref. [210], in the weak confinement limit $h \ll g$, that the false vacuum of the longitudinal field Ising model decay exponentially slow in $1/h$. For long strings, or equivalently heavy mesons, the behavior in the continuum field theory description is, on the contrary, different. This is caused by the fact that in the lattice model the particle and the antiparticle at the boundaries of a gauge field string perform oscillations with a finite amplitude $\sim \xi_{\text{loc}}$, as discussed in Subsec. 5.2.2. In the continuum limit, on the contrary, the kinetic energy is unbounded and therefore the particle and the antiparticle at the extremes of a string can get arbitrarily close and collide, since the reduction of their potential energy can be compensated by an arbitrarily large increase of the kinetic term. If the energy of the pair is sufficiently high, extra particle and antiparticle pairs can then be produced in the scattering event. The rate of occurrence of this phenomenon has been indeed found in Ref. [216], for $h \ll g$, to be proportional to h^3, which is much higher than the exponential suppression in Eq. (5.50).

5.3.2 Velocity propagation of mesons

We have seen in the previous Subsection that in the infinite mass limit, $J \gg g, h$, the dynamics is ruled by H_{eff} for exponentially long times. To disentangle the effect of having a finite particle mass — leading to exponentially slow pair creation — from the intrinsic slow dynamics of H_{eff}, we analyze henceforth the nonequilibrium dynamics generated by the latter truncated at the lowest order, i.e., $H_{\text{eff}} = H_0 + H_1$ with H_0 and H_1 given in Eqs. (5.46) and (5.47), respectively. The effective picture consists of a system of hopping hardcore particles in a constant electric field, subject to interactions. Higher-order terms in H_{eff} do not alter

the physics qualitatively, as they just renormalize the hopping amplitudes with longer-range hopping terms and they introduce the hopping of light mesons.

In this Section we study the problem of a single meson consisting of a kink at position n_1 and an antikink at position $n_2 > n_1$. This two-body problem can be mapped to the problem of a single particle hopping on a two-dimensional lattice with coordinates n_1 and n_2 horizontally and vertically, confined to the half-plane $n_2 > n_1$ by a hard-wall boundary condition along the diagonal and subject to a constant field orthogonal to the boundary. The lowest-order effective Hamiltonian $H_{\rm eff}$ is, in this case, the sum of $H_{\rm g}$ in Eq. (5.29) and the projection of $H_{\rm int}$ in Eq. (5.30) onto the two particle subspace; the mass term in Eq. (5.28) is constant within sectors and will be omitted. When restricted to the two-particle sector, $H_{\rm g}$ accounts for the linear confining potential between the two particles and $H_{\rm int}$ for the particle hopping. Their respective matrix elements read

$$\langle n_1, n_2|H_{\rm g}|m_1, m_2\rangle = 2h(n_2 - n_1)\,\delta_{n_1,m_1}\delta_{n_2,m_2} \tag{5.52}$$

and

$$\begin{aligned}\langle n_1, n_2|H_{\rm int}|m_1, m_2\rangle = g(&\delta_{n_1+1,m_1}\delta_{n_2,m_2} + \delta_{n_1-1,m_1}\delta_{n_2,m_2} + \delta_{n_1,m_1}\delta_{n_2+1,m_2} \\ &+ \delta_{n_1,m_1}\delta_{n_2-1,m_2}).\end{aligned} \tag{5.53}$$

We emphasize here that the analysis reported below is actually is *nonperturbative* in the ratio g/h. Since the interaction part depends only on the positive distance $n_2 - n_1$, it is convenient to consider the coordinates $n_\pm = n_2 \pm n_1$. Accordingly, by plugging the ansatz $\psi^{(K)}_{n_+,n_-} = e^{iKn_+}\psi^{(K)}_{n_-}$ into the Schrödinger equation $H\psi = E\psi$, one realizes that the plane wave e^{iKn_+} factors out, and the problem reduces to

$$2hn_-\psi^{(K)}_{n_-} + 2g\cos K\left[\psi^{(K)}_{n_--1} + \psi^{(K)}_{n_-+1}\right] = E\psi^{(K)}_{n_-} \tag{5.54}$$

subject to a hard wall at the origin $n_- = 0$, i.e., to the boundary condition $\psi^{(K)}_{n_-=0} \equiv 0$. Eq. (5.54), a part from the boundary condition $n_=0$, is equal (up to an additive constant) to the effective Hamiltonian in Eq. (5.39) upon replacing the hopping term $g \to 2g\cos K$. In the absence of the hard wall condition, therefore, the exact eigenfunctions are of the form $\Psi^{(j,K)}_{n_-} = J_{n_- - j}(2\xi_{\rm loc}\cos K)$, with energy $E_j = 2hj$, independent of K (see Appendix 5.B for details). These wavefunctions, according to the asymptotics of the Bessel function $J_{n_- - j}$ for large index $j - n_-$ [330], decay faster than exponentially as the relative distance n_- moves away from $j > 0$ by more than $2\xi_{\rm loc}$ lattice spacings. Hence, for $j \gg 2\xi_{\rm loc}$, the effect of the boundary condition is negiglible. The dispersion relations E_j vs K of bound states labelled by j become completely flat in this limit. If the initial particles' wavefunction is concentrated on widely separated regions, their center of mass does not move and the two particles perform uncorrelated Bloch oscillations around their initial positions, as shown in the right panel of Fig. 5.9. The hard wall in $n_- = 0$ is responsible for the failure of this occurrence, and its effect becomes manifest as j approaches twice the extent $\xi_{\rm loc}$ of the Bloch oscillations, such that the two particles' wavefunction tails overlap significantly. In order to quantify the bending of the bands $E_j(K)$ we exploit the fact that the spectrum of the two body problem in

Eq. (5.54) can be obtained exactly from the implicit equation

$$J_{-E_j/2h}\left(2\xi_{\rm loc}\cos K\right)=0, \tag{5.55}$$

as first shown in Ref. [405]. From the series expansion of the Bessel function [330]

$$J_\nu(z)=\left(\frac{z}{2}\right)^\nu\sum_{p=0}^{\infty}\frac{(-1)^p}{\Gamma(p+1)\Gamma(p+1+\nu)}\left(\frac{z}{2}\right)^{2p} \tag{5.56}$$

one readily realizes that the leading correction $\delta E_j(K)$ in $z=2\xi_{\rm loc}\cos K$ to the flat band energy level $E_j^0(K)=2hj$ is given by

$$\begin{aligned}E_j(K)&=E_j^0(K)+\delta E_j(k),\\ \delta E_j(K)&=-\frac{2\left(g\cos K\right)^{2j}}{j!(j-1)!\,h^{2j-1}}.\end{aligned} \tag{5.57}$$

We observe Eq. (5.57) agrees with the perturbation-theory argument for which nonvanishing corrections to the eigenenergy of the j-th bound state occur only at the $2j$-th order in g/h (see Fig. 5.10); we emphasize, however, that the equations above are valid for arbitrarily large localization lengths $\xi_{\rm loc}=g/h$, provided the string length is even larger. From the above result, the maximal group velocity

$$v_j^{\max}=\max_{K\in[0,\pi)}\left|\partial_K\,\delta E_j(K)\right)\big| \tag{5.58}$$

of the j-th two-kinks bound state can be computed. In particular, for $j\gg 2\xi_{\rm loc}$, one finds

$$v_j^{\max}\simeq h\frac{(2j)^{3/2}}{(j!)^2}\left(\frac{g}{2h}\right)^{2j}\mathrm{e}^{-1/2}. \tag{5.59}$$

Note that these speeds dramatically drop to zero for $j\gg g/h$. When g is set to zero, the quantum number j in Eq. (5.57) coincides with the length of the meson and the correction $\delta E_j(K)$ vanishes. For a weak transverse field g, as a consequence, short mesons will propagate much faster than long ones.

5.3.3 Stark localization localization of dilute mesons

According to the discussion of Sec. 5.3.1, the dynamics of the system is determined by $H_{\rm eff}$ for exponentially long times in J. The latter Hamiltonian is nonintegrable and therefore, according to the discussion in Sec. 1.5 of Chapter 1, the nonequilibrium dynamics starting from a generic initial state may be expected to undergo *prethermalization* to the Gibbs ensemble $e^{-\beta H_{\rm eff}}/Z$, at the inverse temperature β uniquely determined by the energy density of the initial state [54]. Contrarily to this expectation, we demonstrate that the combination of confinement and lattice effects leads to a dramatic slowdown of prethermalization in a thermodynamically significant portion of the many-body Hilbert space. This phenomenon is due to the Stark localization of particles [411–413], discussed in

Subsecs. 5.2.2 and 5.3.2, which suppresses spatial propagation and energy transport for *arbitrary* interaction strength. We consider below many-particles states, with a diluteness parameter p, i.e., with an average separation of $1/p$ lattice sites between consecutive particles. In the extremely dilute limit $p \ll 1$ the system consists of isolated particles moving in a linear potential, which are therefore described by the Wannier-Stark ladder. According to results of Subsec. 5.3.2, if the distance between consecutive particles is much larger than $\xi_{\rm loc}$, transport, the dispersion relation $E_j(k)$ is flat and the velocity of the mesons is zero. Transport and thermalization are suppressed, and particles perform coherent (Bloch) oscillations around their initial position, with spatial amplitude $\xi_{\rm loc}$ and temporal period π/h, as shown in Subsec. 5.2.2 and pictorially in the right panel of Fig. 5.9. However, delocalization gradually occurs as $\ell = 1/p$ is made comparable with twice the localization length $2\xi_{\rm loc}$. In this case from Eqs. (5.57) - (5.59) the string edges propagate ballistically, and hence spatial delocalization and entanglement growth take place. From Eq. (5.59), we are led to define a sequence of time scales depending on the quantum number j, $T_{\rm dloc}(j,\xi_{\rm loc})$, rapidly growing as the ratio $j/\xi_{\rm loc}$ increases. Taking the inverse of $v_j^{\rm max}$ in Eq. (5.59), with $j = 1/p$ being the average distance between consecutive kinks along the chain, one has

$$T_{\rm dloc}(j,\xi_{\rm loc}) \;\sim\; g^{-1}\,(j!)^2 j^{-3/2}\,\xi_{\rm loc}^{-2j+1}. \tag{5.60}$$

As a result, the typical delocalization time scale $T_{\rm dloc}(j,\xi_{\rm loc})$ is state-dependent via the diluteness parameter p, unlike the string-breaking time scale $T_{\rm sb}$ in Eq. (5.50). In particular, for sufficiently large j, $T_{\rm dloc}(j,\xi_{\rm loc})$ becomes larger than the string-breaking time $T_{\rm sb}$, with the latter therefore providing the dominant time scale. We stress that the above equations, based on the analysis of Subsec. 5.3.2, are nonperturbative in $\xi_{\rm loc} = g/h$ and hence valid for arbitrarily large values of this ratio.

5.3.4 Slow entanglement growth

The scenario outlined in Subsecs. 5.3.1, 5.3.2 and 5.3.3 sheds light on the effects of confinement on the nonequilibrium evolution of entanglement. In Subsec. 5.2.1, we have seen that in homogeneous quenches the growth of the bipartite entanglement entropy $S(t)$, defined in Eq. (1.40), is drastically suppressed by the confinement of the quasi-particles, in contrast to the cases where the latter freely propagate (see Fig. 5.6). According to the picture discussed in Subsecs. 5.3.1, 5.3.2 and 5.3.3 we expect a similar suppression of the growth of $S(t)$, despite the finite energy density, also for quenches from inhomogeneous initial states. Moreover, based on the quasilocalization of the mesons, one expects a growth akin to the one of disordered and glassy quantum systems, see e.g., Refs. [97, 99, 420, 421]. This expectation is confirmed by numerical simulations using the time-evolving-block-decimation algorithm on matrix-product states, with maximum bond dimension $D = 300$. In particular, we initialize a quantum Ising chain of $L = 100$ spins in nonentangled product states with a spatial density p of domain-walls: in Fig. 5.11 these states are drawn from a thermal ensemble $\rho_0 = e^{-\mu H_0}/Z$ of

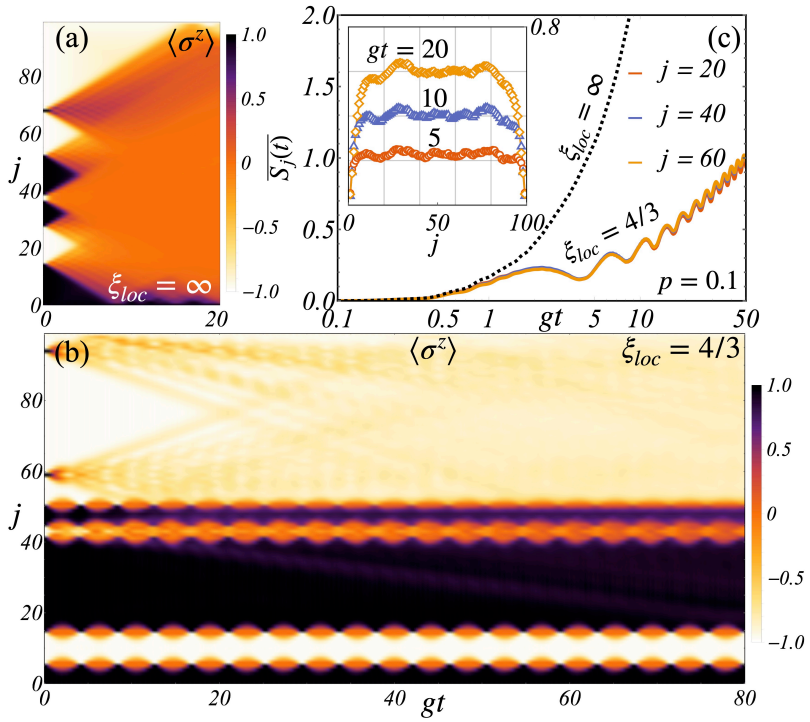

FIGURE 5.11: Effects of confinement on the nonequilibrium evolution of the magnetization profile [panels (a) and (b)] and of entanglement (c) in a quantum Ising chain. $L = 100$ spins are initialized in a random product state with a density $p = 0.1$ of longitudinal domain-walls. The dynamics are generated by H in Eq. (5.1) with $J = 5g$, and (a) $h = 0$: in the absence of confinement, domain-walls freely propagate, smoothening out all spatial inhomogeneities; (b) $h = 0.75g$: while confined bound states of closeby domain-walls ballistically propagate (upper half of the plot), isolated domain-walls are Stark-localized by linear confining potentials, and perform coherent Bloch oscillations of spatial amplitude $\xi_{\rm loc} = g/h$ (lower half of the plot). Panel (c): dynamics of the von Neumann entanglement entropy $S_j(t)$ for different position j of the bipartition cut, averaged over 500 initial states. $S_j(t)$ grows linearly in the deconfined limit (a), $\xi_{\rm loc} = \infty$ and logarithmically in the presence of confinement (b), $\xi_{\rm loc} = 4/3$, as also emphasized by the inset. These qualitative features are unaltered upon varying the localization length $\xi_{\rm loc}$ while keeping $p \lesssim 1/(2\xi_{\rm loc})$ and $J \gg g, h$. Image taken from Ref. [7].

the "unperturbed" classical Ising chain with $p = [1 - \tanh(\mu J)]/2$. The numerical results reported in Fig. 5.11 are compatible with a logarithmic growth of the bipartite entanglement entropy $S_j(t)$ superimposed to coherent oscillations of period π/h, ascribed to Bloch oscillations. In Fig. 5.11(b) we further see that short bound states (closeby domain-walls) ballistically propagate, while the long ones (pair of domain walls far apart from each other) are Stark localized, according to the discussion of Subsecs. 5.3.2 and 5.3.3. In the regime of low density p here explored, regions with closeby domain-walls are rare. Moreover, one can see that the propagation of short bound states does not induce any delocalization of the longer domains. In particular, the light cone emanating from the rare regions with closeby domain walls seems to be totally reflected upon scattering with the longer bound states present in the initial state. At present, unfortunately, we have no quantitative understanding of this effect, which should be related to a suppressed

transmission coefficient in the scattering between short and long bound states. In Fig. 5.12, instead, regularly arranged initial states are considered with equispaced domain-walls at a distance $\ell = 1/p$ and $L = 120$. The fast convergence of $S(t)$ to that generated by the effective Hamiltonian H_{eff} upon increasing J (Fig. 5.12, left panel) leads us to rule out the hypothesis that the slow vacuum decay is responsible for the entanglement growth. Furthermore, the bottom right panel of Fig. 5.12 shows that the initial growth of $S(t)$ is captured by the delocalization of individual strings described in Eq. (5.60). However, at longer times, many-particle effects lead to a slow unbounded growth. The contribution to the entanglement growth

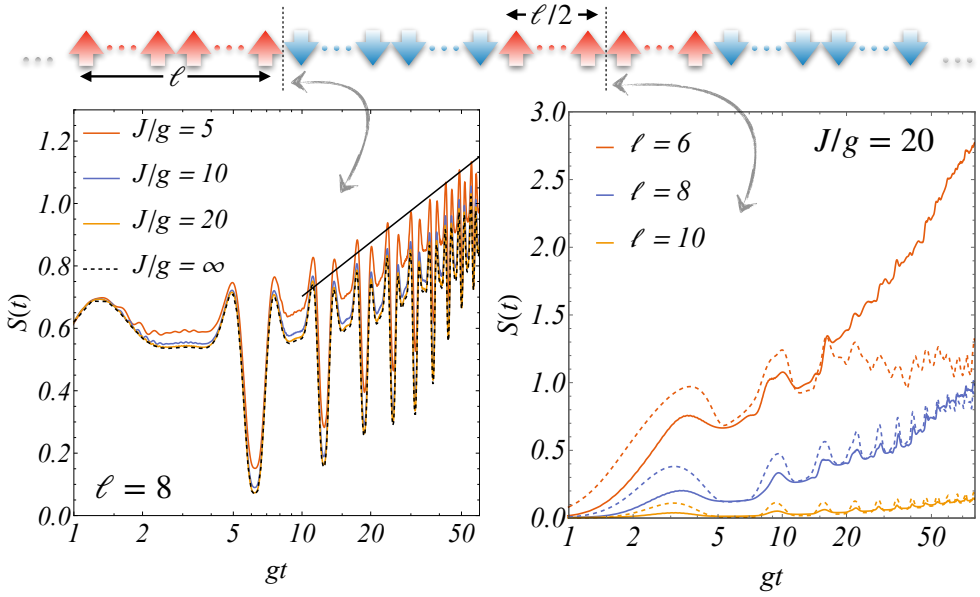

FIGURE 5.12: Growth of the von Neumann entanglement entropy $S(t)$ starting from a state with equally spaced domain-walls at a distance ℓ; the cartoon above the plots indicates the position of the bipartition cuts along the chain. Left: $S(t)$ exhibits pronounced coherent oscillations with frequency $2h$ superimposed to a slow growth (the straight line is a guide for the eye). Right: The growth of $S(t)$ slows down upon increasing the diluteness. Dotted lines represent the growth of $S(t)$ in the evolution of a single isolated string formed by the two domain-walls adjacent to the cut. The latter can be obtained analytically, is upper-bounded by $\log \ell + \text{const}$, and reaches its maximum around the time T_{dloc}, cf. Eq. (5.60). Parameters: $\xi_{\text{loc}} = 2$, $L = 120$. Image taken from Ref. [7].

determined by the propagation of individual strings can be obtained from the exact eigenvalues and eigenfunctions of the two-kink problem of Subsec. 5.3.2. For an initial condition given by kinks located at sites $i, j = n_{1,2}$ and bipartition cut at site r, the growth of $S(t)$ turns out to approximately consist of a discrete sequence of "jumps", associated with the delocalization of the various components of the initial state on the eigenstates with quantum number $j = 1, 2, \ldots$, their weight being maximal around $j \approx |n_2 - n_1|$. Eventually, $S(t)$ converges to $\log 2$ as $t \to \infty$, since the propagating string will asymptotically be either entirely on the left or entirely on the right of the cut, with equal amplitude. Before this eventual saturation, $S(t)$ can attain values larger than $\log 2$, caused by transient correlations between the two particles located on opposite sides of the cut. Using the fact that particles are confined, it is straightforward to formulate an upper bound for $S(t)$.

In fact, for wavefunctions supported in the region $|i-j| \leq d$, i.e., with the two particles separated by no more than d lattice sites, the maximal von Neumann entanglement entropy is $\log(d+1)$. For the considered initial condition, this bound holds with $d \approx |n_2 - n_1| + 2\xi_{\rm loc}$.

5.4 Concluding remarks

In this Chapter we have investigated quantum statistical systems exhibiting the confinement of the quasi-particle excitations, focusing on two main classes of models: one-dimensional spin chains, in Subsec. 5.1.1, and one-dimensional Abelian lattice gauge theories, in Subsecs. 5.1.2, 5.1.3 and 5.1.4. In both cases, we have briefly recalled how the effective confining interactions among the quasi-particles are internally generated within the systems. Upon applying an external field, the energy cost required to separate a kink and an antikink (particle and antiparticle in the lattice gauge theory) increases linearly upon increasing their distance, resulting into an effective long-range interaction which confines the pair. In Subsec. 5.1.5 we have indeed shown that the Ising spin chain in Eq. (5.1) can be exactly mapped onto a $U(1)$ lattice gauge theory, in Eq. (5.27). Kink and antikinks translate, in the gauge-theory language, into particle and antiparticles, while their bound states, the "mesons", into strings of the Abelian gauge field. In Sec. 5.2 we have considered the real-time dynamics in the presence of a confining post-quench Hamiltonian. For an homogeneous quench, discussed in Subsec. 5.2.1, we have recalled some fundamental results, from Refs. [223, 226, 239], showing that the confinement of excitations severely hinders the spreading of correlations and the entanglement growth. In these cases, despite the post-quench Hamiltonian is non-integrable and the initial state has a finite energy density, local observables experience extraordinarily long-lived oscillations and the system does not thermalize within the numerically accessible time-scales.

In Subsec. 5.2.2 we have presented our results from Ref. [6]. Namely, we have shown that confinement has significant consequences even in inhomogeneous quenches, as it can lead to suppression of energy transport in the Ising spin chain in Eq. (5.1) initialized in a domain-wall state along the longitudinal field direction. This lack of transport in the presence of an initial gradient actually mirrors the fact that the spatial inhomogeneity in the longitudinal magnetization persists at long times, in stark contrast with the dynamics we observed in Chapters 3 and 4, where an initial step inhomogeneity, in the partitioning protocol, gets fastly smoothed out by the dynamics, eventually resulting into an hydrodynamic regime. This, in turn, implies that the system fails to locally relax to the thermal ensemble up to the largest accessible and explored times, $t_M = 10^3 J^{-1}$, which are longer than those currently accessible in experiments. Within this perspective, the approach to thermal equilibrium and the emergence of an hydrodynamic description, in the spirit of Chapter 4, are intertwined. Any Euler scale description of the system would require a smearing of the initial magnetization inhomogenity, the latter being, indeed, a necessary condition for the ultimate thermalization of the system. At low density, in particular, the two-body scattering among the mesons should be enough to describe the system. Since energy and momentum are conserved in a two-body scattering in one-dimension, an effective thermodynamic

Bethe ansatz description should be possible and therefore the generalized hydrodynamics description applicable. However, putting this statement into practice is tremendously hard. At present, to our knowledge, no attempt to give an hydrodynamic description to transport in systems with confinement has been pursued. This problem remains an unexplored and challenging direction for future research.

In Sec. 5.3 the results from Ref. [7] have been presented. We considered inhomogeneous initial states with a dilute density of kinks. In this regime, we have established, in Subsecs. 5.3.1, 5.3.2, and 5.3.3, the role of confinement as a robust mechanism capable of dramatically slowing down the approach to equilibrium, see e.g., Refs. [223, 226–228, 247–249]. We emphasize that the specific choice of the class of inhomogeneous initial states plays an important role. As we have shown, in the low density regime, the non-equilibrium dynamics is accurately captured by the Bloch oscillations of the kinks at the boundaries of a meson domain (or string, according to the mapping of Subsec. 5.1.5). The effective dynamics of the systems considered experiences the Wannier-Stark localization, the latter being characteristic of interacting particles in a constant field [411, 413]. In this sense, the entanglement growth, in Subsec. 5.3.4, presents similarities with corresponding behavior characteristic of localized systems [97, 99, 420, 421], see Figs. 5.11 and 5.12. It is important to remark that this localization picture requires a low-density of kinks, but not a low-energy density of the initial state. Our numerical results, see Fig. 5.11, further suggest that rare high-density regions embedded in dilute systems do *not* thermalize the rest of the system within the explored time scales; however, a complete analysis of this problem calls for further investigations which we leave to future studies.

Appendix of Chapter 5

5.A The quantum Ising chain as a $U(1)$ LGT

In the main text, we have argued that the quantum Ising chain can be mapped to a $U(1)$-LGT, with two species of fermions ("positrons" and "electrons"). In this Section, we detail the explicit mapping of the operators which allow one to transform the $U(1)$ lattice gauge theory in Eq. (5.27) of the main text into the quantum Ising chain in Eq. (5.1).

The first step consists in mapping the fermions $c^p_{j+1/2}$ and $c^e_{j+1/2}$ to hardcore bosons, by defining the Pauli spin-1/2 operators $\tau^\alpha_{j+1/2,\,p}$ and $\tau^\alpha_{j+1/2,\,e}$ as

$$\begin{aligned}
\tau^-_{j+1/2,\,p} &= \prod_{k<j}\left[(-1)^{n^e_{k+1/2}}(-1)^{n^p_{k+1/2}}\sigma^z_k\sigma^z_{k+1}\right] c^p_{j+1/2}\,,\\
\tau^-_{j+1/2,\,e} &= \prod_{k<j}\left[(-1)^{n^e_{k+1/2}}(-1)^{n^p_{k+1/2}}\sigma^z_k\sigma^z_{k+1}\right] (-1)^{n^e_{j+1/2}}(-1)^{n^p_{j+1/2}}\sigma^z_j\sigma^z_{j+1}c^e_{j+1/2}\,,
\end{aligned} \tag{5.61}$$

with

$$\tau^z_{j+1/2,\,p} = 2n^p_{j+1/2} - 1, \quad \tau^z_{j+1/2,\,e} = 2n^e_{j+1/2} - 1\,, \tag{5.62}$$

and $\tau^+_{j+1/2,\,p} = (\tau^-_{j+1/2,\,p})^\dagger$, $\tau^+_{j+1/2,\,e} = (\tau^-_{j+1/2,\,e})^\dagger$. By exponentiating the Gauss law introduced in the main text, we find that in the gauge-invariant subspace one has

$$(-1)^{G_j} = (-1)^{n^e_{j+1/2}}(-1)^{n^p_{j+1/2}}\sigma^z_j\sigma^z_{j+1} \equiv 1 \tag{5.63}$$

for every j. Plugging this relation into Eqs. (5.61) we get that the equivalences $\tau^-_{j+1/2,\,p} = c^p_{j+1/2}$ and $\tau^-_{j+1/2,\,e} = c^e_{j+1/2}$ hold in this subspace. Note that in this step, we have been able to cancel the string coming from the Jordan-Wigner transformation by exploiting only the fact that $\mathbb{Z}_2$ is a normal subgroup of $U(1)$ [410]: this method is quite general and can be applied in any number of spatial dimensions. After this procedure, the Gauss law takes the form $G_j = (\sigma^z_{j+1} - \sigma^z_j - \tau^z_{j+1/2,\,p} + \tau^z_{j+1/2,\,e})/2 = 0$. In addition, the constraint given by the infinite Hubbard interaction (Eq. (5.27) of the main text) excludes the state $|\uparrow\uparrow_{j+1/2}\rangle$ (where the first and second spins refer to the eigenvectors of $\tau^z_{j+1/2,\,p}$ and $\tau^z_{j+1/2,\,e}$, respectively).

We will use both the Gauss law and the aforementioned constraint to perform the next step of the mapping, which is the elimination of the matter degrees of freedom (the general procedure can be found in Ref. [410]). It is useful to work in the basis of the eigenstates of σ^z and τ^z operators, where both constraints are diagonal. The basic observation is that, for a given spin configuration of the gauge

fields, the state of the matter particles is uniquely fixed by Gauss law, with the following rules:

$$\begin{cases} \sigma^z_{j+1} = +1, \sigma^z_j = -1 & \rightarrow \quad \tau^z_{j+1/2,\,p} = +1, \tau^z_{j+1/2,\,e} = -1\,, \\ \sigma^z_{j+1} = \sigma^z_j & \rightarrow \quad \tau^z_{j+1/2,\,p} = -1, \tau^z_{j+1/2,\,e} = -1\,, \\ \sigma^z_{j+1} = -1, \sigma^z_j = +1 & \rightarrow \quad \tau^z_{j+1/2,\,p} = -1, \tau^z_{j+1/2,\,e} = +1\,. \end{cases} \tag{5.64}$$

In the case $\sigma^z_{j+1} = \sigma^z_j$, the option $\tau^z_{j+1/2,\,p} = +1, \tau^z_{j+1/2,\,e} = +1$, allowed by the Gauss law, is excluded by the constraint given by the Hubbard interaction, thus ensuring that the mapping is one-to-one. The fact that the configuration of matter particles is completely determined by that of the gauge field in the gauge-invariant sector can be reformulated as follows: We can find a unitary transformation $U = e^{iA}$ which maps each gauge-invariant state to a product state of a gauge field state and a single reference state of the matter field (e.g., the matter vacuum state $|0\rangle_{\rm m}$, with $\tau^z_{j+1/2,\,p,e}|0\rangle_{\rm m} = -|0\rangle_{\rm m}$ for every j). This can be done for example via the Hermitian operator

$$A = \frac{\pi}{2}\sum_j \left(P^{\uparrow}_j \tau^x_{j+1/2,\,e} P^{\downarrow}_{j+1} + P^{\downarrow}_j \tau^x_{j+1/2,\,p} P^{\uparrow}_{j+1}\right), \tag{5.65}$$

where $P^{\uparrow}_j$ and $P^{\downarrow}_j$ are the projectors on the $|\uparrow\rangle_j$ and $|\downarrow\rangle_j$ states respectively. By using Eq. (5.64), one can see that, on gauge invariant states, the action of U consists in flipping all and only the τ^z-spins in the state $|\uparrow\rangle$. Moreover, for each state of our basis, the gauge field part is left invariant by U.

The unitary transformation U effectively eliminates the redundant matter degrees of freedom. In fact, we can now define the transformed Hamiltonian $H' = {}_{\rm m}\langle 0|UHU^{\dagger}|0\rangle_{\rm m}$ which acts on the non-trivial part (the gauge-field configurations) of the transformed states. We apply the transformation to each term of Eq. (2) of the main text. The mass term $H_{\rm m}$ can be transformed by noting that, on gauge-invariant states, $(n^p_{j+1/2} + n^e_{j+1/2}) = (1 - \sigma^z_j \sigma^z_{j+1})/2$. Then, by using the fact that U acts as the identity on the gauge field part for each state of our basis, we find that

$$H'_{\rm m} = \frac{m}{2}\sum_j (1 - \sigma^z_j \sigma^z_{j+1}), \qquad H'_{\rm g} = \frac{\tau}{2}\sum_j \sigma^z_j, \qquad H'_{\rm int} = w\sum_j \sigma^x_j, \tag{5.66}$$

i.e., H' is a quantum Ising chain in a transverse and longitudinal field. In addition, this establishes the correspondence between the parameters of the LGT and those of the quantum Ising chain in Eq. (5.1).

5.B Wannier-Stark localization

In this Section we report the details about the Wannier-Stark eigenfunctions [412, 413] in Eq. (5.38), which are useful for the description of both the single-kink problem in Subsec. 5.2.2 and the two kinks one in Subsec. 5.3.2. The starting point is the effective Hamiltonian $H_{\rm eff}$ in Eq. (5.39), which in the single-kink basis $\{|n\rangle\}$

can be written as

$$H_{\text{eff}} = 2h \sum_{n=-\infty}^{+\infty} n|n\rangle\langle n| - g \sum_{n=-\infty}^{\infty} \left(|n\rangle\langle n+1| + |n+1\rangle\langle n|\right), \tag{5.67}$$

where we have changed the sing of h to conform to the notation in Eq. (5.54). We have also dropped the additive constant $2J - 2Lh$, related to the ground state energy, and we extended the summation over the whole set of integer numbers since we are taking the thermodynamic limit. Upon writing the stationary Schrödinger equation $H|\Psi_j\rangle = E|\Psi_j\rangle$ with

$$|\Psi^{(j)}\rangle = \sum_{n=-\infty}^{\infty} \psi_n^{(j)}|n\rangle, \tag{5.68}$$

one obtains the following equation for $\psi_n^{(j)}$

$$\psi_{n+1}^{(j)} + \psi_{n-1}^{(j)} = \frac{2hn - E}{g}\psi_n^{(j)}. \tag{5.69}$$

Upon comparing with the following identity valid for the modified Bessel function $J_\nu(z)$ [330]

$$J_{\nu-1}(z) + J_{\nu+1}(z) = \frac{2\nu}{z}J_\nu(z), \tag{5.70}$$

one concludes that

$$\psi_n^{(j)} = J_{n-j}(\xi_{\text{loc}}), \quad \text{with} \quad E_j = 2hj \; j \in \mathbb{Z}, \tag{5.71}$$

which is the result we anticipated in Subsec. (5.3.2) upon replacing $g \to 2g\cos K$. Let us now consider the time evolution starting from a localized state on some lattice site n_0, such that

$$|\Psi\rangle = \sum_{n=-\infty}^{\infty} \psi_n(t)|n\rangle, \quad \text{with} \quad \psi_n(0) = \delta_{n,n_0}. \tag{5.72}$$

The expression of $c_n(t)$ can be determined exactly by inserting the resolution of the identity in the basis of the eigenstates $|\Psi^j\rangle$

$$\begin{aligned}\psi_n(t) = \langle n|e^{-iH_{\text{eff}}t}|n_0\rangle = \sum_{j=-\infty}^{\infty} \langle n|\Psi^{(j)}\rangle \exp(-iE_j t)\langle\Psi^{(j)}|n_0\rangle = \\ = J_{n-n_0}\left(2\xi_{\text{loc}}\sin(ht)\right)\exp(in(\pi + 2ht)/2),\end{aligned} \tag{5.73}$$

where in the last we used the identity [330]

$$\sum_{k=-\infty}^{\infty} J_k(z)J_{k+p}(z)\exp(ik\alpha) = J_p\left(2z\sin(\alpha/2)\right)\exp(ip(\pi - \alpha)/2). \tag{5.74}$$

The result in Eq. (5.38) follows upon setting the initial kink position in $n_0 = L/2$. To be precise, here, we are making an approximation. Indeed the results in

Eqs. (5.71) and (5.73) apply in the thermodynamic limit, where $L \to \infty$. In Eq. (5.67) we are, instead, considering a finite size system, with $n = 0, 1 \dots L-1$. Notice, however, that $J_{n-j}(\xi_{\rm loc})$ is mostly localized in the interval $(j-\xi_{\rm loc}, j+\xi_{\rm loc})$ and decays faster than exponentially outside it (see also the discussion in Subsec. 5.3.2). As a consequence, only the eigenstates of the Hamiltonian in Eq. (5.39) with j close to zero will feel the effect of the boundary in $n = 0$ and slightly deviate from the solution in the thermodynamic limit in Eq. (5.71). Setting $j = L/2$, with $L = 20$ and $\xi_{\rm loc}$ as in Figs. 5.7 and 5.8, we have numerically checked that the eigenstates in Eq. (5.71) are perfectly in agreement with the eigenstates of Eq. (5.39). Inserting Eq. (5.73), with $n_0 = L/2$, into Eq. (5.42) for $e_n(t)$, and into the similar expression for the energy current $j_n(t)$, the following expressions are found

$$\begin{aligned} e_n(t) &= -J + |\psi_n(t)|^2\,[2J + h(1+n-L/2)] - h\,m_n(t), \\ j_n(t) &= 2g\cos(ht) J_{n-L/2}(z) J_{n-L/2-1}(z)[2J + h(n-L/2-1)] \\ &\quad - g^2 \sin(2ht)[J^2_{n-L/2}(z) - J_{n-L/2+1}(z) J_{n-L/2-1}(z)], \end{aligned} \tag{5.75}$$

where $\psi_n(t)$ is given in Eq. (5.73), $m_n(t)$ in Eq. (5.37) and we have denoted for brevity the argument of the Bessel function J_n with $z = 2\xi_{\rm loc}\sin(ht)$. In concluding, we mention that analogous calculations can be done for the XXZ chain in a staggered field in Eq. (5.3). In this case, the very same formulas derived in this Section, and in Subsec. 5.2.2 of the main text, apply provided the following replacements are done $g \to 2J$, $h \to 2h$ and $J \to J\Delta$.

5.C The lattice Schwinger model: effective Hamiltonian and string breaking

In this Section we detail the construction of the effective Schrieffer-Wolff Hamiltonian in Eq. (5.16) following the method of Subsec. 5.3.1. We then report some results which show that the effects of particle confinement on the string dynamics of the lattice Schwinger are similar to those of the linear potential between domain-walls in the quantum Ising chain with a tilted magnetic field, in Eq. (5.1).

In order to derive the effective Hamiltonian governing the dynamics of the model in the limit of a large electron/positron mass m, we split the Hamiltonian of Eq. (5.16) as follows:

$$H = H_0 + V, \tag{5.76}$$

$$H_0 = m\sum_{j=1}^{L}(-1)^j \phi_j^\dagger \phi_j, \tag{5.77}$$

$$V = H_1 + R_1 = J\sum_{j=1}^{L} L^2_{j,j+1} - w\sum_{j=1}^{L-1}(\phi_j^\dagger U_{j,j+1}\phi_{j+1} + \phi_{j+1}^\dagger U^\dagger_{j,j+1}\phi_j), \tag{5.78}$$

where the perturbation V has been in turn decomposed into a diagonal part $V_{\rm diag} \equiv H_1$ given by the electrostatic term J conserving the particle/antiparticle number (mass) and an off-diagonal one $V_{\rm offdiag} \equiv R_1$, coupling sectors of the Hilbert space with different particle/antiparticle number (mass). By performing

the unitary transformation as explained in Subsec. 5.3.1, the effective Hamiltonian $H^{(2)}_{\text{eff}}$, which is block-diagonal up to second order in $1/m$, is found to be

$$H^{(2)}_{\text{eff}} = H_0 + H_1 + H_2, \tag{5.79}$$

$$H_2 = \frac{w^2}{2m}\sum_{j=1}^{L}(-1)^j\phi^\dagger_j\phi_j + \frac{w^2}{2m}\sum_{j=1}^{L}(-1)^j(\phi^\dagger_j U_{j,j+1}U_{j+1,j+2}\phi_{j+2} + \text{h.c.}, \tag{5.80}$$

with h.c. the Hermitean conjugate and H_0 given in Eq. (5.77). The lowest-order generators S_1 and S_2 of the unitary transformation $\exp(S)$ bringing H to the block-diagonal form $H^{(2)}_{\text{eff}}$ in Eq. (5.80) may be written as

$$S_1 = -\frac{w}{2m}\sum_{j=1}^{L}(-1)^j(\phi^\dagger_j U_{j,j+1}\phi_{j+1} - \text{h.c.} \tag{5.81}$$

$$S_2 = \frac{wJ}{4m^2}\sum_{j=1}^{L}\phi^\dagger_j(E_{j,j+1}U_{j,j+1} + U_{j,j+1}E_{j,j+1})\phi_{j+1} - \text{h.c.} \tag{5.82}$$

The allowed processes at the second order in perturbation theory are described by

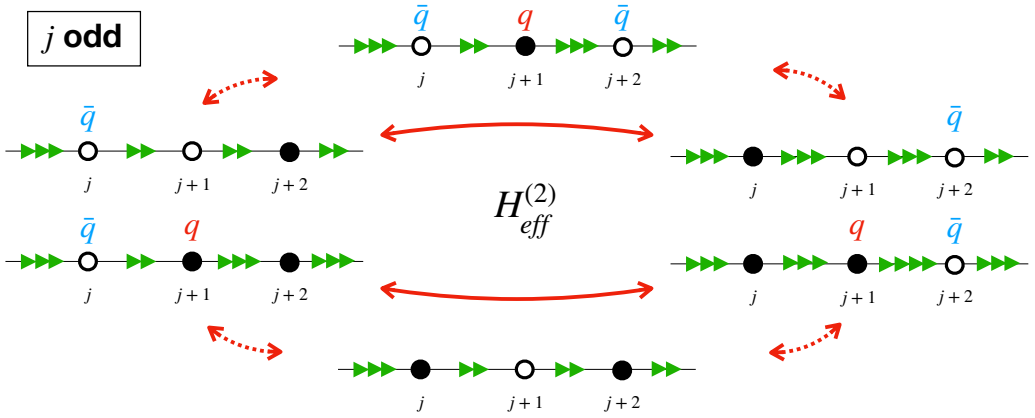

FIGURE 5.C.1: Sketch of the perturbative transitions described by the effective Hamiltonian $H^{(2)}_{\text{eff}}$ of the lattice Schwinger model in Eq. (5.79) up to the second order in $1/m$. With reference to the Hamiltonian H in Eq. (5.16), black and white dots denote empty and occupied staggered-fermion sites, respectively; q ($\bar{q}$) denote the presence of a particle (antiparticle) at the corresponding site, with positive (negative) electric charge; the green arrows represent the value of the electric flux on the chain bonds. By virtue of the Gauss law, the electric flux jumps up (down) by one unit as a particle (antiparticle) is traversed from the left along the chain. Considering for simplicity an odd lattice site j, one can either have hopping by two lattice sites of an antiquark (top row) or hopping by two lattices of an antiquark in the presence of a quark occupying the site $j+1$ (bottom row). For even j analogous processes take place, in which the role of the quark and the antiquark are exchanged. Solid arrows show the block-diagonal transitions described by the effective Hamiltonian. The intermediate states mediating the processes, indicated by dashed arrows, involve "virtual" states belonging to a different block. The amplitude of these transitions are proportional to w^2/m, see Eq. (5.79). Image taken from Ref. [7].

H_2 and consist of a particle (antiparticle) hopping by two lattice sites mediated by

a virtual state where a particle-antiparticle pair is either annihilated or created, as shown pictorially in Fig. 5.C.1. We remark that in the lattice Schwinger model, the off-diagonal part R_1 of the perturbation in Eq. (5.78) has no diagonal component and therefore the first non-trivial transitions appear in the effective Hamiltonian at the second order. This differs from the case of the Ising chain in Subsec. 5.3.1, where the perturbation has a non-trivial diagonal component H_1 already at the first order, given in Eq. (5.47). This, in turn, implies that the dynamics in the lattice Schwinger model will be comparatively slower than that of the Ising chain.

For the purpose of studying the effect of confinement of particle and antiparticle pairs, let us consider "string" initial states, i.e., gauge-invariant eigenstates of the Hamiltonian in the non-interacting limit $w = 0$, with a particle q and an antiparticle $\bar{q}$ located at a distance d along the chain, and let us measure the evolution of the electric flux spatial profile, $\langle E_{j,j+1}(t) \rangle$. Numerical simulations are performed with exact diagonalization techniques applied to the model obtained after integrating out the gauge field, i.e., a globally neutral system of fermionic charges with long-range Coulomb interactions [409]. Results are shown in Fig. 5.C.2 for $d = 5$. Away from the initial particles, vacuum fluctuations made up of virtual particle-antiparticle pairs appear, as signaled by the small coherent oscillations of the local electric field, cf. Refs. [223, 227, 247]. However, the spatial inhomogeneity of the electric field persists for long times, due to the suppression of string breaking, despite the sizeable strength $w = m$ of the interactions.

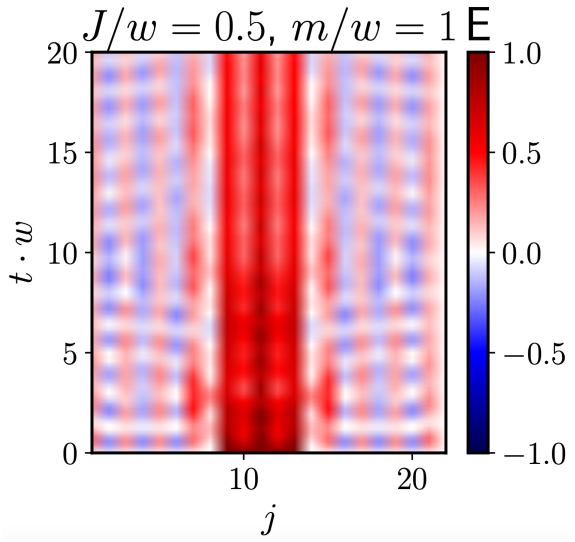

FIGURE 5.C.2: Space-time dependence of the electric field $\langle E_{j,j+1}(t) \rangle$ starting from a nonentangled initial state with one $q - \bar{q}$ pair, governed by the Hamiltonian (5.16) with the indicated values of the coupling J/w and of the mass m/w. Image taken from Refs. [7, 247].

Bibliography

[1] G. Perfetto and A. Gambassi, Ballistic front dynamics after joining two semi-infinite quantum ising chains, Phys. Rev. E **96**, 012138 (2017).

[2] G. Perfetto, L. Piroli, and A. Gambassi, Quench action and large deviations: work statistics in the one-dimensional bose gas, Phys. Rev. E **100**, 032114 (2019).

[3] F. S. Møller, G. Perfetto, B. Doyon, and J. Schmiedmayer, Euler-scale dynamical correlations in integrable systems with fluid motion, SciPost Phys. Core **3**, 16 (2020).

[4] G. Perfetto and A. Gambassi, Dynamics of large deviations in the hydrodynamic limit: noninteracting systems, Phys. Rev. E **102**, 042128 (2020).

[5] G. Perfetto and B. Doyon, Euler-scale dynamical fluctuations in non-equilibrium interacting integrable systems, arXiv:2012.06496 (2020).

[6] P. P. Mazza, G. Perfetto, A. Lerose, M. Collura, and A. Gambassi, Suppression of transport in nondisordered quantum spin chains due to confined excitations, Phys. Rev. B **99**, 180302 (2019).

[7] A. Lerose, F. M. Surace, P. P. Mazza, G. Perfetto, M. Collura, and A. Gambassi, Quasilocalized dynamics from confinement of quantum excitations, Phys. Rev. B **102**, 041118 (2020).

[8] K. Huang, Statistical mechanics, john wily & sons, New York (1963).

[9] J. B. Kogut, An introduction to lattice gauge theory and spin systems, Rev. Mod. Phys. **51**, 659–713 (1979).

[10] L. Onsager, Crystal statistics. i. a two-dimensional model with an order-disorder transition, Phys. Rev. **65**, 117–149 (1944).

[11] G. Mussardo, *Statistical field theory: an introduction to exactly solved models in statistical physics* (Oxford University Press, 2010).

[12] R. J. Baxter, *Exactly solved models in statistical mechanics* (Elsevier, 2016).

[13] S. Sachdev, Quantum phase transitions, Handbook of Magnetism and Advanced Magnetic Materials (2007).

[14] P. Francesco, P. Mathieu, and D. Sénéchal, *Conformal field theory* (Springer Science & Business Media, 2012).

[15] M. D. Donsker and S. R. S. Varadhan, Asymptotic evaluation of certain markov process expectations for large time, i, Commun. Pure Appl. Math. **28**, 1–47 (1975).

[16] M. D. Donsker and S. R. S. Varadhan, Asymptotic evaluation of certain markov process expectations for large time, ii, Commun. Pure Appl. Math. **28**, 279–301 (1975).

[17] M. D. Donsker and S. R. S. Varadhan, Asymptotic evaluation of certain markov process expectations for large time—iii, Commun. Pure Appl. Math. **29**, 389–461 (1976).

[18] M. D. Donsker and S. R. S. Varadhan, Asymptotic evaluation of certain markov process expectations for large time. iv, Commun. Pure Appl. Math. **36**, 183–212 (1983).

[19] R. S. Ellis, *Entropy, large deviations, and statistical mechanics*, Vol. 271, 821 (Springer-Verlag New York, 1985).

[20] R. S. Ellis, An overview of the theory of large deviations and applications to statistical mechanics, Scand. Actuarial J. **1995**, 97–142 (1995).

[21] R. S. Ellis, The theory of large deviations: from boltzmann's 1877 calculation to equilibrium macrostates in 2d turbulence, Physica D **133**, 106–136 (1999).

[22] H. Touchette, The large deviation approach to statistical mechanics, Phys. Rep. **478**, 1–69 (2009).

[23] S. N. Majumdar and G. Schehr, Large deviations, arXiv:1711.07571 **3** (1999).

[24] J. v. Tiel, *Convex analysis*, BOOK (John Wiley, 1984).

[25] C. E. Pfister, Large deviations and phase separation in the two-dimensional ising model, Helvetica Physica Acta **64**, 953–1054 (1991).

[26] C. E. Pfister, Thermodynamical aspects of classical lattice systems, In and Out of Equilibrium. Probability with a Physics Flavor, 393–472 (2002).

[27] T. Dauxois, S. Ruffo, E. Arimondo, and M. Wilkens, eds., *Dynamics and thermodynamics of systems with long-range interactions*, Vol. 602 (Springer, 2002).

[28] A. Campa, A. Giansanti, G. Morigi, and F. S. Labini, Dynamics and thermodynamics of systems with long range interactions: theory and experiments, AIPC **970** (2008).

[29] A. Campa, T. Dauxois, and S. Ruffo, Statistical mechanics and dynamics of solvable models with long-range interactions, Phys. Rep. **480**, 57–159 (2009).

[30] D. S. Dean and S. N. Majumdar, Large deviations of extreme eigenvalues of random matrices, Phys. Rev. Lett. **97**, 160201 (2006).

[31] P. Vivo, S. N. Majumdar, and O. Bohigas, Large deviations of the maximum eigenvalue in wishart random matrices, J. Phys. A: Math. Theor. **40**, 4317 (2007).

[32] D. S. Dean and S. N. Majumdar, Extreme value statistics of eigenvalues of gaussian random matrices, Phys. Rev. E **77**, 041108 (2008).

[33] S. N. Majumdar and M. Vergassola, Large deviations of the maximum eigenvalue for wishart and gaussian random matrices, Phys. Rev. Lett. **102**, 060601 (2009).

[34] S. N. Majumdar and G. Schehr, Top eigenvalue of a random matrix: large deviations and third order phase transition, J. Stat. Mech.: Theory Exp **2014**, P01012 (2014).

[35] M. Heyl, A. Polkovnikov, and S. Kehrein, Dynamical quantum phase transitions in the transverse-field ising model, Phys. Rev. Lett. **110**, 135704 (2013).

[36] C. Karrasch and D. Schuricht, Dynamical phase transitions after quenches in nonintegrable models, Phys. Rev. B **87**, 195104 (2013).

[37] M. Heyl, Dynamical quantum phase transitions in systems with broken-symmetry phases, Phys. Rev. Lett. **113**, 205701 (2014).

[38] P. Jurcevic, H. Shen, P. Hauke, C. Maier, T. Brydges, C. Hempel, B. P. Lanyon, M. Heyl, R. Blatt, and C. F. Roos, Direct observation of dynamical quantum phase transitions in an interacting many-body system, Phys. Rev. Lett. **119**, 080501 (2017).

[39] M. Heyl, Dynamical quantum phase transitions: a review, Rep. Prog. Phys. **81**, 054001 (2018).

[40] S. Genway, J. M. Hickey, J. P. Garrahan, and A. D. Armour, Dynamical phases in the full counting statistics of the resonant-level model, arXiv:1212.5200 (2012).

[41] J. M. Hickey, S. Genway, I. Lesanovsky, and J. P. Garrahan, Time-integrated observables as order parameters for full counting statistics transitions in closed quantum systems, Phys. Rev. B **87**, 184303 (2013).

[42] J. M. Hickey, C. Flindt, and J. P. Garrahan, Trajectory phase transitions and dynamical lee-yang zeros of the glauber-ising chain, Phys. Rev. E **88**, 012119 (2013).

[43] J. M. Hickey, S. Genway, and J. P. Garrahan, Dynamical phase transitions, time-integrated observables, and geometry of states, Phys. Rev. B **89**, 054301 (2014).

[44] J. M. Hickey, E. Levi, and J. P. Garrahan, Cumulants of time-integrated observables of closed quantum systems and $\mathcal{PT}$ symmetry with an application to the quantum ising chain, Phys. Rev. B **90**, 094301 (2014).

[45] J. P. Garrahan and I. Lesanovsky, Thermodynamics of quantum jump trajectories, Phys. Rev. Lett. **104**, 160601 (2010).

[46] C. Ates, B. Olmos, J. P. Garrahan, and I. Lesanovsky, Dynamical phases and intermittency of the dissipative quantum ising model, Phys. Rev. A **85**, 043620 (2012).

[47] J. M. Hickey, S. Genway, I. Lesanovsky, and J. P. Garrahan, Thermodynamics of quadrature trajectories in open quantum systems, Phys. Rev. A **86**, 063824 (2012).

[48] I. Lesanovsky, M. van Horssen, M. Guţă, and J. P. Garrahan, Characterization of dynamical phase transitions in quantum jump trajectories beyond the properties of the stationary state, Phys. Rev. Lett. **110**, 150401 (2013).

[49] I. Bloch, J. Dalibard, and W. Zwerger, Many-body physics with ultracold gases, Rev. Mod. Phys. **80**, 885–964 (2008).

[50] M. A. Cazalilla, R. Citro, T. Giamarchi, E. Orignac, and M. Rigol, One dimensional bosons: from condensed matter systems to ultracold gases, Rev. Mod. Phys. **83**, 1405–1466 (2011).

[51] X.-W. Guan, M. T. Batchelor, and C. Lee, Fermi gases in one dimension: from bethe ansatz to experiments, Rev. Mod. Phys. **85**, 1633–1691 (2013).

[52] A. Polkovnikov, K. Sengupta, A. Silva, and M. Vengalattore, Colloquium: nonequilibrium dynamics of closed interacting quantum systems, Rev. Mod. Phys. **83**, 863–883 (2011).

[53] T. Kinoshita, T. Wenger, and D. S. Weiss, A quantum newton's cradle, Nature **440**, 900–903 (2006).

[54] T. Langen, T. Gasenzer, and J. Schmiedmayer, Prethermalization and universal dynamics in near-integrable quantum systems, J. Stat. Mech.: Theory Exp. **2016**, 064009 (2016).

[55] P. Calabrese and J. Cardy, Time dependence of correlation functions following a quantum quench, Phys. Rev. Lett. **96**, 136801 (2006).

[56] P. Calabrese and J. Cardy, Quantum quenches in extended systems, J. Stat. Mech.: Theory Exp. **2007**, P06008 (2007).

[57] F. H. Essler and M. Fagotti, Quench dynamics and relaxation in isolated integrable quantum spin chains, J. Stat. Mech.: Theory Exp. **2016**, 064002 (2016).

[58] P. Bocchieri and A. Loinger, Quantum recurrence theorem, Phys. Rev. **107**, 337–338 (1957).

[59] L. D'Alessio, Y. Kafri, A. Polkovnikov, and M. Rigol, From quantum chaos and eigenstate thermalization to statistical mechanics and thermodynamics, Adv. Phys. **65**, 239–362 (2016).

[60] M. Srednicki, Chaos and quantum thermalization, Phys. Rev. E **50**, 888–901 (1994).

[61] M. Rigol, V. Dunjko, and M. Olshanii, Thermalization and its mechanism for generic isolated quantum systems, Nature **452**, 854–858 (2008).

[62] M. Rigol, Breakdown of thermalization in finite one-dimensional systems, Phys. Rev. Lett. **103**, 100403 (2009).

[63] M. Rigol, Quantum quenches and thermalization in one-dimensional fermionic systems, Phys. Rev. A **80**, 053607 (2009).

[64] G. Biroli, C. Kollath, and A. M. Läuchli, Effect of rare fluctuations on the thermalization of isolated quantum systems, Phys. Rev. Lett. **105**, 250401 (2010).

[65] L. F. Santos and M. Rigol, Localization and the effects of symmetries in the thermalization properties of one-dimensional quantum systems, Phys. Rev. E **82**, 031130 (2010).

[66] M. Rigol and L. F. Santos, Quantum chaos and thermalization in gapped systems, Phys. Rev. A **82**, 011604 (2010).

[67] A. Silva, Statistics of the work done on a quantum critical system by quenching a control parameter, Phys. Rev. Lett. **101**, 120603 (2008).

[68] F. N. C. Paraan and A. Silva, Quantum quenches in the dicke model: statistics of the work done and of other observables, Phys. Rev. E **80**, 061130 (2009).

[69] A. Gambassi and A. Silva, Large deviations and universality in quantum quenches, Phys. Rev. Lett. **109**, 250602 (2012).

[70] S. Sotiriadis, A. Gambassi, and A. Silva, Statistics of the work done by splitting a one-dimensional quasicondensate, Phys. Rev. E **87**, 052129 (2013).

[71] P. Talkner, E. Lutz, and P. Hänggi, Fluctuation theorems: work is not an observable, Phys. Rev. E **75**, 050102 (2007).

[72] E. H. Lieb and D. W. Robinson, The finite group velocity of quantum spin systems, Commun. Math. Phys. **28**, 251–257 (1972).

[73] B. Nachtergaele and R. Sims, Lieb-robinson bounds in quantum many-body physics, Contemp. Math **529**, edited by R. Sims and D. Ueltschi, 141 (2010).

[74] P. Calabrese and J. Cardy, Evolution of entanglement entropy in one-dimensional systems, J. Stat. Mech.: Theory Exp. **2005**, P04010 (2005).

[75] E. Lieb, T. Schultz, and D. Mattis, Two soluble models of an antiferromagnetic chain, Ann. Phys. **16**, 407–466 (1961).

[76] V. Gritsev, E. Demler, M. Lukin, and A. Polkovnikov, Spectroscopy of collective excitations in interacting low-dimensional many-body systems using quench dynamics, Phys. Rev. Lett. **99**, 200404 (2007).

[77] B. Bertini, D. Schuricht, and F. H. Essler, Quantum quench in the sine-gordon model, J. Stat. Mech.: Theory Exp. **2014**, P10035 (2014).

[78] M. Kormos and G. Zaránd, Quantum quenches in the sine-gordon model: a semiclassical approach, Phys. Rev. E **93**, 062101 (2016).

[79] D. Fioretto and G. Mussardo, Quantum quenches in integrable field theories, New J. Phys. **12**, 055015 (2010).

[80] B. Bertini, L. Piroli, and P. Calabrese, Quantum quenches in the sinh-gordon model: steady state and one-point correlation functions, J. Stat. Mech.: Theory Exp. **2016**, 063102 (2016).

[81] M. Fagotti and P. Calabrese, Evolution of entanglement entropy following a quantum quench: analytic results for the xy chain in a transverse magnetic field, Phys. Rev. A **78**, 010306 (2008).

[82] G. De Chiara, S. Montangero, P. Calabrese, and R. Fazio, Entanglement entropy dynamics of heisenberg chains, J. Stat. Mech.: Theory Exp. **2006**, P03001 (2006).

[83] L. Bonnes, F. H. L. Essler, and A. M. Läuchli, "light-cone" dynamics after quantum quenches in spin chains, Phys. Rev. Lett. **113**, 187203 (2014).

[84] A. M. Läuchli and C. Kollath, Spreading of correlations and entanglement after a quench in the one-dimensional bose–hubbard model, J. Stat. Mech.: Theory Exp. **2008**, P05018 (2008).

[85] G. Carleo, F. Becca, L. Sanchez-Palencia, S. Sorella, and M. Fabrizio, Light-cone effect and supersonic correlations in one- and two-dimensional bosonic superfluids, Phys. Rev. A **89**, 031602 (2014).

[86] S. R. Manmana, S. Wessel, R. M. Noack, and A. Muramatsu, Time evolution of correlations in strongly interacting fermions after a quantum quench, Phys. Rev. B **79**, 155104 (2009).

[87] M. Cheneau, P. Barmettler, D. Poletti, M. Endres, P. Schauß, T. Fukuhara, C. Gross, I. Bloch, C. Kollath, and S. Kuhr, Light-cone-like spreading of correlations in a quantum many-body system, Nature **481**, 484–487 (2012).

[88] T. Langen, R. Geiger, M. Kuhnert, B. Rauer, and J. Schmiedmayer, Local emergence of thermal correlations in an isolated quantum many-body system, Nat. Phys. **9**, 640–643 (2013).

[89] P. Jurcevic, B. P. Lanyon, P. Hauke, C. Hempel, P. Zoller, R. Blatt, and C. F. Roos, Quasiparticle engineering and entanglement propagation in a quantum many-body system, Nature **511**, 202–205 (2014).

[90] P. Richerme, Z.-X. Gong, A. Lee, C. Senko, J. Smith, M. Foss-Feig, S. Michalakis, A. V. Gorshkov, and C. Monroe, Non-local propagation of correlations in quantum systems with long-range interactions, Nature **511**, 198–201 (2014).

[91] M. Kormos, M. Collura, and P. Calabrese, Analytic results for a quantum quench from free to hard-core one-dimensional bosons, Phys. Rev. A **89**, 013609 (2014).

[92] B. Bertini, Approximate light cone effects in a nonrelativistic quantum field theory after a local quench, Phys. Rev. B **95**, 075153 (2017).

[93] V. Alba and P. Calabrese, Entanglement dynamics after quantum quenches in generic integrable systems, SciPost Phys. **4**, 17 (2018).

[94] P. Hauke and L. Tagliacozzo, Spread of correlations in long-range interacting quantum systems, Phys. Rev. Lett. **111**, 207202 (2013).

[95] J. Schachenmayer, B. P. Lanyon, C. F. Roos, and A. J. Daley, Entanglement growth in quench dynamics with variable range interactions, Phys. Rev. X **3**, 031015 (2013).

[96] J. Eisert, M. van den Worm, S. R. Manmana, and M. Kastner, Breakdown of quasilocality in long-range quantum lattice models, Phys. Rev. Lett. **111**, 260401 (2013).

[97] M. Serbyn, Z. Papić, and D. A. Abanin, Universal slow growth of entanglement in interacting strongly disordered systems, Phys. Rev. Lett. **110**, 260601 (2013).

[98] M. Žnidarič, T. Prosen, and P. Prelovšek, Many-body localization in the heisenberg XXZ magnet in a random field, Phys. Rev. B **77**, 064426 (2008).

[99] J. H. Bardarson, F. Pollmann, and J. E. Moore, Unbounded growth of entanglement in models of many-body localization, Phys. Rev. Lett. **109**, 017202 (2012).

[100] J.-S. Caux and J. Mossel, Remarks on the notion of quantum integrability, J. Stat. Mech.: Theory Exp. **2011**, P02023 (2011).

[101] V. I. Arnol'd, *Mathematical methods of classical mechanics*, Vol. 60 (Springer Science & Business Media, 2013).

[102] A. Izergin and V. Korepin, *Quantum inverse scattering method* (Cambridge university press, 1993).

[103] G. Mussardo, Infinite-time average of local fields in an integrable quantum field theory after a quantum quench, Phys. Rev. Lett. **111**, 100401 (2013).

[104] F. H. L. Essler, G. Mussardo, and M. Panfil, Generalized gibbs ensembles for quantum field theories, Phys. Rev. A **91**, 051602 (2015).

[105] F. Essler, G. Mussardo, and M. Panfil, On truncated generalized gibbs ensembles in the ising field theory, J. Stat. Mech.: Theory Exp. **2017**, 013103 (2017).

[106] E. T. Jaynes, Information theory and statistical mechanics, Phys. Rev. **106**, 620–630 (1957).

[107] M. Rigol, V. Dunjko, V. Yurovsky, and M. Olshanii, Relaxation in a completely integrable many-body quantum system: an ab initio study of the dynamics of the highly excited states of 1d lattice hard-core bosons, Phys. Rev. Lett. **98**, 050405 (2007).

[108] A. C. Cassidy, C. W. Clark, and M. Rigol, Generalized thermalization in an integrable lattice system, Phys. Rev. Lett. **106**, 140405 (2011).

[109] M. Fagotti and F. H. L. Essler, Reduced density matrix after a quantum quench, Phys. Rev. B **87**, 245107 (2013).

[110] M. Fagotti and F. H. Essler, Stationary behaviour of observables after a quantum quench in the spin-1/2 heisenberg XXZ chain, J. Stat. Mech.: Theory Exp. **2013**, P07012 (2013).

[111] B. Pozsgay, The generalized gibbs ensemble for heisenberg spin chains, J. Stat. Mech.: Theory Exp. **2013**, P07003 (2013).

[112] E. Ilievski, J. De Nardis, B. Wouters, J.-S. Caux, F. H. L. Essler, and T. Prosen, Complete generalized gibbs ensembles in an interacting theory, Phys. Rev. Lett. **115**, 157201 (2015).

[113] L. Vidmar and M. Rigol, Generalized gibbs ensemble in integrable lattice models, J. Stat. Mech.: Theory Exp. **2016**, 064007 (2016).

[114] T. Langen, S. Erne, R. Geiger, B. Rauer, T. Schweigler, M. Kuhnert, W. Rohringer, I. E. Mazets, T. Gasenzer, and J. Schmiedmayer, Experimental observation of a generalized gibbs ensemble, Science **348**, 207–211 (2015).

[115] P. Calabrese, F. H. L. Essler, and M. Fagotti, Quantum quench in the transverse-field ising chain, Phys. Rev. Lett. **106**, 227203 (2011).

[116] P. Calabrese, F. H. Essler, and M. Fagotti, Quantum quench in the transverse field ising chain: i. time evolution of order parameter correlators, J. Stat. Mech.: Theory Exp. **2012**, P07016 (2012).

[117] P. Calabrese, F. H. Essler, and M. Fagotti, Quantum quenches in the transverse field ising chain: ii. stationary state properties, J. Stat. Mech.: Theory Exp. **2012**, P07022 (2012).

[118] E. Ilievski, M. Medenjak, and T. Prosen, Quasilocal conserved operators in the isotropic heisenberg spin-1/2 chain, Phys. Rev. Lett. **115**, 120601 (2015).

[119] E. Ilievski, J. De Nardis, B. Wouters, J.-S. Caux, F. H. L. Essler, and T. Prosen, Complete generalized gibbs ensembles in an interacting theory, Phys. Rev. Lett. **115**, 157201 (2015).

[120] E. Ilievski, M. Medenjak, T. Prosen, and L. Zadnik, Quasilocal charges in integrable lattice systems, J. Stat. Mech.: Theory Exp. **2016**, 064008 (2016).

[121] L. Piroli and E. Vernier, Quasi-local conserved charges and spin transport in spin-1 integrable chains, J. Stat. Mech.: Theory Exp. **2016**, 053106 (2016).

[122] L. Piroli, E. Vernier, and P. Calabrese, Exact steady states for quantum quenches in integrable heisenberg spin chains, Phys. Rev. B **94**, 054313 (2016).

[123] E. Ilievski, E. Quinn, J. De Nardis, and M. Brockmann, String-charge duality in integrable lattice models, J. Stat. Mech.: Theory Exp. **2016**, 063101 (2016).

[124] J.-S. Caux and F. H. L. Essler, Time evolution of local observables after quenching to an integrable model, Phys. Rev. Lett. **110**, 257203 (2013).

[125] J.-S. Caux, The quench action, J. Stat. Mech.: Theory Exp. **2016**, 064006 (2016).

[126] B. Wouters, J. De Nardis, M. Brockmann, D. Fioretto, M. Rigol, and J.-S. Caux, Quenching the anisotropic heisenberg chain: exact solution and generalized gibbs ensemble predictions, Phys. Rev. Lett. **113**, 117202 (2014).

[127] M. Brockmann, B. Wouters, D. Fioretto, J. De Nardis, R. Vlijm, and J.-S. Caux, Quench action approach for releasing the néel state into the spin-1/2 XXZ chain, J. Stat. Mech.: Theory Exp. **2014**, P12009 (2014).

[128] B. Pozsgay, M. Mestyán, M. A. Werner, M. Kormos, G. Zaránd, and G. Takács, Correlations after quantum quenches in the xxz spin chain: failure of the generalized gibbs ensemble, Phys. Rev. Lett. **113**, 117203 (2014).

[129] J. De Nardis, B. Wouters, M. Brockmann, and J.-S. Caux, Solution for an interaction quench in the lieb-liniger bose gas, Phys. Rev. A **89**, 033601 (2014).

[130] J. De Nardis and J.-S. Caux, Analytical expression for a post-quench time evolution of the one-body density matrix of one-dimensional hard-core bosons, J. Stat. Mech.: Theory Exp. **2014**, P12012 (2014).

[131] L. Piroli, P. Calabrese, and F. H. L. Essler, Quantum quenches to the attractive one-dimensional Bose gas: exact results, SciPost Phys. **1**, 001 (2016).

[132] L. Piroli, P. Calabrese, and F. H. L. Essler, Multiparticle bound-state formation following a quantum quench to the one-dimensional bose gas with attractive interactions, Phys. Rev. Lett. **116**, 070408 (2016).

[133] B. Bertini, D. Schuricht, and F. H. Essler, Quantum quench in the sine-gordon model, J. Stat. Mech.: Theory Exp. **2014**, P10035 (2014).

[134] B. Bertini, L. Piroli, and P. Calabrese, Quantum quenches in the sinh-gordon model: steady state and one-point correlation functions, J. Stat. Mech.: Theory Exp. **2016**, 063102 (2016).

[135] M. Žnidarič, A matrix product solution for a nonequilibrium steady state of an XX chain, J. Phys. A: Math. Theor. **43**, 415004 (2010).

[136] T. Prosen, Exact nonequilibrium steady state of a strongly driven open XXZ chain, Phys. Rev. Lett. **107**, 137201 (2011).

[137] M. Žnidarič, B. Žunkovič, and T. Prosen, Transport properties of a boundary-driven one-dimensional gas of spinless fermions, Phys. Rev. E **84**, 051115 (2011).

[138] E. Ilievski and T. Prosen, Exact steady state manifold of a boundary driven spin-1 lai–sutherland chain, Nucl. Phys. B **882**, 485–500 (2014).

[139] F. Carollo, J. P. Garrahan, I. Lesanovsky, and C. Pérez-Espigares, Fluctuating hydrodynamics, current fluctuations, and hyperuniformity in boundary-driven open quantum chains, Phys. Rev. E **96**, 052118 (2017).

[140] F. Carollo, J. P. Garrahan, and I. Lesanovsky, Current fluctuations in boundary-driven quantum spin chains, Phys. Rev. B **98**, 094301 (2018).

[141] H. Spohn and J. L. Lebowitz, Stationary non-equilibrium states of infinite harmonic systems, Commun. Math. Phys. **54**, 97–120 (1977).

[142] D. Bernard and B. Doyon, Energy flow in non-equilibrium conformal field theory, J. Phys. A: Math. Theor. **45**, 362001 (2012).

[143] D. Bernard and B. Doyon, Non-equilibrium steady states in conformal field theory, Ann. Henri Poincaré **16**, 113–161 (2015).

[144] D. Bernard and B. Doyon, Conformal field theory out of equilibrium: a review, J. Stat. Mech.: Theory Exp. **2016**, 064005 (2016).

[145] D. Bernard and B. Doyon, Time-reversal symmetry and fluctuation relations in non-equilibrium quantum steady states, J. Phys. A: Math. Theor. **46**, 372001 (2013).

[146] A. De Luca, J. Viti, D. Bernard, and B. Doyon, Nonequilibrium thermal transport in the quantum ising chain, Phys. Rev. B **88**, 134301 (2013).

[147] A. De Luca, G. Martelloni, and J. Viti, Stationary states in a free fermionic chain from the quench action method, Phys. Rev. A **91**, 021603 (2015).

[148] B. Doyon, A. Lucas, K. Schalm, and M. Bhaseen, Non-equilibrium steady states in the klein–gordon theory, J. Phys. A: Math. Theor. **48**, 095002 (2015).

[149] T. Antal, Z. Rácz, A. Rákos, and G. Schütz, Transport in the XX chain at zero temperature: emergence of flat magnetization profiles, Phys. Rev. E **59**, 4912 (1999).

[150] D. Karevski, Scaling behaviour of the relaxation in quantum chains, Eur. Phys. J. B **27**, 147–152 (2002).

[151] T. Platini and D. Karevski, Scaling and front dynamics in ising quantum chains, Eur. Phys. J. B **48**, 225–231 (2005).

[152] M. Collura and G. Martelloni, Non-equilibrium transport in d-dimensional non-interacting fermi gases, J. Stat. Mech.: Theory Exp. **2014**, P08006 (2014).

[153] N. Allegra, J. Dubail, J.-M. Stéphan, and J. Viti, Inhomogeneous field theory inside the arctic circle, J. Stat. Mech.: Theory Exp. **2016**, 053108 (2016).

[154] J. Viti, J.-M. Stéphan, J. Dubail, and M. Haque, Inhomogeneous quenches in a free fermionic chain: exact results, EPL **115**, 40011 (2016).

[155] B. Bertini and M. Fagotti, Determination of the nonequilibrium steady state emerging from a defect, Phys. Rev. Lett. **117**, 130402 (2016).

[156] V. Eisler, F. Maislinger, and H. G. Evertz, Universal front propagation in the quantum ising chain with domain-wall initial states, SciPost Phys. **1**, 014 (2016).

[157] M. Kormos, Inhomogeneous quenches in the transverse field ising chain: scaling and front dynamics, SciPost Phys. **3**, 020 (2017).

[158] M. Ljubotina, S. Sotiriadis, and T. Prosen, Non-equilibrium quantum transport in presence of a defect: the non-interacting case, SciPost Phys. **6**, 4 (2019).

[159] B. Bertini, M. Collura, J. De Nardis, and M. Fagotti, Transport in out-of-equilibrium XXZ chains: exact profiles of charges and currents, Phys. Rev. Lett. **117**, 207201 (2016).

[160] O. A. Castro-Alvaredo, B. Doyon, and T. Yoshimura, Emergent hydrodynamics in integrable quantum systems out of equilibrium, Phys. Rev. X **6**, 041065 (2016).

[161] H. Spohn, *Large scale dynamics of interacting particles* (Springer Science & Business Media, 2012).

[162] B. Doyon and H. Spohn, Dynamics of hard rods with initial domain wall state, J. Stat. Mech.: Theory Exp **2017**, 073210 (2017).

[163] A. Bastianello, B. Doyon, G. Watts, and T. Yoshimura, Generalized hydrodynamics of classical integrable field theory: the sinh-Gordon model, SciPost Phys. **4**, 45 (2018).

[164] H. Spohn, Generalized gibbs ensembles of the classical toda chain, J. Stat. Phys., 1–19 (2019).

[165] B. Doyon, Generalized hydrodynamics of the classical toda system, J. Math. Phys. **60**, 073302 (2019).

[166] V. B. Bulchandani, R. Vasseur, C. Karrasch, and J. E. Moore, Bethe-boltzmann hydrodynamics and spin transport in the XXZ chain, Phys. Rev. B **97**, 045407 (2018).

[167] V. B. Bulchandani, R. Vasseur, C. Karrasch, and J. E. Moore, Solvable hydrodynamics of quantum integrable systems, Phys. Rev. Lett. **119**, 220604 (2017).

[168] L. Piroli, J. De Nardis, M. Collura, B. Bertini, and M. Fagotti, Transport in out-of-equilibrium XXZ chains: nonballistic behavior and correlation functions, Phys. Rev. B **96**, 115124 (2017).

[169] M. Collura, A. De Luca, and J. Viti, Analytic solution of the domain-wall nonequilibrium stationary state, Phys. Rev. B **97**, 081111 (2018).

[170] E. Ilievski and J. De Nardis, Ballistic transport in the one-dimensional hubbard model: the hydrodynamic approach, Phys. Rev. B **96**, 081118 (2017).

[171] B. Bertini, L. Piroli, and P. Calabrese, Universal broadening of the light cone in low-temperature transport, Phys. Rev. Lett. **120**, 176801 (2018).

[172] B. Bertini and L. Piroli, Low-temperature transport in out-of-equilibrium XXZ chains, J. Stat. Mech.: Theory Exp. **2018**, 033104 (2018).

[173] B. Doyon and T. Yoshimura, A note on generalized hydrodynamics: inhomogeneous fields and other concepts, SciPost Phys. **2**, 014 (2017).

[174] J.-S. Caux, B. Doyon, J. Dubail, R. Konik, and T. Yoshimura, Hydrodynamics of the interacting Bose gas in the Quantum Newton Cradle setup, SciPost Phys. **6**, 70 (2019).

[175] B. Doyon, J. Dubail, R. Konik, and T. Yoshimura, Large-scale description of interacting one-dimensional bose gases: generalized hydrodynamics supersedes conventional hydrodynamics, Phys. Rev. Lett. **119**, 195301 (2017).

[176] B. Doyon, H. Spohn, and T. Yoshimura, A geometric viewpoint on generalized hydrodynamics, Nucl. Phys. B **926**, 570–583 (2018).

[177] B. Doyon, Exact large-scale correlations in integrable systems out of equilibrium, SciPost Phys. **5**, 54 (2018).

[178] E. Ilievski and J. De Nardis, Microscopic origin of ideal conductivity in integrable quantum models, Phys. Rev. Lett. **119**, 020602 (2017).

[179] B. Doyon and H. Spohn, Drude Weight for the Lieb-Liniger Bose Gas, SciPost Phys. **3**, 039 (2017).

[180] B. Bertini, M. Fagotti, L. Piroli, and P. Calabrese, Entanglement evolution and generalised hydrodynamics: noninteracting systems, J. Phys. A: Math. Theor. **51**, 39LT01 (2018).

[181] V. Alba and P. Calabrese, Entanglement dynamics after quantum quenches in generic integrable systems, SciPost Phys. **4**, 17 (2018).

[182] V. Alba, Entanglement and quantum transport in integrable systems, Phys. Rev. B **97**, 245135 (2018).

[183] V. Alba, B. Bertini, and M. Fagotti, Entanglement evolution and generalised hydrodynamics: interacting integrable systems, SciPost Phys. **7**, 5 (2019).

[184] M. Schemmer, I. Bouchoule, B. Doyon, and J. Dubail, Generalized hydrodynamics on an atom chip, Phys. Rev. Lett. **122**, 090601 (2019).

[185] M. Moeckel and S. Kehrein, Interaction quench in the hubbard model, Phys. Rev. Lett. **100**, 175702 (2008).

[186] A. Rosch, D. Rasch, B. Binz, and M. Vojta, Metastable superfluidity of repulsive fermionic atoms in optical lattices, Phys. Rev. Lett. **101**, 265301 (2008).

[187] M. Moeckel and S. Kehrein, Real-time evolution for weak interaction quenches in quantum systems, Ann. Phys. **324**, 2146–2178 (2009).

[188] M. Gring, M. Kuhnert, T. Langen, T. Kitagawa, B. Rauer, M. Schreitl, I. Mazets, D. A. Smith, E. Demler, and J. Schmiedmayer, Relaxation and prethermalization in an isolated quantum system, Science **337**, 1318–1322 (2012).

[189] J. Marino and A. Silva, Nonequilibrium dynamics of a noisy quantum ising chain: statistics of work and prethermalization after a sudden quench of the transverse field, Phys. Rev. B **89**, 024303 (2014).

[190] F. H. L. Essler, S. Kehrein, S. R. Manmana, and N. J. Robinson, Quench dynamics in a model with tuneable integrability breaking, Phys. Rev. B **89**, 165104 (2014).

[191] B. Bertini, F. H. L. Essler, S. Groha, and N. J. Robinson, Prethermalization and thermalization in models with weak integrability breaking, Phys. Rev. Lett. **115**, 180601 (2015).

[192] B. Bertini, F. H. L. Essler, S. Groha, and N. J. Robinson, Thermalization and light cones in a model with weak integrability breaking, Phys. Rev. B **94**, 245117 (2016).

[193] M. Marcuzzi, J. Marino, A. Gambassi, and A. Silva, Prethermalization in a nonintegrable quantum spin chain after a quench, Phys. Rev. Lett. **111**, 197203 (2013).

[194] M. Marcuzzi, J. Marino, A. Gambassi, and A. Silva, Prethermalization from a low-density holstein-primakoff expansion, Phys. Rev. B **94**, 214304 (2016).

[195] D. Abanin, W. De Roeck, W. W. Ho, and F. Huveneers, A rigorous theory of many-body prethermalization for periodically driven and closed quantum systems, Commun. Math. Phys. **354**, 809–827 (2017).

[196] R. Vasseur and J. E. Moore, Nonequilibrium quantum dynamics and transport: from integrability to many-body localization, J. Stat. Mech.: Theory Exp. **2016**, 064010 (2016).

[197] R. Nandkishore and D. A. Huse, Many-body localization and thermalization in quantum statistical mechanics, Annu. Rev. Condens. Matter Phys. **6**, 15–38 (2015).

[198] D. A. Abanin, E. Altman, I. Bloch, and M. Serbyn, Colloquium: many-body localization, thermalization, and entanglement, Rev. Mod. Phys. **91**, 021001 (2019).

[199] C. J. Turner, A. A. Michailidis, D. A. Abanin, M. Serbyn, and Z. Papić, Weak ergodicity breaking from quantum many-body scars, Nature Phys. **14**, 745–749 (2018).

[200] C. J. Turner, A. A. Michailidis, D. A. Abanin, M. Serbyn, and Z. Papi ć, Quantum scarred eigenstates in a rydberg atom chain: entanglement, breakdown of thermalization, and stability to perturbations, Phys. Rev. B **98**, 155134 (2018).

[201] A. A. Michailidis, C. J. Turner, Z. Papi ć, D. A. Abanin, and M. Serbyn, Stabilizing two-dimensional quantum scars by deformation and synchronization, Phys. Rev. Research **2**, 022065 (2020).

[202] S. Weinberg, *The Quantum Theory of Fields, Volume 2: Modern Applications* (Cambridge University Press, 2005).

[203] B. M. McCoy and T. T. Wu, Two-dimensional ising field theory in a magnetic field: breakup of the cut in the two-point function, Phys. Rev. D **18**, 1259–1267 (1978).

[204] H. Shiba, Quantization of magnetic excitation continuum due to interchain coupling in nearly one-dimensional ising-like antiferromagnets, Prog. Theor. Phys **64**, 466–478 (1980).

[205] G. Delfino, G. Mussardo, and P. Simonetti, Non-integrable quantum field theories as perturbations of certain integrable models, Nucl. Phys. B **473**, 469–508 (1996).

[206] I. Affleck, Soliton Confinement and the Excitation Spectrum of Spin-Peierls Antiferromagnets, In: Dynamical Properties of Unconventional Magnetic Systems. NATO ASI Series (Series E: Applied Sciences) **349** (1998).

[207] E. Sørensen, I. Affleck, D. Augier, and D. Poilblanc, Soliton approach to spin-peierls antiferromagnets: large-scale numerical results, Phys. Rev. B **58**, R14701–R14704 (1998).

[208] D. Augier, E. Sørensen, J. Riera, and D. Poilblanc, Soliton bound states in the raman spectrum of pure and doped spin-peierls chains, Phys. Rev. B **60**, 1075–1081 (1999).

[209] G. Delfino and G. Mussardo, Non-integrable aspects of the multi-frequency sine-gordon model, Nucl. Phys. B **516**, 675–703 (1998).

[210] S. B. Rutkevich, Decay of the metastable phase in $d = 1$ and $d = 2$ ising models, Phys. Rev. B **60**, 14525–14528 (1999).

[211] R. Shankar and G. Murthy, Deconfinement in $d = 1$: asymptotic and half-asymptotic particles, Phys. Rev. B **72**, 224414 (2005).

[212] G. Delfino, Integrable field theory and critical phenomena: the ising model in a magnetic field, J. Phys. A **37**, R45 (2004).

[213] G. Mussardo, Integrability, non-integrability and confinement, J. Stat. Mech.: Theory Exp. **2011**, P01002 (2011).

[214] G. Delfino, P. Grinza, and G. Mussardo, Decay of particles above threshold in the ising field theory with magnetic field, Nucl. Phys. B **737**, 291–303 (2006).

[215] P. Fonseca and A. Zamolodchikov, Ising spectroscopy I: mesons at $T < T_c$, arXiv:hep-th/0612304 (2006).

[216] S. B. Rutkevich, Large-n excitations in the ferromagnetic ising field theory in a weak magnetic field: mass spectrum and decay widths, Phys. Rev. Lett. **95**, 250601 (2005).

[217] Z. Cai, C. Wu, and U. Schollwöck, Confinement: a real-time visualization, Phys. Rev. B **85**, 075102 (2012).

[218] S. B. Rutkevich, Energy spectrum of bound-spinons in the quantum ising spin-chain ferromagnet, J. Stat. Phys. **131**, 917–939 (2008).

[219] S. B. Rutkevich, Kink confinement in the antiferromagnetic XXZ spin-(1/2) chain in a weak staggered magnetic field, EPL (Europhysics Letters) **121**, 37001 (2018).

[220] T. Suzuki and S.-i. Suga, Quantized excitation spectra by magnon confinement in quasi-one-dimensional $s = 1$ spin systems, Phys. Rev. B **98**, 180406 (2018).

[221] Z. Wang, M. Schmidt, A. K. Bera, A. T. M. N. Islam, B. Lake, A. Loidl, and J. Deisenhofer, Spinon confinement in the one-dimensional ising-like antiferromagnet $SrCo_2V_2O_8$, Phys. Rev. B **91**, 140404 (2015).

[222] A. K. Bera, B. Lake, F. H. L. Essler, L. Vanderstraeten, C. Hubig, U. Schollwöck, A. T. M. N. Islam, A. Schneidewind, and D. L. Quintero-Castro, Spinon confinement in a quasi-one-dimensional anisotropic heisenberg magnet, Phys. Rev. B **96**, 054423 (2017).

[223] M. Kormos, M. Collura, G. Takács, and P. Calabrese, Real-time confinement following a quantum quench to a non-integrable model, Nat. Phys. **13**, 246 (2016).

[224] M. C. Bañuls, J. I. Cirac, and M. B. Hastings, Strong and weak thermalization of infinite nonintegrable quantum systems, Phys. Rev. Lett. **106**, 050405 (2011).

[225] T. Rakovszky, M. Mestyán, M. Collura, M. Kormos, and G. Takács, Hamiltonian truncation approach to quenches in the ising field theory, Nucl. Phys. B **911**, 805–845 (2016).

[226] C.-J. Lin and O. I. Motrunich, Quasiparticle explanation of the weak-thermalization regime under quench in a nonintegrable quantum spin chain, Phys. Rev. A **95**, 023621 (2017).

[227] F. Liu, R. Lundgren, P. Titum, G. Pagano, J. Zhang, C. Monroe, and A. V. Gorshkov, Confined quasiparticle dynamics in long-range interacting quantum spin chains, Phys. Rev. Lett. **122**, 150601 (2019).

[228] A. Lerose, B. Žunkovič, A. Silva, and A. Gambassi, Quasilocalized excitations induced by long-range interactions in translationally invariant quantum spin chains, Phys. Rev. B **99**, 121112 (2019).

[229] J. Vovrosh and J. Knolle, Confinement dynamics on a digital quantum computer, arXiv:2001.03044 (2020).

[230] O. A. Castro-Alvaredo, M. Lencsés, I. M. Szécsényi, and J. Viti, Entanglement oscillations near a quantum critical point, Phys. Rev. Lett. **124**, 230601 (2020).

[231] G. Lagnese, F. M. Surace, M. Kormos, and P. Calabrese, Confinement in the spectrum of a heisenberg-ising spin ladder, arXiv:2005.03131 (2020).

[232] R. J. V. Tortora, P. Calabrese, and M. Collura, Relaxation of the order-parameter statistics and dynamical confinement, arXiv:2005.01679 (2020).

[233] A. J. A. James, R. M. Konik, and N. J. Robinson, Nonthermal states arising from confinement in one and two dimensions, Phys. Rev. Lett. **122**, 130603 (2019).

[234] N. J. Robinson, A. J. A. James, and R. M. Konik, Signatures of rare states and thermalization in a theory with confinement, Phys. Rev. B **99**, 195108 (2019).

[235] Z.-C. Yang, F. Liu, A. V. Gorshkov, and T. Iadecola, Hilbert-space fragmentation from strict confinement, Phys. Rev. Lett. **124**, 207602 (2020).

[236] K. G. Wilson, Confinement of quarks, Phys. Rev. D **10**, 2445–2459 (1974).

[237] J. Kogut and L. Susskind, Hamiltonian formulation of wilson's lattice gauge theories, Phys. Rev. D **11**, 395–408 (1975).

[238] J. Schwinger, Gauge invariance and mass. II, Phys. Rev. **128**, 2425–2429 (1962).

[239] B. Buyens, J. Haegeman, F. Hebenstreit, F. Verstraete, and K. Van Acoleyen, Real-time simulation of the schwinger effect with matrix product states, Phys. Rev. D **96**, 114501 (2017).

[240] T. Pichler, M. Dalmonte, E. Rico, P. Zoller, and S. Montangero, Real-time dynamics in U(1) lattice gauge theories with tensor networks, Phys. Rev. X **6**, 011023 (2016).

[241] Y. Kuno, S. Sakane, K. Kasamatsu, I. Ichinose, and T. Matsui, Quantum simulation of $(1+1)$-dimensional U(1) gauge-higgs model on a lattice by cold bose gases, Phys. Rev. D **95**, 094507 (2017).

[242] P. Sala, T. Shi, S. Kühn, M. C. Bañuls, E. Demler, and J. I. Cirac, Variational study of U(1) and SU(2) lattice gauge theories with gaussian states in $1+1$ dimensions, Phys. Rev. D **98**, 034505 (2018).

[243] F. Hebenstreit, J. Berges, and D. Gelfand, Simulating fermion production in 1+1 dimensional QED, Phys. Rev. D **87**, 105006 (2013).

[244] F. Hebenstreit, J. Berges, and D. Gelfand, Real-time dynamics of string breaking, Phys. Rev. Lett. **111**, 201601 (2013).

[245] J. Park, Y. Kuno, and I. Ichinose, Glassy dynamics from quark confinement: atomic quantum simulation of the gauge-higgs model on a lattice, Phys. Rev. A **100**, 013629 (2019).

[246] S. Notarnicola, M. Collura, and S. Montangero, Real-time-dynamics quantum simulation of $(1+1)$-dimensional lattice QED with rydberg atoms, Phys. Rev. Research **2**, 013288 (2020).

[247] F. M. Surace, P. P. Mazza, G. Giudici, A. Lerose, A. Gambassi, and M. Dalmonte, Lattice gauge theories and string dynamics in rydberg atom quantum simulators, Phys. Rev. X **10**, 021041 (2020).

[248] G. Magnifico, M. Dalmonte, P. Facchi, S. Pascazio, F. V. Pepe, and E. Ercolessi, Real time dynamics and confinement in the $\mathbb{Z}\_\{n\}$ schwinger-weyl lattice model for 1+ 1 QED, Quantum **4**, 281 (2020).

[249] T. Chanda, J. Zakrzewski, M. Lewenstein, and L. Tagliacozzo, Confinement and lack of thermalization after quenches in the bosonic schwinger model, Phys. Rev. Lett. **124**, 180602 (2020).

[250] S. Pai and M. Pretko, Fractons from confinement in one dimension, Phys. Rev. Research **2**, 013094 (2020).

[251] A. C. Cubero and N. J. Robinson, Lack of thermalization in (1+ 1)-d quantum chromodynamics at large N_c, J. Stat. Mech.: Theory Exp. **2019**, 123101 (2019).

[252] C. Jarzynski, Nonequilibrium equality for free energy differences, Phys. Rev. Lett. **78**, 2690–2693 (1997).

[253] J. Goold, F. Plastina, A. Gambassi, and A. Silva, "The role of quantum work statistics in many-body physics", in *Thermodynamics in the quantum regime*, edited by F. Binder, L. Correa, C. Gogolin, J. Anders, and G. Adesso (Springer, 2018), pp. 317–336.

[254] P. Smacchia and A. Silva, Work distribution and edge singularities for generic time-dependent protocols in extended systems, Phys. Rev. E **88**, 042109 (2013).

[255] J. Marino and A. Silva, Nonequilibrium dynamics of a noisy quantum ising chain: statistics of work and prethermalization after a sudden quench of the transverse field, Phys. Rev. B **89**, 024303 (2014).

[256] T. Pálmai and S. Sotiriadis, Quench echo and work statistics in integrable quantum field theories, Phys. Rev. E **90**, 052102 (2014).

[257] T. Palmai, Edge exponents in work statistics out of equilibrium and dynamical phase transitions from scattering theory in one-dimensional gapped systems, Phys. Rev. B **92**, 235433 (2015).

[258] P. Rotondo, J. Minář, J. P. Garrahan, I. Lesanovsky, and M. Marcuzzi, Singularities in large deviations of work in quantum quenches, Phys. Rev. B **98**, 184303 (2018).

[259] C. Rylands and N. Andrei, Loschmidt amplitude and work distribution in quenches of the sine-gordon model, Phys. Rev. B **99**, 085133 (2019).

[260] C. Rylands and N. Andrei, Quantum work of an optical lattice, Phys. Rev. B **100**, 064308 (2019).

[261] I. Lovas, A. Grabarits, M. Kormos, and G. Zaránd, Theory of quantum work in metallic grains, Phys. Rev. Research **2**, 023224 (2020).

[262] G. Bunin, L. D'Alessio, Y. Kafri, and A. Polkovnikov, Universal energy fluctuations in thermally isolated driven systems, Nature Physics **7**, 913–917 (2011).

[263] A. Gambassi and A. Silva, Statistics of the work in quantum quenches, universality and the critical casimir effect, arXiv:1106.2671 (2011).

[264] K. Hepp and E. H. Lieb, Equilibrium statistical mechanics of matter interacting with the quantized radiation field, Phys. Rev. A **8**, 2517–2525 (1973).

[265] C. Emary and T. Brandes, Chaos and the quantum phase transition in the dicke model, Phys. Rev. E **67**, 066203 (2003).

[266] H. Bethe, Zur theorie der metalle, Zeitschrift für Physik **71**, 205–226 (1931).

[267] E. H. Lieb and W. Liniger, Exact analysis of an interacting bose gas. i. the general solution and the ground state, Phys. Rev. **130**, 1605–1616 (1963).

[268] E. H. Lieb, Exact analysis of an interacting bose gas. ii. the excitation spectrum, Phys. Rev. **130**, 1616–1624 (1963).

[269] T. Kinoshita, T. Wenger, and D. S. Weiss, Observation of a one-dimensional tonks-girardeau gas, Science **305**, 1125–1128 (2004).

[270] T. Kinoshita, T. Wenger, and D. S. Weiss, Local pair correlations in one-dimensional bose gases, Phys. Rev. Lett. **95**, 190406 (2005).

[271] A. H. van Amerongen, J. J. P. van Es, P. Wicke, K. V. Kheruntsyan, and N. J. van Druten, Yang-yang thermodynamics on an atom chip, Phys. Rev. Lett. **100**, 090402 (2008).

[272] E. Haller, M. Gustavsson, M. J. Mark, J. G. Danzl, R. Hart, G. Pupillo, and H.-C. Nägerl, Realization of an excited, strongly correlated quantum gas phase, Science **325**, 1224–1227 (2009).

[273] N. Fabbri, D. Clément, L. Fallani, C. Fort, and M. Inguscio, Momentum-resolved study of an array of one-dimensional strongly phase-fluctuating bose gases, Phys. Rev. A **83**, 031604 (2011).

[274] N. Fabbri, M. Panfil, D. Clément, L. Fallani, M. Inguscio, C. Fort, and J.-S. Caux, Dynamical structure factor of one-dimensional bose gases: experimental signatures of beyond-luttinger-liquid physics, Phys. Rev. A **91**, 043617 (2015).

[275] M. Takahashi, *Thermodynamics of one-dimensional solvable models* (Cambridge university press, 2005).

[276] M. Olshanii, Atomic scattering in the presence of an external confinement and a gas of impenetrable bosons, Phys. Rev. Lett. **81**, 938–941 (1998).

[277] S. Inouye, M. Andrews, J. Stenger, H.-J. Miesner, D. Stamper-Kurn, and W. Ketterle, Observation of feshbach resonances in a bose–einstein condensate, Nature **392**, 151–154 (1998).

[278] C.-N. Yang and C. P. Yang, Thermodynamics of a one-dimensional system of bosons with repulsive delta-function interaction, J. Math. Phys. **10**, 1115–1122 (1969).

[279] K. Kozlowski and B. Pozsgay, Surface free energy of the open XXZ spin-1/2 chain, J. Stat. Mech.: Theory Exp. **2012**, P05021 (2012).

[280] B. Pozsgay, Overlaps between eigenstates of the XXZ spin-1/2 chain and a class of simple product states, J. Stat. Mech.: Theory Exp. **2014**, P06011 (2014).

[281] L. Piroli and P. Calabrese, Recursive formulas for the overlaps between bethe states and product states in XXZ heisenberg chains, J. Phys. A: Math. Theor. **47**, 385003 (2014).

[282] M. Brockmann, J. De Nardis, B. Wouters, and J.-S. Caux, A gaudin-like determinant for overlaps of néel and XXZ bethe states, J. Phys. A: Math. Theor. **47**, 145003 (2014).

[283] B. Pozsgay, Overlaps with arbitrary two-site states in the XXZ spin chain, J. Stat. Mech.: Theory Exp. **2018**, 053103 (2018).

[284] P. P. Mazza, J.-M. Stéphan, E. Canovi, V. Alba, M. Brockmann, and M. Haque, Overlap distributions for quantum quenches in the anisotropic heisenberg chain, J. Stat. Mech.: Theory Exp. **2016**, 013104 (2016).

[285] L. Piroli, B. Pozsgay, and E. Vernier, What is an integrable quench?, Nucl. Phys. B **925**, 362–402 (2017).

[286] B. Pozsgay, L. Piroli, and E. Vernier, Integrable Matrix Product States from boundary integrability, SciPost Phys. **6**, 62 (2019).

[287] J. De Nardis, L. Piroli, and J.-S. Caux, Relaxation dynamics of local observables in integrable systems, J. Phys. A: Math. Theor. **48**, 43FT01 (2015).

[288] L. Piroli and P. Calabrese, Exact dynamics following an interaction quench in a one-dimensional anyonic gas, Phys. Rev. A **96**, 023611 (2017).

[289] V. Gritsev, T. Rostunov, and E. Demler, Exact methods in the analysis of the non-equilibrium dynamics of integrable models: application to the study of correlation functions for non-equilibrium 1d bose gas, J. Stat. Mech.: Theory Exp. **2010**, P05012 (2010).

[290] M. Kormos, A. Shashi, Y.-Z. Chou, J.-S. Caux, and A. Imambekov, Interaction quenches in the one-dimensional bose gas, Phys. Rev. B **88**, 205131 (2013).

[291] J. De Nardis and J.-S. Caux, Analytical expression for a post-quench time evolution of the one-body density matrix of one-dimensional hard-core bosons, J. Stat. Mech.: Theory Exp. **2014**, P12012 (2014).

[292] J. C. Zill, T. M. Wright, K. V. Kheruntsyan, T. Gasenzer, and M. J. Davis, A coordinate bethe ansatz approach to the calculation of equilibrium and nonequilibrium correlations of the one-dimensional bose gas, New J. Phys. **18**, 045010 (2016).

[293] J. C. Zill, T. M. Wright, K. V. Kheruntsyan, T. Gasenzer, and M. J. Davis, Quantum quench dynamics of the attractive one-dimensional Bose gas via the coordinate Bethe ansatz, SciPost Phys. **4**, 011 (2018).

[294] M. Brockmann, Overlaps of q-raised néel states with XXZ bethe states and their relation to the lieb–liniger bose gas, J. Stat. Mech.: Theory Exp. **2014**, P05006 (2014).

[295] M. Brockmann, J. De Nardis, B. Wouters, and J.-S. Caux, Néel-XXZ state overlaps: odd particle numbers and lieb–liniger scaling limit, J. Phys. A: Math. Theor. **47**, 345003 (2014).

[296] L. Piroli, B. Pozsgay, and E. Vernier, From the quantum transfer matrix to the quench action: the loschmidt echo in XXZ heisenberg spin chains, J. Stat. Mech.: Theory Exp. **2017**, 023106 (2017).

[297] L. Piroli, B. Pozsgay, and E. Vernier, Non-analytic behavior of the loschmidt echo in XXZ spin chains: exact results, Nucl. Phys. B **933**, 454–481 (2018).

[298] A. Klauser and J.-S. Caux, Equilibrium thermodynamic properties of interacting two-component bosons in one dimension, Phys. Rev. A **84**, 033604 (2011).

[299] M. Takahashi, Low-temperature specific heat of spin-1/2 anisotropic heisenberg ring, Prog. Theor. Phys. **50**, 1519–1536 (1973).

[300] M. Girardeau, Relationship between systems of impenetrable bosons and fermions in one dimension, J. Math. Phys. **1**, 516–523 (1960).

[301] P. Le Doussal and P. Calabrese, The kpz equation with flat initial condition and the directed polymer with one free end, J. Stat. Mech.: Theory Exp. **2012**, P06001 (2012).

[302] P. Calabrese and P. Le Doussal, Interaction quench in a lieb–liniger model and the kpz equation with flat initial conditions, J. Stat. Mech.: Theory Exp. **2014**, P05004 (2014).

[303] D. Zagier, Evaluation of the multiple zeta values ζ (2,..., 2, 3, 2,..., 2), Ann. Math., 977–1000 (2012).

[304] G. Huber, F. Schmidt-Kaler, S. Deffner, and E. Lutz, Employing trapped cold ions to verify the quantum jarzynski equality, Phys. Rev. Lett. **101**, 070403 (2008).

[305] R. Dorner, S. R. Clark, L. Heaney, R. Fazio, J. Goold, and V. Vedral, Extracting quantum work statistics and fluctuation theorems by single-qubit interferometry, Phys. Rev. Lett. **110**, 230601 (2013).

[306] L. Mazzola, G. De Chiara, and M. Paternostro, Measuring the characteristic function of the work distribution, Phys. Rev. Lett. **110**, 230602 (2013).

[307] M. Campisi, R. Blattmann, S. Kohler, D. Zueco, and P. Hänggi, Employing circuit qed to measure non-equilibrium work fluctuations, New J. Phys. **15**, 105028 (2013).

[308] T. B. Batalhão, A. M. Souza, L. Mazzola, R. Auccaise, R. S. Sarthour, I. S. Oliveira, J. Goold, G. De Chiara, M. Paternostro, and R. M. Serra, Experimental reconstruction of work distribution and study of fluctuation relations in a closed quantum system, Phys. Rev. Lett. **113**, 140601 (2014).

[309] S. An, J.-N. Zhang, M. Um, D. Lv, Y. Lu, J. Zhang, Z.-Q. Yin, H. Quan, and K. Kim, Experimental test of the quantum jarzynski equality with a trapped-ion system, Nature Phys. **11**, 193–199 (2015).

[310] B. Derrida, Microscopic versus macroscopic approaches to non-equilibrium systems, J. Stat. Mech.: Theory Exp. **2011**, P01030 (2011).

[311] L. Bertini, A. De Sole, D. Gabrielli, G. Jona-Lasinio, and C. Landim, Macroscopic fluctuation theory, Rev. Mod. Phys. **87**, 593–636 (2015).

[312] L. Bertini, A. De Sole, D. Gabrielli, G. Jona-Lasinio, and C. Landim, Fluctuations in stationary nonequilibrium states of irreversible processes, Phys. Rev. Lett. **87**, 040601 (2001).

[313] L. Bertini, A. De Sole, D. Gabrielli, G. Jona-Lasinio, and C. Landim, Macroscopic fluctuation theory for stationary non-equilibrium states, J. Stat. Phys. **107**, 635–675 (2002).

[314] J. Sirker, R. G. Pereira, and I. Affleck, Diffusion and ballistic transport in one-dimensional quantum systems, Phys. Rev. Lett. **103**, 216602 (2009).

[315] K. Schwab, E. Henriksen, J. Worlock, and M. L. Roukes, Measurement of the quantum of thermal conductance, Nature **404**, 974 (2000).

[316] S. Jezouin, F. Parmentier, A. Anthore, U. Gennser, A. Cavanna, Y. Jin, and F. Pierre, Quantum limit of heat flow across a single electronic channel, Science **342**, 601–604 (2013).

[317] S. Lievens, N. Stoilova, and J. Van der Jeugt, Harmonic oscillator chains as wigner quantum systems: periodic and fixed wall boundary conditions in gl (1 | n) solutions, J. Math. Phys. **49**, 073502 (2008).

[318] S. Sachdev and A. P. Young, Low temperature relaxational dynamics of the ising chain in a transverse field, Phys. Rev. Lett. **78**, 2220–2223 (1997).

[319] S. Sachdev and K. Damle, Low temperature spin diffusion in the one-dimensional quantum $O(3)$ nonlinear σ model, Phys. Rev. Lett. **78**, 943–946 (1997).

[320] K. Damle and S. Sachdev, Spin dynamics and transport in gapped one-dimensional heisenberg antiferromagnets at nonzero temperatures, Phys. Rev. B **57**, 8307–8339 (1998).

[321] K. Damle and S. Sachdev, Universal relaxational dynamics of gapped one-dimensional models in the quantum sine-gordon universality class, Phys. Rev. Lett. **95**, 187201 (2005).

[322] K. Saito and A. Dhar, Fluctuation theorem in quantum heat conduction, Phys. Rev. Lett. **99**, 180601 (2007).

[323] V. Eisler and Z. Rácz, Full counting statistics in a propagating quantum front and random matrix spectra, Phys. Rev. Lett. **110**, 060602 (2013).

[324] M. Fagotti, Higher-order generalized hydrodynamics in one dimension: the noninteracting test, Phys. Rev. B **96**, 220302 (2017).

[325] J. De Nardis, D. Bernard, and B. Doyon, Hydrodynamic diffusion in integrable systems, Phys. Rev. Lett. **121**, 160603 (2018).

[326] C. A. Tracy and H. Widom, Level-spacing distributions and the airy kernel, Commun. Math. Phys. **159**, 151–174 (1994).

[327] V. Eisler, Universality in the full counting statistics of trapped fermions, Phys. Rev. Lett. **111**, 080402 (2013).

[328] D. S. Dean, P. Le Doussal, S. N. Majumdar, and G. Schehr, Finite-temperature free fermions and the kardar-parisi-zhang equation at finite time, Phys. Rev. Lett. **114**, 110402 (2015).

[329] D. S. Dean, P. Le Doussal, S. N. Majumdar, and G. Schehr, Noninteracting fermions at finite temperature in a d-dimensional trap: universal correlations, Phys. Rev. A **94**, 063622 (2016).

[330] *NIST DIGITAL LIBRARY OF MATHEMATICAL FUNCTIONS*, Release 1.0.27 of 2020-06-15, F. W. J. Olver, A. B. Olde Daalhuis, D. W. Lozier, B. I. Schneider, R. F. Boisvert, C. W. Clark, B. R. Miller, B. V. Saunders, H. S. Cohl, and M. A. McClain, eds., 2020.

[331] L. S. Levitov and G. B. Lesovik, Charge distribution in quantum shot noise, JETP Lett. **58**, 230–230 (1993).

[332] L. S. Levitov and G. B. Lesovik, Quantum measurement in electric circuit, arXiv:cond-mat/9401004 (1994).

[333] L. S. Levitov, H. Lee, and G. B. Lesovik, Electron counting statistics and coherent states of electric current, J. Math. Phys. **37**, 4845–4866 (1996).

[334] K. Schönhammer, Full counting statistics for noninteracting fermions: exact results and the levitov-lesovik formula, Phys. Rev. B **75**, 205329 (2007).

[335] I. Klich, "An elementary derivation of Levitov's formula", in *Quantum noise in mesoscopic physics* (Springer, 2003), pp. 397–402.

[336] I. Klich, A note on the full counting statistics of paired fermions, J. Stat. Mech.: Theory Exp. **2014**, P11006 (2014).

[337] D. Bernard and B. Doyon, Full counting statistics in the resonant-level model, J. Math. Phys. **53**, 122302 (2012).

[338] T. Yoshimura, Full counting statistics in the free dirac theory, J. Phys. A: Math. Theor. **51**, 475002 (2018).

[339] J. Myers, M. J. Bhaseen, R. J. Harris, and B. Doyon, Transport fluctuations in integrable models out of equilibrium, SciPost Phys. **8**, 7 (2020).

[340] B. Doyon and J. Myers, Fluctuations in ballistic transport from euler hydrodynamics, Ann. Henri Poincaré **21**, 255–302 (2020).

[341] M. Žnidarič, Exact large-deviation statistics for a nonequilibrium quantum spin chain, Phys. Rev. Lett. **112**, 040602 (2014).

[342] M. Kormos, C. P. Moca, and G. Zaránd, Semiclassical theory of front propagation and front equilibration following an inhomogeneous quantum quench, Phys. Rev. E **98**, 032105 (2018).

[343] M. A. Werner, C. P. ş. Moca, Ö. Legeza, M. Kormos, and G. Zaránd, Spin fluctuations after quantum quenches in the $s = 1$ haldane chain: numerical validation of the semi-semiclassical theory, Phys. Rev. B **100**, 035401 (2019).

[344] S. Sotiriadis and J. Cardy, Inhomogeneous quantum quenches, J. Stat. Mech.: Theory Exp. **2008**, P11003 (2008).

[345] P. Calabrese, C. Hagendorf, and P. Le Doussal, Time evolution of one-dimensional gapless models from a domain wall initial state: stochastic loewner evolution continued?, J. Stat. Mech.: Theory Exp. **2008**, P07013 (2008).

[346] E. Langmann, J. L. Lebowitz, V. Mastropietro, and P. Moosavi, Steady states and universal conductance in a quenched luttinger model, Commun. Math. Phys. **349**, 551–582 (2017).

[347] J. Dubail, J.-M. Stéphan, J. Viti, and P. Calabrese, Conformal Field Theory for Inhomogeneous One-dimensional Quantum Systems: the Example of Non-Interacting Fermi Gases, SciPost Phys. **2**, 002 (2017).

[348] D. Gobert, C. Kollath, U. Schollwöck, and G. Schütz, Real-time dynamics in spin-$\frac{1}{2}$ chains with adaptive time-dependent density matrix renormalization group, Phys. Rev. E **71**, 036102 (2005).

[349] T. Sabetta and G. Misguich, Nonequilibrium steady states in the quantum xxz spin chain, Phys. Rev. B **88**, 245114 (2013).

[350] A. De Luca, J. Viti, L. Mazza, and D. Rossini, Energy transport in heisenberg chains beyond the luttinger liquid paradigm, Phys. Rev. B **90**, 161101 (2014).

[351] A. Biella, A. De Luca, J. Viti, D. Rossini, L. Mazza, and R. Fazio, Energy transport between two integrable spin chains, Phys. Rev. B **93**, 205121 (2016).

[352] X. Zotos, A tba approach to thermal transport in the xxz heisenberg model, J. Stat. Mech.: Theory Exp. **2017**, 103101 (2017).

[353] A. Bastianello and A. De Luca, Nonequilibrium steady state generated by a moving defect: the supersonic threshold, Phys. Rev. Lett. **120**, 060602 (2018).

[354] A. Bastianello and A. De Luca, Superluminal moving defects in the ising spin chain, Phys. Rev. B **98**, 064304 (2018).

[355] S. Gopalakrishnan, D. A. Huse, V. Khemani, and R. Vasseur, Hydrodynamics of operator spreading and quasiparticle diffusion in interacting integrable systems, Phys. Rev. B **98**, 220303 (2018).

[356] M. Panfil and J. Pawełczyk, Linearized regime of the generalized hydrodynamics with diffusion, SciPost Phys. Core **1**, 2 (2019).

[357] A. J. Friedman, S. Gopalakrishnan, and R. Vasseur, Diffusive hydrodynamics from integrability breaking, Phys. Rev. B **101**, 180302 (2020).

[358] A. Bastianello, J. De Nardis, and A. De Luca, Generalized hydrodynamics with dephasing noise, Phys. Rev. B **102**, 161110 (2020).

[359] I. Bouchoule, B. Doyon, and J. Dubail, The effect of atom losses on the distribution of rapidities in the one-dimensional Bose gas, SciPost Phys. **9**, 44 (2020).

[360] A. Bastianello, V. Alba, and J.-S. Caux, Generalized hydrodynamics with space-time inhomogeneous interactions, Phys. Rev. Lett. **123**, 130602 (2019).

[361] J. Durnin, M. Bhaseen, and B. Doyon, Non-equilibrium dynamics and weakly broken integrability, arXiv:2004.11030 (2020).

[362] B. Doyon, Lecture Notes On Generalised Hydrodynamics, SciPost Phys. Lect. Notes, 18 (2020).

[363] C. Boldrighini, R. Dobrushin, and Y. M. Sukhov, One-dimensional hard rod caricature of hydrodynamics, J. Stat. Phys. **31**, 577–616 (1983).

[364] C. Boldrighini and Y. M. Suhov, One-dimensional hard-rod caricature of hydrodynamics:"navier–stokes correction" for local equilibrium initial states, Commun. Math. Phys. **189**, 577–590 (1997).

[365] B. Doyon, T. Yoshimura, and J.-S. Caux, Soliton gases and generalized hydrodynamics, Phys. Rev. Lett. **120**, 045301 (2018).

[366] A. Urichuk, Y. Oez, A. Klümper, and J. Sirker, The spin Drude weight of the XXZ chain and generalized hydrodynamics, SciPost Phys. **6**, 5 (2019).

[367] D.-L. Vu and T. Yoshimura, Equations of state in generalized hydrodynamics, SciPost Phys. **6**, 23 (2019).

[368] H. Spohn, Collision rate ansatz for the classical toda lattice, Phys. Rev. E **101**, 060103 (2020).

[369] T. Yoshimura and H. Spohn, Collision rate ansatz for quantum integrable systems, arXiv:2004.07113 (2020).

[370] M. Borsi, B. Pozsgay, and L. Pristyák, Current operators in bethe ansatz and generalized hydrodynamics: an exact quantum-classical correspondence, Phys. Rev. X **10**, 011054 (2020).

[371] B. Pozsgay, Current operators in integrable spin chains: lessons from long range deformations, SciPost Phys. **8**, 16 (2020).

[372] B. Pozsgay, Algebraic construction of current operators in integrable spin chains, Phys. Rev. Lett. **125**, 070602 (2020).

[373] J. Sirker, R. G. Pereira, and I. Affleck, Diffusion and ballistic transport in one-dimensional quantum systems, Phys. Rev. Lett. **103**, 216602 (2009).

[374] C. Karrasch, J. E. Moore, and F. Heidrich-Meisner, Real-time and real-space spin and energy dynamics in one-dimensional spin-$\frac{1}{2}$ systems induced by local quantum quenches at finite temperatures, Phys. Rev. B **89**, 075139 (2014).

[375] C. Karrasch, D. M. Kennes, and J. E. Moore, Transport properties of the one-dimensional hubbard model at finite temperature, Phys. Rev. B **90**, 155104 (2014).

[376] R. Steinigeweg, F. Jin, H. De Raedt, K. Michielsen, and J. Gemmer, Charge diffusion in the one-dimensional hubbard model, Phys. Rev. E **96**, 020105 (2017).

[377] M. Medenjak, C. Karrasch, and T. Prosen, Lower bounding diffusion constant by the curvature of drude weight, Phys. Rev. Lett. **119**, 080602 (2017).

[378] H. Spohn, Interacting and noninteracting integrable systems, J. Math. Phys. **59**, 091402 (2018).

[379] F. S. Møller and J. Schmiedmayer, Introducing iFluid: a numerical framework for solving hydrodynamical equations in integrable models, SciPost Phys. **8**, 41 (2020).

[380] F. Møller, Ifluidmatlab, GitHub repository (2019).

[381] H. Spohn, Nonlinear fluctuating hydrodynamics for anharmonic chains, J. Stat Phys **154**, 1191–1227 (2014).

[382] R. Chetrite and H. Touchette, Nonequilibrium markov processes conditioned on large deviations, **16**, 2005–2057 (2015).

[383] R. Chetrite and H. Touchette, Nonequilibrium microcanonical and canonical ensembles and their equivalence, Phys. Rev. Lett. **111**, 120601 (2013).

[384] C. Monthus, Boundary-driven lindblad dynamics of random quantum spin chains: strong disorder approach for the relaxation, the steady state and the current, J. Stat. Mech.: Theory Exp. **2017**, 043303 (2017).

[385] F. Carollo, J. P. Garrahan, I. Lesanovsky, and C. Pérez-Espigares, Making rare events typical in markovian open quantum systems, Phys. Rev. A **98**, 010103 (2018).

[386] D. Cilluffo, I. Lesanovsky, G. Buonaiuto, A. Carollo, S. Lorenzo, G. M. Palma, F. Ciccarello, and F. Carollo, Microscopic biasing of discrete-time quantum trajectories, arXiv:2007.15659 (2020).

[387] T. Bodineau and B. Derrida, Distribution of current in nonequilibrium diffusive systems and phase transitions, Phys. Rev. E **72**, 066110 (2005).

[388] C. P. Espigares, P. L. Garrido, and P. I. Hurtado, Dynamical phase transition for current statistics in a simple driven diffusive system, Phys. Rev. E **87**, 032115 (2013).

[389] P. I. Hurtado, C. P. Espigares, J. J. del Pozo, and P. L. Garrido, Thermodynamics of currents in nonequilibrium diffusive systems: theory and simulation, J. Stat. Phys. **154**, 214–264 (2014).

[390] A. Arinshtein, V. Fateyev, and A. Zamolodchikov, Quantum s-matrix of the (1 + 1)-dimensional todd chain, Phys. Lett. B **87**, 389–392 (1979).

[391] M. Kormos, G. Mussardo, and A. Trombettoni, Expectation values in the lieb-liniger bose gas, Phys. Rev. Lett. **103**, 210404 (2009).

[392] M. Kormos, G. Mussardo, and A. Trombettoni, One-dimensional lieb-liniger bose gas as nonrelativistic limit of the sinh-gordon model, Phys. Rev. A **81**, 043606 (2010).

[393] S. Negro and F. Smirnov, On one-point functions for sinh-gordon model at finite temperature, Nucl. Phys. B **875**, 166–185 (2013).

[394] S. Negro, On sinh–gordon thermodynamic bethe ansatz and fermionic basis, Int. J. Mod. Phys. A **29**, 1450111 (2014).

[395] Z. Fodor and C. Hoelbling, Light hadron masses from lattice qcd, Rev. Mod. Phys. **84**, 449–495 (2012).

[396] K. Fukushima and T. Hatsuda, The phase diagram of dense qcd, Rep. Prog. Phys. **74**, 014001 (2010).

[397] R. Soltz, C. DeTar, F. Karsch, S. Mukherjee, and P. Vranas, Lattice qcd thermodynamics with physical quark masses, Annu. Rev. Nucl. Part. Sci. **65**, 379–402 (2015).

[398] E. A. Calzetta, *Nonequilibrium quantum field theory. cambridge monographs on mathematical physics* (Cambridge University Press, 2008).

[399] U.-J. Wiese, Ultracold quantum gases and lattice systems: quantum simulation of lattice gauge theories, Annalen der Physik **525**, 777–796 (2013).

[400] E. Zohar, J. I. Cirac, and B. Reznik, Quantum simulations of lattice gauge theories using ultracold atoms in optical lattices, Rep. Prog. Phys. **79**, 014401 (2015).

[401] M. Dalmonte and S. Montangero, Lattice gauge theory simulations in the quantum information era, Contemp. Phys. **57**, 388–412 (2016).

[402] D. Banerjee, M. Dalmonte, M. Müller, E. Rico, P. Stebler, U.-J. Wiese, and P. Zoller, Atomic quantum simulation of dynamical gauge fields coupled to fermionic matter: from string breaking to evolution after a quench, Phys. Rev. Lett. **109**, 175302 (2012).

[403] A. Celi, B. Vermersch, O. Viyuela, H. Pichler, M. D. Lukin, and P. Zoller, Emerging two-dimensional gauge theories in rydberg configurable arrays, Phys. Rev. X **10**, 021057 (2020).

[404] E. A. Martinez, C. A. Muschik, P. Schindler, D. Nigg, A. Erhard, M. Heyl, P. Hauke, M. Dalmonte, T. Monz, P. Zoller, et al., Real-time dynamics of lattice gauge theories with a few-qubit quantum computer, Nature **534**, 516–519 (2016).

[405] H. C. Fogedby, The ising chain in a skew magnetic field, J. Phys. C: Solid State Phys. **11**, 2801–2813 (1978).

[406] L. Susskind, Lattice fermions, Phys. Rev. D **16**, 3031–3039 (1977).

[407] S. Chandrasekharan and U.-J. Wiese, Quantum link models: a discrete approach to gauge theories, Nucl. Phys. B **492**, 455–471 (1997).

[408] D. Horn, Finite matrix models with continuous local gauge invariance, Physics Letters B **100**, 149–151 (1981).

[409] T. Banks, L. Susskind, and J. Kogut, Strong-coupling calculations of lattice gauge theories: (1 + 1)-dimensional exercises, Phys. Rev. D **13**, 1043–1053 (1976).

[410] E. Zohar and J. I. Cirac, Removing staggered fermionic matter in $u(n)$ and $su(n)$ lattice gauge theories, Phys. Rev. D **99**, 114511 (2019).

[411] G. H. Wannier, Wave functions and effective hamiltonian for bloch electrons in an electric field, Phys. Rev. **117**, 432–439 (1960).

[412] H. Fukuyama, R. A. Bari, and H. C. Fogedby, Tightly bound electrons in a uniform electric field, Phys. Rev. B **8**, 5579–5586 (1973).

[413] T. Hartmann, F. Keck, H. Korsch, and S. Mossmann, Dynamics of bloch oscillations, New J. Phys. **6**, 2 (2004).

[414] N. Schuch, M. M. Wolf, F. Verstraete, and J. I. Cirac, Entropy scaling and simulability by matrix product states, Phys. Rev. Lett. **100**, 030504 (2008).

[415] N. Schuch, M. M. Wolf, K. G. H. Vollbrecht, and J. I. Cirac, On entropy growth and the hardness of simulating time evolution, New J. Phys. **10**, 033032 (2008).

[416] P. Hauke, F. M. Cucchietti, L. Tagliacozzo, I. Deutsch, and M. Lewenstein, Can one trust quantum simulators?, Rep. Prog. Phys. **75**, 082401 (2012).

[417] Á. Perales and G. Vidal, Entanglement growth and simulation efficiency in one-dimensional quantum lattice systems, Phys. Rev. A **78**, 042337 (2008).

[418] P. W. Anderson, Absence of diffusion in certain random lattices, Phys. Rev. **109**, 1492–1505 (1958).

[419] W. De Roeck and F. Huveneers, Scenario for delocalization in translation-invariant systems, Phys. Rev. B **90**, 165137 (2014).

[420] M. van Horssen, E. Levi, and J. P. Garrahan, Dynamics of many-body localization in a translation-invariant quantum glass model, Phys. Rev. B **92**, 100305 (2015).

[421] J. M. Hickey, S. Genway, and J. P. Garrahan, Signatures of many-body localisation in a system without disorder and the relation to a glass transition, J. Stat. Mech.: Theory Exp. **2016**, 054047 (2016).

[422] M. Schiulaz, A. Silva, and M. Müller, Dynamics in many-body localized quantum systems without disorder, Phys. Rev. B **91**, 184202 (2015).

[423] M. Schulz, C. A. Hooley, R. Moessner, and F. Pollmann, Stark many-body localization, Phys. Rev. Lett. **122**, 040606 (2019).

[424] J. Schwinger, On gauge invariance and vacuum polarization, Phys. Rev. **82**, 664–679 (1951).

[425] S. Bravyi, D. P. DiVincenzo, and D. Loss, Schrieffer–wolff transformation for quantum many-body systems, Ann. Phys. **326**, 2793–2826 (2011).